

© Copyright 2006  
Igor V. Novosselov

# Chemical Reactor Networks for Combustion Systems Modeling

Igor V. Novosselov

A dissertation submitted in partial fulfillment of the requirement for the degree  
of

Doctor of Philosophy

University of Washington

2006

Program Authorized to offer Degree: Mechanical Engineering

University of Washington  
Graduate School

This is to certify that I have examined this copy of a doctoral dissertation by

Igor V. Novosselov

and have found that it is complete and satisfactory in all respects,  
and that any and all revisions required by the final  
examining committee have been made.

Chair of the Supervisory Committee:

\_\_\_\_\_  
Philip C. Malte  
Reading Committee:

\_\_\_\_\_  
Philip C. Malte

\_\_\_\_\_  
John C. Kramlich

\_\_\_\_\_  
David G. Nicol

\_\_\_\_\_  
James J. Riley

Date: \_\_\_\_\_

In presenting this dissertation in partial fulfillment of the requirements for the doctoral degree at the University of Washington, I agree that the Library shall make its copies freely available for inspection. I further agree that extensive copying of the dissertation is allowable only for scholarly purposes, consistent with "fair use" as prescribed in the U.S. Copyright Law. Requests for copying or reproduction of this dissertation may be referred to ProQuest Information and Learning, 300 North Zeeb Road, Ann Arbor, MI 48106-1346, 1-800-521-0600, to whom the author has granted "the right to reproduce and sell (a) copies of the manuscript in microform and/or (b) printed copies of the manuscript made from microform."

Signature\_\_\_\_\_

Date\_\_\_\_\_

University of Washington

**Abstract**

Chemical Reactor Networks for Combustion Systems Modeling

Igor V. Novosselov

Chair of the Supervisory Committee:

Professor Philip C. Malte

Department of Mechanical Engineering

This study shows the development and application of chemical reactor networks (CRN) for several combustion systems. The CRN development is based on results from computational fluid dynamics (CFD) simulations.

The University of Washington eight-step global kinetic mechanism for methane oxidation and NO formation is updated and validated in the CFD code for an experimental bluff body combustor. The CFD predicted emissions for the bluff body combustor are found to be in a good agreement with the experimental data. The eight-step global mechanism is then used in CFD modeling of generic and industrial gas turbine combustors.

The flow information from CFD modeling is analyzed and represented as an arrangement of chemical reactor elements. The CRN element arrangement, element volumes, and flow splits between the elements are adjusted based on the best agreement with CFD output over the range of pilot fuel flow rates for different premixer fuel-air ratio distributions. The resulting chemical reactor network consists of 31 elements representing zones typical of the generic

swirl stabilized combustor: main premixer flame, pilot flame, post-flame, and center and dome recirculation zones. The  $\text{NO}_x$  emissions predicted by CFD and CRN are in good agreement with one another for different injector configurations and for a range of pilot fuel flow rates.

By taking advantage of this detailed information for the generic combustor, the methodology for CFD to CRN translation is then developed. This methodology is applied to the industrial lean-premixed gas combustor. This CRN is applied to two test rig engine configurations for different engine sizes and injector circuit setups. The predicted  $\text{NO}_x$  emissions are compared to the test rig emissions data for a range of pilot fuel flow rates and fuel types. Good agreement between the predicted  $\text{NO}_x$  and the experiment data is found using both the GRI 3.0 mechanism and the global mechanism.

The CRN is able to handle complex chemical mechanisms and can provide significant insight into pollutant formation. Because of its small computational time requirement, the CRN can be used as tool for analysis of combustion systems and can be integrated into combustor design.

## Table of Contents

List of Figures .....	iv
List of Tables .....	xix
1. Introduction and Objectives .....	1
2. Literature Review .....	5
Chemical Reactor Modeling of Combustion .....	5
Introduction.....	5
Gas Turbine Application .....	6
Other applications for continuous combustion systems.....	13
Conclusions for Chemical Reactor Modeling Overview .....	16
Premixed Turbulent Combustion Regimes and Numerical Modeling Techniques .....	17
Regimes of premixed turbulent combustion .....	19
Turbulence modeling .....	27
Incorporating Chemistry into RANS Models .....	36
Summary: Turbulence Modeling.....	48
Heat Transfer Modeling .....	50
Convective Heat Transfer .....	50
Radiative Heat Transfer Modeling .....	50
Conclusions for Modeling Approaches Used in This Research.....	52
3. Eight-Step Global Mechanism for Methane Oxidation with Nitrogen Oxides Formation .....	54
Development of the Eight-Step Global Mechanism.....	54
Upgrade to the Eight-Step Global Mechanism .....	60
4. Application of the Eight-Step Global Mechanism in CFD for Bluff Body Experimental Combustor .....	64
Bluff Body Modeling .....	65
Numerical approach .....	65
Limiting Reaction Rate Approach .....	66
Results and Discussion of the Bluff Body Modeling .....	68
Oxides of Nitrogen Emissions for Bluff Body .....	73
Spatial and Temporal Premixer Non-uniformity .....	74
Turbulent Flame Fluctuations .....	74
Flame Temperature Considerations .....	76
5. Generic, Lean-premixed, Single-injector, Can-type Combustor CFD .....	87
Combustor design.....	87
Injector Profiles.....	89
Numerical Approach for the Single Injector Combustor Modeling .....	91
Results and Discussions .....	93
Non-uniform Injector Mixing Profile .....	108

6.	Development of Chemical Reactor Network for the Gas Turbine	
	Combustor .....	122
	Introduction .....	122
	Injector Modeling.....	126
	Jet Cross Mixing .....	129
	Flame Modeling .....	131
	Introduction.....	131
	Main flame .....	131
	CRN Element Volume Considerations .....	135
	Pilot Flame .....	136
	Post Flame Zone Modeling .....	141
	Recirculation Zones Modeling.....	143
	Main Recirculation Zone.....	143
	Dome Recirculation Zone .....	144
	Results of the Can-type Combustor CRN Modeling.....	148
7.	Application of CRN to Industrial Gas Turbine Combustor.....	153
	Introduction .....	153
	Gas Turbine Combustor CFD .....	157
	Effect of Temperature Fluctuations on NO Formation.....	158
	Injector 1 Profiles .....	159
	Engine Test Rig Combustor 1 with Injector 1: CRN Predictions.....	161
	NO Formation Mechanisms and Zones of Formation.....	164
	Engine Test Rig 2 with Injector 2: CRN.....	165
	Conclusion .....	168
8.	Modeling the Combustion of Hydrocarbon Fuel Blends .....	169
	Hydrocarbon Fuel Blends Combustion in Can-type Combustor.....	169
	CFD modeling .....	169
	CRN modeling: results and discussion.....	179
	Hydrocarbon Fuel Blend Combustion in Engine Test Rig 2 .....	181
	CRN with Mixing Control Rate for Hydrocarbon Fuel Blends .....	184
9.	Chemical Reactor Modeling of Jet Stirred Reactor.....	187
	Modeling Approach .....	188
	Hydrocarbon Combustion Modeling.....	192
	Hydrogen Combustion Modeling.....	194
	H <sub>2</sub> -CO Fuel Blend Combustion Modeling.....	196
10.	Conclusions .....	199
	References .....	202
	Appendix 1: University of Washington Chemical Kinetic Code.....	214
	Introduction .....	214
	The present form of the UW chemical kinetic code has evolved from the work of .....	214

Code Networking Capabilities .....	216
Input Data File.....	218
Appendix 2: Turbulent Mixing Rate for Use in Global Mechanism and Limiting Rate Approach .....	220
Appendix 3: CRN Sample Calculation .....	223
Generic, Single-Injector, Can-type Combustor.....	223
13-element CRN for JSR .....	230
Appendix 4: Atmospheric Pressure Jet–Stirred Reactor Measurements .....	234
Appendix 5: Modeling the Emissions of Wood Dust Burners.....	239
Introduction .....	239
Development of Finite Rate Global Chemistry for Wood Dust Combustion.....	240
Wood Composition .....	241
Thermo-Chemical Properties.....	244
Rates of Pyrolysis.....	246
Development of the Global Kinetic Mechanism for Wood Combustion .....	247
Global Chemistry Modeling Approach in the Laboratory Wood Dust Combustor .....	252
CFD Simulation of the Laboratory Wood Dust Burner .....	257
Effect of Soot on the Combustion Temperature .....	259
CFD Results for the Laboratory Wood Dust Burner .....	259
Chemical Reactor Network for UW Laboratory Wood Dust Burner .....	272
Industrial Wood Dust Burner .....	278
CRN Modeling of the Industrial Cyclone Burner.....	287

## List of Figures

Figure 2-1. The CRN for evaluating NO <sub>x</sub> and CO emissions (from Rubins and Pratt 1991).....	8
Figure 2-2. Network for evaluating LBO conditions (from Sturgess, 1996). ....	9
Figure 2-3. Network for evaluating jet fuel chemical mechanism for perforated plate flame holder (from Sturgess, 1997). ....	10
Figure 2-4. CRN incorporating finite-rate mixing model (from Nicol et al 1997). ....	11
Figure 2-5. Schematic of the TSL model (from Broadwell and Lutz, 1998). ....	11
Figure 2-6. Network for evaluating NO <sub>x</sub> emissions for high fuel-air ratio turbines (from Roby et al. 2003). ....	12
Figure 2-7. An arrangement of chemical reactor elements for early region of a wood dust burner (from Malte et al., 1996). ....	13
Figure 2-8. Ideal reactors network for furnace from Faravelli et al. (2001). ....	15
Figure 2-9. Network developed by Niksa and Lui (2002). ....	16
Figure 2-10. Schematic illustration of a premixed methane-air flame, from Peters (2000). ....	22
Figure 2-11. Regimes of premixed turbulent combustion, from Peters (2000). ....	22
Figure 2-12. Schematic illustration of the corrugated flamelets regime from Peters (2000). ....	24
Figure 2-13. Inertial range scale for corrugated flamelets regime, from Peters (2000). ....	25
Figure 2-14. Schematic illustration of the thin reaction zone regime, from Peters (2000). ....	26
Figure 2-15. Inertial range for the thin reaction zones regime, from Peters (2000). ....	27
Figure 2-16. Assumed PDF of the progress variable for BML model. ....	40
Figure 2-17. Graphical interpretation of G field. ....	42
Figure 3-1. Formation of NO in the flame (modeled as PSR) via prompt NO and NNH mechanisms versus global reaction 5. Inlet temperature: 5 atm (483 K), 10 atm (592 K), 20 atm (716 K); temperature in the PSR corresponds to the adiabatic flame temperature. Residence time in the PSR varies from the blowout to 2.5 ms. Longer residence times lead to quenching of the prompt and NNH chemistry. ....	63

Figure 4-1. Schematic of the modeled bluff body combustor: side (upper diagram) and top (lower diagram) views. The 2D modeling plane is shown in the upper drawing. Because of symmetry only the upper half of the plane is modeled.....	70
Figure 4-2. The end view of the bluff body combustor is shown. The position of the test probe location is shown in grey, red dash line show the direction of imaginary probe rotation used in the emission analysis. ....	71
Figure 4-3. Carbon monoxide emissions for bluff body burner. ....	72
Figure 4-4. NO <sub>x</sub> exit plane emissions for bluff body burner. ....	73
Figure 4-5. Turbulent fluctuation correction for CFD modeling of NO <sub>x</sub> emissions for bluff body burner.....	76
Figure 4-6. Velocity magnitude (m/s). ....	80
Figure 4-7. Velocity vectors colored by the velocity magnitude in the recirculation region. ....	80
Figure 4-8. Temperature profile, K, maximum temperature 1930 K.....	81
Figure 4-9. Velocity vectors colored by temperature in the recirculation region. ....	81
Figure 4-10. Methane mole fraction profile. ....	82
Figure 4-11. Methane mole fraction for the exit plane and upstream.....	82
Figure 4-12. Carbon monoxide mole fraction, maximum CO is 2.15%, wet basis actual O <sub>2</sub> . ....	83
Figure 4-13. Nitrogen oxides mole fraction, maximum is 13.9 ppmv, wet basis actual O <sub>2</sub> . ....	83
Figure 4-14. NO mole fraction in the recirculation region. ....	84
Figure 4-15. NO rate of formation via N <sub>2</sub> O and non-equilibrium Zeldovich mechanism combined, maximum rate is 2.23e-3 kmol/m <sup>3</sup> /s.....	84
Figure 4-16. Same as above for forward part of burner.....	85
Figure 4-17. NO rate of formation via prompt and NNH mechanisms combined, maximum rate is 1.834e-4 kmol/m <sup>3</sup> /s. ....	85
Figure 4-18. NO rate of formation via thermal Zeldovich mechanism, maximum rate is 3.45e-5 kmol/m <sup>3</sup> /s.....	86
Figure 4-19. NO rate of formation via thermal N <sub>2</sub> O+H reaction, maximum rate is 2.04e-6 kmol/m <sup>3</sup> /s.....	86
Figure 4-20. NO rate of formation via thermal N <sub>2</sub> O+O reaction, maximum rate is 2.58e-5 kmol/m <sup>3</sup> /s. ....	86
Figure 5-1. Schematic drawing of the modeled system for a single-injector, can-type combustor.....	88
Figure 5-2. Axial velocity and mass flux at the exit of the injector.....	91

Figure 5-3. Computation grid for the can-type combustor with refined grid in the pilot flame zone and at the combustor walls, only the first half of the combustor is shown. ....	92
Figure 5-4. Temperature contours plot from the CFD simulation showing the presence of the different combustion zones, case with flat injector fuel–air ratio profile and neutral pilot is shown. ....	94
Figure 5-5. NO formation in can-type combustor.....	95
Figure 5-6. Temperature contour plot for the 50% pilot case, maximum value is 1710 K. ....	97
Figure 5-7. Temperature contour plot for the 150% pilot case, maximum value is 2166 K. ....	97
Figure 5-8. Temperature contour plot for the 50% pilot case, maximum value is 1710 K, the first half of the combustor is shown. ....	97
Figure 5-9. Temperature contour plot for the 150% pilot case, maximum value is 2166 K, the first half of the combustor is shown.....	97
Figure 5-10. Velocity magnitude, 50% pilot, maximum is 120 m/s.....	98
Figure 5-11. Velocity magnitude, 150% pilot, maximum is 120 m/s.....	98
Figure 5-12. Streamlines colored by temperature, 50% pilot case. ....	98
Figure 5-13. Streamlines colored by temperature, 150% pilot case. ....	98
Figure 5-14. Streamlines colored by temperature for 50% pilot.....	99
Figure 5-15. Streamlines colored by temperature, 150% pilot case. ....	99
Figure 5-16. Vectors of velocity colored by temperature, the first half of the combustor for the 50% pilot case. ....	99
Figure 5-17. Vectors of velocity colored by temperature, the first half of the combustor for the 150% pilot case. ....	99
Figure 5-18. Contour of the local fuel-air equivalence ratio, the 50% pilot case, maximum value is 0.492 at the main swirler inlet. ....	100
Figure 5-19. Contour of the local fuel-air equivalence ratio, the 50% pilot case, maximum value is 0.723 at the pilot inlet.....	100
Figure 5-20. Contour of the local fuel-air equivalence ratio for the 50% pilot case, for the first half of the combustor (refined palette). ....	100
Figure 5-21. Contour of the local fuel-air equivalence ratio for the 150% pilot case, for the first half of the combustor (refined palette). ....	100
Figure 5-22. Mole fraction of O <sub>2</sub> for the 50% pilot case for the first half of the combustor, minimum value is 0.106 kmolCO <sub>2</sub> /kmol tot in the center recirculation zone and the post flame zone. ....	101
Figure 5-23. Mole fraction of O <sub>2</sub> for the 50% pilot case for the first half of the combustor, minimum value is 0.0575 kmolCO <sub>2</sub> /kmol tot in the pilot flame zone, the value in the center recirculation zone is 0.106 kmolO <sub>2</sub> /kmol tot. ....	101

Figure 5-24. Mole fraction of CH <sub>4</sub> for the 50% pilot case for the first half of the combustor, maximum value is 0.0485 kmolCH <sub>4</sub> /kmol tot at the main swirler inlet. ....	101
Figure 5-25. Mole fraction of CH <sub>4</sub> for the 150% pilot case for the first half of the combustor, maximum value is 0.0695 kmolCH <sub>4</sub> /kmol tot at the pilot inlet. ....	101
Figure 5-26. Rate of methane destruction (reaction 1) for the 50% pilot case, maximum rate is 65 kmol/m <sup>3</sup> /s. ....	102
Figure 5-27. Rate of methane destruction (reaction 1) for the 150% pilot case, maximum rate is 595 kmol/m <sup>3</sup> /s. ....	102
Figure 5-28. Mole fraction of CO <sub>2</sub> for the 50% pilot case for the first half of the combustor, maximum value is 0.0456 kmolO <sub>2</sub> /kmol tot in the center recirculation zone and the post flame zone. ....	102
Figure 5-29. Mole fraction of CO <sub>2</sub> for the 150% pilot case for the first half of the combustor, maximum value is 0.067 kmolO <sub>2</sub> /kmol tot in the pilot flame zone, the value in the center recirculation zone is 0.045 kmolO <sub>2</sub> /kmol tot. ....	102
Figure 5-30. Mole fraction of CO for the 50% pilot case for the first half of the combustor, maximum value is 0.016 kmolCO/kmol tot in the main flame zone. ....	103
Figure 5-31. Mole fraction of CO for the 150% pilot case for the first half of the combustor, maximum is 0.02 kmolCO/kmol tot in the pilot flame zone, the value in the main flame zone is 0.015 kmolO <sub>2</sub> /kmol tot. ....	103
Figure 5-32. Rate of CO destruction (reaction 2) for 50% pilot case, maximum rate is 30 kmol/m <sup>3</sup> /s. ....	103
Figure 5-33. Rate of CO destruction (reaction 2) for 150% pilot case, maximum rate is 240 kmol/m <sup>3</sup> /s. ....	103
Figure 5-34. Rate of CO <sub>2</sub> dissociation (reaction 3) for 50% pilot case, maximum rate is 0.002 kmol/m <sup>3</sup> /s. ....	104
Figure 5-35. Rate of CO <sub>2</sub> dissociation (reaction 3) for 150% pilot case, maximum rate is 3.35 kmol/m <sup>3</sup> /s. ....	104
Figure 5-36. Mole fraction of NO for the 50% pilot case for the first half of the combustor, maximum value is 3.1 ppmv NO, wet, not corrected. ....	104
Figure 5-37. Mole fraction of NO for the 150% pilot case for the first half of the combustor, maximum value is 93 ppmv NO, wet, not corrected. ....	104
Figure 5-38. Rate of NO formation via non-thermal nitrous oxide and Zeldovich mechanisms (reaction 4) for the 50% pilot case, maximum rate is 5.78e-4 kmol/m <sup>3</sup> /s. ....	105

Figure 5-39. Rate of NO formation via non-thermal nitrous oxide and Zeldovich mechanisms (reaction 4) for the 150% pilot case, maximum rate is $1.78\text{e-}2 \text{ kmol/m}^3/\text{s}$ .	105
Figure 5-40. Rate of NO formation via prompt and NNH mechanisms (reaction 5) for the 50% pilot case, maximum rate is $7.25\text{e-}4 \text{ kmol/m}^3/\text{s}$ .	105
Figure 5-41. Rate of NO formation via prompt and NNH mechanisms (reaction 5) for the 150% pilot case, maximum rate is $1.23\text{e-}1 \text{ kmol/m}^3/\text{s}$ .	105
Figure 5-42. Rate of NO formation via thermal nitrous oxide mechanism assuming H-atom equilibrium (reaction 6) for the 50% pilot case, maximum rate is $3.9\text{e-}8 \text{ kmol/m}^3/\text{s}$ .	106
Figure 5-43. Rate of NO formation via thermal nitrous oxide mechanism assuming H-atom equilibrium (reaction 6) for the 150% pilot case, maximum rate is $1.03\text{e-}4 \text{ kmol/m}^3/\text{s}$ .	106
Figure 5-44. Rate of NO formation via thermal nitrous oxide mechanism assuming O-atom equilibrium (reaction 7) for the 50% pilot case, maximum rate is $1.85\text{e-}6 \text{ kmol/m}^3/\text{s}$ .	106
Figure 5-45. Rate of NO formation via thermal nitrous oxide mechanism assuming O-atom equilibrium (reaction 7) for the 150% pilot case, maximum rate is $3.9\text{e-}4 \text{ kmol/m}^3/\text{s}$ .	106
Figure 5-46. Rate of NO formation via thermal Zeldovich mechanism (reaction 8) for the 50% pilot case, maximum rate is $7.74\text{e-}7 \text{ kmol/m}^3/\text{s}$ .	107
Figure 5-47. Rate of NO formation via thermal Zeldovich mechanism (reaction 8) for the 50% pilot case, maximum rate is $1.56\text{e-}3 \text{ kmol/m}^3/\text{s}$ .	107
Figure 5-48. Linear fuel-air equivalence ratio distribution for the modeled injector.	108
Figure 5-49. NO formation mechanisms in can combustor with linear injector fuel-air mixing profile.	110
Figure 5-50. Temperature contour plot for flat injector mixing profile, maximum value is 1750 K.	112
Figure 5-51. Temperature contour plot for linear injector mixing profile, maximum value is 1950 K.	112
Figure 5-52. Temperature contour plot for flat injector profile, maximum value is 1750 K, only the first half of the combustor is shown.	112
Figure 5-53. Temperature contour plot for linear mixing profile, maximum value is 1950 K, only the first half of the combustor is shown.	112
Figure 5-54. Velocity magnitude for flat profile, max. is 120 m/s.	113
Figure 5-55. Velocity magnitude for linear profile, max. is 120 m/s.	113
Figure 5-56. Streamlines colored by temperature for flat profile.	113
Figure 5-57. Streamlines colored by temperature for linear profile.	113
Figure 5-58. Streamlines colored by temperature for flat profile.	113

Figure 5-59. Streamlines colored by temperature for linear profile. ....	113
Figure 5-60. Vectors of velocity colored by temperature for the first half of the combustor for flat injector mixing profile. ....	114
Figure 5-61. Vectors of velocity colored by temperature for the first half of the combustor for linear injector mixing profile. ....	114
Figure 5-62. Contour of local fuel-air equivalence ratio for flat injector mixing profile, maximum value is 0.475. ....	114
Figure 5-63. Contour of local fuel-air equivalence ratio for linear mixing profile, maximum value is 0.623 at the inner part of injector inlet. ....	114
Figure 5-64. Contour of local fuel-air equivalence ratio for flat injector profile, for the first half of the combustor (refined palette). ....	115
Figure 5-65. Contour of local fuel-air equivalence ratio for linear injector profile case, for the first half of the combustor (refined palette). ....	115
Figure 5-66. Mole fraction of $O_2$ for a flat injector mixing profile case for the first half of the combustor, minimum value is 0.104 kmol $O_2$ /kmol tot in the center recirculation zone and the post flame zone. ....	115
Figure 5-67. Mole fraction of $O_2$ for linear injector profile case for the first half of the combustor, minimum value is 0.08 kmol $O_2$ /kmol tot in the inner part of the main flame zone, the value in the center recirculation zone is 0.106 kmol $O_2$ /kmol tot. ....	115
Figure 5-68. Mole fraction of $CH_4$ for a flat injector profile case (first half of the combustor), maximum value is 0.0473 kmol $CH_4$ /kmol tot. ....	116
Figure 5-69. Mole fraction of $CH_4$ for linear injector profile case (first half of the combustor), maximum value is 0.0619 kmol $CH_4$ /kmol tot. ....	116
Figure 5-70. Rate of methane destruction (reaction 1) for flat injector mixing profile, maximum value is 79 kmol/ $m^3$ /s. ....	116
Figure 5-71. Rate of methane destruction (reaction 1) for linear injector mixing profile, maximum value is 149 kmol/ $m^3$ /s. ....	116
Figure 5-72. Mole fraction of $CO_2$ for flat injector mixing profile for the first half of the combustor, maximum value is 0.0464 kmol $CO_2$ /kmol tot in the center recirculation zone and the post flame zone. ....	117
Figure 5-73. Mole fraction of $CO_2$ for linear injector profile for the first half of the combustor, maximum value is 0.0574 kmol $CO_2$ /kmol tot, the value in the center recirculation zone is 0.045 kmol $CO_2$ /kmol tot. ....	117
Figure 5-74. Mole fraction of CO for flat injector profile for the first half of the combustor, maximum value is 0.016 kmolCO/kmol tot in the main flame zone. ....	117
Figure 5-75. Mole fraction of CO for linear injector profile for the first half of the combustor, maximum value is 0.015 kmolCO/kmol tot in the main flame zone. ....	117

Figure 5-76. Rate of CO destruction (reaction 2) for flat injector mixing profile, maximum value is 31 kmol/m <sup>3</sup> /s.....	118
Figure 5-77. Rate of CO destruction (reaction 2) for linear injector mixing profile, maximum value is 80 kmol/m <sup>3</sup> /s. ....	118
Figure 5-78. Rate of CO <sub>2</sub> dissociation (reaction 3) for flat injector mixing profile, maximum value is 0.004 kmol/m <sup>3</sup> /s. ....	118
Figure 5-79. Rate of CO <sub>2</sub> dissociation (reaction 3) for linear injector mixing profile, maximum value is 0.14 kmol/m <sup>3</sup> /s. ....	118
Figure 5-80. Mole fraction of NO for flat injector mixing profile for the first half of the combustor, maximum value is 4.2 ppmv NO, wet, not corrected. ....	119
Figure 5-81. Mole fraction of NO for linear injector mixing profile for the first half of the combustor, maximum value is 33 ppmv NO, wet, not corrected. ....	119
Figure 5-82. Rate of NO formation via non-thermal nitrous oxide and Zeldovich mechanisms (reaction 4) for flat injector mixing profile, maximum value is 6.7e-4 kmol/m <sup>3</sup> /s. ....	119
Figure 5-83. Rate of NO formation via non-thermal nitrous oxide and Zeldovich mechanisms (reaction 4) for linear injector mixing profile, maximum value is 4.5e-3 kmol/m <sup>3</sup> /s. ....	119
Figure 5-84. Rate of NO formation via prompt and NNH mechanisms (reaction 5) for flat injector profile, maximum value is 7.6e-4 kmol/m <sup>3</sup> /s. ....	120
Figure 5-85. Rate of NO formation via prompt and NNH mechanisms (reaction 5) for linear injector profile, maximum value is 1.4e-2 kmol/m <sup>3</sup> /s. ....	120
Figure 5-86. Rate of NO formation via thermal nitrous oxide mechanism assuming H-atom equilibrium (reaction 6) for flat injector mixing profile, maximum value is 8.6e-8 kmol/m <sup>3</sup> /s. ....	120
Figure 5-87. Rate of NO formation via thermal nitrous oxide. mechanism assuming H-atom equilibrium (reaction 6) for linear injector mixing profile, maximum value is 3.85e-6 kmol/m <sup>3</sup> /s. ....	120
Figure 5-88. Rate of NO formation via thermal nitrous oxide mechanism assuming O-atom equilibrium (reaction 7) for flat injector mixing profile, maximum value is 3.2e-6 kmol/m <sup>3</sup> /s. ....	121
Figure 5-89. Rate of NO formation via thermal nitrous oxide mechanism assuming O-atom equilibrium (reaction 7) for linear injector mixing profile, maximum value is 4.5e-4 kmol/m <sup>3</sup> /s. ....	121
Figure 5-90. Rate of NO formation via thermal Zeldovich mechanism (reaction 8) for flat injector mixing profile, maximum value is 1.7e-6 kmol/m <sup>3</sup> /s. ....	121

Figure 5-91. Rate of NO formation via thermal Zeldovich mechanism (reaction 8) for linear injector mixing profiles, maximum value is $6.61 \times 10^{-5}$ kmol/m <sup>3</sup> /s.....	121
Figure 6-1. Main zones of the generic GT combustor for the flat injector fuel-air ratio profile with neutral pilot case, overall injector $\Phi = 0.475$ . Temperature contour plot is shown, maximum is 1750K, and minimum is 685K. Repeat of Figure 5-4.....	123
Figure 6-2. Flame zone for the flat fuel-air ratio profile with neutral pilot case. Carbon monoxide profiles are shown; maximum value of CO is 1.58%. Overall injector $\Phi = 0.475$ .....	124
Figure 6-3. 31-element CRN for the single-injector, can-type, GT combustor.....	125
Figure 6-4. Axial velocity and air mass flux distribution at the injector outlet, repeat of Figure 5-2. ....	126
Figure 6-5. Mapping of the air mass flow rates and the fuel air equivalence ratio onto CRN. Red line in the injector mixing profile plot corresponds to flat profile, black line corresponds to linear profile. ....	128
Figure 6-6. Injector flow splits for the can-type combustor CRN; $\Phi_{\text{flat}}$ indicates the fuel-air equivalence ratio for the flat injector profile case; $\Phi_{\text{linear}}$ indicates the fuel-air equivalence ratio for the linear injector mixing profile from Figure 6-5. ....	129
Figure 6-7. Relative $\Phi$ distribution in can-type combustor with linear fuel-air ratio in injector, repeat of Figure 5-64. ....	130
Figure 6-8. Cross-stream mixing sub-model in CRN. ....	130
Figure 6-9. Flame zone mapping onto the CRN. Carbon monoxide mole fraction contours are shown. Maximum value is 1.58% by volume. ....	134
Figure 6-10. Flow rates in the center recirculation zone, dome recirculation zone, and the stream from the injector ("jet") for Combustor A (single-injector, can-type-type) operated with $\Phi = 0.49$ . The distance from the front of the combustor = x, (from Novosselov 2002). ....	134
Figure 6-11. Iso-CO lines (CO=0.3%) colored by temperature, neutral pilot case with flat injector profile. ....	135
Figure 6-12. Streamlines colored by temperature for flat injector mixing profile and neutral pilot, repeat of Figure 5-58.....	137
Figure 6-13. Mole fraction of CO for the 50% pilot case (pilot $\Phi$ is 0.24); maximum value is 0.016 kmolCO/kmol tot in the main flame zone. Low levels of CO indicate that well defined pilot flame does not exist. Repeat of Figure 5-30.....	138

Figure 6-14. Mole fraction of CO for the 150% pilot case (pilot $\Phi$ is 0.71), maximum value is 0.02 kmolCO/kmol tot in the pilot flame zone, the value in the main flame zone is 0.015 kmolO <sub>2</sub> /kmol tot. Repeat of Figure 5-31. ....	138
Figure 6-15. Pilot flame zone mapping onto the CRN. Carbon monoxide mole fraction contours are shown. Maximum value is 1.5% by volume. Flat injector profile with 50% pilot case is shown. ....	140
Figure 6-16. CRN flow split diagram for the pilot sub-model. ....	141
Figure 6-17. Local fuel-air equivalence ratio in the can-type combustor, neutral pilot case with flat injector mixing profile is shown, maximum value is 0.475, blue - below 0.35. ....	142
Figure 6-18. Temperature in the can-type combustor, the neutral pilot case with flat injector mixing profile case is shown, maximum value is 1750K, blue – below 1500K. ....	142
Figure 6-19. Flow field mapping onto the CRN for post flame and recirculation zones, temperature field for flat injector profile simulation is shown, neutral pilot. ....	142
Figure 6-20. CRN post-flame zone sub-model. ....	143
Figure 6-21. Recirculation region defined by $V_x=0$ m/s iso-surface, repeat of the Figure 5-4. ....	144
Figure 6-22. CRN Recirculation flow splits for recirculation zone sub-model. ....	145
Figure 6-23. 31-element chemical reactor network for single-injector, can-type GT combustor. ....	146
Figure 6-24. Nodal diagram of the 31-element chemical reactor network for single-injector, can-type GT combustor. ....	147
Figure 6-25. Comparison of predicted NO <sub>x</sub> emissions between CFD and CRN models for single injector, can-type combustor with uniform injector fuel-air equivalence ratio. ....	151
Figure 6-26. Comparison of predicted NO <sub>x</sub> emissions between CFD and CRN models for single injector, can-type combustor with linear injector fuel-air equivalence ratio. ....	151
Figure 7-1. 31-element CRN for evaluating the NO and CO emissions of engine test rig combustor. ....	156
Figure 7-2. Engine test rig combustor 1 configuration and typical CFD predicted temperature profile plot at full load condition. Temperature normalized by the adiabatic equilibrium temperature calculated for the mean fuel-air ratio of the premixer, from manufacturer. ....	158

Figure 7-3. Fuel-air ratio profile at the premixer outlet, i.e., main circuit of injector, for engine test rig 1. The fuel-air ratio is normalized by its mean value. The radial distance shown is the distance outward from the inner radius of premixer divided by the outer to inner radius difference (Injector 1).....	160
Figure 7-4. Comparison of measured and predicted NO <sub>x</sub> emissions for engine test rig1 with injector 1. ....	162
Figure 7-5. Comparison of measured and predicted NO emissions for engine test rig combustor 2 with injector 2. ....	167
Figure 8-1. Temperature contour plot for methane combustion, max. value is 1750 K, the first half of the combustor is shown, repeat of Figure 5-53. ....	172
Figure 8-2. Temperature contour plot for combustion of blend 3, max. value is 1740 K, the first half of the combustor is shown. ....	172
Figure 8-3. Mole fraction of CH <sub>4</sub> for methane combustion (first half of the combustor), maximum value is 0.0473 kmolCH <sub>4</sub> /kmol total, repeat of Figure 5-69. ....	172
Figure 8-4. Mole fraction of CH <sub>4</sub> for combustion of blend 3 (first half of the combustor), maximum value is 0.007 kmolCH <sub>4</sub> /kmol total. ....	172
Figure 8-5. Rate of methane destruction for methane combustion, maximum value is 79 kmol/m <sup>3</sup> /s, repeat of Figure 5-7. ....	173
Figure 8-6. Rate of methane destruction for combustion of blend 3, maximum value is 11 kmol/m <sup>3</sup> /s. ....	173
Figure 8-7. Mole fraction of C <sub>3</sub> H <sub>8</sub> for blend 3 (first half of the combustor), maximum value is 0.016 kmolC <sub>3</sub> H <sub>8</sub> /kmol total. ....	173
Figure 8-8. Rate of propane destruction for blend 3, maximum value is 42 kmol/m <sup>3</sup> /s. ....	174
Figure 8-9. Mole fraction of CO for methane combustion for the first half of the combustor, maximum value is 0.016 kmolCO/kmol total in the main flame zone, repeat of Figure 5-75. ....	174
Figure 8-10. Mole fraction of CO for combustion of blend 3 for the first half of the combustor, maximum value is 0.037 kmolCO/kmol total in the main flame zone. ....	174
Figure 8-11. Rate of CO destruction for methane combustion, maximum value is 31 kmol/m <sup>3</sup> /s repeat of Figure 5-77. ....	175
Figure 8-12. Rate of CO destruction for combustion of blend 3, maximum value is 31 kmol/m <sup>3</sup> /s. ....	175

Figure 8-13. Mole fraction of NO for methane combustion for the first half of the combustor, maximum value is 4.2 ppmv NO, at the combustor exit the NO is 2.0 ppmv, wet, not corrected, repeat of Figure 5-81. ....	175
Figure 8-14. Mole fraction of NO for combustion of blend 3 for the first half of the combustor, maximum value is 5.3 ppmv NO, at the combustor exit NO is 2.6 ppmv, wet, not corrected. ....	175
Figure 8-15. Rate of NO formation via non-thermal nitrous oxide and Zeldovich mechanisms (reaction 4) for methane combustion, maximum value is $6.7\text{e-}4 \text{ kmol/m}^3/\text{s}$ , repeat of Figure 5-83. ....	176
Figure 8-16. Rate of NO formation via non-thermal nitrous oxide and Zeldovich mechanisms (reaction 4) for combustion of blend 3, maximum value is $5.2\text{e-}4 \text{ kmol/m}^3/\text{s}$ . ....	176
Figure 8-17. Rate of NO formation via prompt and NNH mechanisms (reaction 5) for methane combustion, maximum value is $7.6\text{e-}4 \text{ kmol/m}^3/\text{s}$ , repeat of Figure 5-85. ....	176
Figure 8-18. Rate of NO formation via prompt and NNH mechanisms (reaction 5) for combustion of gas3, maximum value is $6.8\text{e-}4 \text{ kmol/m}^3/\text{s}$ . ....	176
Figure 8-19. Rate of NO formation via thermal nitrous oxide mechanism assuming H-atom equilibrium (reaction 6) for methane combustion, maximum value is $8.6\text{e-}8 \text{ kmol/m}^3/\text{s}$ . ....	177
Figure 8-20. Rate of NO formation via thermal nitrous oxide mechanism assuming H-atom equilibrium (reaction 6) for combustion of blend 3, maximum value is $5.85\text{e-}8 \text{ kmol/m}^3/\text{s}$ . ....	177
Figure 8-21. Rate of NO formation via thermal nitrous oxide mechanism assuming O-atom equilibrium (reaction 7) for methane combustion, maximum value is $3.2\text{e-}6 \text{ kmol/m}^3/\text{s}$ . ....	177
Figure 8-22. Rate of NO formation via thermal nitrous oxide mechanism assuming O-atom equilibrium (reaction 7) for combustion of blend 3, maximum value is $2.8\text{e-}8 \text{ kmol/m}^3/\text{s}$ . ....	177
Figure 8-23. Rate of NO formation via thermal Zeldovich mechanism (reaction 8) for methane combustion, maximum value is $1.7\text{e-}6 \text{ kmol/m}^3/\text{s}$ . ....	178
Figure 8-24. Rate of NO formation via thermal Zeldovich mechanism (reaction 8) for combustion of gas3, maximum value is $1.23\text{e-}6 \text{ kmol/m}^3/\text{s}$ . ....	178
Figure 8-25. Comparison of the CFD and CRN NO predictions for methane and the hydrocarbon fuel blends as a function of the percentage of neutral pilot for the can-type combustor. ....	180

Figure 8-26. Comparison of the CFD and CRN NO prediction for methane and the hydrocarbon fuel blends as a function C/H fuel ratio for can-type combustor.....	181
Figure 8-27. Engine test rig 2 NO <sub>x</sub> emissions for hydrocarbon blends with uniform fuel-air ratio injector profile and CRN predictions with GRI 3.0 mechanism as a function of percent pilot. ....	183
Figure 8-28. Engine test rig 2 NO <sub>x</sub> emissions for hydrocarbon blends with uniform fuel-air ratio injector profile and CRN predictions with GRI 3.0 mechanism as a function C/H fuel ratio. ....	183
Figure 8-29. Predicted NO <sub>x</sub> emissions for CRN using detailed chemical kinetic mechanism GRI3.0 and global mechanism with mixing controlled reaction for fuel oxidation. ....	185
Figure 8-30. Engine test rig 2 NO <sub>x</sub> emissions for hydrocarbon blends with uniform fuel-air ratio injector profile and CRN predictions with global mechanism with mixing control as a function of percent pilot.....	186
Figure 8-31. Engine test rig 2 NO <sub>x</sub> emissions for hydrocarbon blends with uniform fuel-air ratio injector profile and CRN predictions with global mechanism with mixing control as a function of C/H fuel ratio. ....	186
Figure 9-1. Schematic representation of the jet-stirred reactor.....	191
Figure 9-2. 13-element CRN for evaluating NO <sub>x</sub> and CO behavior of the JSR.....	192
Figure 9-3. Modeled and measured NO <sub>x</sub> for the hydrocarbon-fuels experiments of Malte for the 64 cm <sup>3</sup> JSR. ....	193
Figure 9-4. Modeled and measured CO for the hydrocarbon-fuels experiments of Malte for the 64 cm <sup>3</sup> JSR. ....	194
Figure 9-5. Modeled and measured NO <sub>x</sub> for the hydrogen combustion .....	196
Figure 9-6. Modeled and measured NO for the H <sub>2</sub> -CO fuels blend.....	197
Figure 9-7. Modeled and measured NO for the H <sub>2</sub> -CO fuels blend.....	198
Figure A1-0-1 Nodal diagram for two reactor in series arrangement.....	217
Figure A1-0-2 Nodal diagram for two reactor in series arrangement.....	217
Figure A1-0-3 Nodal diagram for three reactor arrangement including a recycle element .....	218
Figure A4-0-1 Schematic drawing of the experimental setup from Lee (2000). ....	237
Figure A4-0-2. Experimental data for 16cm <sup>3</sup> and 64cm <sup>3</sup> JSRs. ....	238
Figure A5-1. Diagram of devolatilization and combustion for a wood particle. ....	241
Figure A5-2. Polynomial fits for heat capacity of wood and char. ....	246
Figure A5-3. Schematic drawing of the laboratory wood dust burner, the dimension is in meters. ....	253

Figure A5-4. Schematic diagram of the flow pattern in the lower part of the burner. ....	254
Figure A5-5. Wood dust burner for computational grid. ....	255
Figure A5-6. Primary combustion zone. ....	256
Figure A5-7. Throat section. ....	256
Figure A5-8. Main burner section. ....	257
Figure A5-9. Burner extension. ....	257
Figure A5-10 Axial temperature profile for UW laboratory wood dust burner. The CFD calculations are shown at the probe location and as the cross-sectional, area-averaged values at the probe axial coordinate. At the first two locations the wall temperature is higher than the gas temperature, thus the thermocouple corrected value is less than the raw data. ....	261
Figure A5-11. Axial CO profile for UW laboratory wood dust burner. The maximum resolution for the experimental sampling equipment is 5%. ....	262
Figure A5-12. Axial CO <sub>2</sub> profile for UW laboratory wood dust burner. ....	262
Figure A5-13. Axial O <sub>2</sub> profile for UW laboratory wood dust burner. ....	263
Figure A5-14. Velocity magnitude plot, maximum value is about 17 m/s. ....	264
Figure A5-15. Axial velocity, maximum value is 11 m/s. ....	264
Figure A5-16. Tangential velocity, maximum value is 16.5 m/s. ....	264
Figure A5-17. Gas temperature in the combustor, maximum value is 2260 K. ....	265
Figure A5-18. Mole fraction of O <sub>2</sub> . ....	265
Figure A5-19. Mole fraction of carbon monoxide, maximum value is about 22%. ....	265
Figure A5-20. Mole fraction CO <sub>2</sub> , maximum value is about 17%. ....	266
Figure A5-21. Mole fraction of H <sub>2</sub> O, maximum is about 20%. ....	266
Figure A5-22. Mole fraction of methane, maximum value is about 12%. ....	266
Figure A5-23. Mole fraction of tar, maximum value is about 30%, typical concentration near the throat is 5%. ....	267
Figure A5-24. Inside wall temperature, maximum value is 1480K. ....	267
Figure A5-25. 20 micron particle that burns out, particle track colored by the particle residence time. ....	268
Figure A5-26. 20 micron particle that burns out, particle track colored by the mass of the particle. ....	268
Figure A5-27. 20 micron particle that burns out, particle track colored by the particle temperature. ....	268

Figure A5-28. 20 micron particle that burns out, particle track colored by $O_2$ mole fraction in the vicinity of the particle. The $O_2$ concentration at the end of the particle track is 2%.....	269
Figure A5-29. 600 micron particle that does not burn out, particle track colored by the particle residence time. ....	269
Figure A5-30. 600 micron particle that does not burn out, particle track colored by the mass of the particle. ....	269
Figure A5-31. 600 micron particle that does not burn out, particle track colored by the particle temperature. ....	270
Figure A5-32. 600 micron particle that does not burn out, particle track colored by $O_2$ mole fraction in the vicinity of the particle. ....	270
Figure A5-33. 20 micron particle that does not burn out, particle track colored by the mass of the particle. ....	270
Figure A5-34. 20 micron particle that does not burn out, particle track colored by $O_2$ mole fraction in the vicinity of the particle. ....	271
Figure A5-35. Percentage conversion of fuel nitrogen to $NO_x$ emission at the exit of CRN as a function of fuel-air equivalence ratio. ....	276
Figure A5-36. Diagram of chemical reactor network for laboratory wood dust burner. ....	277
Figure A5-37. Combustion system using the industrial wood dust burner. ....	278
Figure A5-38. Grid for McConnell 48 wood dust burner. ....	280
Figure A5-39. Contour plot of velocity magnitude in xy-plane, choke cross-section and exit plane. ....	280
Figure A5-40. Contour plot of temperature in xy-plane, choke cross-section and exit plane, Maximum value is 2200K, average flame temperature is 1800 K, choke exit temperature is 1130K. ....	281
Figure A5-41. Contour plot of oxygen mole fraction in xy-plane, choke cross-section and exit plane, the plot shows characteristics of diffusion flame: fuel rich and oxygen rich regions are depicted.....	281
Figure A5-42. Contour plot of carbon monoxide mole fraction in xy-plane, choke cross-section and exit plane, the plot shows high concentration (15%) of carbon monoxide in the fuel rich region, CO concentration at the choke plane is 1.9%. ....	282
Figure A5-43. Contour plot of carbon dioxide mole fraction in xy-plane, choke cross-section and exit plane. $CO_2$ concentrations in the rich core flame varies between 6-10%, the concentration in the flame is about 13%. ....	282

Figure A5-44. Contour plot of tar mole fraction in xy-plane, choke cross-section, fuel injection plane and exit plane, figure shows high concentration of tar near the fuel inlet. The maximum tar concentration reaches 50% by volume. ....	283
Figure A5-45. Contour plot of particle concentration ( $\text{kg/m}^3$ ), figure shows high concentration of particles near the fuel inlet Maximum value is $12 \text{ kg/m}^3$ at the inlet. The values on the plot are clipped to $1 \text{ kg/m}^3$ for better resolution, all concentrations above this value are in red. ....	283
Figure A5-46. Contour plot of particle concentration ( $\text{kg/m}^3$ ), the values on the plot are clipped to $0.01 \text{ kg/m}^3$ , all concentrations above this value are in red. ....	284
Figure A5-47. Contour plot of particle concentration ( $\text{kg/m}^3$ ), the values on the plot are clipped to $0.0001 \text{ kg/m}^3$ , all concentrations above this value are in red. ....	284
Figure A5-48. Particle tracks colored by their residence time. Maximum residence time is about 1 second, 400 particles tracked -- 12 of them do not burn out completely ....	285
Figure A5-49. Particle tracks colored by their diameter. Diameter range is 25 -600 microns (mean 250). Swelling coefficient is assigned as unity, so the particle diameter does not change throughout. The minimum diameter of escaped particle is 350 micron, all of the small particles burned out completely. ....	285
Figure A5-50. Particle tracks colored by their diameter. The original density of the particle is $700 \text{ kg/m}^3$ (red). As the volatiles escape from the particle the density drops. The density of char is $49 \text{ kg/m}^3$ (dark blue). ....	285
Figure A5-51. Particle tracks colored by their temperature. Particles trapped near the wall have enough oxygen, but do not have sufficient temperature to burn, these particles have the longest residence time. ....	286
Figure A5-52. Chemical reactor network for industrial cyclone wood dust burner ....	291
Figure A5-53. CRN fuel N to $\text{NO}_x$ conversion prediction for industrial cyclone wood dust burner. ....	292
Figure A5-54. CRN NO emission prediction (ppmvd at $18\% \text{O}_2$ ) for industrial cyclone wood dust burner. ....	292
Figure A5-55. CRN $\text{NO}_x$ emission prediction (lb/MMBTU) for industrial cyclone wood dust burner. ....	293

## List of Tables

Table 2-1. Summary of the models for premixed turbulent combustion.....	49
Table 2-2. Summary of the models for premixed turbulent combustion.....	53
Table 3-1. Major elemental reactions of NO <sub>x</sub> formation. The forward reaction rate is shown; the backward rate is calculated by code using detailed balance of the reaction constant. The “direction” column shows the most likely direction of the reaction under the lean-premixed combustion regime. The notation and units of the reaction rates are: “A” - exponent in the pre-exponential factor 10 <sup>A</sup> , kmol/m <sup>3</sup> /s, “b” - temperature exponent in (T/T <sub>0</sub> ) <sup>b</sup> , “E <sub>a</sub> ” – activation energy kcal/mole. ....	56
Table 3-2. Reactor schemes used for modeling high-intensity lean-premixed combustion for generating database for global mechanism development. ....	58
Table 4-1. Operating conditions for high pressure bluff body combustor.....	64
Table 4-2. Modeling assumptions and boundary conditions for the bluff body combustor. ....	66
Table 5-1. Design parameters for the single-injector, can-type combustor.....	89
Table 5-2. Modeling approach for the can combustor. ....	92
Table 5-3. CFD simulation of the methane combustion in the single-injector, can-type combustor.....	97
Table 5-4. Boundary conditions for linear and uniform injector mixing profiles. ....	109
Table 5-5. CFD simulation of methane combustion in the single-injector, can-type-type combustor for flat and linear injector fuel mixing profiles and for neutral pilot. ....	112
Table 6-1. Comparison of predicted carbon monoxide emissions between CFD and CRN models for single injector, can-type combustor with uniform injector fuel-air equivalence ratio.....	149
Table 6-2. Comparison of predicted carbon monoxide emissions between CFD and CRN models for single injector, can-type combustor with linear injector fuel-air equivalence ratio. ....	149
Table 7-1. Correction of premixer circumferential fuel-air mixture non-uniformity on NO <sub>x</sub> prediction in CRN.....	161
Table 7-2. CO predictions in the CRN. ....	163
Table 7-3. NO Formation Pathways. ....	165
Table 7-4. NO Formation Zones. ....	165
Table 8-1. Fuel composition for the hydrocarbon blends used in modeling. ....	170

Table 8-2.CFD simulation of methane and blend 3 (30%CH <sub>4</sub> , 70%C <sub>3</sub> H <sub>8</sub> ) combustion in the single-injector, can-type combustor with uniform injector fuel-air ratio and neutral pilot.....	172
Table A3-1. Input for the UW chemical kinetic code for 31-element CRN.....	223
Table A3-2 Output data from UW chemical kinetic code for 31-element CRN.....	224
Table A3-3 Input for the UW chemical kinetic code for 13-element CRN.....	231
Table A3-4 Output data from the UW chemical kinetic code for 13-element CRN.....	231
Table A5-1. Results of ultimate analysis of Weyerhaeuser sawdust samples.....	242
Table A5-2. Yield data for primary pyrolysis of wood based on Nunn et al. (1995) .....	243
Table A5-3. Yield data for tar pyrolysis of wood based on Boroson et al. (1989) .....	243
Table A5-4. Enthalpy of formation and HHV for wood, char, tar, and resin. The wood and tar compositions are normalized to C <sub>1</sub> basis. ....	245
Table A5-5. Heat capacity and entropy of wood, char, tar, and resin. ....	246
Table A5-6. Kinetic rates and the heats of reaction used for modeling of wood pyrolysis. ....	247
Table A5-7. Reactor arrangements and fuel-air equivalence ratios used in the development of the global chemical kinetic mechanism. ....	248
Table A5-8 Yield and rate data for wood and tar pyrolysis (from Malte et al., 1996) .....	274
Table A5-9 Yield and rate data for resin pyrolysis (from Malte et al., 1996) .....	275
Table A5-10. Char Particle oxidation rate used in the UW chemical kinetic code for reaction Char+0.5O <sub>2</sub> →CO, temperature range is 1200-2000K; the units are .....	275

## Acknowledgments

I would like to thank Professor Philip C. Malte for being my advisor and for his tutoring and support throughout the course of my graduate studies. I would also like to acknowledge the other member of my committee: Professor John C. Kramlich, Dr. David G. Nicol, and Professor James J. Riley for their help in my research and Professor David Russell for being the graduate school representative on my committee.

I would also like to thank the gas turbine OEM for my fellowship support, MEC Company and the Weyerhaeuser Technical Center for providing information for wood dust combustion systems, and the US Dept of Energy for the wood burner modeling research support.

This dissertation would not be possible without the moral support of my wife and son.

## 1. Introduction and Objectives

In light of increasing environmental concerns on one hand and growing energy demand on the other, human society is moving towards technologies that can be applied with smaller ecological impact on the planet. Development of the renewable energy technologies has been substantial over the last decade; however these technologies are slow to penetrate the energy market due to their high upfront cost, lack of infrastructure, and inherent intermittency in the case of wind, solar, and ocean energy systems. While introducing new cleaner energy sources, the use of fossil fuels appears to be unavoidable. The combustion process has been a very reliable energy source for transportation, industrial, and power generation applications. Some of the most frequently used technologies are coal-fired power plants, land-based gas turbines (GT) in simple and combined cycle applications, and internal combustion engines (ICE). Each technology has benefits associated with its use.

Land-based gas turbine (GT) engines operated on natural gas are considered one of the cleanest combustion technologies. Among the fossil fuels, natural gas has the highest hydrogen to carbon ratio, thus it produces the least amount of carbon dioxide per unit power output. Although carbon dioxide is not viewed as a pollutant by US government current standards, it is a green house gas that contributes to global warming. There are additional environmental advantages of natural gas over the other fossil fuels. In particular, the absence of sulfur in commercial natural gas implies that there are practically no sulfur dioxide emissions present. Sulfur dioxide is a known precursor to acid rain. Particulate emissions are also typically not a concern in natural gas combustion. The best first-law efficiency of gas-fired simple cycle

gas turbines is just above 40%, and that of the best gas-fired combined cycle power plants has just reached 60%.

However, the high temperatures associated with gas turbine combustion can lead to high levels of nitrogen oxides ( $\text{NO}_x$ ) emissions. Reducing the  $\text{NO}_x$  without compromising the low CO levels is one of the main concerns in the design of GT combustors. One of the major techniques in reducing nitrogen oxide emission is lean premixed (LP) combustion. By burning the mixture lean, the combustor can avoid high local fuel-air equivalence ratios that increase the flame temperature. Since the  $\text{NO}_x$  formation rate exponentially depends on combustion temperature, its reduction greatly benefits  $\text{NO}_x$  emission control. Modern LP combustors can achieve  $\text{NO}_x$  emission levels that are less than ten parts per million (adjusted to 15%  $\text{O}_2$  dry).

Unfortunately it is impossible to eliminate the carbon dioxide emissions from the combustion process that uses carbon containing fuel. While the carbon sequestration from the power plants has not been demonstrated at industrial scale, one way to avoid net  $\text{CO}_2$  production in combustion is to use biomass (e.g., agricultural waste) or fuels obtained from biomass such as biodiesel and ethanol. The wood products and pulp/paper industries use byproducts of the manufacturing process to supplement their energy consumption. The combustion of wood dust in cyclone burners, bark in hog-fuel boilers, and black liquor in recovery boilers produce the heat and steam for mill processes. The high price of natural gas has made wastes and alternative fuels such as these attractive for energy.

Controlling pollution emission remains one of the most important design goals in developing modern combustion systems. Detailed knowledge of  $\text{NO}_x$  formation in the flame is required for the development of sub-10 ppm lean

premixed combustors. Relatively small changes in the system boundary conditions can lead to a large emission increase. As an example, for the lean-premixed GT combustor the changes in the premixer (injector) exit profiles of velocity and fuel concentration can significantly change the  $\text{NO}_x$  emission. Nowadays, modeling of the combustion process becomes an integral part of the gas turbine engine design process.

Different methods have been presented in the literature for modeling the turbulent combustion process. However, there are no computer models available that incorporate the full set of chemical kinetic reactions coupled with turbulent flow modeling. Attempts have been made to include the complex chemistry in turbulent models, but such models are limited to rather simple systems and still require great amounts of computer time. In order to model complex combustion systems, various simplified global kinetic mechanisms have been developed. These mechanisms are limited by their operating conditions and may fail to predict CO and  $\text{NO}_x$  emissions accurately. However, even the use of simplified chemistry in conjunction with computational fluid dynamics (CFD) for an industrial combustor can take weeks to obtain a converged solution, which is a prohibitively long time for a GT designer. An intelligently designed chemical reactor network (CRN) can provide answers regarding the quantitative  $\text{NO}_x$  and CO behavior of the combustor. These results can be very helpful in combustor design and modification stages and can aid in the emissions reduction program for the combustion system. The CRN can be used for parametric analysis, since its turnaround time is typically several orders of magnitude less than the simplest CFD simulation.

The objective of this thesis research is to show the development and application of CRN modeling for a range of combustion systems with a

purpose of predicting exhaust emissions. The development of the CRN model is guided by CFD solutions for the combustors, with CFD requiring the development and use of verified global chemical kinetic mechanisms. Thus contributions of this research are:

1. Development and validation of global chemical kinetic mechanisms for fuel oxidation with the formation of nitrogen oxides ( $\text{NO}_x$ ).
2. CFD modeling for selected combustors, in which the global chemical kinetics are used. The CFD modeling is performed for: a high-pressure, lean-premixed, bluff body combustor fueled on commercial grade methane; a generic, lean premixed, single-injector, can-type gas turbine combustor; and atmospheric pressure laboratory and industrial combustors fired on wood dust. The other necessary information for CRN development, such as 3D CFD solutions for an industrial, multi-injector, gas turbine combustor, and operating and boundary conditions for this combustor have been obtained from the GT manufacturer.
3. Development of the CRN model for the lean-premixed, generic, single-injector, can-type combustor and CRN application for a range of the fuels: natural gas and hydrocarbon fuel blends.
4. Development and application of the CRN model for the industrial lean-premixed gas turbine combustor.
5. Development of CRN models for two phase combustion in wood dust burners.

The work on the gaseous fuels combustion and gas turbine applications is contained in the following 10 chapters of the main body of this thesis, while the work on the wood dust is given in the appendix.

## **2. Literature Review**

### ***Chemical Reactor Modeling of Combustion***

#### **Introduction**

Starting in the nineteen fifties, engineers have used chemical kinetic models to understand the combustion process. The concept of modeling the flame by a perfectly stirred reactor (PSR) followed by a plug flow reactor (PFR) was introduced by S.L. Bragg (1953). Experimental verification of the concept was shown by Longwell and Weiss (1955) in their back-mixed well stirred reactor at near blow-out conditions, where the back mixing of recirculating gas was assumed infinitely fast compared to the controlling chemical reaction rate. Zonal combustion modeling was proposed by Swithenbank (1970) as an improvement for combustor design via correlation parameters, and followed experimental testing. The combustor volume was divided into zones represented by idealized reactor elements, such as PSR, PFR, and MIX. The flow conditions corresponding to the perfectly stirred reactor could be calculated based on the dissipation gradient method, which is based on the knowledge of the pressure drop and volumetric flow rate.

The concept of modeling the combustor by a PSR followed by a PFR is known as a Bragg cell (S.L. Bragg, 1953). In the PSR the chemical time is assumed to be much slower than the mixing time, in this case the chemistry becomes the rate limiting step of combustion process. The author suggested that to have self-sustained combustion, the efficiency of the combustion in the PSR should be between 60 and 80%.

The numerical implementation of chemical reactor theory has been investigated by a number of authors. Wormeck (1976), Pratt and Wormeck

(1976), and Pratt (1977) developed a computer program designated as Combustion Reaction Equilibrium and Kinetics (CREK). The PSR reactor concept is implemented by balancing the Arrhenius source terms of net production of each species by convective removal of that species from the PSR control volume. The resulting system of non-linear differential equations is solved by the method of under-relaxed Newton iteration, but since then the CREK code has been updated with new convergence algorithms (Pratt and Radhakrishnan, 1984). A number of chemical reactor codes such as the commercially available CHEMKIN have been developed. In the development of CHEMKIN (Kee et al., 1986), similar approaches are employed for solving the system of resulting equations. Currently there are a number of PSR/PFR codes available. The chemical industry uses codes such as ASPEN, CHEMCad, Pro/II. These codes have great ability to link the flow elements to a network, but have difficulty handling large chemical kinetic mechanisms, which is imperative in order to predict emissions and blow-out conditions. The codes CHEMKIN, MODLINK and Cantera, DSMOKE, FLAMEMaster, and Mark3 are able to handle the large chemical kinetic mechanisms and have some degree of networking capability.

## **Gas Turbine Application**

Chemical reactor modeling of combustion systems is not necessarily limited to the use of extensive chemical reactor networks. Simple two/three reactor models have been found useful in modeling research combustion reactors. Recently, Rutar et al. (2000) and Rutar and Malte (2002) showed the methodology for modeling the NO<sub>x</sub> emissions of the experimental jet stirred reactor with a simple two or three idealized reactor scheme. There are a number of investigations using simple chemical reactor models to evaluate

the emission trends for gas turbine combustor applications (e.g., Schlegel et al., 1996, and Feitelberg et al., 2001). These approaches provide quick and useful ways to evaluate the emission trends and the effects of parameters of interest using detailed chemical kinetic mechanisms. However, to go beyond the modeling of intensely stirred laboratory reactors and the trend evaluations of industrial systems, more complicated models are required due to the complexities of the flow field and the boundary conditions.

The development and application of the zonal model for studying emission control in gas turbine combustion was described by Rubins and Pratt (1991). The authors tested several possible configurations for the annular ALF-502 GT combustor with the purpose of exploring CO and NO<sub>x</sub> reduction. Their model included several MIX, WRS (PSR), and PFR elements in series, including air injection from the wall. In order to evaluate the flow field in the combustor, the combustion geometry was evaluated in a water tunnel with air bubbles used in the visualization of the flow patterns. As shown in Figure 2-1, the reactor is divided into the zones corresponding to the flow patterns; the highly mixed recirculation zone is represented by a WSR (PSR), the areas of jet penetration represented by MIX zones, and the PFRs are used downstream of the turbulent mixing regions.

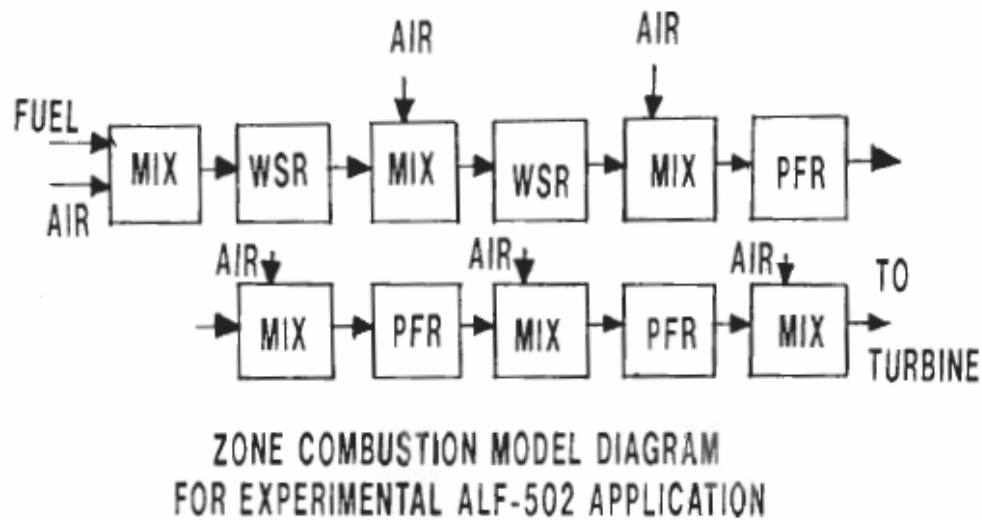


**Figure 2-1. The CRN for evaluating NO<sub>x</sub> and CO emissions (from Rubins and Pratt 1991).**

Lean blow out modeling for an aircraft engine application using zonal modeling was investigated by Sturgess et al. (1991) and Ballal et al. (1993). Later, a hybrid CFD-CRN model for gas turbine combustors was proposed by Sturgess and Shouse (1996), see Figure 2-2. The development of their model employed the post-processing of CFD simulations. The authors used Lagrangian particle tracking techniques for fuel droplets to determine the properties of the recirculation zone, such as: volume, flow rate, temperature, and degree of mixing. The gradient dissipation method of Swithenbank is used for determining whether the element qualifies as a PSR; in the analysis of such a method, the authors say that non-dimensionalized turbulent kinetic energy can be used for this purpose.



Sturgess (1997), using the same approach, developed a chemical reactor network for evaluation of an abbreviated chemical kinetic mechanism for Jet-A/JP-5/JP-8 fuels by comparing CRN predictions with experimental emissions data. The network was designed for the perforated-plate flame holders. The CO/CO<sub>2</sub> ratio, NO<sub>x</sub>, and temperature were compared for different fuel-air equivalence ratios and different flame holder configurations. Figure 2-3 shows a layout of this network.

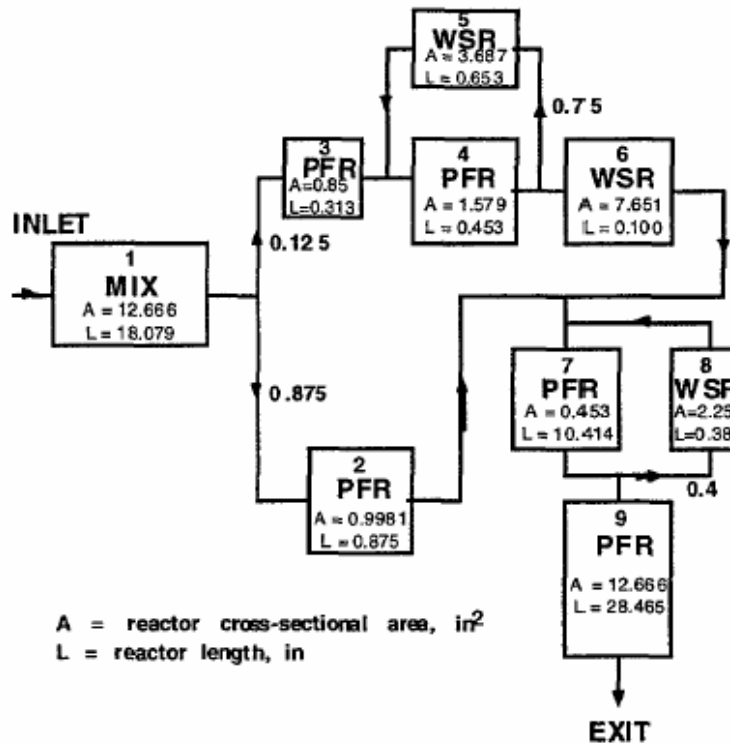


Figure 2-3. Network for evaluating jet fuel chemical mechanism for perforated plate flame holder (from Sturgess, 1997).

The injector boundary conditions play a significant role in the levels of nitrogen oxide emission. The effect of fuel-air unmixedness in the chemical reactor model was investigated by Nicol et al. (1997) and Rutar et al. (1997). The model of Nicol et al. divided the fuel-air stream into five parallel flow paths with the discrete fuel-air equivalence ratio obtained from a Gaussian distribution function. A finite-rate mixing model was used to incorporate the effects of large and small scale mixing into the chemical reactor scheme (Tonouchi and Pratt, 1995, and Tonouchi 1996).

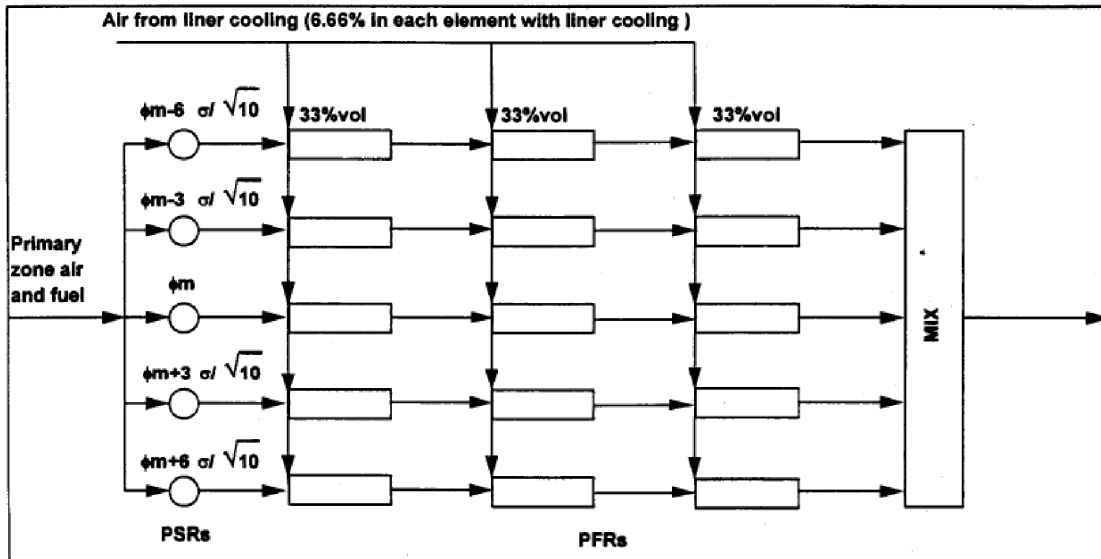


Figure 2-4. CRN incorporating finite-rate mixing model (from Nicol et al 1997).

Another approach of incorporating finite mixing into the flame modeling is shown in Broadwell and Lutz (1998). In their Two-Stage Lagrangian (TSL) model, the authors resolve the flame structure using a PSR as a flame-sheet reactor and a PFR as a core reactor. The entrainment of the surrounding gas into the flame is calculated based on empirical relations. Figure 2-5 shows the schematic of such a model.

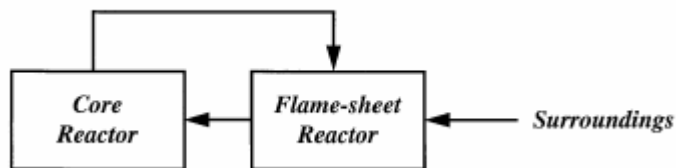
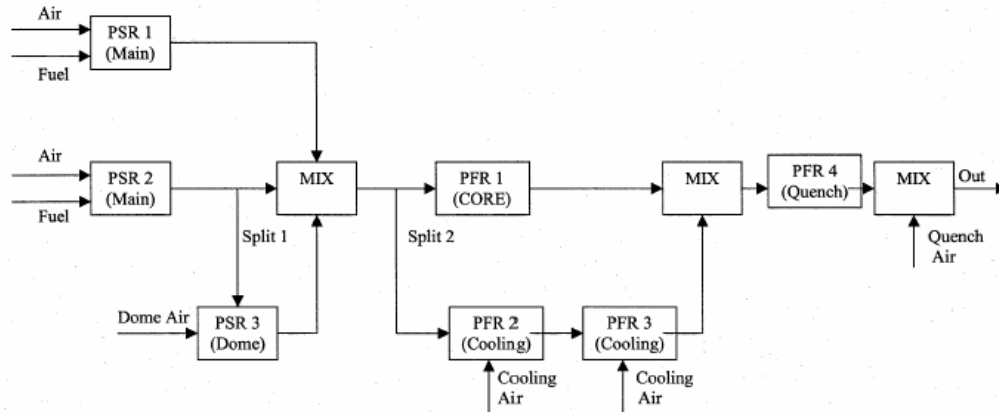


Figure 2-5. Schematic of the TSL model (from Broadwell and Lutz, 1998).

Roby et al. (2003) modeled the gas turbine combustor experimental results of Mellor (1996) using a chemical reactor network with the main combustion zone split into two streams to account for imperfect fuel-air premixing. The

authors also discussed the ability of the network to predict non-linear emission trends for high fuel–air equivalence ratio combustors.



**Figure 2-6. Network for evaluating NO<sub>x</sub> emissions for high fuel-air ratio turbines (from Roby et al. 2003).**

Novosselov (2002) employed a chemical reactor network for NO<sub>x</sub> and CO emissions prediction of the same lean-premixed gas turbine combustor. The CRN development was based on the CFD solution of the combustor using eight-step global chemistry. The network consisted with two parallel streams for the main jet with some cross-mixing and a recirculation zone which was divided into two parallel streams to represent slow moving gas near the center of the combustor and faster moving gas near the eye of the recirculation zone. This network did not incorporate the non-uniformity of the injector profile nor the adiabaticity of the combustor; it has been used for the comparison of the eight-step global mechanism against the GRI 3.0 mechanism.

### ***Other applications for continuous combustion systems***

Among other combustion applications of chemical reactor modeling are: gas and oil fired furnaces, coal combustors, municipal solid waste (MSW) incinerators, biomass burners, and various research reactors.

Robertus et al. (1975) investigated the feasibility of simple furnace alterations for reducing NO<sub>x</sub> emissions from pulverized coal-fired furnaces. In this work, pulverized coal was fluidized with a methane-air mixture. The combustion was modeled as a simple plug flow reactor.

Malte et al. (1996) and Malte and Nicol (1997) developed and applied a CRN model for predicting NO<sub>x</sub> emissions of cyclonic wood dust suspension burners. As shown in Figure 2-7 their CRN has multiple reactors in series with the addition of combustion and dilution air. The model has a recirculation zone element to capture the fluid dynamics of the burner. The addition of the recycle element aids the devolatilization (cooking) of the wood particles in the first PFR. The model has been implemented using the UW chemical kinetic code which has origins in Pratt's CREK code (discussed above).

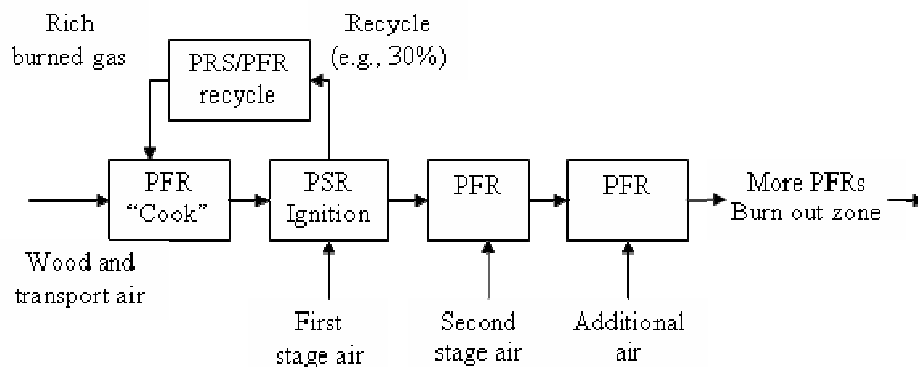


**Figure 2-7. An arrangement of chemical reactor elements for early region of a wood dust burner (from Malte et al., 1996).**

Pedersen and Glarborg (1998) and Antifora et al. (1999) represented pulverized fuel (p.f.) furnaces as ideal reactor models in order to incorporate detailed NO<sub>x</sub> formation chemistry. Similar work by Bendetto et al. (2000), Faravelli et al. (2001), and Falcitelli et al. (2002a, 2002b) used chemical reactor networks for representing combustion in industrial furnaces with the purpose of predicting NO<sub>x</sub> emissions using a detailed kinetic mechanism. The authors approach has been: analyze the CFD flow field and construct chemical reactor networks with appropriate reactor residence times and overall properties. The furnace is subdivided into distinct regions based of the flow properties of each region.

The networks discussed above have similar features; they have two parallel streams with cross-mixing between the streams. These networks also incorporate downstream addition of dilution air, and fuel for reburning. The approach has been applied to different types of furnaces, such as pilot plants and industrial boilers, low- NO<sub>x</sub> burners, and glass furnaces. Figure 2-8 shows the example of such network.

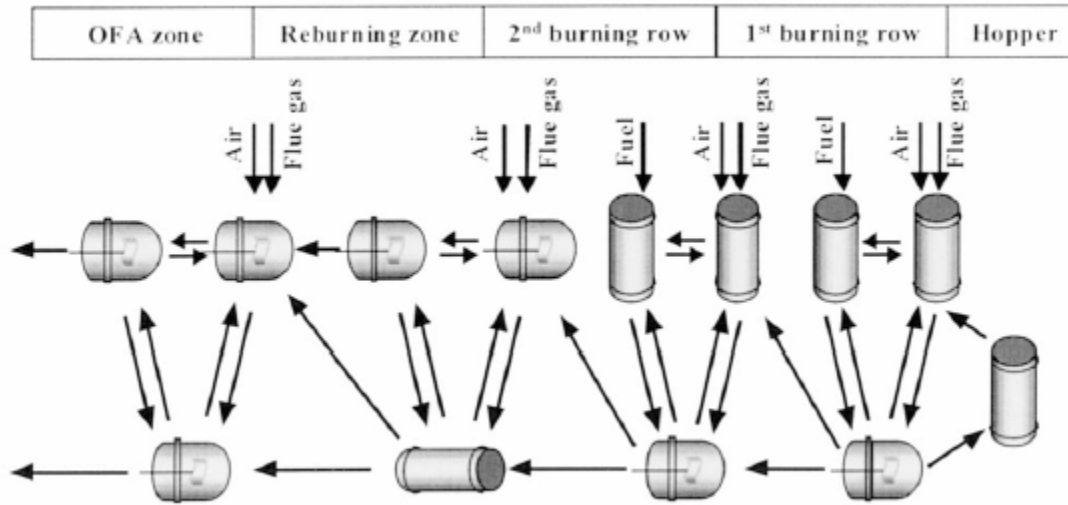


**Figure 2-8. Ideal reactors network for furnace from Faravelli et al. (2001).**

Niksa and Lui (2002a, 2002b) use a different approach in developing CRNs for p.f. furnaces. Instead of dividing the furnace into different volumes based on the physical location, they divide the flow based on the characteristic chemical process prevailing in that region, such as: main flame, recirculation zone, over-fire air zone, mixing layer, or burnout zone. The main flame zone is represented by two parallel streams: core and sheath layer, which further subdivided into devolatilization zone and NO reduction zone. As shown in Figure 2-9, each of the zones is represented by a series of PSR elements and the burnout zone is modeled as a PFR. In Niska et al. (2003), the authors apply this model for the NO<sub>x</sub> prediction of biomass combustion.

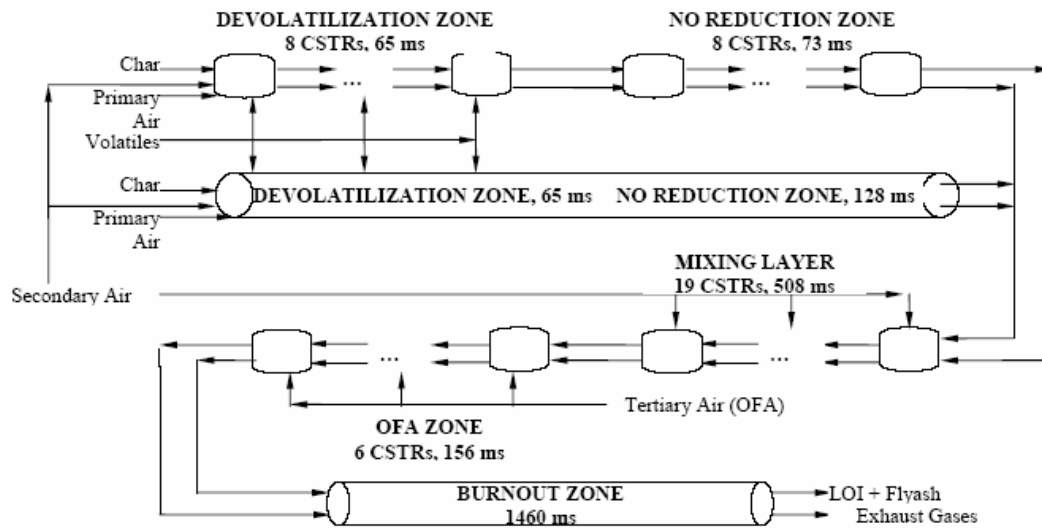


Figure 2-9. Network developed by Niksa and Lui (2002).

## Conclusions for Chemical Reactor Modeling Overview

Chemical reactor modeling is found to be a valuable tool in the evaluation of pollutant formation and blowout performance of combustion systems. The methodologies of the development vary between the authors. While most authors address the modeling of the combustion processes in the flame and the post-flame regions, only a few investigators have looked at the possible effects of the fuel-air mixture non-uniformities. This is not a pressing issue in the cases of the two phase combustion due to the time scale difference between the turbulent mixing and the evaporation/devolatilization rate of the fuel. Also, the levels of NO<sub>x</sub> emissions in such systems are relatively high due to the high temperature and prevailing thermal and fuel NO<sub>x</sub> formation. However, in lean premixed gas turbine combustion with sub-ten parts per million NO<sub>x</sub>, the effects of the premixer non-uniformity and turbulent fluctuations may account for large relative increases in NO<sub>x</sub> levels. Thus, the

need exists for models that can account, not only for the detailed flame chemistry, but also for the interactions between the chemistry and mixing and the complex injector boundary conditions.

## ***Premixed Turbulent Combustion Regimes and Numerical Modeling Techniques***

### **Introduction**

In industrial applications, combustion is normally associated with turbulence. Large flow rates, enhanced mixing designs, and heat release during combustion increase the turbulence. In this section the turbulent combustion regimes, the criteria to determine them, and the modeling techniques are discussed. The section primarily addresses the description and treatment of premixed turbulent combustion. Modeling techniques like direct numerical simulation (DNS) and large eddy simulation (LES) are mentioned, however the majority of discussion is focused on the Reynolds averaged Navier-Stokes (RANS) equations and the Reynolds stress model (RSM) closure model. Additional consideration is given to integrating chemical and heat source terms into the turbulent models. A number of approaches is considered such as: simple heat release model, eddy break-up (EBU) model, flamelets model, G-equation, and probability density function (PDF) approach. Finally, treatment of radiative heat transfer in CFD is described.

Combustion systems can be divided into premixed, partially premixed, and non-premixed. Industrial examples of premixed combustion are the carbureted and port-injected internal combustion engine with spark ignition and the lean-premixed combustor for the gas turbine engine. In the GT application, the fuel and air come to the combustor premixed. Turbulence is

necessary for such mixing. Partially premixed combustion can be observed in direct injection spark ignition combustion engines. Non-premixed combustion takes place in diesel engines and in aero engines where the fuel is injected separately from the air and in cases where solid fuels are used.

A useful criterion for division of turbulent combustion is the ratio of turbulent and chemical scales. The rate of chemical reaction during the combustion process depends on the type of fuel and the conditions in the combustor. One can distinguish two different rates at which combustion occurs: the mixing rate, in which case the fuel reacts as fast as the mixing occurs, and the chemical kinetic rate, which assumes that mixing is infinitely fast and the chemistry is slow. This division is described by the Damköhler number ( $Da$ ), which is defined as chemical rate divided by mixing rate. The regime associated with large-scale turbulence is called corrugated flamelets and with small-scale turbulence is called thin reaction zone.

The combustion rate modeling approaches can be based on several concepts. One of the oldest and the most used models in current commercially available computation fluid dynamics codes is the eddy dissipation model (Magnusen and Hjetager, 1977) that is based on the idea of eddy-breakup (EBU). The flamelet modeling concept for premixed combustion is introduced in the Bray-Moss-Libby (BML) model (Bray and Libby, 1994). It based on a combustion progress variable, which is normalized by temperature or by product mass fraction. The G-equation is an approach that is based on a non-reacting scalar rather than on a combustion progress variable (Peters, 2000). This scalar describes the flame surface area in the given volume of the flame zone. An alternative way to model premixed turbulent combustion is the PDF approach (Pope, 1985, and Correa and

Pope, 1992), which is used to solve for the reacting species mass fractions. Both PDF and G-equation methods do not require modeling of the chemical reaction term, as required by the other methods mentioned. The ultimate way to model turbulent combustion is by direct numerical simulation (DNS). However, for practical reasons it remains prohibitively expensive due to the mesh size required to resolve the Kolmogorov scale ( $\eta$ ), which can be three orders of magnitude smaller than integral scale of the turbulence.

### **Regimes of premixed turbulent combustion**

There are a number of authors who represent the regimes of turbulent combustion based on the velocity to length scale ratio. In order to break the combustion into the regimes the flame thickness,  $l_F$ , is defined:

$$l_F = D / s_L, \quad [2-1]$$

where  $D$  is molecular diffusivity and  $s_L$  is laminar burning velocity. The flame time is defined:

$$t_F = D / s_L^2. \quad [2-2]$$

The turbulent Reynolds number can be written as

$$Re = v' l / s_L l_F, \quad [2-3]$$

where  $l$  is characteristic length and  $v'$  is turbulent intensity or eddy turn over velocity. The turbulent Damköhler number, defined as  $Da$  = mixing time/chemical time can be written as:

$$Da = s_L l / v' l_F . \quad [2-4]$$

Based on the definition of the Kolmogorov length scale:

$$\eta = (v^3 / \varepsilon)^{1/4} , \quad [2-5]$$

where  $v$  is kinematic viscosity and  $\varepsilon$  is viscous dissipation, the Kolmogorov time scale is:

$$t_\eta = (v / \varepsilon)^{1/2} \quad [2-6]$$

The Kolmogorov velocity scale is:

$$v_\eta = (\varepsilon v)^{1/4} . \quad [2-7]$$

Karlovits number shows the ratio of the flame scale to the Kolmogorov scale:

$$Ka = t_F / t_\eta = l_F^2 / \eta^2 = v_\eta^2 / s_L^2 , \quad [2-8]$$

If the Schmidt number is unity, then  $v = D$ , and:

$$Re = Da^2 Ka^2 . \quad [2-9]$$

The second Karlovits number is based on the inner layer thickness  $l_\delta$ , defined as

$$l_\delta = \delta l_F, \quad [2-10]$$

where  $\delta$  is non-dimensional inner layer thickness – which is the reaction layer where the fuel is consumed and the free radicals are depleted (see Figure 2-10). The scale separation between turbulence and chemistry requires the thickness of the inner layer to be smaller than the Kolmogorov scale; otherwise the entire flame structure will be disrupted.

The second Karlovits number is:

$$Ka_\delta = l_\delta^2 / \eta^2 = \delta^2 Ka. \quad [2-11]$$

The relation between the ratios  $\nu/s_L$  and  $l/l_F$  can be expressed in terms of Reynolds and Karlovits numbers as:

$$\nu/s_L = Re (l/l_F)^{-1} = Ka^{2/3} (l/l_F)^{1/3}. \quad [2-12]$$

Figure 2-11 shows the regimes of premixed turbulent combustion.

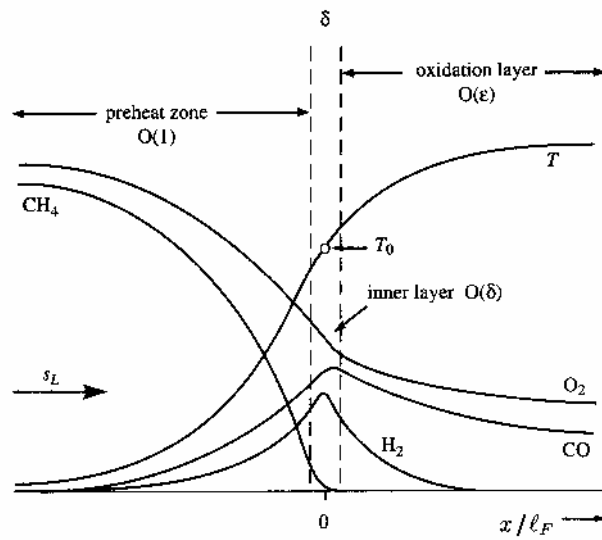


Figure 2-10. Schematic illustration of a premixed methane-air flame, from Peters (2000).

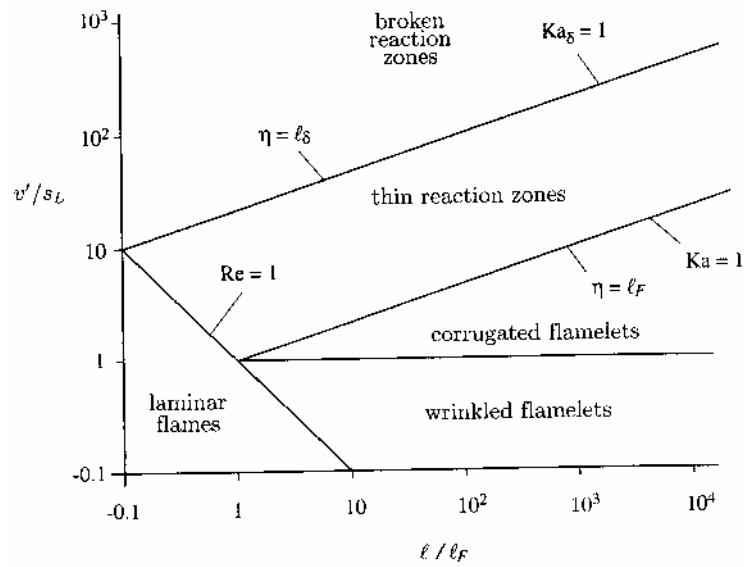


Figure 2-11. Regimes of premixed turbulent combustion, from Peters (2000).

The separation between the regimes is described by non-dimensional numbers – though it should be noted the separation is somewhat arbitrary. The regimes are separated by the lines  $Re = 1$ ,  $Ka = 1$ , and  $Ka_{\delta} = 1$  (see Figure 2-11.). For all Reynolds numbers less than unity the flames are laminar. In the wrinkled flamelets regime  $\nu' < s_L$ , meaning that the turnover velocity of the eddies ( $\nu'$ ) is smaller than the laminar flame speed, and thus cannot influence the flame front propagation by the laminar burning speed. These two regimes (laminar and wrinkled flamelets) are not considered in this review since there is limited or no turbulence interaction in the flow.

The other regime that is not included in this analysis is the broken reaction zone regime. This regime lies beyond  $Ka_{\delta} > 1$ , or if the non-dimensional flame thickness ( $\delta$ ) is taken to be 0.1, corresponds to  $Ka=100$ . Here the Kolmogorov size eddies are smaller than the inner layer thickness ( $l_{\delta}$ ) and they can penetrate into the inner layer disrupting the chain branching mechanism of the chemical reaction. This is caused by turbulence-enhanced heat and free radicals loss to the preheat layer of the flame. In this regime combustion cannot be sustained.

The two remaining regimes in the diagram are of a practical interest. The corrugated flamelets regime is located where  $Re > 1$  and  $Ka < 1$ ; this corresponds to the thickness of the flame front being smaller than the Kolmogorov scale eddies. Thus, the flame structure is located inside the small eddies and is not influenced by turbulence and remains quasi-laminar. There is a strong interaction between the laminar flame and turbulent eddies. This regime corresponds to:

$$\nu' \geq s_L \geq \nu_{\eta}. \quad [2-13]$$

The smallest eddy that will influence the shape of the flame surface can be determined by setting the eddy turnover velocity equal to the laminar flame speed:

$$\varepsilon = \nu_n^3 / l_n = s_L^3 / l_n \quad [2-14]$$

The eddy size  $l_G = l_n$  is defined as the Gibson scale, which is the smallest size eddy that has enough turnover velocity to bend the flame front:

$$l_G = s_L^3 / \varepsilon. \quad [2-15]$$

The larger eddies will push the flame front around causing flame corrugation. Figure 2-12 and 2-13 show correspondence of the eddy size and the turnover velocity and the range for the corrugated flamelets regime.

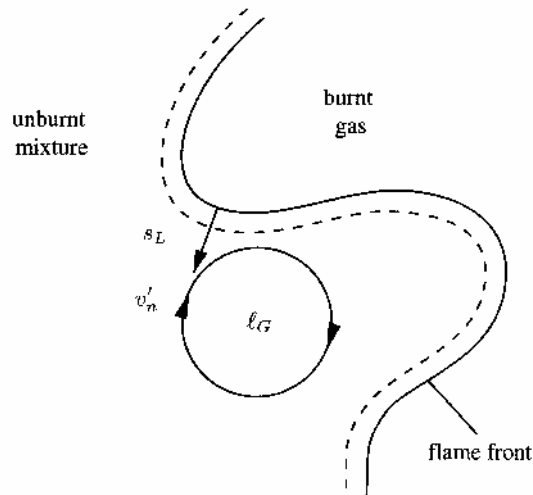


**Figure 2-12. Schematic illustration of the corrugated flamelets regime from Peters (2000).**

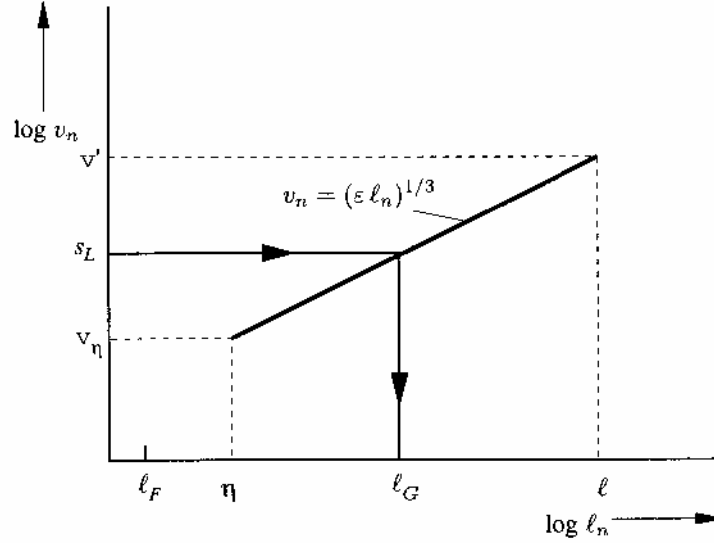


**Figure 2-13. Inertial range scale for corrugated flamelets regime, from Peters (2000).**

The second turbulent combustion regime of interest is the thin reaction zone regime. Here the Kolmogorov scale is smaller than the laminar flame front but larger than the inner layer  $l_F \geq \eta \geq l_\delta$ ; thus, the small eddies can penetrate into the flame (preheated zone, see Figure 2-10), but cannot enter the inner layer. Kolmogorov scale velocity is larger than the laminar flame speed and the Gibson scale is smaller than Kolmogorov scale; thus, the Gibson length scale has no meaning in this regime. A more appropriate criterion describing this regime is a mixing length scale that can be derived from the quench time  $t_q$ , which is the inverse of the strain rate needed to extinguish the flame. This time is on the same order of magnitude as the flame time:

$$t_q \sim t_F = D / s_L^2, \quad [2-16]$$

This leads to the definition of diffusion thickness:

$$l_D = (D t_q)^{1/2} \quad [2-17]$$

From the dimensional analysis of viscous dissipation, one obtains:

$$\varepsilon \sim v_n^2/t_n \sim v_n^3/l_n \sim l_n^2/t_n^3, \quad [2-18]$$

The mixing length scale can be obtained by setting  $t_n = t_q$ :

$$l_m = (\varepsilon t_q^3)^{1/2} \quad [2-19]$$

The concept of mixing length can be interpreted as the eddy of size  $l_m$  that will turnover interacting with the reaction front and transport preheated fluid from a region of thickness  $l_D$  in front of the reaction zone to unburnt mixture. This is schematically illustrated in Figure 2-14.

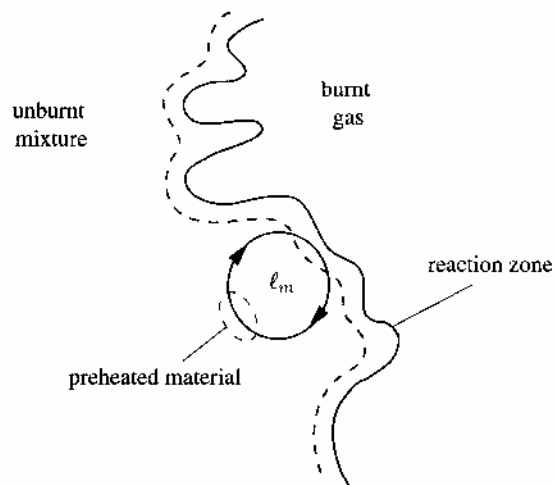


**Figure 2-14. Schematic illustration of the thin reaction zone regime, from Peters (2000).**

The larger eddies are responsible for transporting the structure thicker than the size of  $l_D$  and will broaden the flame structure. The eddy smaller than  $l_m$

will not contribute to the transport as much as eddies of  $l_m$  size. Therefore, the physical interpretation of the mixing length is maximum distance that the preheated mixture can travel ahead of the flame. The Figure 2-15 shows a log plot of the time scale over the length scale:

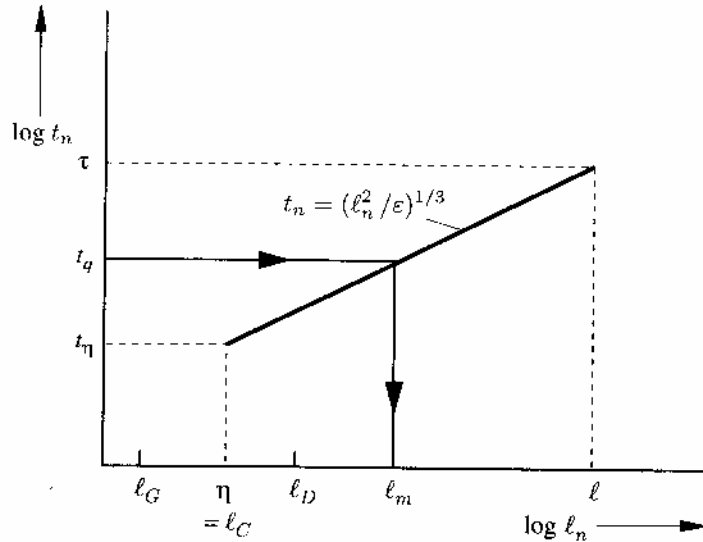


Figure 2-15. Inertial range for the thin reaction zones regime, from Peters (2000).

Note that the mixing length is equal to the Kolmogorov scale at the border of the corrugated flamelets and the thin reaction zone regimes. If the quench time is equal to the integral time scale, then mixing time is equal to the integral length scale which corresponds to the border of the laminar flame regime.

## Turbulence modeling

There are a number of ways to model turbulent combustion. CFD computation, with an appropriate turbulence model, has ability to provide

valuable insight on the flow and temperature fields of the combustor, which are difficult to obtain experimentally.

### ***Direct Numerical Simulation***

Direct numerical simulation (DNS) solves the unsteady, three-dimensional Navier-Stokes equations with no modeling approximations. In order to achieve this, the grid must be fine enough to capture the Kolmogorov size eddies.

### ***Large Eddy Simulation***

Large eddy simulation (LES), before being used for turbulent combustion, was developed for atmospheric science applications. Here, the large-scale three-dimensional, time dependent motion is solve directly, but the small-scale turbulence is modeled. The idea of LES is that the small-scale turbulence can be modeled more accurately since it is more uniform than the large scale.

### ***Reynolds-averaged Navier-Stokes Approach***

Time-dependent flow simulations, such as DNS and LES remain for a large part research tools. Because of the need to accurately resolve the energy-containing turbulent eddies in both space and time, LES for high Reynolds number industrial flows requires a significant amount of computational resource. Near wall region treatment becomes problematic as the scales that need to be resolved become increasingly smaller. Wall functions in combination with a coarse near wall mesh can be employed; however, one

needs to be careful considering such a function. A subgrid-scale model also needs to be considered.

An alternative way to address the problem is to average the Navier-Stokes equations so that the small-scale turbulent fluctuations do not need to be directly simulated: Reynolds-averaging is normally performed; the averaging introduces additional terms into the equations. Additional modeling of these terms is needed and is known as "closure".

The Reynolds-averaged Navier-Stokes (RANS) equations govern the transport of the average flow quantities, with the whole range of the scales of turbulence being modeled. The RANS-based modeling approach therefore greatly reduces the required computational effort and resources, and is widely adopted for practical engineering applications. Several closure models are available:

- Spalart-Allmaras
- k- $\epsilon$  and its variants
- k- $\omega$  and its variants
- Reynolds stress model (RSM)

In Reynolds averaging, the solution variables in the instantaneous (exact) Navier-Stokes equations are decomposed into the mean (ensemble-averaged or time-averaged) and fluctuating components. For the velocity components:

$$u_i = \overline{u_i} + u_i' \quad [2-20]$$

where  $\langle u \rangle_i$  and  $u'_i$  are the mean and fluctuating velocity components, respectively. For scalar quantities:

$$\varphi = \langle \varphi \rangle + \varphi', \quad [2-21]$$

where  $\varphi$  is a scalar such as pressure, energy, or species concentration.

Substituting expressions of this form for the flow variables into the instantaneous continuity and momentum equations and taking a time (or ensemble) average is conducted. The time-averaged momentum equation becomes:

$$\begin{aligned} \frac{\partial}{\partial t}(\rho u_i) + \frac{\partial}{\partial x_j}(\rho u_i u_j) = \\ - \frac{\partial p}{\partial x_i} + \frac{\partial}{\partial x_j} \left[ \mu \left( \frac{\partial u_i}{\partial x_j} + \frac{\partial u_j}{\partial x_i} - \frac{2}{3} \delta_{ij} \frac{\partial u_k}{\partial x_k} \right) \right] + \frac{\partial}{\partial x_j} (-\rho \langle u'_i u'_j \rangle) \end{aligned} \quad [2-22]$$

The velocities in the above expression are averaged and the scalars  $\mu$  and  $p$  are included in the averaging. The treatment of variable density is discussed later in the chapter. The expression  $\langle u'_i u'_j \rangle$  is called Reynolds stress and it needs to be modeled to “close” the equation. A common method employs the Boussinesq (1877) approximation that relates the Reynolds stress components to the mean velocity gradients: The Boussinesq hypothesis is used in the Spalart-Allmaras model (1994), the  $k$ - $\epsilon$  models, and the  $k$ - $\omega$  models. The advantage of this approach is the relatively low computational cost associated with the computation of the turbulent viscosity ( $\mu_t$ ), which defined as:

$$\mu_t = \rho C_\mu \frac{k^2}{\varepsilon}, \quad [2-23]$$

where coefficient  $C_\mu=0.09$ .

In the case of the Spalart-Allmaras model, only one additional transport equation (representing turbulent viscosity) is solved. The  $k$ - $\varepsilon$  and the  $k$ - $\omega$  models use two additional transport equations: one for the turbulence kinetic energy ( $k$ ), and either the turbulence dissipation rate ( $\varepsilon$ ), or the specific dissipation rate ( $\omega$ ). Then, the turbulent viscosity is computed as a function of  $k$  and  $\varepsilon$ . The disadvantage of the Boussinesq approximation as presented is that it assumes  $\mu_t$  is an isotropic scalar quantity.

### ***Reynolds Stress Model***

In many cases, models based on the Boussinesq hypothesis perform well, and the additional computational expense of the Reynolds stress model (RSM) is not justified. However, one needs to seriously consider the use of RSM when flow anisotropy is present. Wilcox (1993) notes that among the applications for which the Boussinesq hypothesis is not valid are flow over curved surfaces, flow in rotating and stratified fluids, and three-dimensional flow; therefore,  $k$ -epsilon and its derivative - renormalization group RNG model are not expected to be effective for the current flow with recirculation and three-dimensionality. (The RNG model is derived using the statistical technique - renormalization group theory.)

RSM solves transport equations for each of the terms in the Reynolds stress tensor. An additional equation (normally for  $\varepsilon$ ) is required. Thus, 2D simulation would use five additional transport equations, and the 3D case requires seven additional transport equations.

The Reynolds stress model (Launder et al., 1975; Gibson and Launder, 1978; Launder, 1989) involves calculation of the individual Reynolds stresses,  $\langle u'_i u'_j \rangle$ . The individual Reynolds stresses are used to obtain closure of the Reynolds-averaged momentum equation. The term  $\rho \langle u'_i u'_j \rangle$  from the Reynolds-averaged momentum equation in differential transport form can be written as:

$$\begin{aligned}
 & \frac{\partial}{\partial t} (\rho \langle u'_i u'_j \rangle) + \frac{\partial}{\partial x_k} (\rho u_k \langle u'_i u'_j \rangle) = \\
 & - \frac{\partial}{\partial x_k} (\rho \langle u'_i u'_j u'_k \rangle + \langle p (\delta_{kj} u'_i + \delta_{ik} u'_j) \rangle) + \frac{\partial}{\partial x_j} \left( \mu \frac{\partial}{\partial x_k} \langle u'_i u'_j \rangle \right) - \\
 & \rho \left( \langle u'_i u'_k \rangle \frac{\partial u_j}{\partial x_k} + \langle u'_j u'_k \rangle \frac{\partial u_i}{\partial x_k} \right) - \rho \beta (g_i \langle u'_j \theta \rangle + g_j \langle u'_i \theta \rangle) + \\
 & \langle p \left( \frac{\partial u'_j}{\partial x_i} + \frac{\partial u'_i}{\partial x_j} \right) \rangle - 2\mu \langle \frac{\partial u'_i}{\partial x_k} \frac{\partial u'_j}{\partial x_k} \rangle - \\
 & 2\rho \Omega_k (\langle u'_i u'_m \rangle \varepsilon_{jkm} + \langle u'_j u'_m \rangle \varepsilon_{ikm}) + S,
 \end{aligned} \tag{2-24}$$

Some terms in equation 2-23 can be calculated directly, however, a few terms need modeling in order to close the equation. These terms are:

$$\frac{\partial}{\partial x_k} \left( \mu \frac{\partial}{\partial x_k} \langle u'_i u'_j \rangle \right) \equiv D_{L,ij} \quad - \quad \text{molecular diffusion term}$$

$$\rho \beta (g_i \langle u'_j \theta \rangle + g_j \langle u'_i \theta \rangle) \equiv G_{ij} \quad - \quad \text{buoyancy production}$$

$$\langle p \left( \frac{\partial u'_j}{\partial x_i} + \frac{\partial u'_i}{\partial x_j} \right) \rangle \equiv \phi_{ij} \quad - \quad \text{pressure strain}$$

$$2\mu < \frac{\partial u'_i}{\partial x_k} \frac{\partial u'_j}{\partial x_k} > \equiv \varepsilon_{ij} \quad - \quad \text{dissipation}$$

In the turbulent flow applications the diffusion term can be written as:

$$D_{T,ij} = \frac{\partial}{\partial x_k} \left( \frac{\mu_t}{\sigma_k} \frac{\partial}{\partial x_k} < u'_i u'_j > \right), \quad [2-25]$$

The value for coefficient  $\sigma_k = 0.82$  is derived by Lien and Leschziner (1994).

The effect of the buoyancy on turbulence is described in the model as:

$$G_{ij} = \beta \frac{\mu_t}{\text{Pr}_t} \left( g_i \frac{\partial T}{\partial x_j} + g_j \frac{\partial T}{\partial x_i} \right), \quad [2-26]$$

where  $\text{Pr}_t$  is the turbulent Prandtl number and  $\beta$  is coefficient of thermal expansion defined as:

$$\beta = -\frac{1}{\rho} \left( \frac{\partial \rho}{\partial T} \right)_p. \quad [2-27]$$

One of the greatest challenges in modeling swirling flows using RSM is the pressure-strain term. Proposed by Speziale et al. (1991), the quadratic pressure-strain model has been demonstrated to give better performance for a range of basic flows, including plane strain, rotating plane shear, as well as

axisymmetric expansion/contraction flows. The pressure-strain term can be written as:

$$\begin{aligned} \phi_{ij} = & -(C_1 \rho \varepsilon + C^*_1 P) b_{ij} + C_2 \rho \varepsilon \left( b_{ik} b_{kj} - \frac{1}{3} b_{mn} b_{mn} \delta_{ij} \right) + \left( C_3 - C^*_3 \sqrt{b_{ij} b_{ij}} \right) + \\ & + C_4 \rho k \left( b_{ik} S_{jk} - \frac{2}{3} b_{mn} S_{mn} \delta_{ij} \right) + C_5 \rho k (b_{ik} \Omega_{jk} + b_{jk} \Omega_{ik}), \end{aligned} \quad [2-28]$$

where the Reynolds stress anisotropy tensor,  $b_{ij}$ , is defined as:

$$b_{ij} = - \left( \frac{-\rho \langle u'_i u'_j \rangle + \frac{2}{3} \rho k \delta_{ij}}{2 \rho k} \right). \quad [2-29]$$

The mean strain rate,  $S_{ij}$ , is

$$S_{ij} = \frac{1}{2} \left( \frac{\partial u_j}{\partial x_i} + \frac{\partial u_i}{\partial x_j} \right). \quad [2-30]$$

The mean rate-of-rotation tensor,  $\Omega_{ij}$  is:

$$\Omega_{ij} = \frac{1}{2} \left( \frac{\partial u_i}{\partial x_j} - \frac{\partial u_j}{\partial x_i} \right). \quad [2-31]$$

The coefficients in the equation 2-28 are:

$$C_1=3.4, C^*_1=1.8, C_2=4.2, C_3=0.8, C^*_3=1.3, C_4=1.25, C_5=0.4$$

The dissipation tensor is modeled as:

$$\varepsilon_{ij} = \frac{2}{3} \delta_{ij} (\rho \varepsilon + Y_M), \quad [2-32]$$

where  $Y_M$  is additional dissipation (dilatation dissipation) modeled by Sarkar and Balakrishnan (1990) as:

$$Y_M = 2\rho \varepsilon M_t^2. \quad [2-33]$$

$M_t$  is turbulent Mach number - the ratio between velocity fluctuation amplitude and sound speed.

### ***Favre Averaging***

Normally the averaging is performed on the incompressible form of the equations. However, in the combustion applications temperatures and densities can be variable; to overcome this Favre averaging is used.

Decomposing a scalar into a Favre mean value and a fluctuation is conducted:

$$\psi_i(\mathbf{x}, t) = \langle \psi_i(\mathbf{x}, t) \rangle + \psi_i'(\mathbf{x}, t). \quad [2-34]$$

The equation for the reactive scalar is:

$$\rho (\partial \psi_i / \partial t) + \rho \mathbf{v} \cdot \nabla \psi_i = \nabla \cdot (\rho D_i \nabla \psi_i) + \omega_i, \quad [2-35]$$

Where  $\mathbf{v}$  is a velocity vector and  $\omega_i$  is a chemical source term:

$$\omega_i = \rho S_i. \quad [2-36]$$

This term can be Favre averaged as follows:

$$\rho (\partial \psi_i / \partial t) + \rho \mathbf{v} \cdot \nabla \psi_i = \nabla \cdot (\rho D_i \nabla \psi_i) - \nabla \cdot (\rho \mathbf{v}' \psi_i') + \rho S_i. \quad [2-37]$$

The left-hand side of the averaged equation is closed. The first term on the right-hand side contains the molecular diffusivity and can be neglected in the limit of high Reynolds number. Then the closure is required for the turbulent transport term and the mean chemical source term.

## Incorporating Chemistry into RANS Models

In the last several years, the knowledge of combustion chemistry has led to the development of sophisticated detailed chemical kinetic mechanisms that include at least about 50 species and more than 300 reactions for simple fuels like methane. The full kinetic mechanisms for higher order hydrocarbons may contain more species and reactions. Employing such a mechanism in CFD simulations for any practical combustion problem is prohibitive. The complicated turbulence models require the development of a simple model for the chemistry.

### **Heat Release Model**

The simplest way to model the chemical source term is as a heat release equation. One assumes the heat release has exponential dependency on temperature as follows:

$$\omega_T(T) = \rho S_T(T) = \rho B (T_b - T) \exp(-Ea / RT), \quad [2-38]$$

where:

$B$  = pre-exponential factor that contains the heat of reaction and a frequency factor

$T_b$  = adiabatic flame temperature

$Ea$  = activation energy of the reaction

$R$  = universal gas constant.

The temperature can be decomposed as  $T = \langle T \rangle + T'$ ; then the exponential term can be expanded as:

$$Ea / RT = Ea / R\langle T \rangle - (Ea T') / (R\langle T \rangle^2). \quad [2-39]$$

The source term becomes:

$$\omega_T(T) = \rho S_T(T) = \rho S_T(\langle T \rangle) [1 - T' / (T_b - \langle T \rangle)] \exp(Ea T' / R\langle T \rangle^2). \quad [2-40]$$

The value of  $(T'/\langle T \rangle)$  is usually taken to be between 0.1 and 0.3, and the value of  $(Ea/RT)$  is about 10 in the reaction zone.

### ***Eddy-Break-Up Model and Eddy Dissipation Model***

Eddy dissipation, as one of the first models, was developed by Magnussen and Hjertager (1977). It is based on the eddy breakup (EBU) model of Spalding (1971). Spalding assumed that as turbulent mixing can be viewed as energy cascade from large scale to molecular scale, this cascade process also controls the chemical reaction rate in the limit of infinitely fast chemistry. This concept was originally developed for one step non-premixed reaction but was adopted later for premixed flames. The rate of the reaction in the EBU model depends on the variance of the mean mass fraction of the product,  $\langle Y_p'^2 \rangle$ . The mean reaction rate is written as:

$$\langle \omega_P \rangle = \rho C_{EBU} \varepsilon / k (\langle Y_p'^2 \rangle)^2. \quad [2-41]$$

In the eddy dissipation model, the variance of the mean mass fraction of the product is substituted by the mean mass fraction of the limiting species (fuel or oxygen) or the product of the reaction. The rate of the reaction is determined by the limiting value of the three following expressions:

$$\langle \omega_F \rangle = \langle \rho \rangle A (\varepsilon / k) \langle Y_F \rangle \quad [2-42]$$

$$\langle \omega_{O_2} \rangle = \langle \rho \rangle A (\varepsilon / k) \langle Y_{O_2} \rangle / \nu \quad [2-43]$$

$$\langle \omega_P \rangle = \langle \rho \rangle [AB/(1+\nu)](\varepsilon / k) (\langle Y_p \rangle), \quad [2-44]$$

where:

$\nu$  = stoichiometric coefficient

A = modeling coefficient (4.0)

B = modeling coefficient (0.5).

The eddy dissipation and EBU models replace the chemical time by introducing the turbulent time scale  $\tau = (k/\varepsilon)$ . This is applicable only in the fast chemistry limit and it eliminates the dependency of chemical kinetics on the flow. In practical CFD simulations the coefficients A and B need to be “tuned” for each case to obtain reasonable results.

### ***Bray Moss Libby Model***

The Bray Moss Libby (BML) model is based on a flamlet concept for premixed combustion. A progress scalar variable is defined and is usually normalized by a product mass fraction or the temperature:

$$c = Y_P / Y_{P,b} \quad [2-45]$$

$$c = (T - T_u) / (T_b - T_u). \quad [2-46]$$

Here the flow is broken into three zones, fully burned mixture, the unburned mixture and the thin flame zone. In the flame zone, the progress variable,  $c$  represents the completeness of the combustion process. This limits the model to the fast chemistry limit and implies the use of a one-step mechanism. An assumed shape PDF is used to describe the flame as a function of the coordinate, time and the progress variable; it often is given by two dirac delta functions:

$$P(c, \mathbf{x}, t) = \alpha(\mathbf{x}, t) \delta(c) + \beta(\mathbf{x}, t) \delta(1-c). \quad [2-47]$$

The PDF has three parts, a spike at the unburned and burned ends and the center portion that gives the probability of being at a certain location in the laminar flame. The laminar flame mixture fractions and temperatures are calculated in advance and multiplied by the PDF to give the averaged results at each point in the flame. See Figure 2-16.

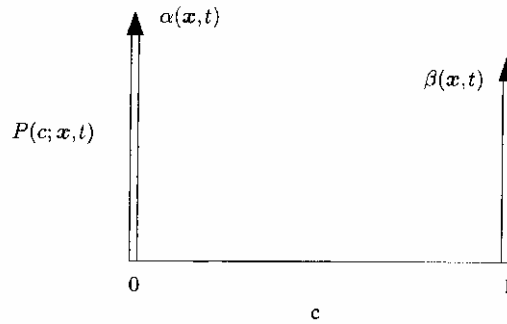


**Figure 2-16. Assumed PDF of the progress variable for BML model.**

Alternatively, a Favre averaged species conservation equation can be written for progress variable:

$$\rho (\partial c / \partial t) + \rho \mathbf{v} \cdot \nabla c = \nabla \cdot (\rho D_i \nabla c) - \nabla \cdot (\rho \mathbf{v}'' c'') + \langle \omega_c \rangle. \quad [2-48]$$

The diffusion term can be neglected for high Reynolds number. The two last terms in this equation need to be modeled. The turbulent scalar transport term depends on the turbulent mixing and gas expansion at the flame front. The gas expansion creates the counter-gradient diffusion term. There are numerous models aimed at closing this term.

In order to model the chemical term one needs to understand the physical structure of the flame. The BML model is based on the flamelet concept and applied for infinitely fast chemistry. The interface between the burnt and unburnt mixtures is very thin; thus, the progress variable has a spike taking large values at the interface and reduces to zero elsewhere. The mean chemical rate can be modeled as a dirac delta function or can be related to the reaction progress variable and the flame speed.

$$\langle \omega_c \rangle = \rho_u s_L^0 l_0 g(\langle c \rangle (1 - \langle c \rangle)) / L_y, \quad [2-49]$$

where:

$s_L^0$  = laminar un-stretched flame speed

$l_0$  = stretch factor

$g$  = coefficient depends on the pdf of the passage times

$L_y$  = crossing length scale, modeled.

Often the flame surface density is introduced:

$$\Sigma = g(\langle c \rangle (1 - \langle c \rangle)) / L_y \quad [2-50]$$

There are many attempts to model  $\Sigma$ ; some of them are based on the results of DNS and the others on experimental measurements.

The weak point of the surface density approach, and the BML concept as well, is that the reaction rates are based on the laminar flame instead of calculated from the chemical kinetics. The chemical reaction rate depends on (1) the density of unburnt mixture, (2) the laminar flame speed, (3) the flame

stretch factor, and (4) the flame surface density. The last two terms require modeling to incorporate turbulence into a laminar model.

The BML model is useful for showing the relative contributions of different scalar transport effects (i.e., turbulent mixing and gas expansion) for the weak turbulence especially. However, for flows with high turbulence the BML model is not appropriate.

### ***Level Set Approach***

The level set approach is used for modeling the corrugated flamelet and thin reaction zone regimes of turbulent premixed combustion. It uses a non-reacting scalar  $G$ ; since the scalar is non-reactive there is no need to model a chemical source term in the species conservation equation. The equation for  $G$  is based on the isoscalar surface  $G_0$ , which is arbitrarily fixed for each combustion event. This isoscalar surface divides the flow field in two parts:  $G < G_0$  for the unburnt region and  $G > G_0$  for burnt gases. See Figure 2-17.

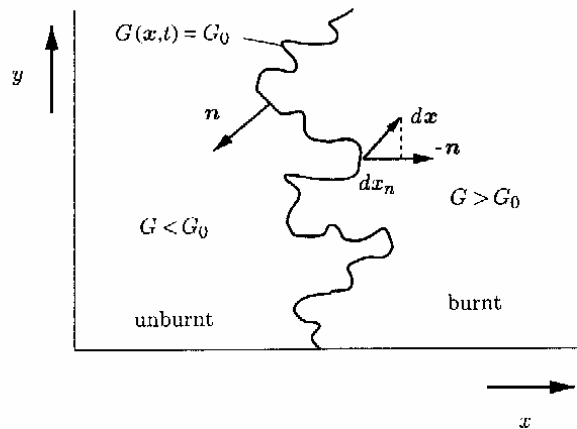


**Figure 2-17. GraPHical interpretation of G field.**

This approach is appropriate to describe premixed turbulent combustion where the thin flame propagates with a well defined speed. This is especially appropriate for the corrugated flamelets regime, because in that regime one assumes that the laminar flame is smaller than the Kolmogorov size eddy. See Figure 2-11.

The equation for the G-field is easily derived:

$$\partial G / \partial t + \mathbf{v}_f \cdot \nabla G = s_L |\nabla G|, \quad [2-51]$$

where  $s_L$  is a local laminar flame speed and  $\mathbf{v}_f$  is flow velocity at the flame surface. Then for a stationary flame (such as a Bunsen flame) one can see the balance between the flow velocity and the laminar flame speed as the time derivative is zero. Generally, the G-field is defined only at the flame surface as a two-dimensional surface area. However, in order to run the numerical simulation one needs to define the values of  $s_L$  and  $\mathbf{v}_f$  for the entire flow field. The flow velocity can be replaced by the local velocity,  $\mathbf{v}$ . The value of local laminar flame velocity should account for flame stretching and flame curvature. For small flame curvature in the corrugated flamelet regime:

$$s_L = s_L^0 - s_L^0 \mathcal{L} k - \mathcal{L} S, \quad [2-52]$$

where:

$s_L^0$  = unstretch laminar flame speed

$\mathcal{L}$  = Markstein length, defines the effect of curvature on a flame. The larger value of the Markstein length is associated with a greater the effect of curvature on burning velocity

$k$  = curvature,  $k = \nabla \cdot \mathbf{n}$  ( $\mathbf{n}$ -normal vector), and can be defined in terms of  $\nabla G$

$S$  = strain rate imposed by the velocity gradient on the flame,  $S = -\mathbf{n} \cdot \nabla \mathbf{v} \cdot \mathbf{n}$ .

Introducing the laminar flame velocity into the general G-equation gives the following equation for corrugated flames:

$$\partial G / \partial t + \mathbf{v} \cdot \nabla G = s_L^0 |\nabla G| + k D_L |\nabla G| + L S |\nabla G|, \quad [2-53]$$

where  $D_L = s_L^0 \mathcal{L}$  is Markstein diffusivity. For strong flame curvature, the second derivative will appear in the G-equation.

In the thin reaction zone regime, the laminar flame velocity is not well defined because the Kolmogorov size eddies enter the preheat zone and the flame structure cannot be assumed quasi-steady. Then the laminar flame velocity is decomposed into velocity due to normal diffusion,  $s_n$ , and reaction displacement speed on the thin reaction zone,  $s_r$ . The sum of these velocities,  $s_{L,s} = s_n + s_r$ , is a fluctuating quantity and it is of the same order as  $s_L^0$ . The value of the sum also depends on the curvature; then the G-equation for the thin reaction zone can be written as:

$$\partial G / \partial t + \mathbf{v} \cdot \nabla G = s_{L,s} |\nabla G| - D |\nabla G|. \quad [2-54]$$

Further, based on order of magnitude analysis, the equation can be written as follows:

$$\rho (\partial G / \partial t) + v \cdot \nabla G = (\rho s_L^0) |\nabla G| - (\rho D) k |\nabla G|. \quad [2-55]$$

The value of  $(\rho s_L^0)$  often is assumed constant and represents the mass flow rate; the quantity  $(\rho D)$  is defined at  $T_0$  and assumed constant. The value of  $G$  in this equation is defined only at the flame surface  $G(\mathbf{x}, t) = G_0$ . In practical modeling the non-uniqueness of the  $G$ -field is ignored and  $G(\mathbf{x}, t)$  is described by a probability density function:  $P(G; \mathbf{x}, t)$ . From  $P(G; \mathbf{x}, t)$  the moment of  $G$  can be calculated. These moments,  $\langle G(\mathbf{x}, t) \rangle$  and  $\langle G'^2(\mathbf{x}, t) \rangle$ , describe non-uniqueness of  $G$  outside of the surface  $G(\mathbf{x}, t) = G_0$ .

Since the  $G$ -equation is derived from the empirical correlations and physics of the flame (i.e., the laminar flame speed and diffusion) and not from first principles, it is decoupled from the Navier Stokes equations. This allows one to solve the Reynolds-averaged Navier Stokes equations and obtain the flame location and flame speed. However, in order to find species concentrations and temperature fields across the flame more modeling is required.

The application of the  $G$ -equation model is valid for flames with a well-defined burning velocity. This approach clearly has benefits of not modeling the turbulent transport and the chemical source terms, unlike the moment closure model. It will also model the counter-gradient diffusion, gas expansion effect on turbulent burning velocity. The  $G$ -equation model looks promising for certain applications such as spark ignition engine, where the flame is well defined. However, it is questionable if the model will work for modeling the LP gas turbine combustors where the flame brush does not have well defined iso-surfaces.

***Probability Density Function Method***

The above moment schemes encounter severe problems for modeling the interaction between the physical properties and the chemical terms.

Probability density function (PDF) methods are based on the stochastic approaches; they appear to deal with these interactions with relative ease.

The main advantage of the PDF method is that there is no need to model the chemical reaction term. This allows the PDF to account for the effects of temperature and species concentration fluctuations on reaction rates. In the PDF method, Lagrangian transport equations can be solved in three ways.

1. Numerically integrate the transport equations. However, numerical integration can be difficult, due to the non-smoothness of the PDF. This can be done for a relatively small domain and not very complicated chemical mechanism.
2. The Monte Carlo method simulates each of the four processes: diffusion, convection, mixing, and reaction in the computational domain of  $N$  elements for each time step. When compared with standard numerical methods (e.g., finite difference or finite volume methods), the method is not efficient for simple problems. However, for the larger problems the computational time required for numerical integration increases exponentially with the number of species, whereas the Monte Carlo method only increases linearly.
3. Assumed shape PDF constrains the first and second moments. The PDF is assumed to be of a certain shape (e.g., Gaussian or beta). The PDF will be different at different locations within the flame. Mean value and variance uniquely determine the shape of the PDF, which become the targets of the solution. This reduces the computational time, but also

reduces the accuracy of the solution. The assumed shape method only will work for perfectly premixed flames and diffusion flames in the fast chemistry limit (Borghi, 1988).

There are several types of joint PDF:

- Species composition PDF – the method does not require any information about the velocity field. The Reynolds-averaged Navier Stokes equations need to be solved simultaneously.
- Joint PDF of the velocity-composition PDF. Here the three velocity terms are accounted for in the PDF. This PDF does carry information about turbulent length and time scales. Only the equations for  $k$  and  $\varepsilon$  need to be solved.
- Joint PDF of the velocity-dissipation-composition. No additional modeling is required, but the PDF is difficult to solve. This PDF assumes that the composition fields are proportional to the time and length scales.

The PDF methods have been applied to premixed and non-premixed combustion. In practice, they are often coupled with separate computations of the flow field as mentioned above. The flow code provides the velocity field with turbulence properties, and the PDF code calculates the density, temperature, and species concentration fields. The PDF code also calculates the velocity field, which is kept consistent with the velocity field and turbulence properties calculated by the flow code. The two codes are converged sequentially, in a loop, with the PDF code providing the density field to the flow code. This is called hybrid approach and it incorporates the Monte Carlo PDF calculations in a finite-volume flow solver; however, the Monte Carlo method may produce statistical error.

There are two major weaknesses of the PDF methods: (1) a much larger computational requirement when compared to the moment methods, and (2) the molecular mixing modeling within the computational cell has uncertainties.

### **Summary: Turbulence Modeling**

While direct numerical simulation remains mostly a research tool and the large eddy simulation method is computationally expansive, the RANS simulations are used for most practical tasks. The above-described models can be applied to premixed combustion when solved for the Reynolds-averaged Navier Stokes equations. Some assumptions are made in order to model the combustion in each method. These assumptions restrict the application of the models to particular regimes of combustion (Figure 2-2). Table 2-1 below summarizes the models with respect to their ability to treat chemistry and their application to particular regimes of premixed turbulent combustion.

The simplest models are the heat release and the eddy dissipation models. Both of these lack physical content and are based on an intuitive understanding of the combustion process. However, such models are used most often in commercially available CFD codes and are relatively easy to apply to practical problems due to fast convergence.

The flamelet approach (BML model) assumes an infinitely fast rate of chemistry and has the mixing as the limiting factor for reaction. The model implies one step reaction where the temperature raises from  $T_u$  to  $T_b$  at the

flame surface. The model is applicable only to combustion regimes where flame surface is defined; thus, it is limited to the corrugated flame regime.

The G-equation model can be applied for corrugated flamelets as well as, with some modification, to the thin reaction zones regime. The level set approach can take into account finite rate chemistry. However, using the G-equation, one can not predict the species concentration field, thus additional modeling is required. This model is less dependent on the defined flame surface, but still needs a well defined flame and cannot be used for the broken reaction zone regime.

The PDF model is based on the stochastic approach in Lagrangian coordinates. This method is able to treat fairly complex chemistry and can be incorporated into the flow model. The greatest draw back is the computational time required for any practical size simulation.

**Table 2-1. Summary of the models for premixed turbulent combustion.**

<b>Model</b>	<b>Chemistry treatment</b>	<b>Regime applicable</b>
Simple heat release	Heat release only	All
Eddy break-up Eddy dissipation	One step, infinite chemistry	All
BML flamelets model	One step, infinite chemistry	Corrugated flames
G-equation	One step, finite chemistry rate	Corrugated flames Thin reaction zones
PDF transport equation	Detailed or reduced chemical kinetic mechanism	All

## Heat Transfer Modeling

### Convective Heat Transfer

Convective heat transfer is modeled using the concept of Reynolds analogy. By analogy with turbulent momentum transfer the energy equation is written as:

$$\frac{\partial}{\partial t}(\rho E) + \frac{\partial}{\partial x_i}(u_i(\rho E + p)) = \frac{\partial}{\partial x_j} \left( \left( k + \frac{c_p \mu_t}{\text{Pr}_t} \right) \frac{\partial T}{\partial x_j} + u_{ij}(\tau_{ij})_{eff} \right) + S_h, \quad [2-56]$$

where  $E$  is a total energy,  $S_h$  is heat source and  $(\tau_{ij})_{eff}$  is a deviatoric stress tensor:

$$(\tau_{ij})_{eff} = \mu_{eff} \left( \frac{\partial u_j}{\partial x_i} + \frac{\partial u_i}{\partial x_j} \right) - \frac{2}{3} \mu_{eff} \frac{\partial u_i}{\partial x_i} \delta_{ij}, \quad [2-57]$$

### Radiative Heat Transfer Modeling

Modeling of radiative heat transfer is important whenever the computation involves heat sources or sinks, and heating or cooling of surfaces due to radiation. The radiative heat transfer governing equation for absorbing, emitting, and scattering media is:

$$\frac{\partial I(\vec{r}, \vec{s})}{\partial s} + (a + \sigma_s) I(\vec{r}, \vec{s}) = an^2 \frac{\sigma T^4}{\pi} + \frac{\sigma_s}{4\pi} \int_0^{4\pi} I(\vec{r}, \vec{s}') \Phi(\vec{s}, \vec{s}') d\Omega', \quad [2-58]$$

where:

$\vec{r}$	=	position vector
$\vec{s}$	=	direction vector
$s$	=	path length
$I$	=	Radiation intensity
$a$	=	absorption coefficient
$\sigma_s$	=	scattering coefficient
$\sigma$	=	Stephan-Boltzmann constant
$\vec{s}'$	=	scattering direction vector
$n$	=	refractive index
$T$	=	local temperature
$\Phi$	=	phase function
$\Omega'$	=	solid angle

Some of the common applications that require radiative heat transfer modeling are: combustion applications with radiative heat transfer from flames, surface heating/cooling, manufacturing processes of glassmaking, fiber drawing, and HVAC applications. There are a number of models available for radiative heat transfer, most common are:

- Discrete transfer radiation model (DTRM) (Carvalho et al., 1991, Shah, 1979)
- P-1 radiation model (Cheng, 1964)
- Rosseland radiation model (Siegel and Howell, 1992)
- Discrete ordinates (DO) radiation model (Chui and Raithby, 1993, Raithby and Chui, 1990).

The choice of the radiation model depends on a number of parameters. Optical thickness of the media is one the most important ones. In cases where the optically thin media ( $\alpha L < 1$ ,  $L = \text{path length}$ ) are modeled, the DO

and DTRM are the most appropriate models. Since the scope of this work includes modeling of lean-premixed combustion in the gas turbine, where optically thin regions are present, the choice of other models would be inappropriate. The greatest problem with DTRM is that the model cannot be applied with parallel processing in the commercial software package that is used for CFD simulation.

The discrete ordinates radiation model is the more universal out of the two; particularly, the DO model can be used over the entire range of optical thicknesses and it can include scattering, anisotropy, semi-transparent media, and particulate effects. Computational requirements are moderate for typical angular discretizations. The model also allows computing non-gray radiation (for gases like  $\text{H}_2\text{O}$  and  $\text{CO}_2$ ) using a gray band model. Fiveland and Jamaluddin (1989) have used gray-band models to model gas behavior by approximating the absorption coefficients within each band as a constant.

### ***Conclusions for Modeling Approaches Used in This Research***

Table 2-2 shows the models that have been used in this research. The choices are based on the discussion above and the availability of the models in the commercial CFD package FLUENT. The chemical source is modeled using limiting reaction rate approach. This approach is a modification of eddy break-up scheme and incorporates the finite global chemistry into CFD simulation. It is discussed below in Chapter 4.

**Table 2-2. Summary of the models for premixed turbulent combustion.**

Turbulence model	RANS
Turbulence closure model	Reynolds stress model
Pressure strain term model	Quadratic pressure strain model
Chemical term model	Limiting rate approach (modified EBU model)
Radiative heat transfer	Discrete ordinates model

### **3. Eight-Step Global Mechanism for Methane Oxidation with Nitrogen Oxides Formation**

The eight-step global mechanism has been developed for use in CFD codes for lean-premixed gas turbine combustors. The mechanism includes seven species and consists of eight reactions in global format. There are three reactions for methane oxidation and five reactions describing the formation of nitrogen oxide. In order to validate the mechanism against the experimentally obtained data, a number of high-pressure, lean-premixed databases have been considered:

1. Jet-stirred reactor database of Bengtsson (1998)
2. Jet-stirred reactor database of Rutar (2000).
3. Bluff body combustor database reported by Butcher et al. (2003).

#### ***Development of the Eight-Step Global Mechanism***

Using the detailed chemical kinetic mechanism GRI3.0, Rutar et al. (2000) and Rutar and Malte (2002) showed that the jet stirred reactors could be successfully modeled using simple two/three reactor models. The development of the eight-step global mechanism is based on the ability of chemical reactor models to predict the emission levels and pollutant species formation rates using simple reactor arrangements. The boundary and operating conditions used for this chemical kinetic modeling reflect the typical operating conditions of the primary zone lean-premixed gas turbine combustors.

The JSR databases provide  $\text{NO}_x$ ,  $\text{N}_2\text{O}$ ,  $\text{CO}$ , and  $\text{O}_2$  concentrations as a function of reactor pressure, temperature, and residence time. Chemical kinetic modeling of these databases using single and two PSR chemical reactor models, with a PFR added as required, allows the rates of fuel (methane) oxidation,  $\text{CO}$  formation and destruction, and  $\text{NO}_x$  formation by four pathways to be calculated. The four  $\text{NO}_x$  formation pathways are the Zeldovich mechanism, the nitrous oxide pathway, Fenimore prompt  $\text{NO}$ , and the  $\text{NNH}$  pathway. The role of these pathways in lean-premixed combustion is discussed in Nicol et al. (1996) and Rutar et al. (2000).

The chemical reactor modeling of combustor provides a database of species concentrations, species formation and destruction rates, temperature and pressure. Regression analysis is then later performed on these databases, arriving at global reaction rates for:

1. Methane oxidation
2. Carbon monoxide oxidation
3. Carbon dioxide dissociation
4. Nitrogen oxide formation in the flame front and near post flame region by nitrous oxide and super-equilibrium Zeldovich mechanisms
5. Nitrogen oxide formation in the flame by the prompt and  $\text{NNH}$  mechanisms.

The rates of  $\text{NO}$  formation in the post flame zone by the nitrous oxide (reactions 6, 7) and Zeldovich (reaction 8) routes are found analytically assuming equilibrium concentration of  $\text{O}$ ,  $\text{H}$ , and  $\text{OH}$ .

The use of chemical reactor models allows to extrapolate JSR database to other high intensity combustion conditions -- i.e. to conditions existing in lean-premixed combustion engines.

**Table 3-1. Major elemental reactions of NO<sub>x</sub> formation. The forward reaction rate is shown; the backward rate is calculated by code using detailed balance of the reaction constant. The “direction” column shows the most likely direction of the reaction under the lean-premixed combustion regime. The notation and units of the reaction rates are: “A” - exponent in the pre-exponential factor 10<sup>A</sup>, kmol/m<sup>3</sup>/s, “b” - temperature exponent in (T/T<sub>0</sub>)<sup>b</sup>, “E<sub>a</sub>” – activation energy kcal/mole.**

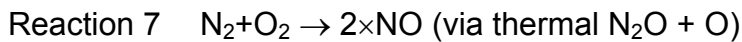
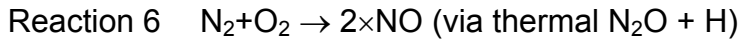
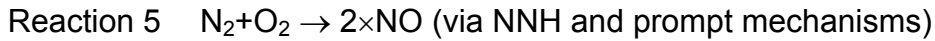
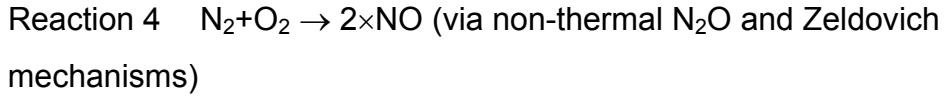
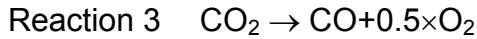
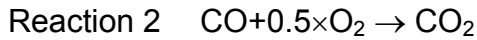
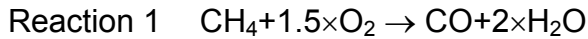
Zeldovich Mechanism									
Reactants			Direction	Products			A	b	Ea
N	NO		←	N <sub>2</sub>	O		13.431	0	0.355
N	O <sub>2</sub>		→	NO	O		9.954	1	6.5
N	OH		→	NO	H		13.526	0	0.385
Nitrous oxide mechanism									
Reactants			Direction	Products			A	b	Ea
N <sub>2</sub> O		M	↔	N <sub>2</sub>	O	M	10.898	0	56.02
N <sub>2</sub> O	O		→	N <sub>2</sub>	O <sub>2</sub>		12.146	0	10.81
N <sub>2</sub> O	O		→	NO	NO		13.462	0	23.15
N <sub>2</sub> O	H		→	N <sub>2</sub>	OH		14.588	0	18.88
N <sub>2</sub> O	OH		→	N <sub>2</sub>	HO <sub>2</sub>		12.301	0	21.06
NNH mechanism									
Reactants			Direction	Products			A	b	Ea
NNH			←	N <sub>2</sub>	H		8.519	0	0
NNH		M	←	N <sub>2</sub>	H	M	14.114	-0.1	4.98
NNH	O <sub>2</sub>		←	HO <sub>2</sub>	N <sub>2</sub>		12.699	0	0
NNH	O		←	OH	N <sub>2</sub>		13.398	0	0
NNH	H		←	H <sub>2</sub>	N <sub>2</sub>		13.699	0	0
NNH	OH		←	H <sub>2</sub> O	N <sub>2</sub>		13.301	0	0
NNH	CH <sub>3</sub>		←	CH <sub>4</sub>	N <sub>2</sub>		13.398	0	0
NNH	O		→	NH	NO		13.845	0	0
NH	OH		→	N	H <sub>2</sub> O		9.301	1.2	0
NH	O		→	NO	H		13.602	0	0
NH	O <sub>2</sub>		→	NO	OH		6.107	1.5	0.1
N	O <sub>2</sub>		→	NO	O		9.954	1	6.5
N	OH		→	NO	H		13.526	0	0.385
Fenimore prompt (CH) mechanism									
Reactants			Direction	Products			A	b	Ea
CH	N <sub>2</sub>		→	HCN	N		9.494	0.88	20.13
HCN	O		→	NCO	H		4.307	2.64	4.98
NCO	O		→	NO	CO		13.371	0	0
NCO	OH		→	NO	H	CO	12.398	0	0
NCO	O <sub>2</sub>		→	NO	CO <sub>2</sub>		12.301	0	20
HCN	O		→	NH	CO		3.705	2.64	4.98
NCO	H		→	NH	CO		13.732	0	0
NH	OH		→	N	H <sub>2</sub> O		9.301	1.2	0
NH	O		→	NO	H		13.602	0	0
NH	O <sub>2</sub>		→	NO	OH		6.107	1.5	0.1
N	O <sub>2</sub>		→	NO	O		9.954	1	6.5
N	OH		→	NO	H		13.526	0	0.385

As discussed in Novosselov (2002), the global mechanism has been developed by finding the best linear square fit for the reaction rates predicted by GRI 3.0 in the UW chemical reactor code. Various arrangements of perfectly stirred reactors followed by a plug flow reactor as shown in Table 3-2 have been used to obtain the database for regression analysis. This work has computed the reaction rates of methane oxidation, CO formation and destruction, and NO formation for pressures between 5 and 20 atmospheres and fuel-air equivalence ratios ( $\phi$ ) of 0.45 to 0.75. These rates have been fitted to the global reaction rate format.

For both of the jet stirred reactors, the NO<sub>x</sub> and CO predictions using the global rates developed by Novosselov (2002) are within 15% agreement of both the experimental JSR data and the chemical reactor model computations with the GRI 3.0 full kinetic mechanism. The reactions and rates obtained in the regression analysis are shown below.

**Table 3-2. Reactor schemes used for modeling high-intensity lean-premixed combustion for generating database for global mechanism development.**

Reaction	Reactor scheme used in chemical reactor modeling
Methane oxidation	<ol style="list-style-type: none"> <li>1. Single PSR from blowout up to 3ms residence time</li> <li>2. PSR at blowout followed by a PSR up to 3 ms residence time</li> </ol>
CO oxidation	<ol style="list-style-type: none"> <li>1. Single PSR from blowout up to 3ms residence time</li> <li>2. PSR at blowout followed by a PSR with up to 3 ms residence time</li> <li>3. PSR from blowout up to 3ms followed by a PFR with varied residence time up to equilibrium concentrations</li> <li>4. PSR from blowout up to 3ms followed by a PFR with cooling air addition with varied residence time up to equilibrium concentrations</li> </ol>
CO <sub>2</sub> dissociation	<ol style="list-style-type: none"> <li>1. Single PSR from blowout up to 3ms residence time</li> <li>2. PSR from blowout up to 3ms followed by a PFR with varied residence time up to equilibrium concentrations</li> <li>3. PSR from blowout up to 3ms followed by a PFR with cooling air addition with varied residence time up to equilibrium concentrations</li> </ol>
NO via non-thermal N <sub>2</sub> O and Zeldovich	<ol style="list-style-type: none"> <li>1. Single PSR from blowout up to 3ms residence time</li> <li>2. PSR at blowout followed by a PSR with up to 3 ms residence time</li> <li>3. PSR from blowout up to 3ms followed by a PFR with up to 3 ms residence time</li> </ol>
NO via prompt and NNH	<ol style="list-style-type: none"> <li>1. Single PSR from blowout up to 3ms residence time</li> <li>2. PSR at blowout followed by a PSR with up to 3 ms residence time</li> </ol>



$$R_1 = 10^{13.354 - 0.004628 \times P} [\text{CH}_4]^{1.3 - 0.01148 \times P} [\text{O}_2]^{0.01426} [\text{CO}]^{0.1987} \exp(- (21932 + 269.4 \times P)/T)$$

$$R_2 = 10^{14.338 + 0.1091 \times P} [\text{CO}]^{1.359 - 0.0109 \times P} [\text{H}_2\text{O}]^{0.0912 + 0.0909 \times P} [\text{O}_2]^{0.891 + 0.0127 \times P} \exp(- (22398 + 75.1 \times P)/T)$$

$$R_3 = 10^{15.8144 - 0.07163 \times P} [\text{CO}_2] \times \exp(- (64925.8 - 334.31 \times P)/T)$$

$$R_4 = 10^{14.122 + 0.0376 \times P} [\text{CO}]^{0.8888 - 0.0006 \times P} [\text{O}_2]^{1.1805 + 0.0344 \times P} \exp(- (46748 + 126.6 \times P)/T)$$

$$R_5 = 10^{29.8327 - 4.7822 \times \log(P)} [\text{CO}]^{2.7911 - 0.04880 \times P} [\text{O}_2]^{2.4613} \exp(- (61265 + 704.7 \times P)/T)$$

$$R_6 = 10^{14.592} [\text{N}_2] [\text{H}_2\text{O}]^{0.5} [\text{O}_2]^{0.25} \times T^{-0.7} \exp(-69158/T)$$

$$R_7 = 10^{10.317} [\text{N}_2] [\text{O}_2] \times \exp(-52861/T)$$

$$R_8 = 10^{14.967} [\text{N}_2] [\text{O}_2]^{0.5} T^{-0.5} \times \exp(-68899/T)$$

The units used in the rate expressions are: activation temperature ( $E_a/R$ ) = K, concentration = [ ] = kmol/m<sup>3</sup>, reaction rate =  $R_i$  = kmol/(m<sup>3</sup>-s), pressure = atm.

Full details on the development of the eight-step mechanisms are given in the MSME thesis of Novosselov (2002).

### ***Upgrade to the Eight-Step Global Mechanism***

Reaction five of the eight-step mechanism originally had a dependency on the methane concentration and an inverse dependency on the oxygen concentration (Novosselov 2002). This reaction accounts for fast formation of NO in the flame front by the Fenimore prompt NO and NNH mechanisms. While CFD modeling the bluff body combustor (discussed later) this form of reaction 5 resulted in numerical instability near the pilot flame. The fuel–air equivalence ratio of the pilot flame is unity, which caused a singularity in the CFD cells near the pilot. In order to avoid division by zero, this reaction rate was revised. The reaction 5 rate now is a function of pressure, temperature, and the concentrations of carbon monoxide and oxygen.

Novosselov (2002) showed the normalized rate of NO formation by the prompt NO and NNH mechanisms for different operating pressures of a combustor. The importance of these pathways diminishes rapidly with the amount of time that the mixture spends in the flame. Since both pathways exhibit similar trends, the rates of prompt NO and NNH-NO are combined and fitted to one global reaction.

Recently, a number of researchers have investigated the NNH mechanism formation rates and possible new pathways of NO formation from NNH (Konnov and Ruyck, 2001a, 2001b; Haworth et al., 2003; Tomeczek and Gradon, 2003). The reported rates and pathways are different from GRI 3.0 and they may play a significant role for atmospheric combustion and combustion of fuels containing hydrogen. It has been found that for elevated

pressure combustor of hydrocarbons, the NNH chemistry is not a large producer of NO and the modified rates of Bozzeli and Dean (1995) used in GRI 3.0 yield reasonable predictions of the NO formation. This can be attributed to the suppression of the free radicals (such as NNH) in the flame zone by the high pressure. Thus, the full GRI 3.0 nitrogen chemistry is assumed valid for the purpose of regression analysis in this work.

The methodology to obtain the revised global rate of reaction 5 is now described. It is illustrative of the procedure used to obtain all of the other global rates. The database used for the upgrade of the global rate that accounts for prompt and NNH-NO (i.e., global reaction 5) is obtained using a single PSR. A single PSR is used since the prompt and NNH chemistry is fast and does not persist once the gas enters a second PSR or PFR reactor. The reactor is adiabatic for most cases, however in some cases, less than the adiabatic temperature is assigned to the reactor. Since the prompt mechanism is most important at the rich fuel-air equivalence ratios and low pressures, more weight is given to these conditions. The conditions where the combined prompt and NNH routes contribute less than 5% of the total NO are not considered.

The least square fit is made to the following global reaction rate form:

$$R_5 = 10^{n_0 + n_1 \times \log(P)} [\text{CO}]^{a_0 + a_1 \times P} [\text{O}_2]^{b_0 + b_1 \times P} \exp(-(T_a + T_{a1} \times P)/T)$$

The diatomic nitrogen is not explicitly included in the reaction since it does not change its concentration sufficiently to influence the reaction rate. However the pre-exponential factor carries the pressure dependency in it, which is an

implicit reference to  $N_2$ . The smallest residuals for the global reaction rate are obtained for the formula:

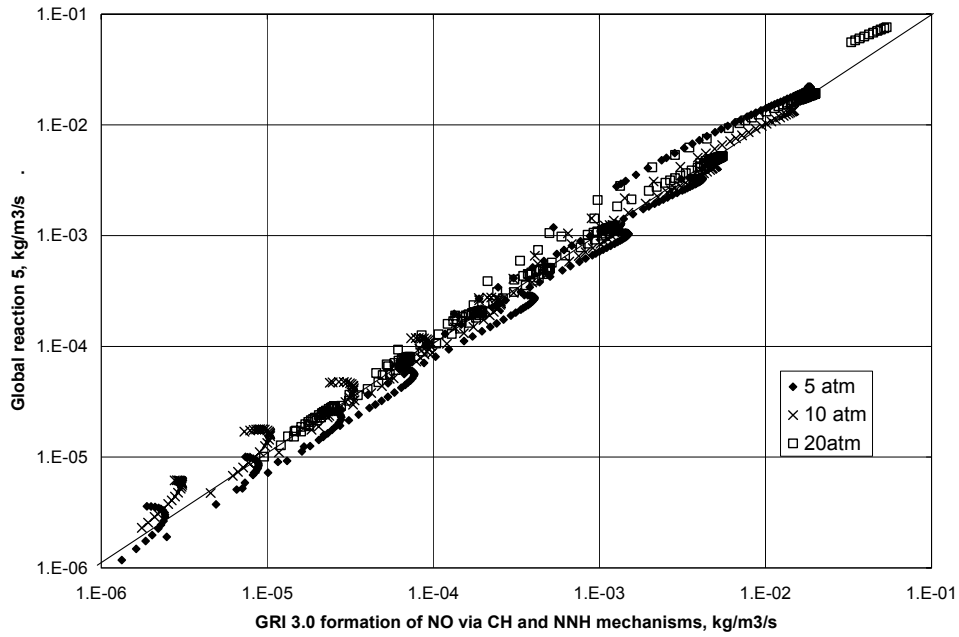
$$R_5 = 10^{29.8327 - 4.7822 \times \log(P)} [\text{CO}]^{2.7911 - 0.04880 \times P} [\text{O}_2]^{2.4613} \exp(-(61265 + 704.7 \times P)/T)$$

Figure 3-1 shows the agreement between the full kinetic mechanism and the global rate of NO formation via the prompt and NNH pathways. The forty five degree line on the plot represents the perfect fit, where the global rate is equal to the rate calculated by the GRI 3.0. The full kinetic mechanism rate is:

$$R_5 = 2 k_1 [\text{CH}][\text{N}_2] + 2 k_2 [\text{NNH}][\text{O}]$$

That is, under lean premixed combustion, each reaction of  $\text{CH} + \text{N}_2 \rightarrow \text{HCN} + \text{N}$  leads to two NO molecules upon oxidation of the HCN and N, and each reaction of  $\text{NNH} + \text{O} \rightarrow \text{NO} + \text{NH}$  leads to leads NO molecules. The concentration of species CH,  $\text{N}_2$ , NNH, and O is obtained from the output of the chemical kinetic code. The rate expression includes rate constants  $k_1$  and  $k_2$ , which are, respectively GRI 3.0 rate constants for  $\text{CH} + \text{N}_2 = \text{HCN} + \text{N}$  and  $\text{NNH} + \text{O} = \text{NO} + \text{NH}$ .

Since the upgraded global mechanism does not have methane concentration dependency in the NO formation chemistry, the NO rates of the mechanism can be used for modeling of other hydrocarbon fuels. The example of modeling of other hydrocarbon fuel blend combustion is found in Chapter 8.



**Figure 3-1. Formation of NO in the flame (modeled as PSR) via prompt NO and NNH mechanisms versus global reaction 5. Inlet temperature: 5 atm (483 K), 10 atm (592 K), 20 atm (716 K); temperature in the PSR corresponds to the adiabatic flame temperature. Residence time in the PSR varies from the blowout to 2.5 ms. Longer residence times lead to quenching of the prompt and NNH chemistry.**

## 4. Application of the Eight-Step Global Mechanism in CFD for Bluff Body Experimental Combustor

In order to evaluate the performance of the eight-step global mechanism in CFD, two different lean premixed combustor geometries are modeled:

1. Bluff body combustor of Butcher et al. (2003) – this chapter
2. Generic single injector can-type gas turbine combustor – next chapter

The experimental setup for bluff body combustor is described by Butcher et al. 2003. The outer walls and the bluff body insert of the combustor are coated with zirconia thermal barrier and cooled by impingement/effusion cooling. A non-premixed pilot is located in the corner of the bluff body insert and this helps to stabilize the flame. The operating conditions are presented in Table 4-1:

**Table 4-1. Operating conditions for high pressure bluff body combustor**

Description	Unit
Length of combustion zone, measured from the bluff body dump plane	0.53m
Width of the combustion chamber	0.071m
Bluff body blockage ratio	0.63
Operating pressure	14.3 atm
Inlet air temperature	678 K
Total air flow rate	1.08 kg/s
Fuel	98% methane
Fuel air equivalence ratio with the addition of cooling air.	0.56-0.71

Can-type combustor geometry is used to gain insight of the flow field in the swirl- stabilized combustor. Although experimental data for the combustor modeled does not exist, CFD modeling of this geometry aids the development of the CRN for the industrial GT combustor examined in Chapter 6.

The generic, lean-premixed, single-injector, can-type gas turbine combustor CFD-modeled here is based on Combustor A tested by Mellor (1996). For the present CFD modeling, Combustor A is modified by replacing the louvered liner cooling with air back-side cooling and the reference velocity is increased to 10 m/s , which is a more representative of GT combustors than the lower value used in Mellor's work. The premixer used a 45 degree swirler with 45% blockage (Beer and Chigier, 1983), with a uniform fuel-air ratio at the premixer exit.

### ***Bluff Body Modeling***

#### **Numerical approach**

The bluff body modeling is conducted using the commercial CFD code Fluent 6.1. A two-dimensional structured grid is used for the simulation. Using the planar symmetry of the burner, only a half of the burner is modeled. The 3-D effects are not considered in this simulation; however, some of the 3-D effects are accounted for in the interpretative analysis. Table 2 summarizes the assumptions and the boundary conditions used in the modeling.

**Table 4-2. Modeling assumptions and boundary conditions for the bluff body combustor.**

Computational domain	2D structured grid, 110 000 cells
Solver	Segregated RANS with species transport and volumetric reactions
Turbulence closure model	Reynolds stress model
Convergence scheme	Second order (QUICK)
Pressure velocity coupling	Pressure implicit splitting of operators (PISO)
Wall treatment	Standard wall function
Heat loss	Convective and radiative heat transfer for top wall
Radiative heat transfer	Discrete ordinates (DO) model
Chemical kinetic rates	Eight-step mechanism
Chemical mixing rates	Modified EBU rates

### Limiting Reaction Rate Approach

The rate limiting approach is used in determining the effective reaction rate. The turbulent reaction rate is computed based on the eddy break-up (EBU) model (Magnussen and Hjertager, 1976), and the chemical kinetic rate is calculated by the global mechanism. The smaller of the two is used in the CFD code in each location of the domain. For example, the two competing rates in the initial fuel break down step are:

$R_{\text{CH}_4 \text{ destruction EBU}}$  - turbulent mixing reaction rate

$R_{\text{CH}_4 \text{ destruction kinetic}}$  - chemical kinetic reaction rate

The combined reaction rate is:

$$1 / R_{\text{CH}_4 \text{ destruction}} = 1 / R_{\text{CH}_4 \text{ destruction EBU}} + 1 / R_{\text{CH}_4 \text{ destruction kinetic}}$$

$$R_{\text{CH}_4 \text{ destruction}} = (R_{\text{CH}_4 \text{ destruction EBU}} + R_{\text{CH}_4 \text{ destruction kin}}) / (R_{\text{CH}_4 \text{ destruction EBU}} R_{\text{CH}_4 \text{ destruction kin}})$$

For this reaction, the turbulent mixing rate is orders of magnitude smaller than the kinetic rate (except at the injector walls). That is:

$$R_{\text{CH}_4 \text{ destruction EBU}} = A_{1,\text{EBU}} \varepsilon / k [\text{CH}_4] \ll R_{\text{CH}_4 \text{ destruction kinetic}} = 10^{13.354 - 0.004628 \times P} [\text{CH}_4]^{1.3 - 0.01148 \times P} [\text{O}_2]^{0.01426} [\text{CO}]^{0.1987} \exp(-(21932 + 269.4 \times P)/T),$$

where:

$\varepsilon$  = turbulent dissipation rate,  $\text{m}^2/\text{s}^3$

$k$  = turbulent kinetic energy,  $\text{m}^2/\text{s}^2$

The fuel (methane) concentration is used in the EBU rate expression since it is the limiting (smallest) concentration in the initial fuel breakdown reaction.

The other species in the reaction is oxygen and its concentration is much higher for the lean-premixed combustion case. Thus, in the flame:

$$R_{\text{CH}_4 \text{ destruction}} = R_{\text{CH}_4 \text{ destruction EBU}}$$

The above expression holds in the jet region where the turbulent dissipation rate limits the turbulent reaction rate. This is not the case in the boundary layer at the injector walls. The chemical rate at the wall is lower not only because of a high dissipation rate in the boundary layer, but also due to the cool thermal boundary at the wall. The chemical kinetic rates are influenced

by the cold wall of the injector and since the rate is exponentially dependent on the temperature, the chemical rate becomes smaller than the EBU rate.

## **Results and Discussion of the Bluff Body Modeling**

The gas concentrations at the exit of the bluff body have been measured by a four-station emission probe located on the symmetry plane of the combustor outlet. The probe sampled combustion gases: CO, CO<sub>2</sub>, NO<sub>x</sub>, O<sub>2</sub>, and total UHC. Such probe sampling has not area-averaged the concentrations of the exhaust, rather it measured the emissions along a line at the exit of the combustor. See Figure 4-1 and 4-2 for an illustration of this situation. In modeling of the bluff body and analyzing the results one needs to realize the following: the shortfalls of 2D modeling and the imperfections of the emission data acquisition. The absence of measurements near the top and bottom walls requires interpretation in the analysis of the experimental results and the comparison with the CFD simulation.

1. It is impossible to measure UHC emissions that would stay near the top and bottom walls.
2. The presence of wall cooling air can create a CO quenching effect not only at the top and bottom walls, but at the side walls as well.
3. The effusion cooling air from the side walls dilutes the sampled exhaust gases near the wall more than it does in the center.
4. The effusion cooling air pushes the flame away from the wall on all four sides, in other words, the flame front in 3-D space looks like a pyramid with a truncated upper portion.

From the experimental results (Butcher et al., 2003), it is noted that at the lower fuel-air equivalence ratios the levels of carbon monoxide are relatively high. This is likely caused by flame quenching as the flame interacts with air

of the effusion cooled side walls. The CFD simulation captures the CO wall quenching at the top (and bottom) walls, however the calculated area averaged values are a factor two higher than the experimental data. This discrepancy is not a surprise; since the experimental probe setup did not measure the total exit area averaged emissions but only the line averaged emissions at the combustor exit plane from side to side. To determine how much CO reaches the probe's holes an interpretative analysis is performed using the CFD solution. In the analysis the emission levels are adjusted to the probe location of the experiment. There are two main issues addressed in the analysis.

1. Due to the gradient in species concentration, the outer probe holes can pick up more CO quenched near the side walls than the inner holes. In the analysis the probe is imagined rotated 90 degrees as shown in Figure 4-2. The CFD species profiles at the combustor exit show that due to turbulent mixing about 80% of effusion cooling air entered at the top wall reaches the location of the outer holes and about 40% reaches the inner holes of the probe. This suggests that 80% of quenched CO at the side walls can be picked up by the outer holes and 40% by the inner holes for the actual probe positioning.
2. Only a relatively small amount of carbon monoxide emission from the top and the bottom walls can reach the test probe's location. The CFD species profiles at the combustor exit show that due to turbulent mixing about 25% of effusion cooling air entered at the top wall reaches the center line. This suggests that only 25% of CO quenched near the top and bottom walls can be picked up by the probe.

Based on the logic presented above it is found that a simple relationship can be used to find carbon monoxide levels at the location of the probe holes. The CO concentration at the probe holes is calculated as:

$$[\text{CO}]_{\text{probe}} = 0.5 [\text{CO}]_{\text{area averaged CFD}} + 0.5 [\text{CO}]_{\text{center line CFD}}$$

This adjustment of the CFD results gives excellent agreement to the measured carbon monoxide emissions for the whole range of fuel-air equivalence ratios.

The results also indicate kinetically controlled CO emission at the premixer fuel-air equivalence ratio below about 0.6, and thermodynamically controlled CO at premixer  $\Phi$  above 0.6. Experimental and modeled carbon monoxide emissions are shown on Figure 4-3. The CFD also reveals the emission of unburned hydrocarbons near the wall for the cases with low fuel-air equivalence ratio, which is not reported in Butcher et al (2003).

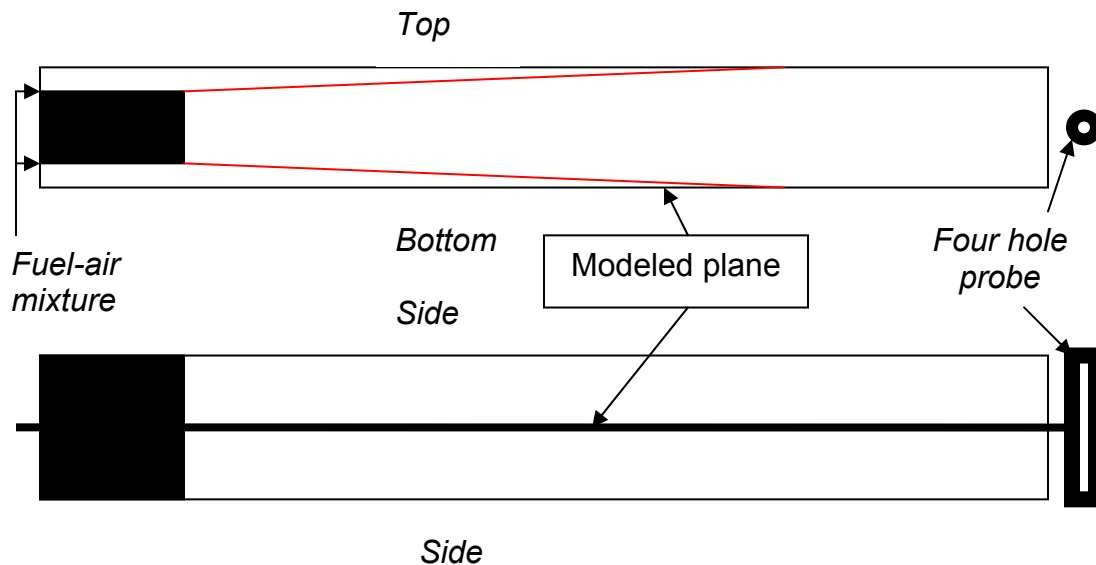


**Figure 4-1. Schematic of the modeled bluff body combustor: side (upper diagram) and top (lower diagram) views. The 2D modeling plane is shown in the upper drawing. Because of symmetry only the upper half of the plane is modeled.**

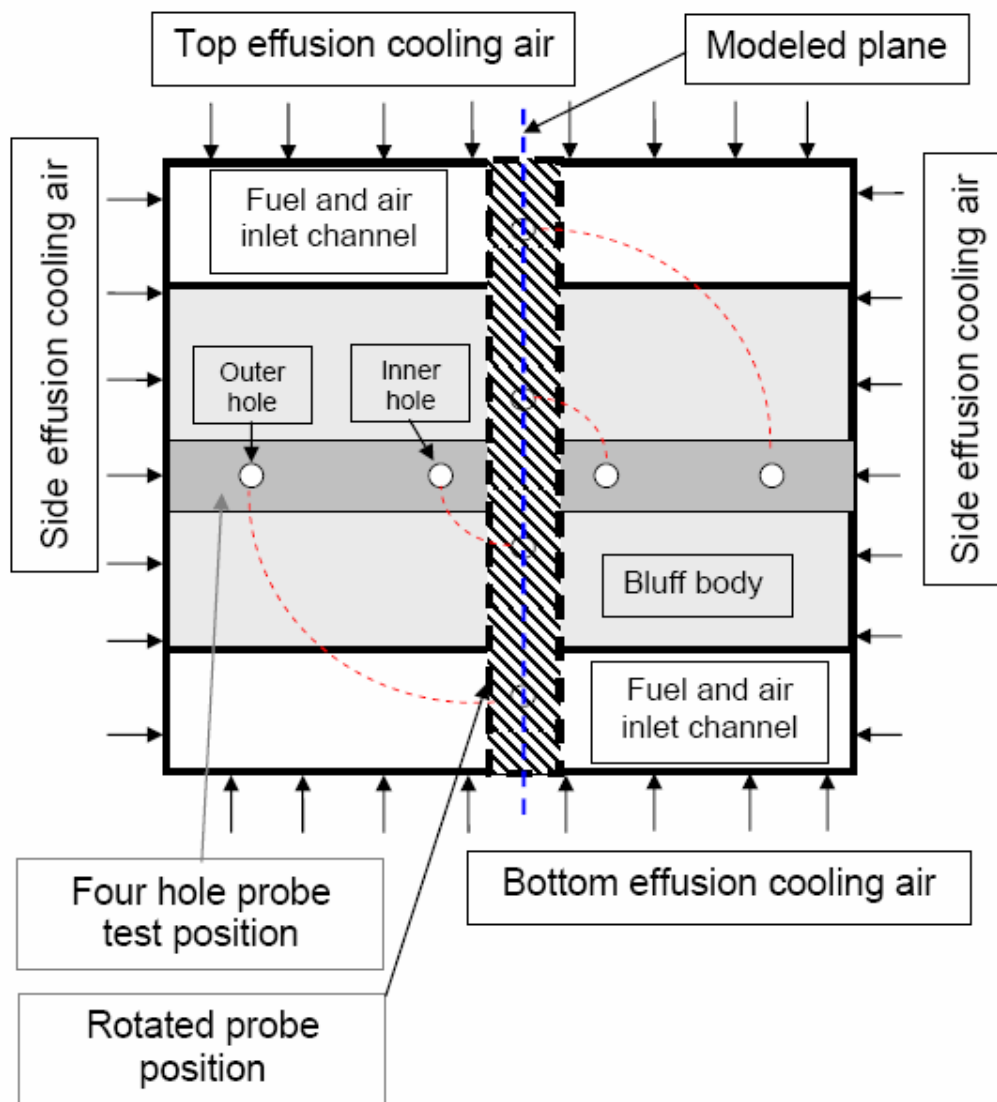


**Figure 4-2.** The end view of the bluff body combustor is shown. The position of the test probe location is shown in grey, red dash line show the direction of imaginary probe rotation used in the emission analysis.

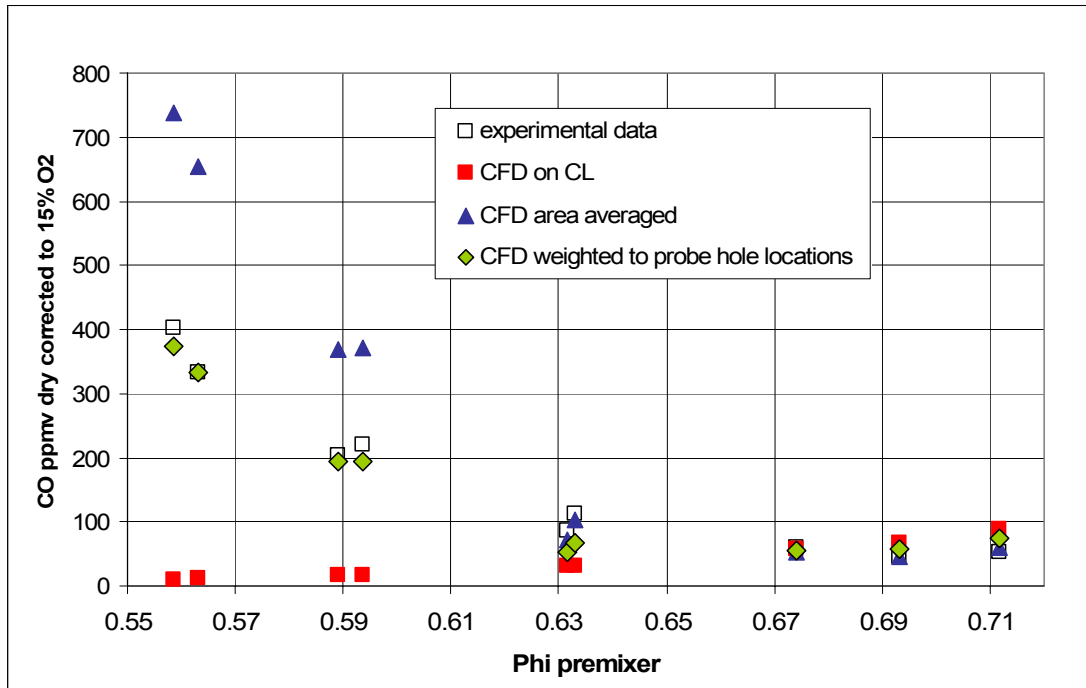


Figure 4-3. Carbon monoxide emissions for bluff body burner.

## Oxides of Nitrogen Emissions for Bluff Body

The oxides of nitrogen emissions are plotted in Figure 4-4. Modeled NO is treated as measure  $\text{NO}_x$ , since only  $\text{NO}_2$  measured will arise for NO formed in the flame and hot gases. The CFD predictions are slightly lower than the experimental data for the lower fuel-air equivalence ratios and a factor two higher for the richest cases. In analyzing the  $\text{NO}_x$  emissions three factors must be addressed:

1. Spatial and temporal non-uniformity of the  $\Phi$  at the burner inlet
2. Turbulent fluctuations
3. Flame temperature considerations

These three points are not directly modeled in the 2D CFD simulation, but their influence on the  $\text{NO}_x$  emissions is discussed below.

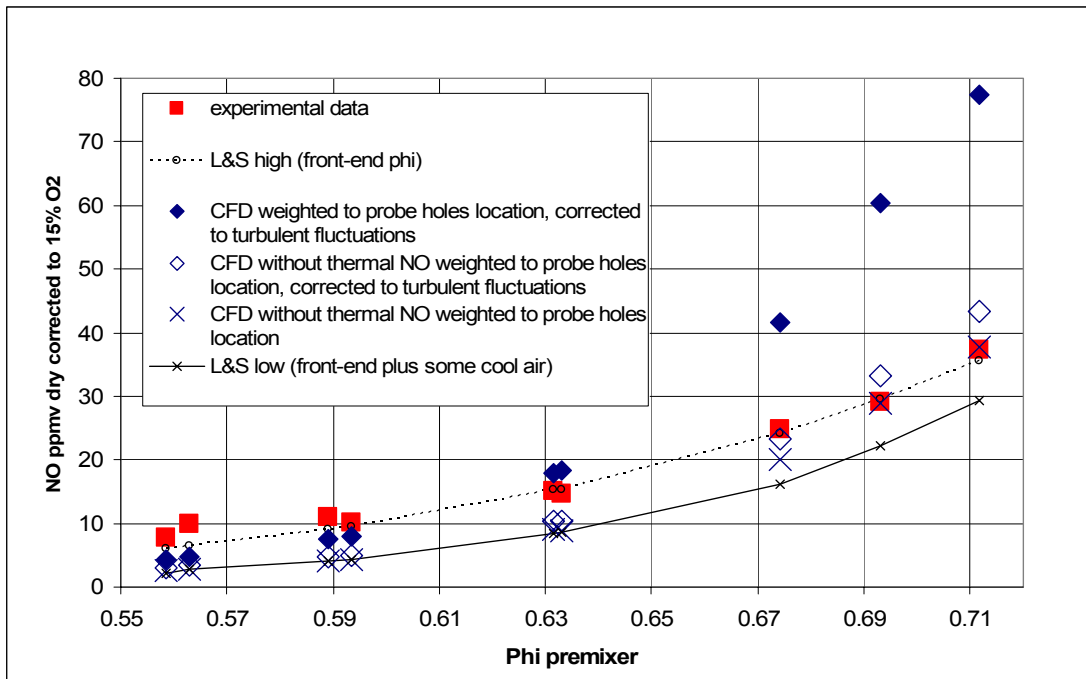


Figure 4-4.  $\text{NO}_x$  exit plane emissions for bluff body burner.

### **Spatial and Temporal Premixer Non-uniformity**

Non-homogeneity in fuel-air equivalence ratio leads to creation of areas where the local flame temperature is higher than the adiabatic flame temperature for the mean  $\Phi$ . These high local temperatures produce higher levels of nitrogen oxide emission. The description of the experimental setup in Butcher et al. (2003) does not contain any information on the levels of unmixedness of the injector, nor does the paper give any indication if the injector has any kind of mixing profile. On the other hand, the authors mention the 50% mixing screen between the premixer and the bluff body added to enhance air-fuel mixing. Additionally, the fuel inlet jets were located far upstream of the bluff body dump plane; thus, premixing should be very good. A flat premixer profile is used in the simulation, and the fuel-air mixture is assumed to be perfectly mixed. The steady state simulation assumes no temporal fuel-air fluctuation in the premixer. That is, both spatial and time uniformity is assumed in the premixer fuel-air equivalence ratio.

### **Turbulent Flame Fluctuations**

For the highly turbulent flow, the turbulent mixing produces temporal fluctuations in flame temperature and species mole fractions. Since the dependence of the rate of NO<sub>x</sub> formation with respect to temperature and species concentration is highly nonlinear, the NO<sub>x</sub> predictions are affected by turbulent fluctuations. The steady state assumption leads to under-predicting the levels of nitrogen oxides emission. Since NO<sub>x</sub> emissions respond to the temperature increase exponentially, the largest relative effect of the fluctuations on the NO<sub>x</sub> emission is found at the lower fuel-air equivalence ratios. The predominant NO<sub>x</sub> formation routes in the cooler combustion regimes are the prompt, NNH, and nitrous oxide mechanisms. All of these mechanisms are active in the flame brush and are subject to the high intensity

turbulent fluctuations. As the mean temperature in the combustor rises, the thermal NO<sub>x</sub> becomes more important, and since the turbulent intensity in the post flame zone is smaller, the effect of turbulent fluctuations diminishes.

In order to account for the effect of turbulent fluctuations on the nitrogen oxide formation, post-processing of the RANS solution is performed.

First step: the nitrogen oxides are calculated using the Fluent NO<sub>x</sub> post-processor chemistry in a time-averaged simulation. With the Fluent chemistry, the post-processor calculates thermal and prompt NO<sub>x</sub> based on instantaneous O-atom and OH-radical models. The kinetic rates of NO<sub>x</sub> formation used in Fluent have been obtained from laboratory experiments for laminar flames. The production via thermal Zeldovich mechanism is relatively close to the corresponding rate of the eight-step global mechanism. The amount of prompt nitrogen oxide produced in FLUENT prediction is of the same magnitude as the reaction 5 contribution, however since the reaction 5 of global mechanism contains also NNH route this comparison may not be valid. The biggest drawback of the FLUENT NO<sub>x</sub> chemistry is the absence of the N<sub>2</sub>O route, which is the biggest contributor to the NO<sub>x</sub> formation at the lean-premixed conditions. Overall, the NO<sub>x</sub> emissions are significantly under-predicted by FLUENT post-processing.

Second step: a joint methane-temperature PDF is added to the model to obtain a second prediction of the NO<sub>x</sub> emission. The PDF calculations are based on the mean temperature and species concentration fields already obtained in the first step.

Third step: the turbulent fluctuation correction is calculated as a ratio of NO<sub>x</sub> using pdf over NO<sub>x</sub> time averaged. Figure 4-4 shows the turbulent fluctuation

correction as a function of the fuel-air equivalence ratio of the premixer. Then, the nitrogen oxides emissions calculated using eight-step global mechanism are corrected for turbulent fluctuations using the PDF correction for NO<sub>x</sub>. The correction value varies from 20% for the leanest  $\Phi$  considered to 15% at the richest  $\Phi$ .

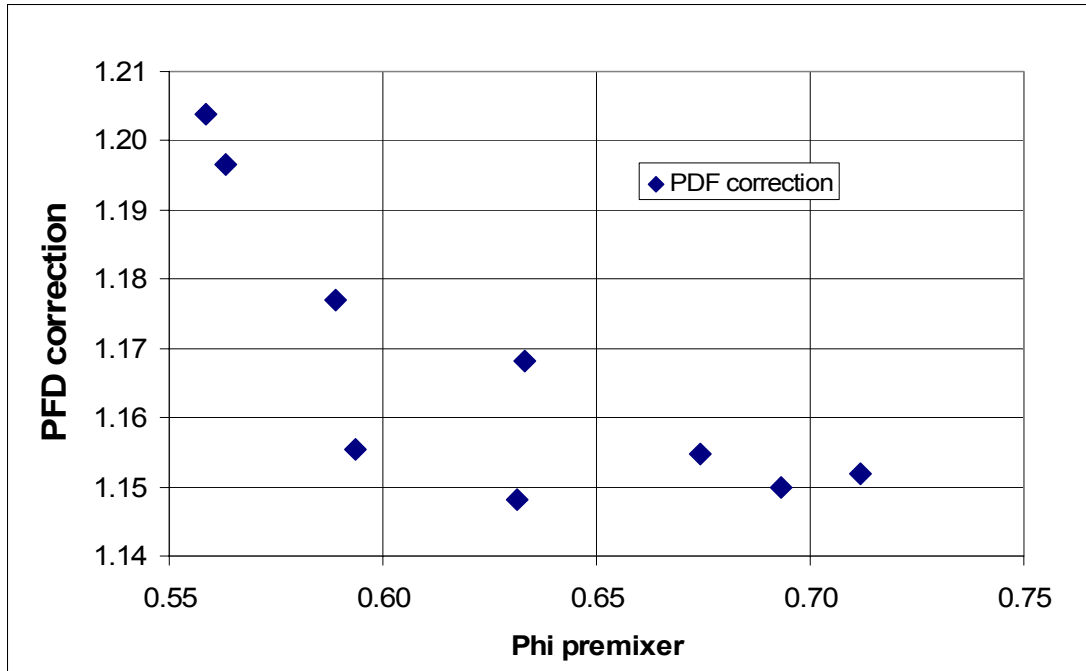


**Figure 4-5. Turbulent fluctuation correction for CFD modeling of NO<sub>x</sub> emissions for bluff body burner.**

## Flame Temperature Considerations

The cooling of the flame in the bluff body burner comes from the effusion cooling air of the walls. In the 2D modeling, this cooling of the top and the bottom walls is included. Although only the top half of the combustor is explicitly modeled, the bottom half is included because of symmetry. However the additional cooling air at the side walls is not included, since if it is modeled the flame angle cannot be predicted correctly. The side air dilution affects

mostly the thermal  $\text{NO}_x$  that is formed in the post-flame zone after the effusion air has a chance to mix with hot combustion gases. The side cooling air has a small effect on the  $\text{NO}_x$  formed in the flame zone since that air cannot penetrate into the flame zone except at the edges.

In the CFD simulation, the heat loss through the side walls is not considered. The top wall of the combustor and the bluff body backward face wall have assigned heat transfer coefficients for their surfaces. Since the combustor becomes a 2D center plane, the model does not include any heat flux through the side walls. This appears to be appropriate for the cases with lower fuel-air equivalence ratio, where the peak flame temperature is below 1800K, and the combustor is close to the adiabatic temperature. However, for the cases with  $\Phi$  of 0.6 and above, local temperatures can be more than 1900K. These high flame temperatures produce enough radiative heat flux to the side walls to reduce the flame temperature, thus impacting the  $\text{NO}_x$  emission.

Furthermore, in order to model the heat transfer through the effusion cooled wall, one would need to resolve the individual effusion hole: and this is not possible in 2D modeling.

Figure 4-3 shows the nitrogen oxides emission results. The dashed and continuous lines are the  $\text{NO}_x$  levels determined by the Leonard and Stegmaier (1993) (L&S) calculation, in which the  $\text{NO}_x$  emission is taken as a function of the calculated adiabatic equilibrium flame temperature for the flame  $\Phi$ . The upper dash line shows the emission based on the fuel-air equivalence ratio of the premixer, bluff body pilot and bluff body cooling air combined. The bluff body has effusion cooling along with the fuel pilot holes. The solid line is based on the  $\Phi$  of the above streams plus wall cooling air added before the location at which flame touches the wall. On the graph,

these lines extend over the whole range of fuel-air equivalence ratio, however, the Leonard and Stegmaier data upon which the curves are generated are only available for the flame temperatures of 1900K and less. This corresponds to the  $\Phi$  of about 0.59-0.6. There is relatively little post-flame thermal  $\text{NO}_x$  formed at these flame temperatures, thus thermal  $\text{NO}_x$  is not significantly counted by using the Leonard and Stegmaier calculations.

The experimental  $\text{NO}_x$  emissions agree with the dashed line Leonard and Stegmaier results very well. The experimental data are slightly higher than the L&S prediction for the lower fuel-air equivalence ratios. One of the most likely explanations is a presence of the pilot flame. The local temperatures near the pilot are higher than the mean flame temperature. This would lead to a higher rate of  $\text{NO}_x$  formation in the pilot zone. At the higher  $\Phi$  the data agree with the L&S curve as well – even though the curve has been extended beyond the 1900K limit of the L&S data. However, the sharp exponential increase in thermal  $\text{NO}_x$  emission at the higher temperatures is not reflected in L&S calculation, so the agreement with the experimental data suggests that thermal  $\text{NO}_x$  has not been significantly formed in the tests. The most likely explanation for relatively low thermal  $\text{NO}_x$  emission in the bluff body experiments is the heat lost that occurs at the higher  $\Phi$  and cools the post-flame zone where the most thermal  $\text{NO}_x$  would be formed. The bluff body burner inherently has a high surface to volume ratio that suggests a non-adiabatic combustion, especially when combustion temperatures are high. Thus, the higher the fuel-air equivalence ratio, the more heat loss would occur.

The CFD calculations for  $\text{NO}_x$  emissions are performed in steady state simulations and then corrected to turbulence fluctuations as described above. Also, the  $\text{NO}_x$  is computed with and without the thermal  $\text{NO}_x$  rates. As

expected, the best agreement of the CFD modeling with the experiment and the Leonard and Stegmaier curves is obtained when thermal NO<sub>x</sub> formation is not considered. In the regime where the thermal NO<sub>x</sub> is not prevalent ( $\Phi < 0.63$ ), the full eight-step mechanism yields good agreement. For the richer cases, there is a factor of two difference between the CFD modeling and the experimental data. This discrepancy is attributed to the thermal NO<sub>x</sub> formation. This suggests greater heat loss than modeled by the 2D approach.

Figures 2-5 through 2-19 show the plots obtained in the 2D CFD simulation of the high pressure bluff body burner. For the cases shown, the fuel-air equivalence ratio at the premixer is 0.589, and the overall fuel-air equivalence ratio is 0.46. The highest rate of NO formation is that caused by the nitrous oxide mechanism (step 4) in the flame zone.

The bluff body combustor modeling using the eight-step global mechanism shows good agreement with the experimental data. This proves that the updated eight-step global mechanism can be used in the commercial CFD packages modeling methane combustion and NO<sub>x</sub> formation for lean-premixed conditions at elevated pressure. The updated prompt and NNH chemistry allows application of the mechanism in the areas of stoichiometric fuel-air ratio (oxygen concentration is zero). Though the mechanism is not tuned for this condition, the CFD simulation will converge to a solution.

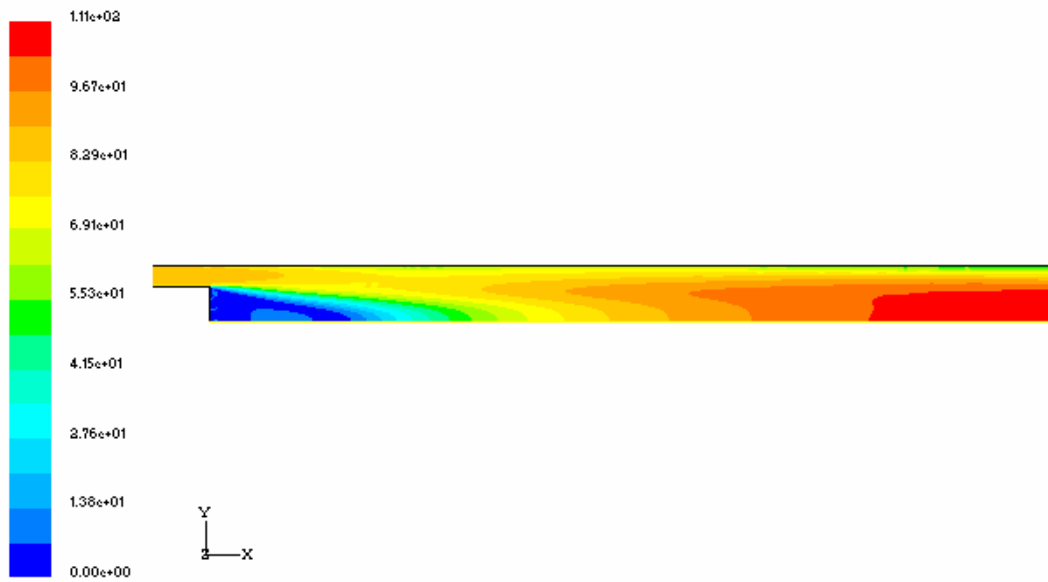


Figure 4-6. Velocity magnitude (m/s).

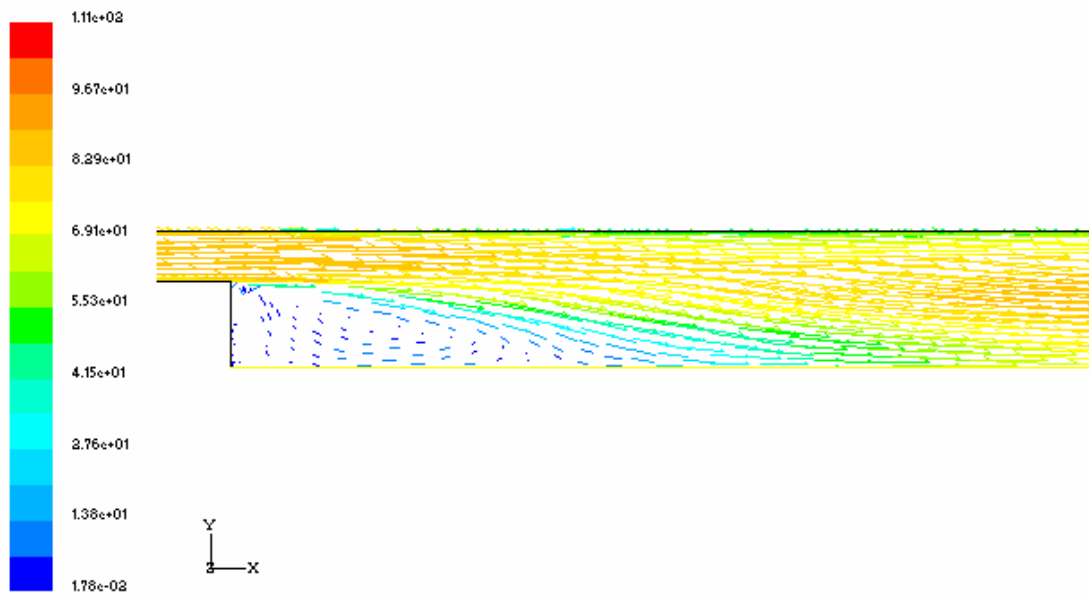


Figure 4-7. Velocity vectors colored by the velocity magnitude in the recirculation region.

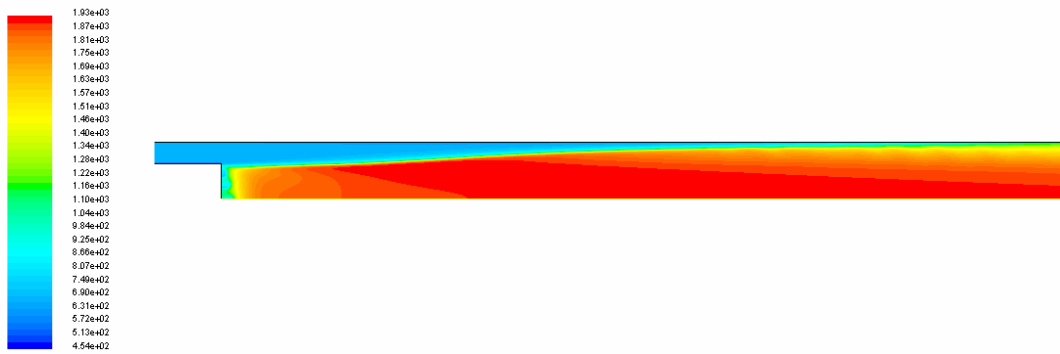


Figure 4-8. Temperature profile, K, maximum temperature 1930 K.

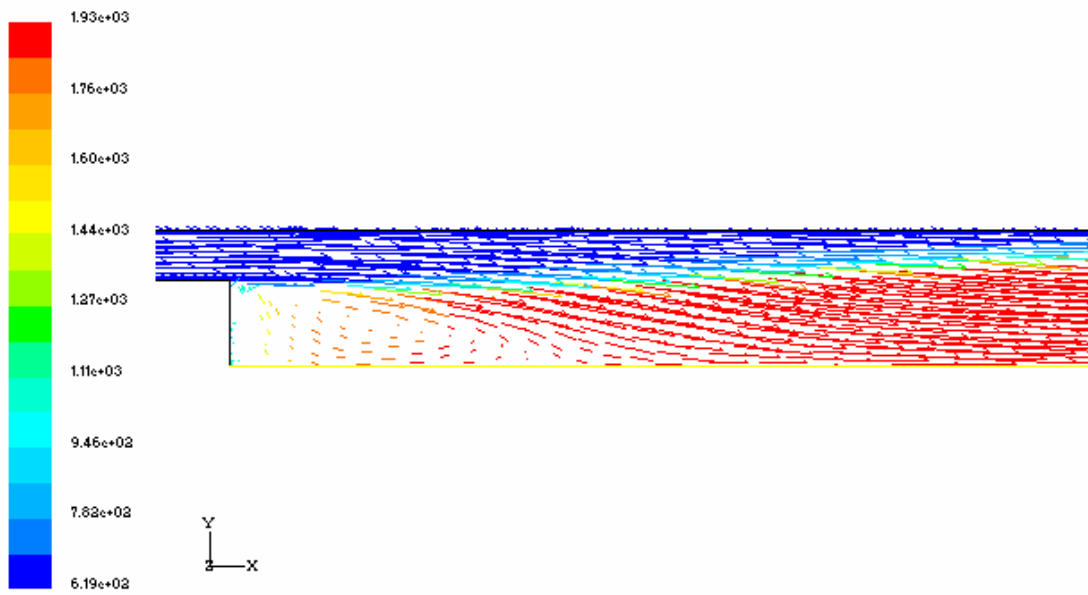


Figure 4-9. Velocity vectors colored by temperature in the recirculation region.

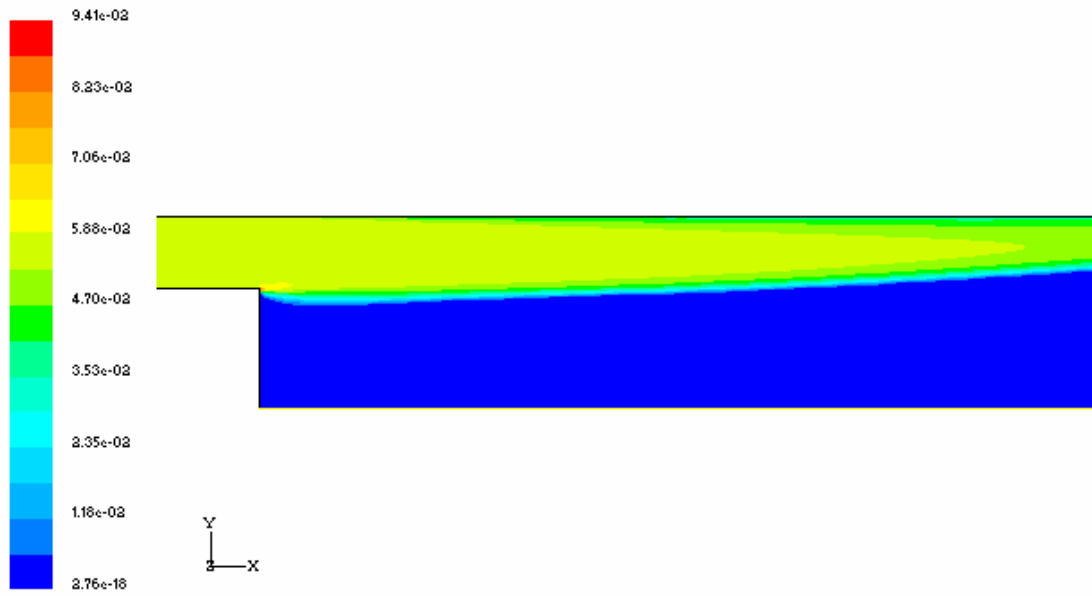


Figure 4-10. Methane mole fraction profile.

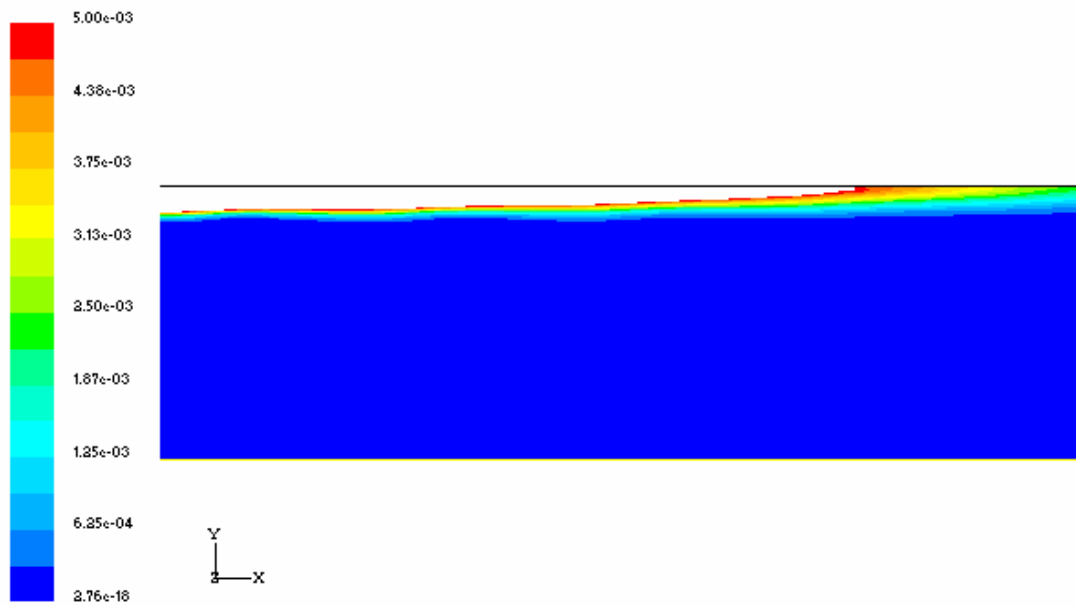
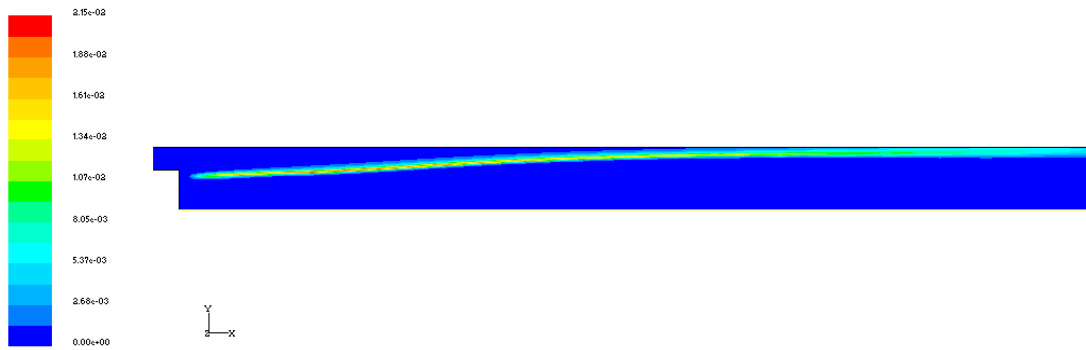
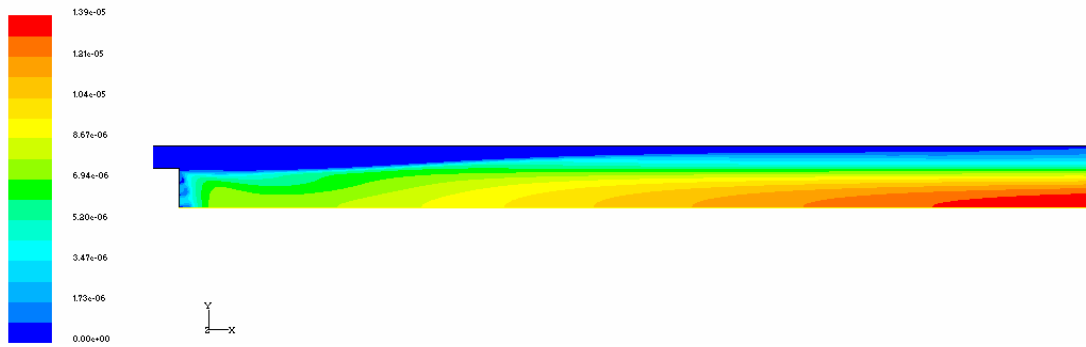


Figure 4-11. Methane mole fraction for the exit plane and upstream.



**Figure 4-12. Carbon monoxide mole fraction, maximum CO is 2.15%, wet basis actual  $O_2$ .**



**Figure 4-13. Nitrogen oxides mole fraction, maximum is 13.9 ppmv, wet basis actual  $O_2$ .**

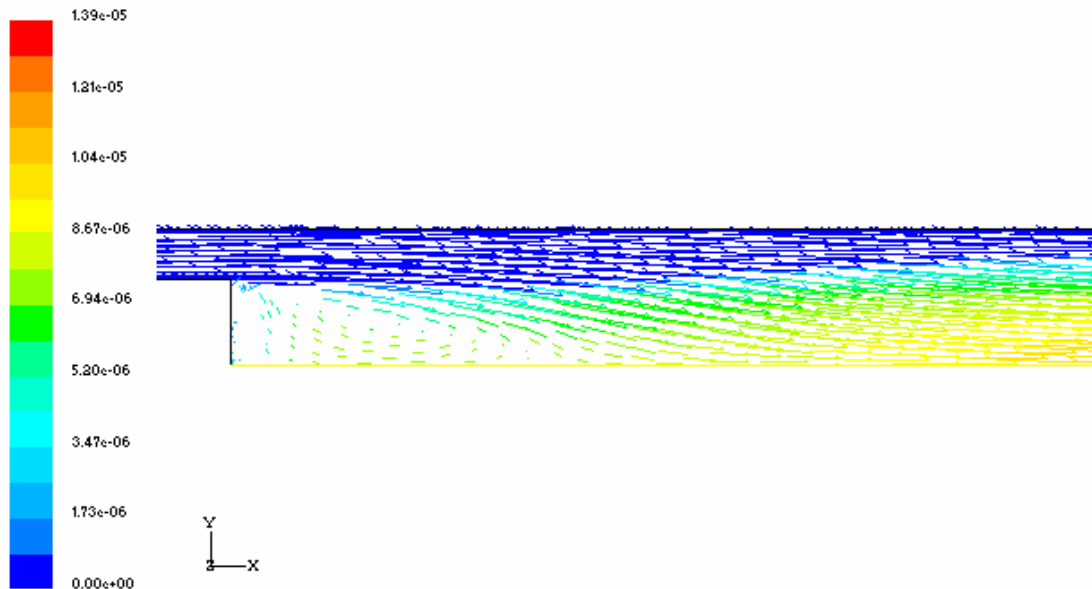


**Figure 4-14. NO mole fraction in the recirculation region.**

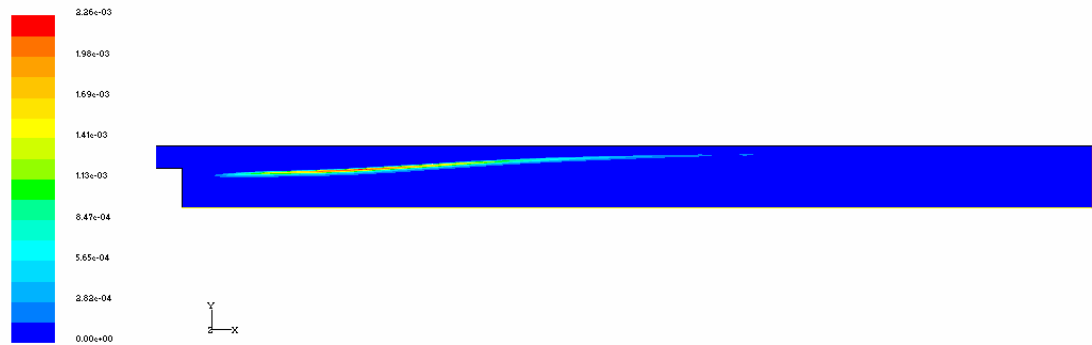


**Figure 4-15. NO rate of formation via  $N_2O$  and non-equilibrium Zeldovich mechanism combined, maximum rate is  $2.23e-3$  kmol/m<sup>3</sup>/s.**

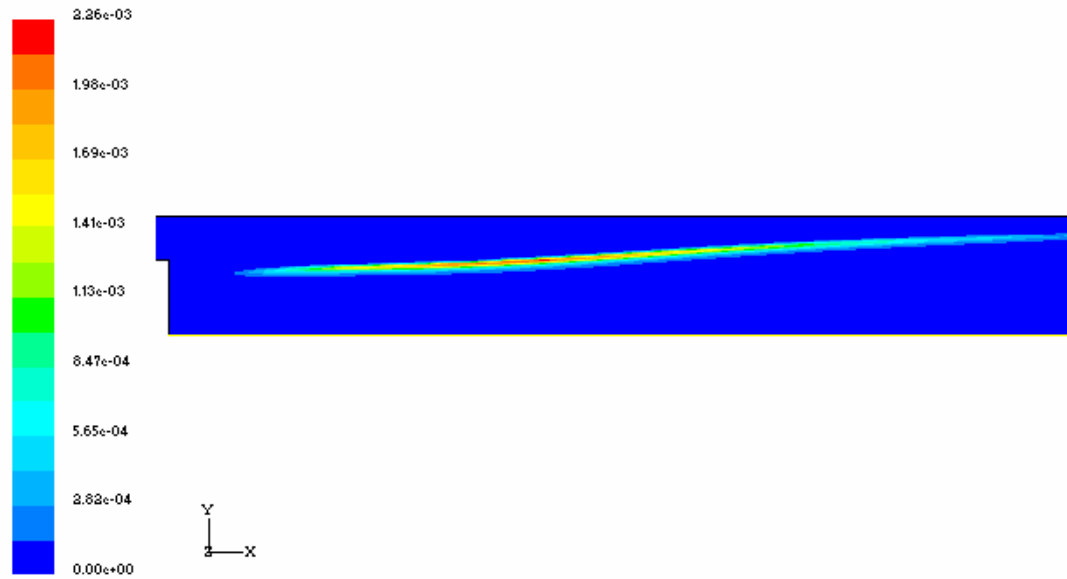


Figure 4-16. Same as above for forward part of burner.

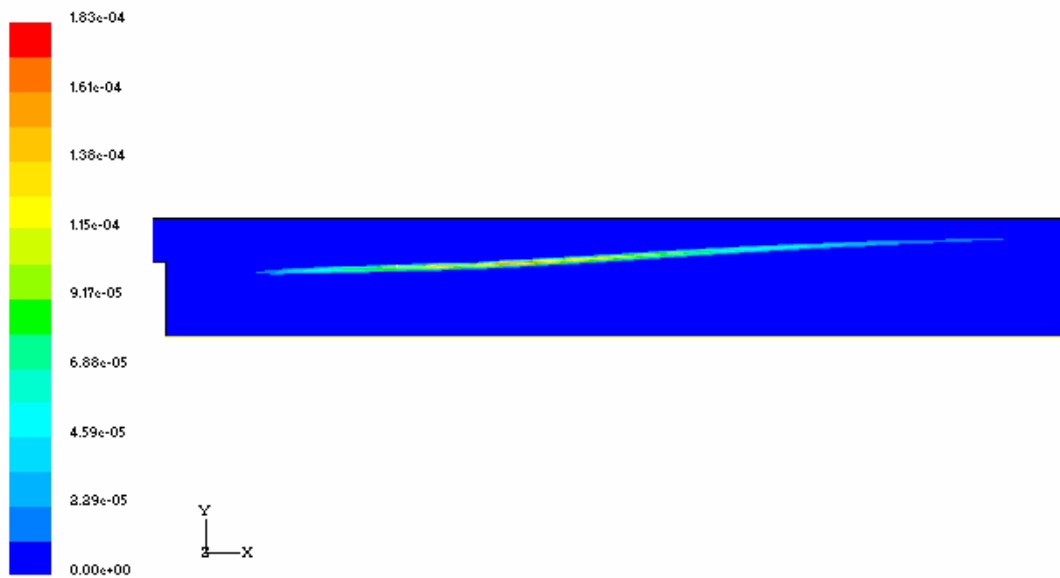
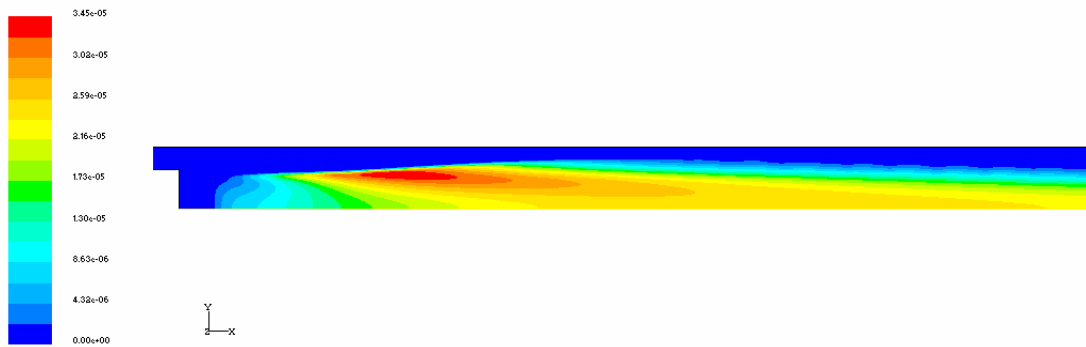
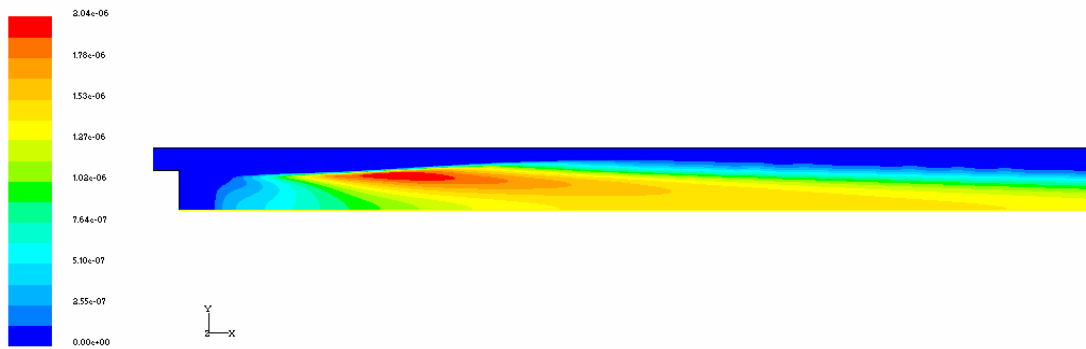


Figure 4-17. NO rate of formation via prompt and NNH mechanisms combined, maximum rate is  $1.834\text{e-}4$  kmol/m<sup>3</sup>/s.



**Figure 4-18. NO rate of formation via thermal Zeldovich mechanism, maximum rate is  $3.45\text{e-}5$  kmol/m<sup>3</sup>/s.**



**Figure 4-19. NO rate of formation via thermal  $\text{N}_2\text{O}+\text{H}$  reaction, maximum rate is  $2.04\text{e-}6$  kmol/m<sup>3</sup>/s.**

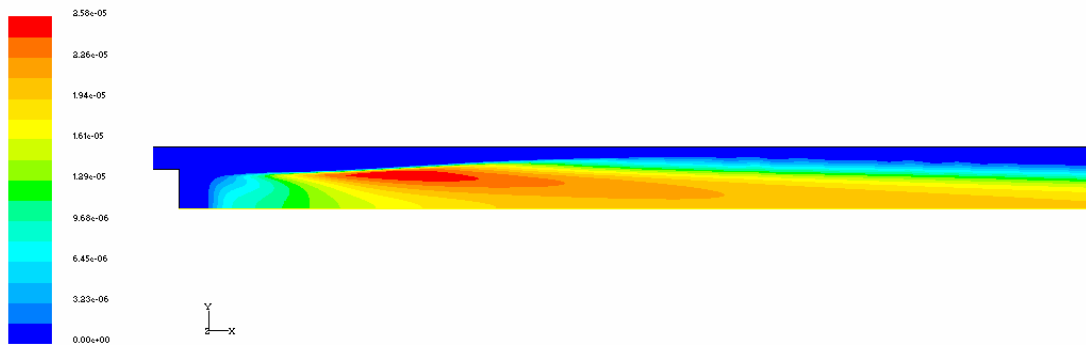


**Figure 4-20. NO rate of formation via thermal  $\text{N}_2\text{O}+\text{O}$  reaction, maximum rate is  $2.58\text{e-}5$  kmol/m<sup>3</sup>/s.**

## **5. Generic, Lean-premixed, Single-injector, Can-type Combustor CFD**

### ***Combustor design***

In order to help understand the fluid dynamics, turbulence-chemistry behavior in the swirl stabilized combustion chamber, and to set as a basis for developing of a chemical reactor network (see next Chapter), the CFD modeling of a generic, lean-premixed, single-injector, can-type combustor is performed. The major design and operating parameters of the modeled combustor are similar to those of a typical industrial gas turbine combustor. The basic geometry is scaled from Combustor A tested by Mellor (1996). The modifications made to the Combustor A are:

- The louvered liner cooling is replaced by air back side cooling.
- The reference velocity of the combustor is increased from 7m/s to 10m/s, which is more realistic value for modern gas turbine systems. The velocity has been increased by the reduction of the combustor cross-sectional area. The reference velocity is calculated as total air flow rate divided by a circumferential area of the combustor and density of air entering the combustor.
- The operating pressure of the combustor is increased from 10 to 16 atmospheres, which is more representative of the new industrial gas turbines.

The system modeled consists of the combustor liners (i.e. combustor) and injector with main circuit (premixer) and pilot circuit (pilot). The modeled liner has dome cooling, which accounts for 4% of the total combustor air flow. The pilot flow rate is set to 3% of the total injector flow rate. The walls of the liner

are cooled by impingement cooling. The dilution effect and the introduction of the back side cooling air into the combustor are not modeled, thus the outlet temperature of the combustor is higher (1670K) than the operating temperature of the turbine. The overall fuel-air equivalence ratio of the injector is set to 0.475, which implies that if the pilot fuel-air equivalence ratio is lower than overall injector  $\Phi$ , the premixer  $\Phi$  is slightly richer than the overall injector  $\Phi$  value and visa versa, the rich pilot corresponds to the lower than nominal premixer  $\Phi$ . The schematic 2D drawing of the combustor with the air flow splits is shown in Figure 5-1.

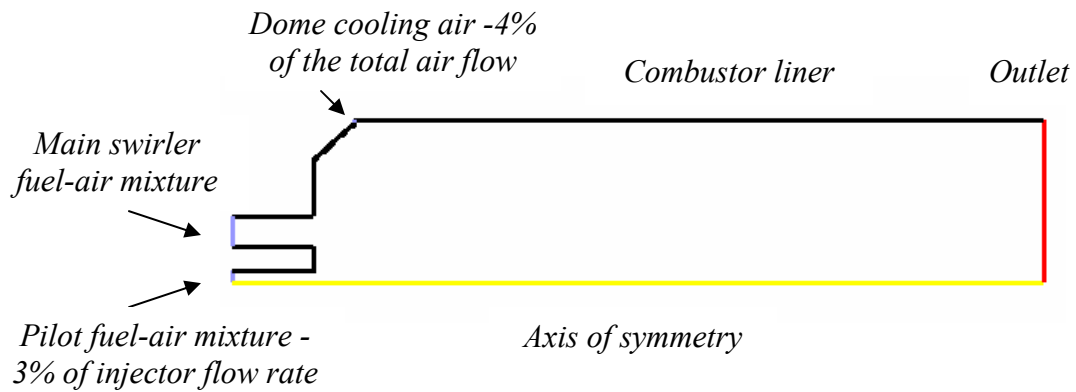


**Figure 5-1. Schematic drawing of the modeled system for a single-injector, can-type combustor.**

The modeled operating conditions are described in Table 5-1.

**Table 5-1. Design parameters for the single-injector, can-type combustor.**

Description	Value, unit
Combustor length	0.36 m
Outer radius of the liner	0.08 m
Injector outer radius	0.032 m
Pilot outer radius	0.0041 m
Reference velocity	10 m/s
Operating pressure	16 atm
Total air flow rate	1.13 kg/s
Dome air, percent of total	4%
Pilot air flow rate, percent of injector air flow rate	3%
Injector fuel-air equivalence ratio	0.475
Pilot fuel flow rate, percent of neutral pilot	50-150%

### Injector Profiles

The mean axial velocity of the injector outlet is 65 m/s. Velocity profiles at the injector outlet plane are determined based on the profiles of the axial swirl injector with a swirl number of 1.1. The swirl number is calculated using methodology given in Beer and Chigier (1983) assuming an axial swirler with the blockage factor of 0.35 and the vane angle of 45 degrees. The swirl number of such injector is calculated by

$$S' = \frac{1}{1-\psi} \left( \frac{1}{2} \right) \frac{1 - \left( \frac{R_h}{R} \right)^4}{1 - \left( \frac{R_h}{R} \right)^2} \tan \alpha_0, \quad [5-1]$$

where:

$S'$	-	swirl number
$\psi$	-	vane blockage factor
$R_h$	-	swirler hub (inside) radius
$R$	-	swirler outside radius
$\alpha_0$	-	vane angle

Since the vanes cannot be explicitly modeled in the 2D CFD simulation, the swirl number is matched by increasing the tangential velocity component. The 2D simulation uses a swirl angle of  $\alpha=54$  degrees corresponding to the relative tangential velocity component of 1.37 and an axial velocity component of unity.

$$S' = \left( \frac{2}{3} \right) \frac{1 - \left( \frac{R_h}{R} \right)^4}{1 - \left( \frac{R_h}{R} \right)^2} \tan \alpha_0, \quad [5-2]$$

The mass flow rate profile at the injector outlet plane is calculated based on the axial velocity profile, see Equation 5-3. Figure 5-2 shows the injector axial velocity profile and corresponding mass flux at the injector outlet:

$$\dot{m}_{air,stream} = \int_A \rho V_x dA, \quad [5-3]$$

where:

$\rho$	-	gas density
$V_x$	-	axial velocity
$A$	-	area of the corresponding injector stream

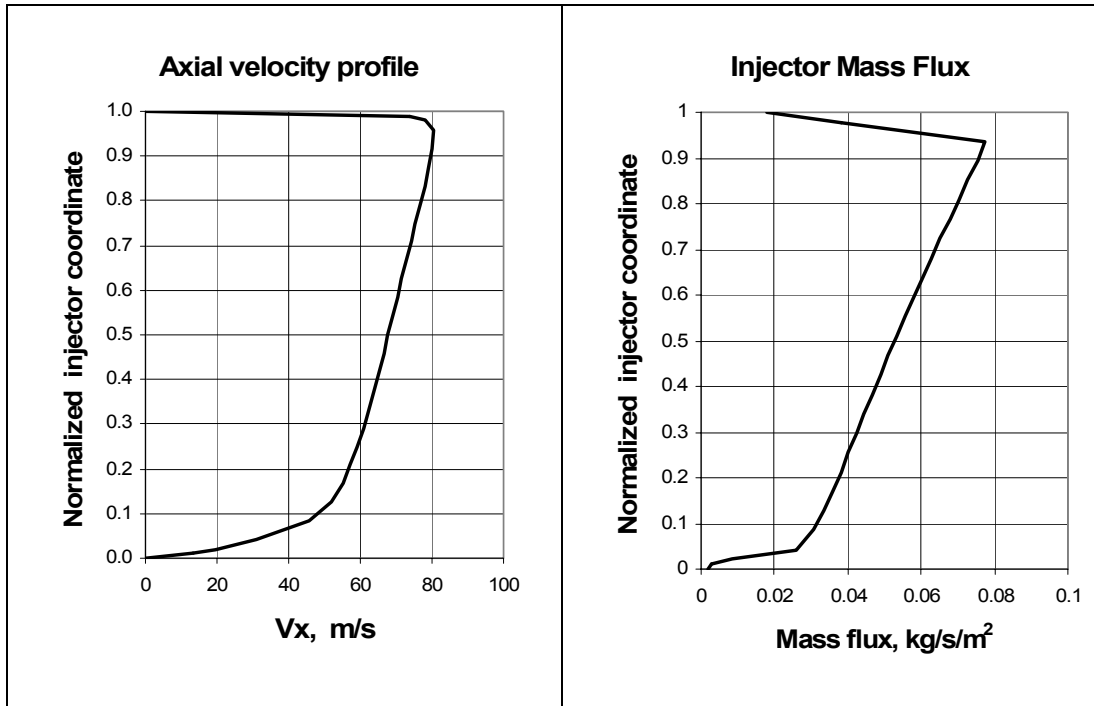


**Figure 5-2. Axial velocity and mass flux at the exit of the injector.**

Generally, the fuel-air mixing profile of the injector is assumed flat; that is there, is no radial or circumferential variation in the fuel-air equivalence ratio in the injector. However, additional calculations are performed for a non-uniform mixing profile: this is discussed later in this chapter.

### **Numerical Approach for the Single Injector Combustor Modeling**

Similar to the bluff body modeling, Fluent 6.1 is used for the simulation. A two-dimensional grid consisting of 31, 000 cells is used. See Figure 5-3. In the case of the richer than neutral pilot, the pilot flame sheet has higher temperature and species concentration gradients. In order to adequately resolve the gradients that exist in the flame front in such cases, the grid resolution is refined in the pilot flame region. The near wall region is also

refined in order to capture the boundary layer effect. The modeling assumptions used in the numerical simulation are listed in Table 5-2.

The rate limiting approach, as discussed in the previous chapter, is used in the calculation of the effective chemical rate. The solution is post-processed to obtain NO<sub>x</sub> emissions using the nitrogen chemistry of the eight-step global mechanism.

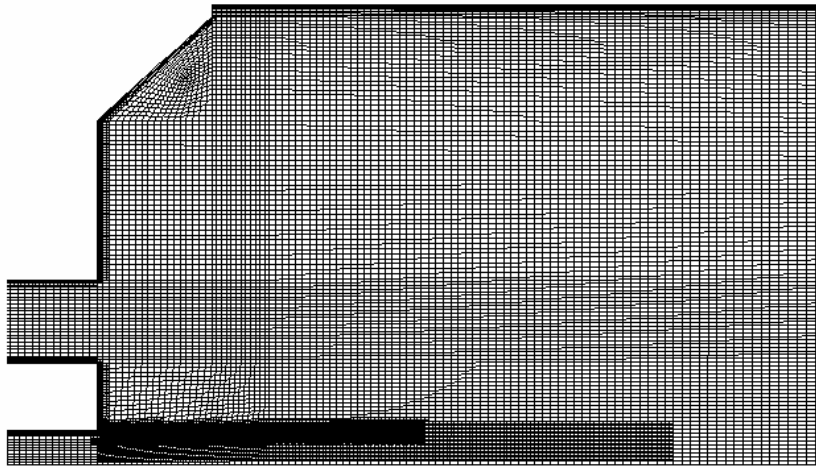


**Figure 5-3. Computation grid for the can-type combustor with refined grid in the pilot flame zone and at the combustor walls, only the first half of the combustor is shown.**

**Table 5-2. Modeling approach for the can combustor.**

Computational domain	2D structured grid, 31, 000 cells
Solver	Segregated RANS with species transport and volumetric reactions
Turbulence closure model	Reynolds stress with quadratic pressure strain
Convergence scheme	Second order (QUICK)
Wall treatment	Standard wall function
Heat loss	Convective and radiative heat transfer
Radiative heat transfer	Discrete Ordinates (DO) Model
Chemical kinetic rates	UW eight-step global mechanism
Chemical mixing rates	Eddy break-up (EBU) model

## Results and Discussions

The modeling has been performed for methane combustion with overall fuel-air equivalence ratio of 0.475. The pilot air flow rate is held constant based on the effective area of the pilot (see Table 5-1). The pilot fuel rate is varied from 50 to 150% of neutral pilot, corresponding to a pilot fuel-air equivalence ratio of 0.24 to 0.7.

The results of the 2D CFD simulation show the presence of regions that are typical to the swirl-stabilized burner: primary and pilot flame zones, main and dome recirculation zones, and a post-flame region. See Figure 5-4. The size of the zones as well as the flow, temperature and gas composition in the zones depend on the boundary conditions of the simulation. The methodology used in defining the zones is discussed in Chapter 6. Figures 5-6 through 5-47 (embedded in Table 5-3) show the results of the CDF simulation for lean and rich pilot cases.

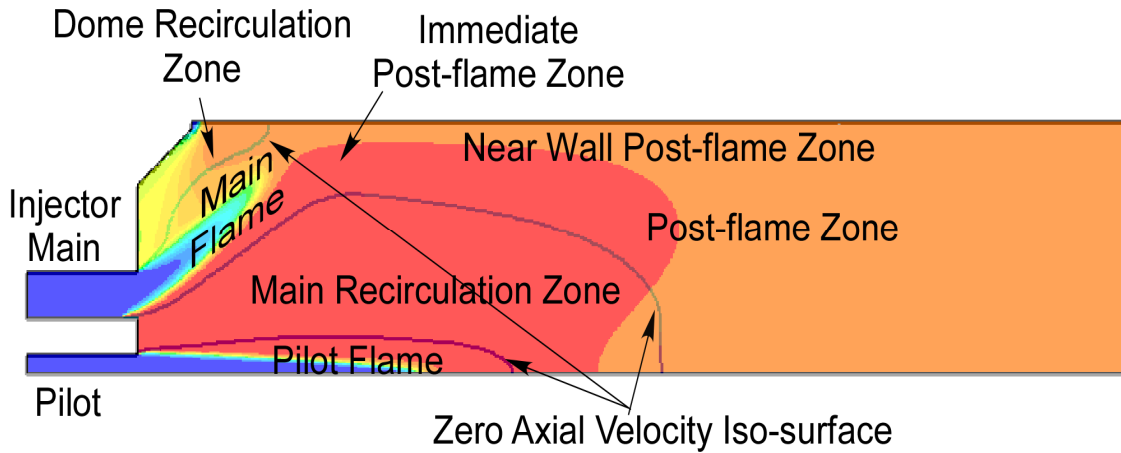


**Figure 5-4. Temperature contours plot from the CFD simulation showing the presence of the different combustion zones, case with flat injector fuel-air ratio profile and neutral pilot is shown.**

The carbon monoxide emission at the exit of the combustor is about one ppmvd, and essentially independent of pilot fuel-air equivalence ratio. The CO predicted emission is a function of the overall combustor fuel air equivalence ratio, which is held constant for all cases.

The NO<sub>x</sub> formation in the combustor is determined by post-processing the CFD solutions of the flow field. The plot of NO emissions for the can-type combustor with flat injector fuel-air ratio profile is shown in the Figure 5-5. Note: the NO formation in the combustor is equivalent to its NO<sub>x</sub> emission. The figure also shows the contributions of each NO formation mechanism. The largest contribution comes from the non-thermal N<sub>2</sub>O and Zeldovich pathways (reaction 4 of the eight-step global mechanism); it accounts for about 50-60% of the total NO. The lower percentage corresponds to the higher pilot  $\Phi$ . The contribution of the prompt and NNH routes (reaction 5 of the global mechanism) is 18-23%, with the higher value corresponding to high pilot case. At this low injector fuel-air equivalence ratio (0.475), the relative contribution of the thermal NO formation route is relatively small (22-27%). At

the high pilot case the temperature of the pilot flame is high enough to trigger the thermal NO production in the pilot flame: see Figures 5-7 and 5-9. However the fraction of the gas that is exposed to this temperature is relatively small (3-5%); thus the total contribution of thermal NO does not increase dramatically for the high pilot case.

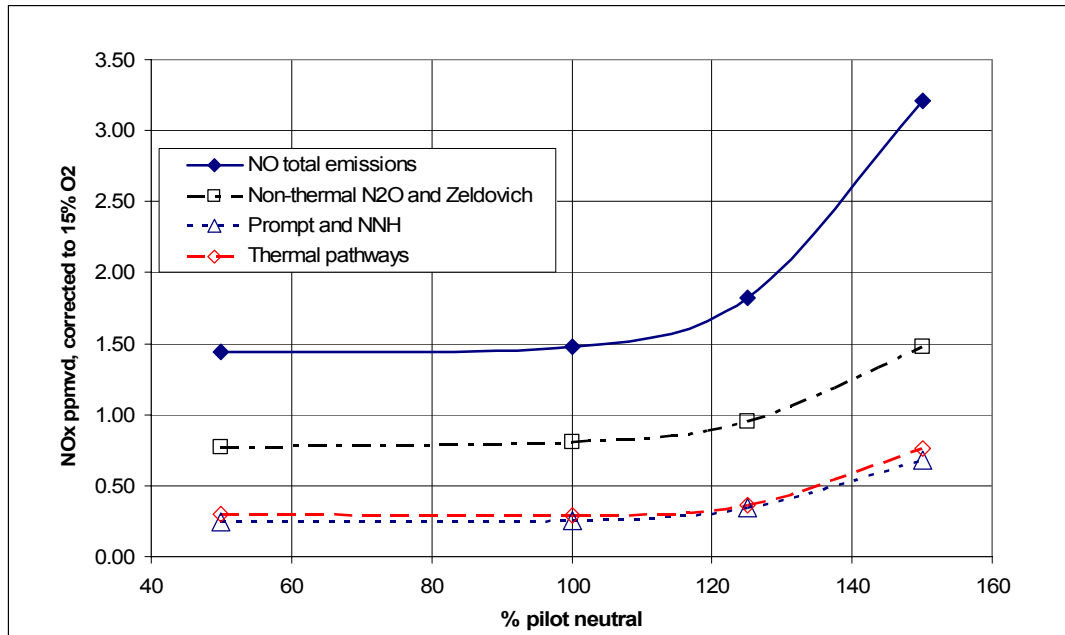


**Figure 5-5. NO formation in can-type combustor.**

The region of nitrogen oxides formation shifts from the main flame for the low pilot cases to the pilot flame for the high pilot cases. This is due to the increased temperature of the pilot flame and presence of high concentrations of CO (2%) in the pilot flame. As described in Chapter 3, carbon monoxide in the eight-step global mechanism is used as surrogate species for representing free radicals; flame NO formation explicitly depends on CO concentration (reactions 4 and 5). This temperature increase affects all NO formation routes. The contours of the NO formation rate are shown in Figures

5-38 through 5-47. These figures use logarithmic color distribution in order to cover the wide range of the rate values.

Table 5-3. CFD simulation of the methane combustion in the single-injector, can-type combustor.

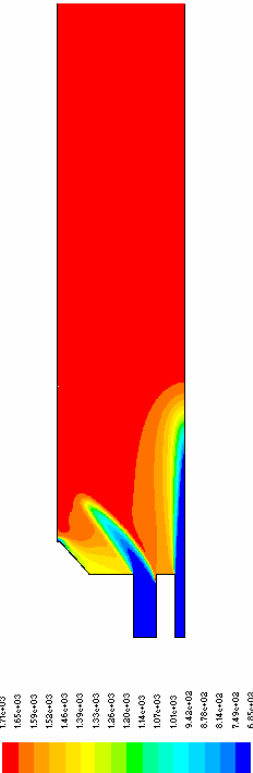
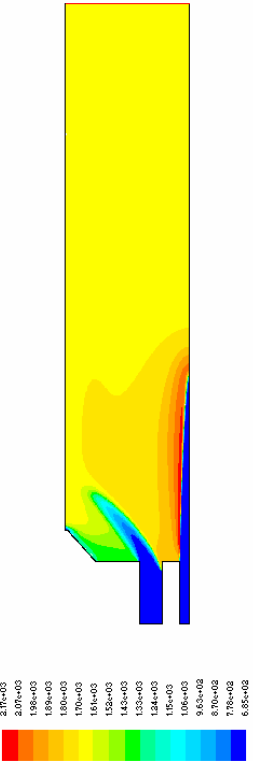
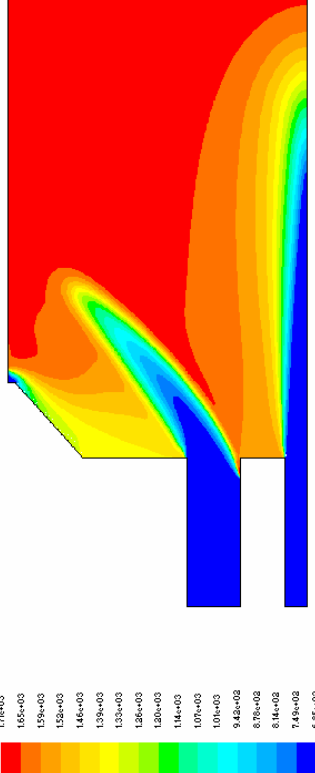
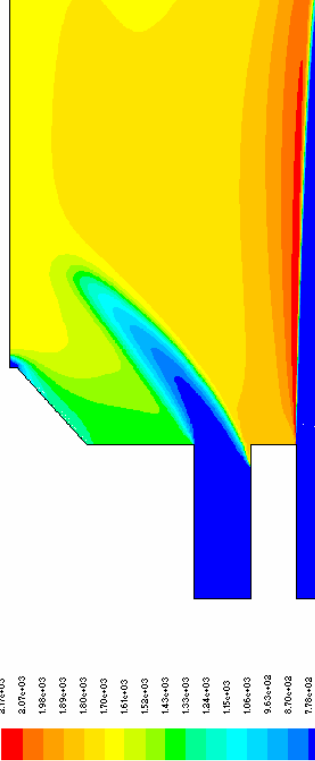
50% pilot case		150% pilot case	
 <p>Figure 5-6. Temperature contour plot for the 50% pilot case, maximum value is 1710 K.</p>		 <p>Figure 5-7. Temperature contour plot for the 150% pilot case, maximum value is 2166 K.</p>	
 <p>Figure 5-8. Temperature contour plot for the 50% pilot case, maximum value is 1710 K, the first half of the combustor is shown.</p>		 <p>Figure 5-9. Temperature contour plot for the 150% pilot case, maximum value is 2166 K, the first half of the combustor is shown.</p>	

Table 5-3 (continued)

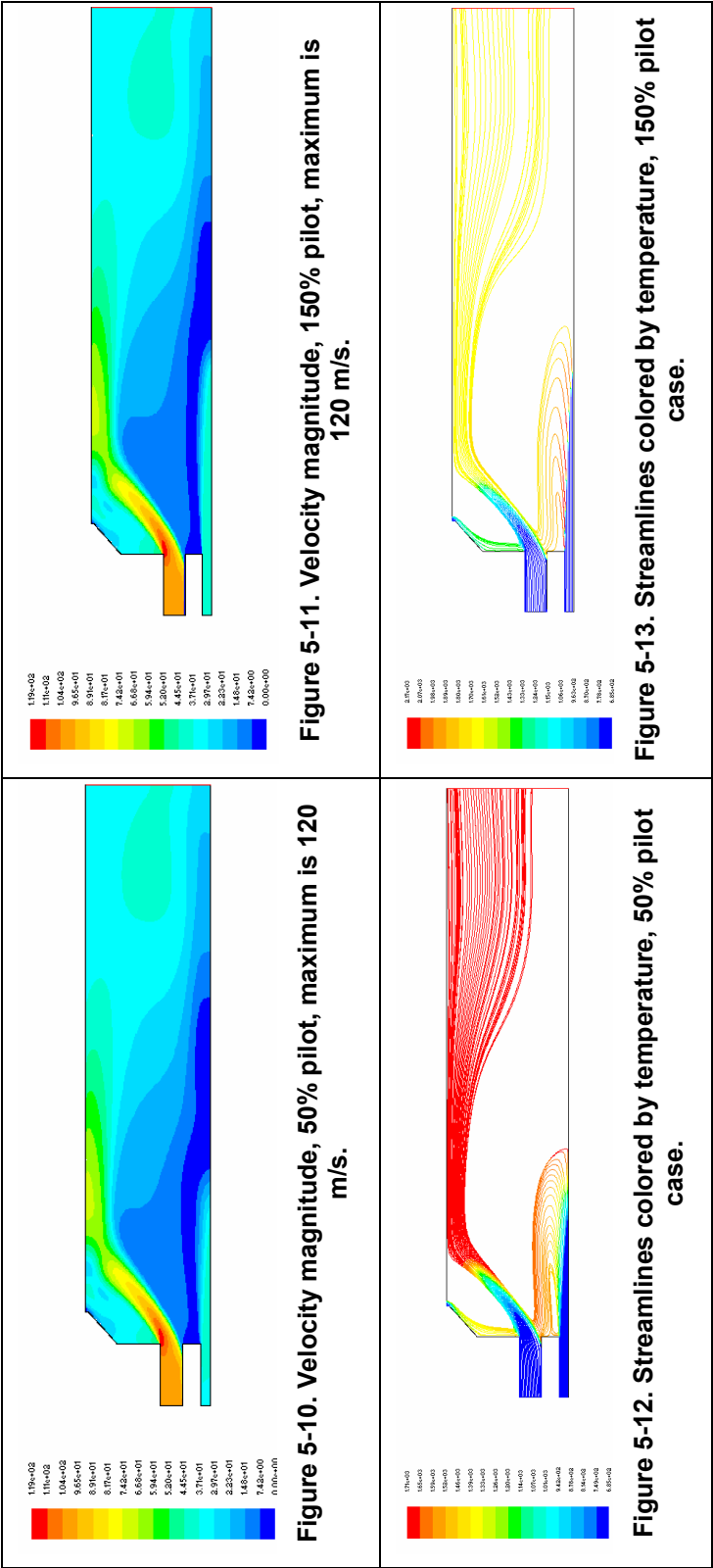


Table 5-3 (continued)

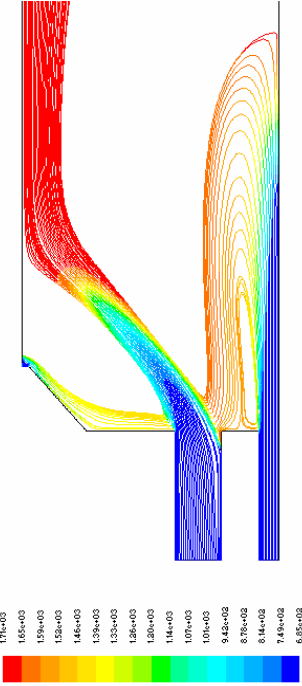
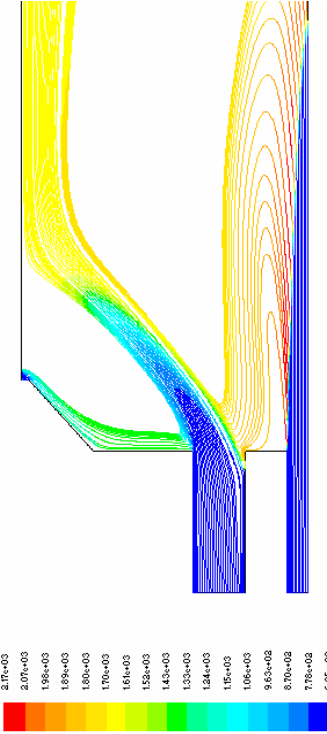
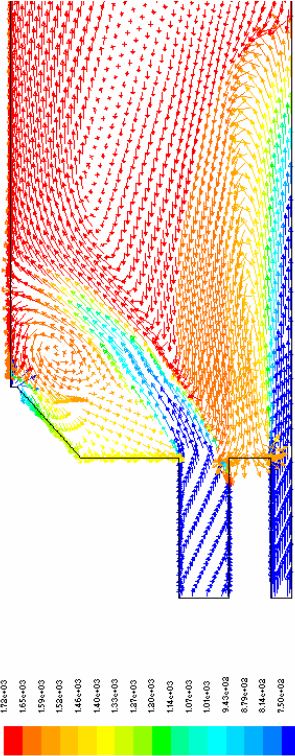
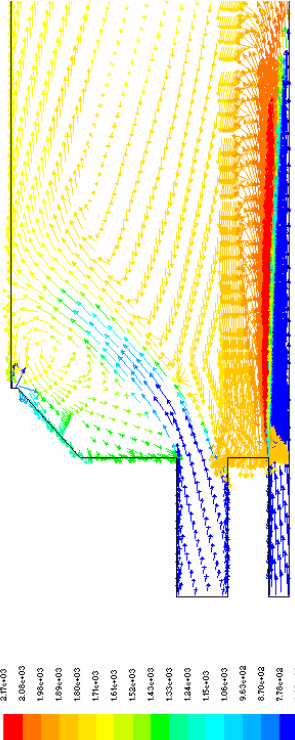
 <p>Figure 5-14. Streamlines colored by temperature for 50% pilot.</p>	 <p>Figure 5-15. Streamlines colored by temperature, 150% pilot case.</p>
 <p>Figure 5-16. Vectors of velocity colored by temperature, the first half of the combustor for the 50% pilot case.</p>	 <p>Figure 5-17. Vectors of velocity colored by temperature, the first half of the combustor for the 150% pilot case.</p>

Table 5-3 (continued)

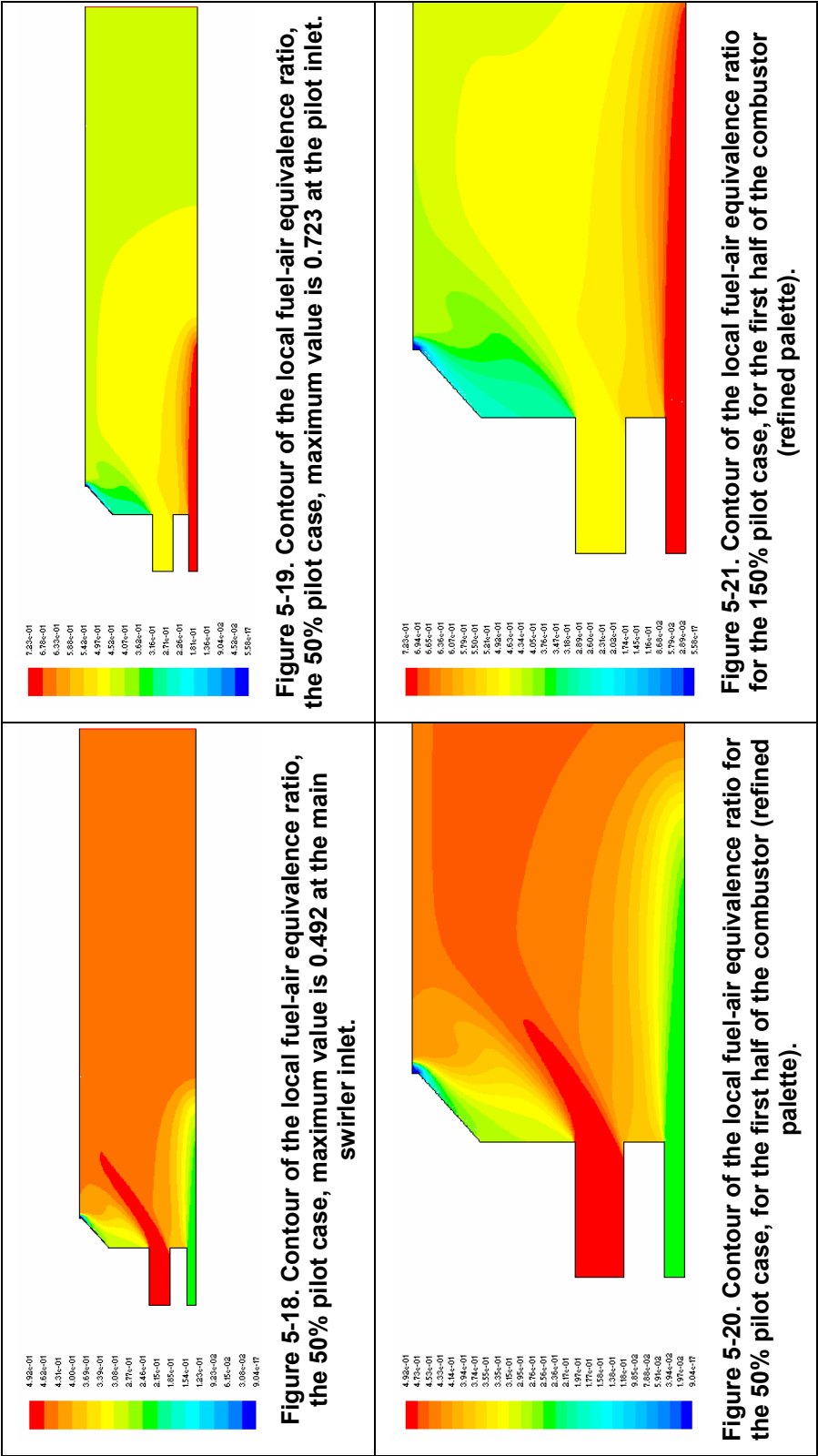


Table 5-3 (continued)

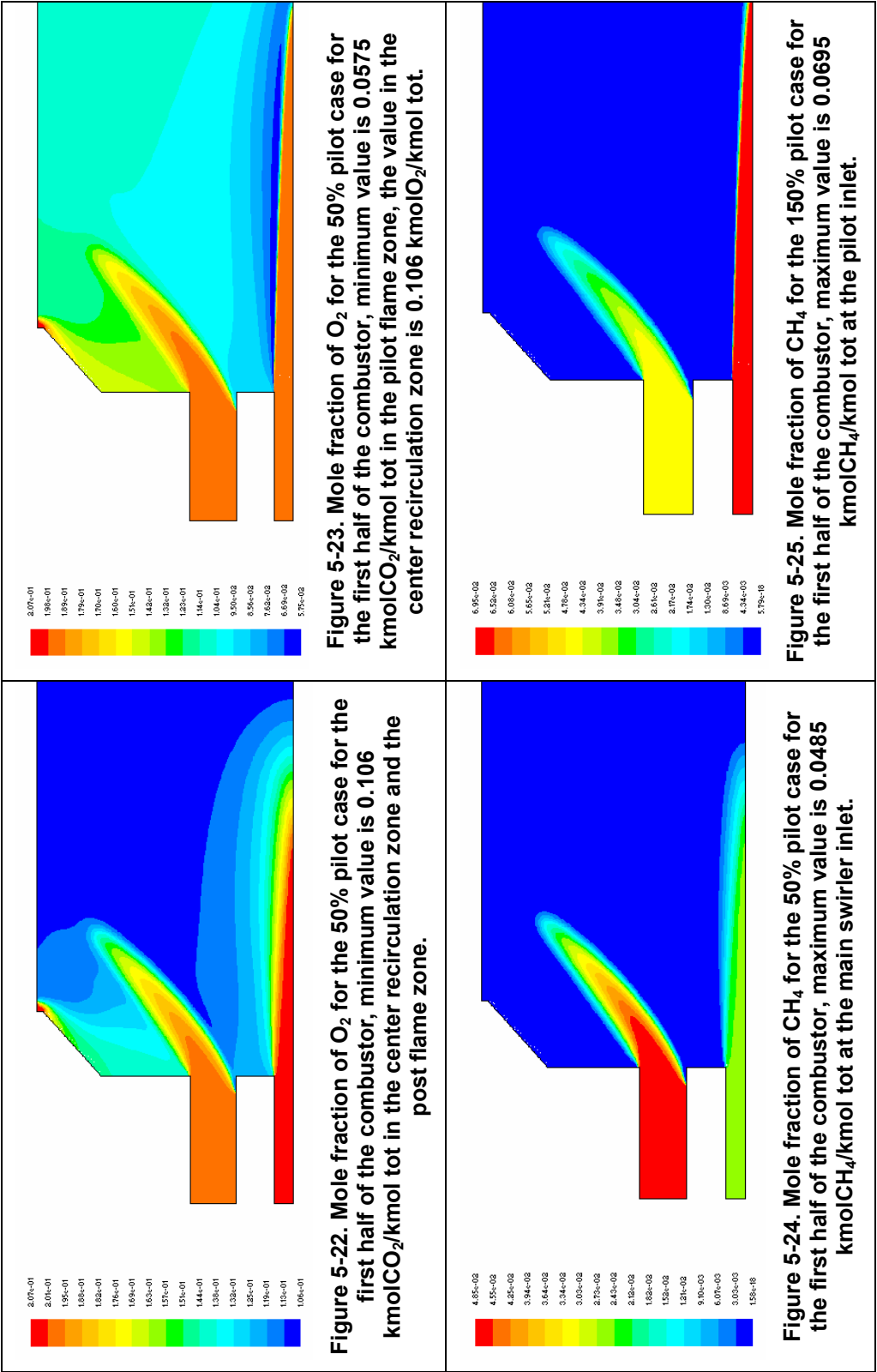


Table 5-3 (continued)

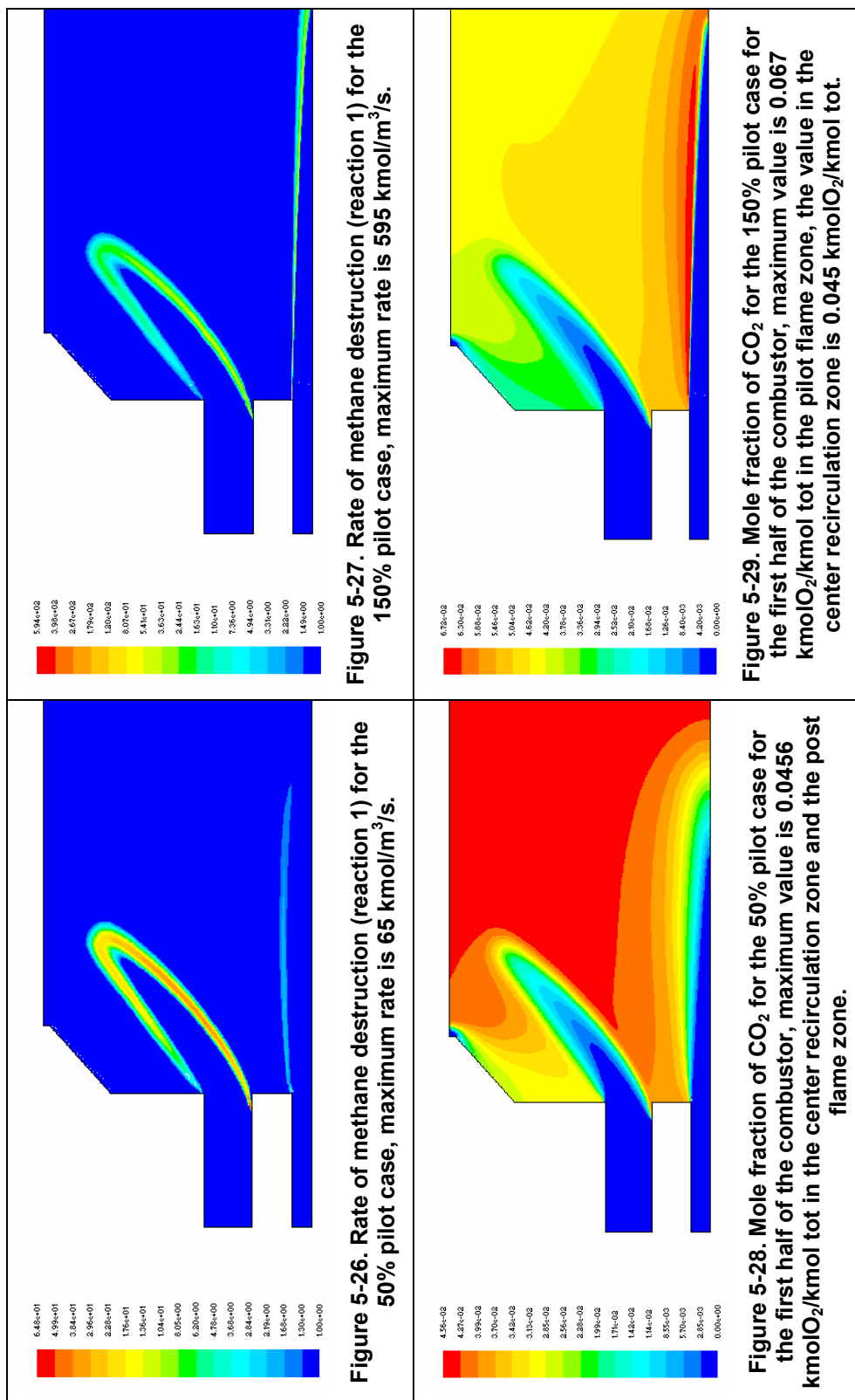


Table 5-3 (continued)

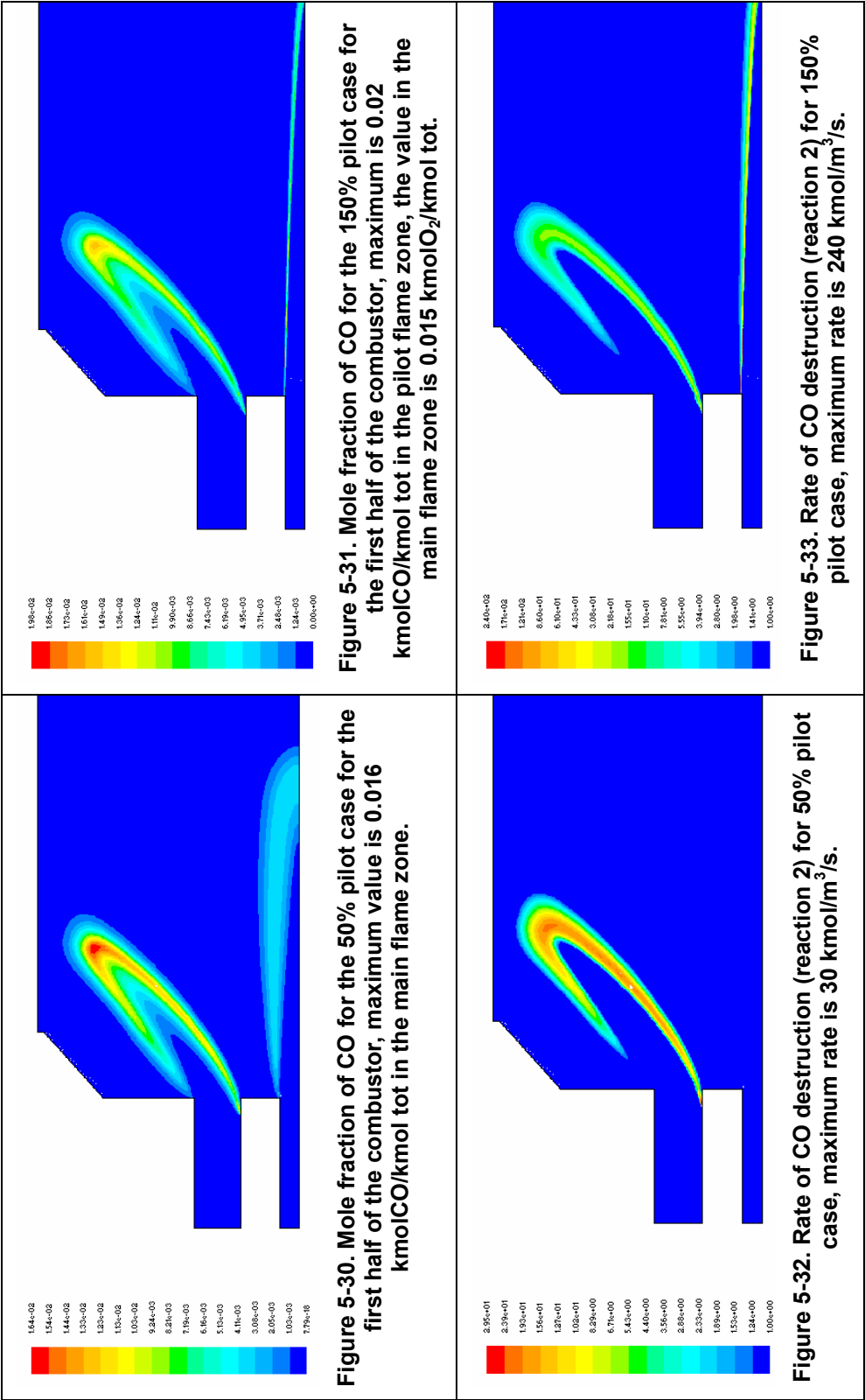


Table 5-3 (continued)

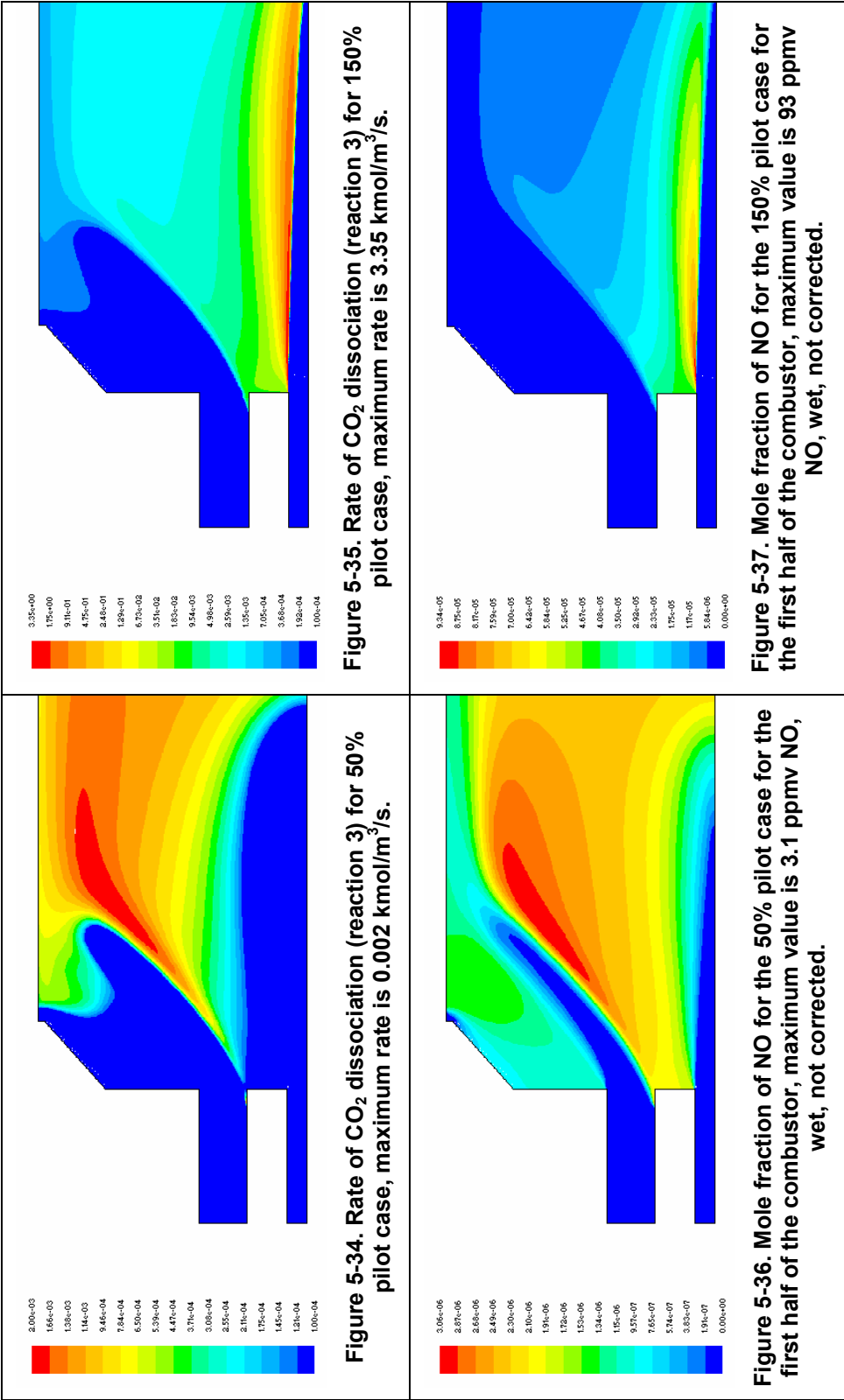


Table 5-3 (continued)

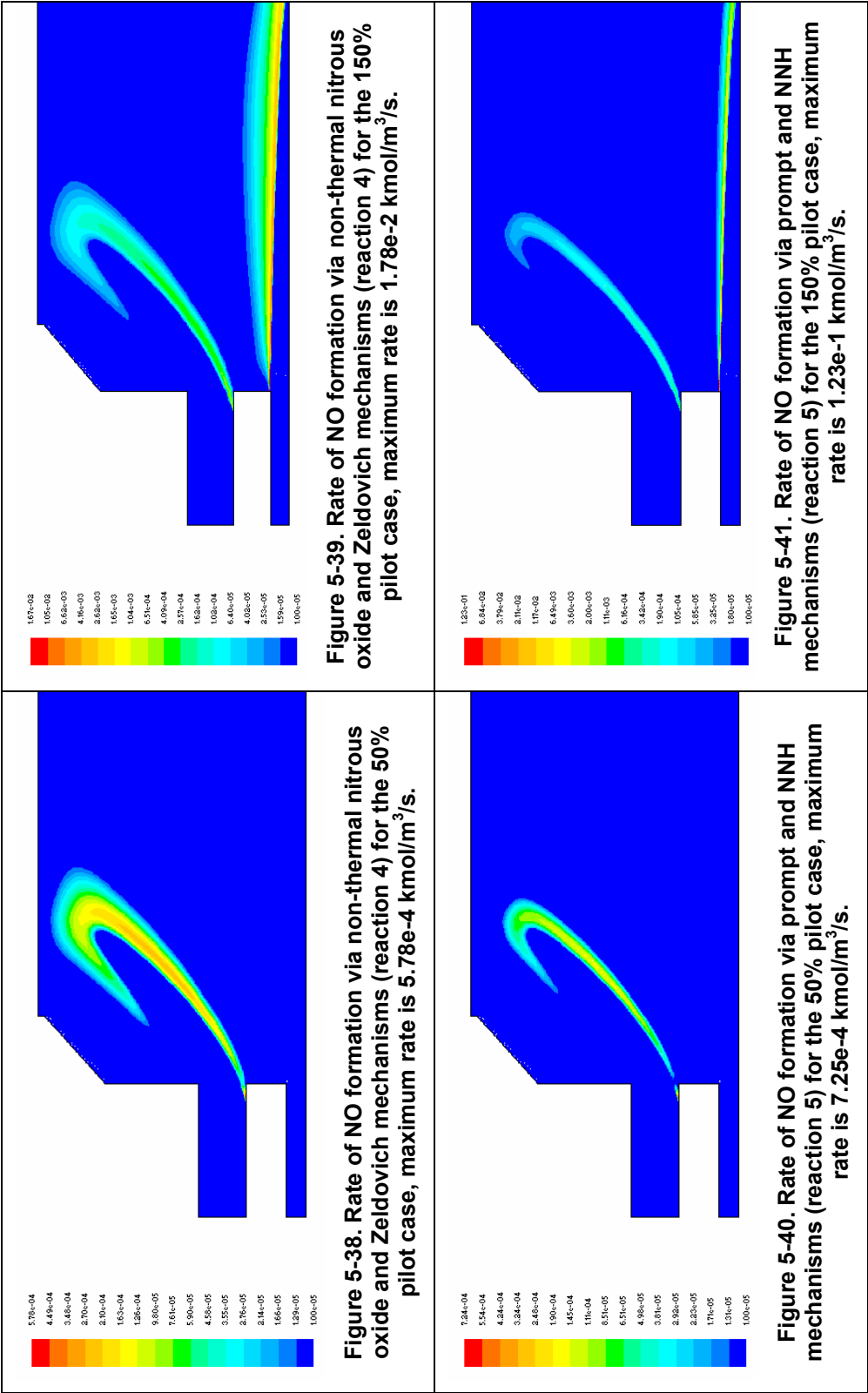


Table 5-3 (continued)

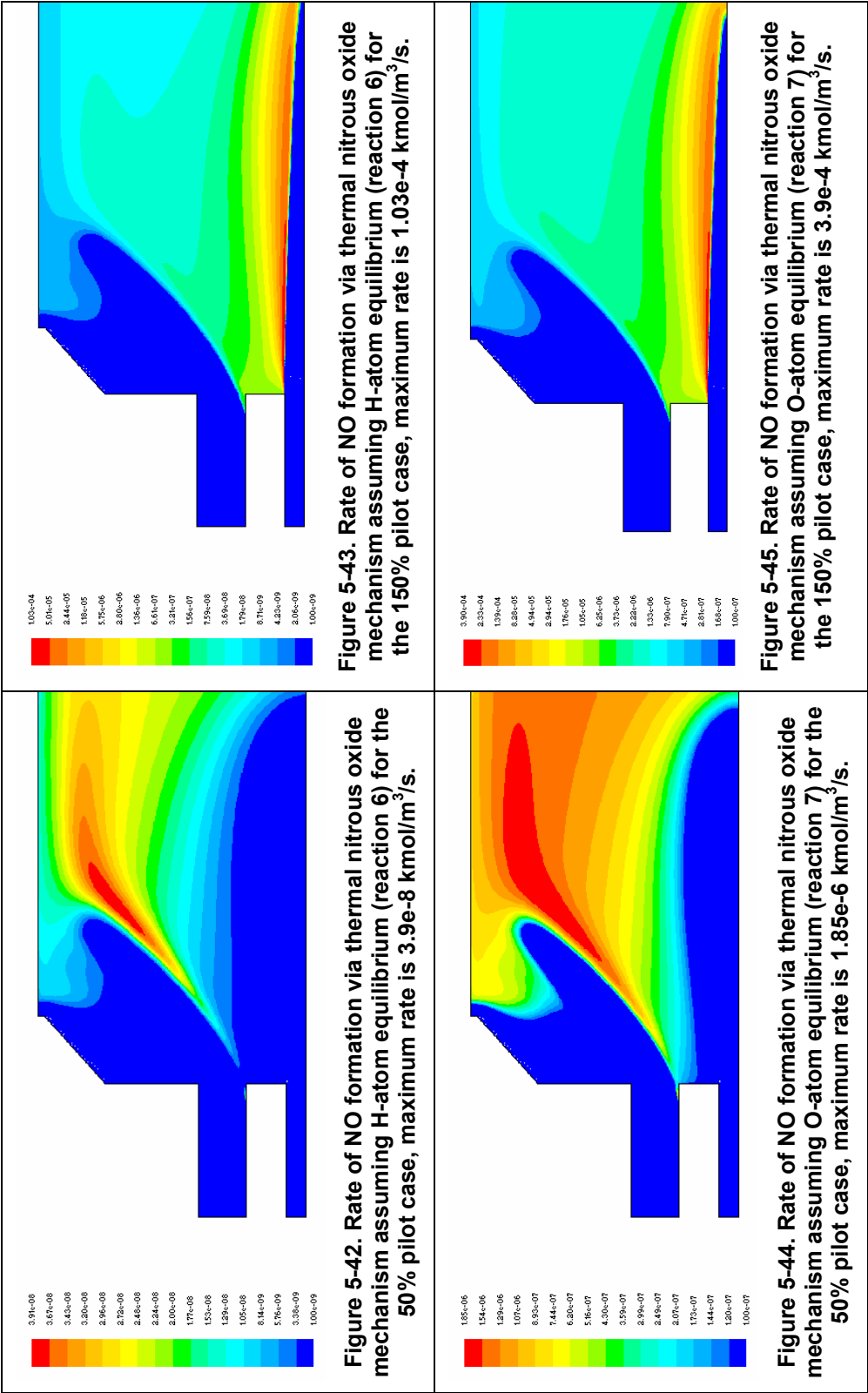
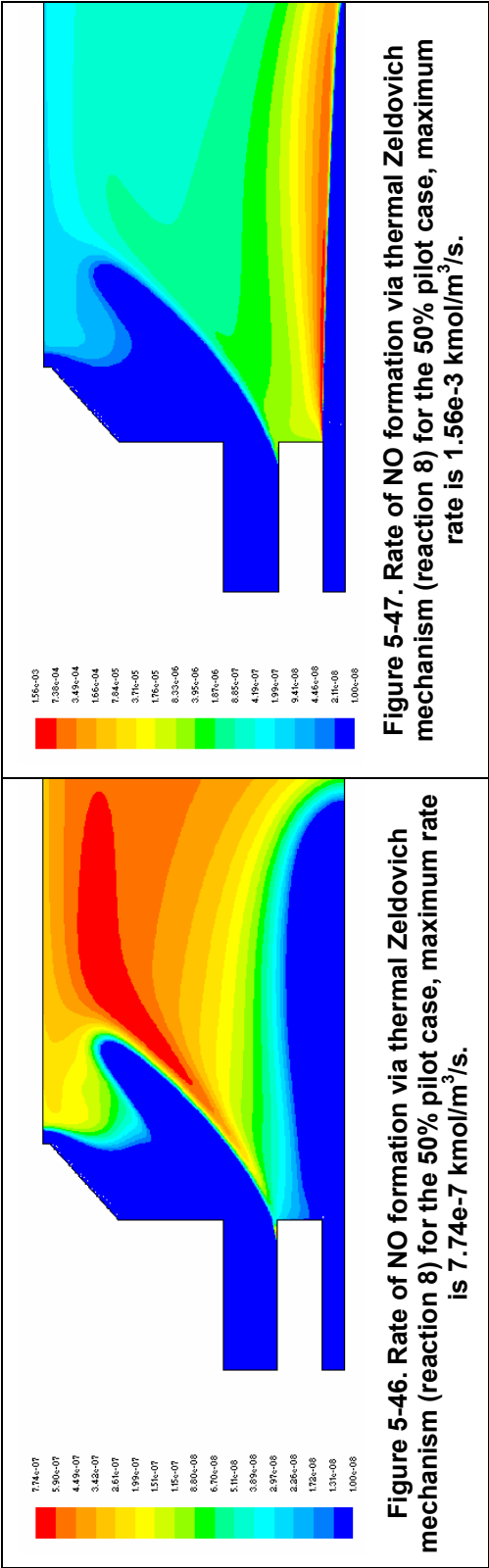


Table 5-3 (continued)



### ***Non-uniform Injector Mixing Profile***

In order to understand the effect of the injector fuel-air mixing profile (i.e., the fuel-air distribution at the exit of the premixer) on the flame position and emission levels, additional calculations with a non-uniform injector mixing profile are performed.

Figure 5-47 shows a radial mixing profile used in the simulation. The profile has a linear fuel-air equivalence ratio distribution with respect to the injector radial coordinate. The mixture is richer at the inner radius of the premixer ( $\Phi$  is 0.63) and leaner at the outer premixer radius ( $\Phi$  is 0.33). The fuel flow rates are calculated based on this assumed fuel-air mixing profile at the injector outlet and the air mass flow rate. The velocity and the air mass flow outlet profiles remain the same as used in the flat injector mixing profile simulation, see Figure 5-2. The pilot fuel-air mixture has a uniform profile.

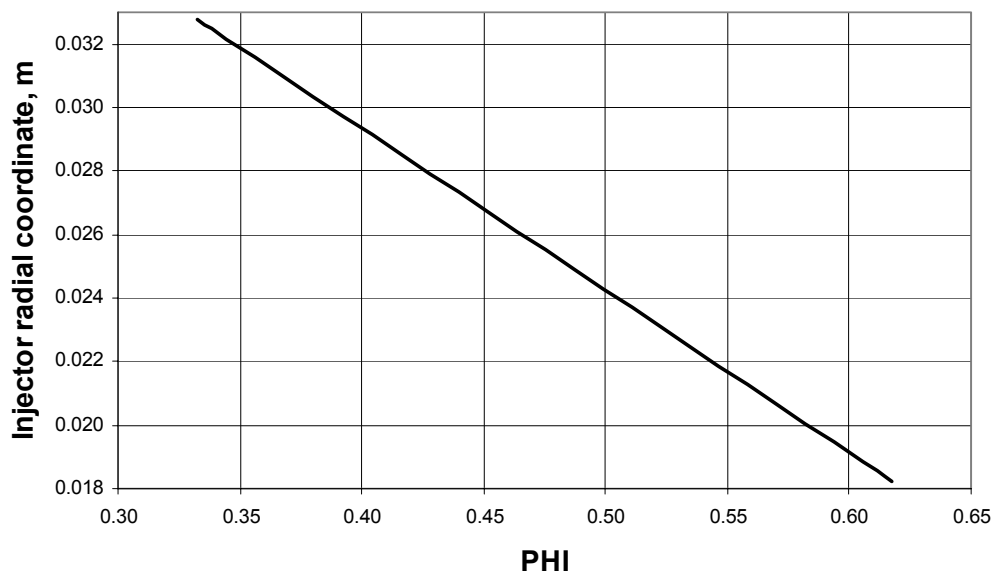


**Figure 5-48. Linear fuel-air equivalence ratio distribution for the modeled injector.**

In the cases with the flat fuel air premixer profile the overall injector  $\Phi$  (combined premixer and pilot flows) is set to 0.475. Unlike the previous case, the fuel-air equivalence ratio of the premixer (main swirler) with linear fuel-air ratio distribution is fixed to 0.475. The pilot air flow rate is held constant. The pilot fuel rate is varied from 50 to 150% of neutral pilot corresponding to the pilot fuel-air equivalence ratio of 0.24 to 0.71. As the pilot  $\Phi$  increases, the total injector  $\Phi$  changes from 0.468 to 0.482. This increase in injector  $\Phi$  raises the combustor outlet temperature from 1658 to 1675 K. The overall injector fuel-air equivalence ratio for 3% pilot air flow rate is calculated according to:

$$\Phi_{\text{injector}} = 0.97 \cdot \Phi_{\text{premix}} + 0.03 \cdot \Phi_{\text{pilot}}, \quad [5-4]$$

where:

- $\Phi_{\text{injector}}$  - overall fuel-air equivalence ratio of the injector
- $\Phi_{\text{premixer}}$  - overall fuel-air equivalence ratio of the premixer
- $\Phi_{\text{pilot}}$  - overall fuel-air equivalence ratio of the pilot

Table 5-4 shows the difference between the CFD boundary conditions for the flat and the linear injector mixing profile simulations. The decrease of the outlet temperature with respect the pilot  $\Phi$  for the flat profile is due to the higher radiative heat transfer rate from the hotter pilot flame zone.

**Table 5-4. Boundary conditions for linear and uniform injector mixing profiles.**

Pilot %	Uniform mixing profile				Linear mixing profile			
	$\Phi_{\text{premix}}$	$\Phi_{\text{pilot}}$	$\Phi_{\text{injector}}$	$T_{\text{out}}, \text{K}$	$\Phi_{\text{premix}}$	$\Phi_{\text{pilot}}$	$\Phi_{\text{injector}}$	$T_{\text{out}}, \text{K}$
50	0.482	0.238	0.475	1670	0.475	0.238	0.468	1658
100	0.475	0.475	0.475	1665	0.475	0.475	0.471	1665
125	0.471	0.594	0.475	1665	0.475	0.594	0.475	1673
150	0.468	0.713	0.475	1664	0.475	0.713	0.482	1675

Table 5-5 with Figures 5-50 through 5-92 compares the CFD results for the can-type burner with flat and linear injector mixing profiles for the neutral pilot cases. As seen in the figures, the pilot and the main flame temperature and species concentrations are different, but the overall flow structure remains similar in both cases.

The plot of the predicted  $\text{NO}_x$  emissions for the injector with linear injector profile is shown in the Figure 5-49. The figure also shows the contributions of the  $\text{NO}$  formation mechanisms. The largest contribution, as in the flat injector profile case, comes from the non-thermal  $\text{N}_2\text{O}$  and Zeldovich pathways (45-50%). The contribution of the prompt and NNH routes is up to 30% due the increased temperature in the flame front. The relative contribution of the thermal  $\text{NO}$  formation route is relatively small, 14-22% of the total  $\text{NO}$  production, due to the relatively cool post-flame and main recirculation zones.

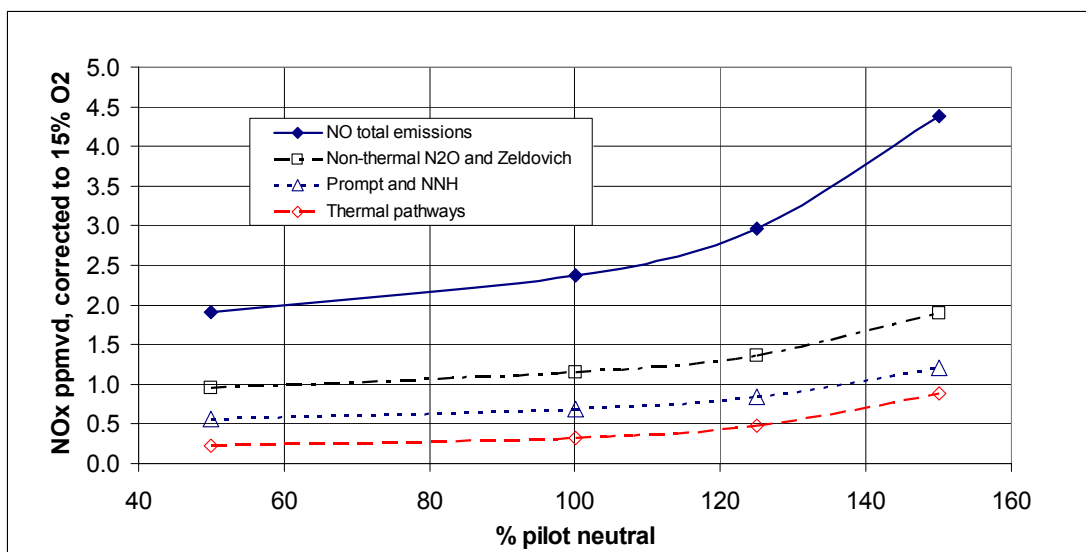


**Figure 5-49.  $\text{NO}$  formation mechanisms in can combustor with linear injector fuel-air mixing profile.**

The rates of the NO production are the highest for the non-uniform injector mixing profile. These high rates persist in the region of the high local fuel-air equivalence ratio (0.6-0.63) at the inner part of the main flame. Figures 5-50 through 5-53 show that the maximum flame temperature for the linear fuel-air mixing profile case is 200K higher. Since the NO formation rates have an exponential dependence on temperature, the increase of the maximum flame temperature contributes to the sharp increase in the NO formation rates. Contours of the NO formation rates are shown in Figures 5-83 through 5-92. NO formation zones are different in these simulations. The figures depicting NO formation rates use logarithmic color scale distribution in order to cover the wide range of the rate values. The color scale for both cases is set to be the same.

**Table 5-5. CFD simulation of methane combustion in the single-injector, can-type-type combustor for flat and linear injector fuel mixing profiles and for neutral pilot.**

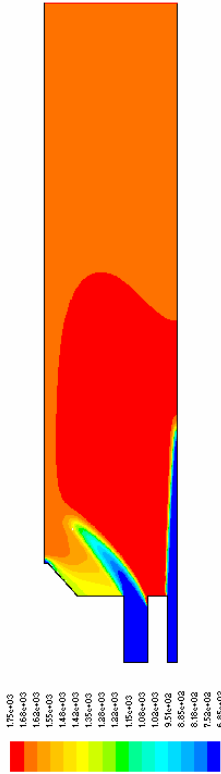
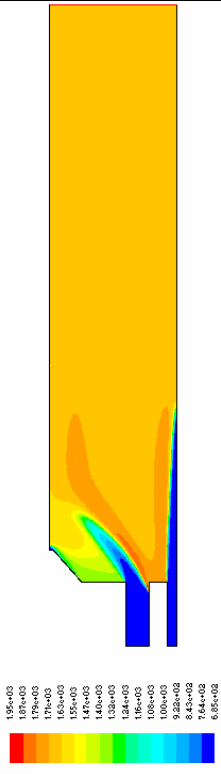
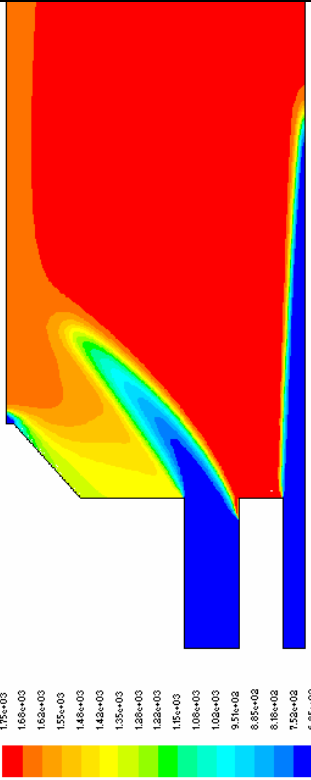
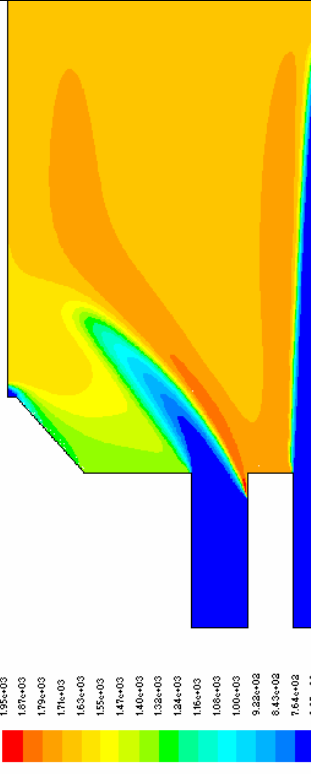
Flat injector mixing profile, neutral pilot case	Linear injector mixing profile, neutral pilot case
 <p><b>Figure 5-50.</b> Temperature contour plot for flat injector mixing profile, maximum value is 1750 K.</p>	 <p><b>Figure 5-51.</b> Temperature contour plot for linear injector mixing profile, maximum value is 1950 K.</p>
 <p><b>Figure 5-52.</b> Temperature contour plot for flat injector profile, maximum value is 1750 K, only the first half of the combustor is shown.</p>	 <p><b>Figure 5-53.</b> Temperature contour plot for linear mixing profile, maximum value is 1950 K, only the first half of the combustor is shown.</p>

Table 5-5 (continued)

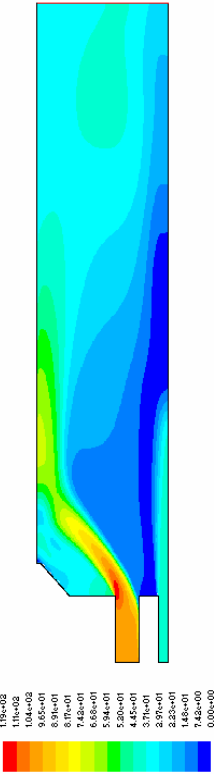
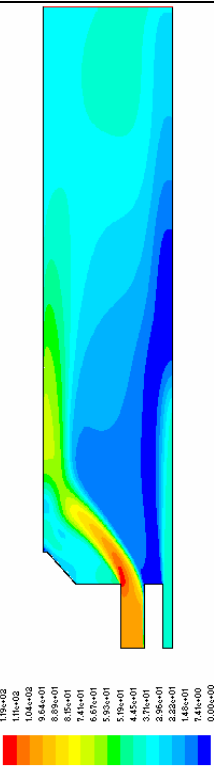
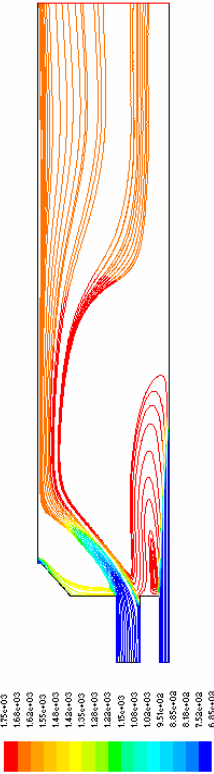
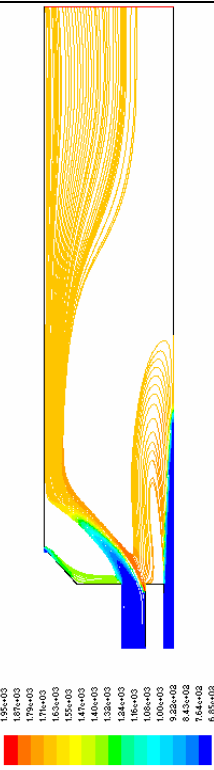
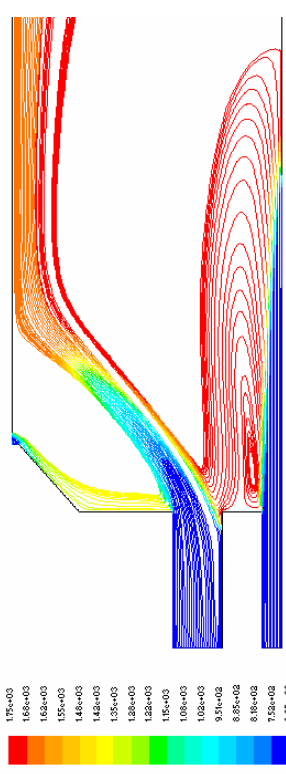
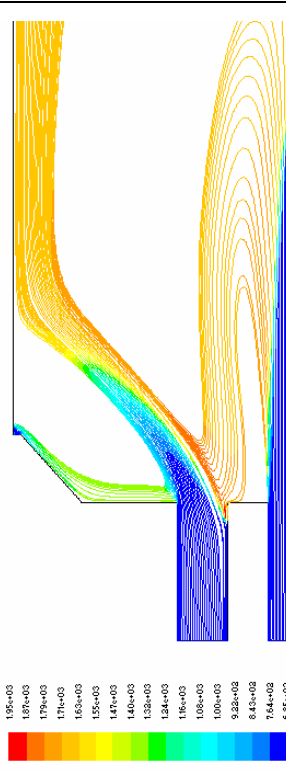
 <p>Figure 5-54. Velocity magnitude for flat profile, max. is 120 m/s.</p>	 <p>Figure 5-55. Velocity magnitude for linear profile, max. is 120 m/s.</p>
 <p>Figure 5-56. Streamlines colored by temperature for flat profile.</p>	 <p>Figure 5-57. Streamlines colored by temperature for linear profile.</p>
 <p>Figure 5-58. Streamlines colored by temperature for flat profile.</p>	 <p>Figure 5-59. Streamlines colored by temperature for linear profile.</p>

Table 5-5 (continued)

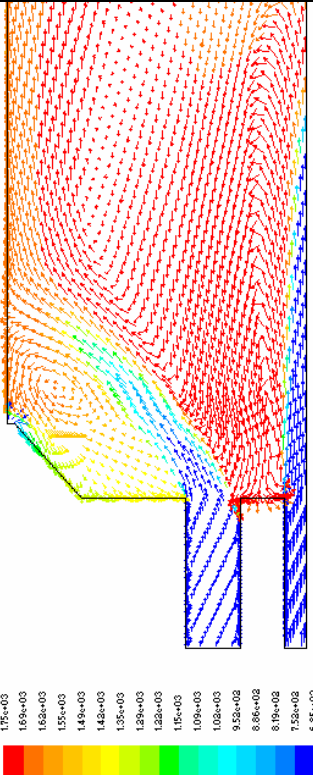
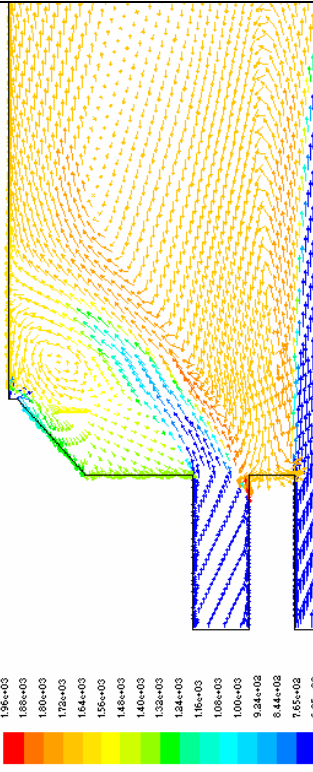
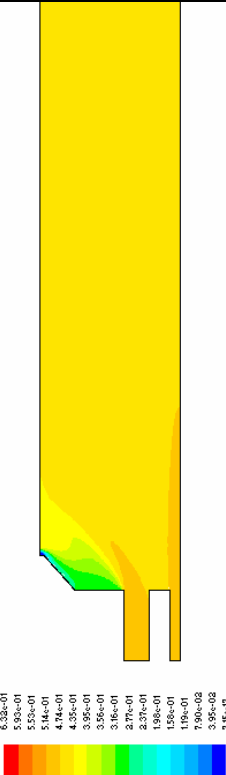
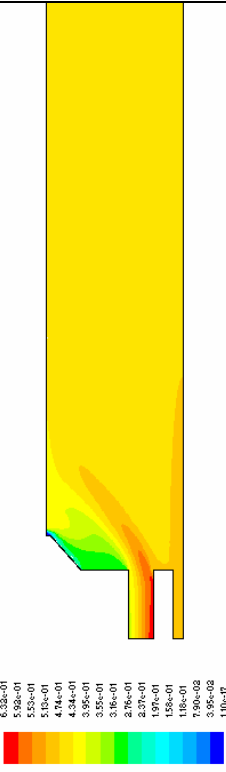
 <p>Figure 5-60. Vectors of velocity colored by temperature for the first half of the combustor for flat injector mixing profile.</p>	 <p>Figure 5-61. Vectors of velocity colored by temperature for the first half of the combustor for linear injector mixing profile.</p>
 <p>Figure 5-62. Contour of local fuel-air equivalence ratio for flat injector mixing profile, maximum value is 0.475.</p>	 <p>Figure 5-63. Contour of local fuel-air equivalence ratio for linear mixing profile, maximum value is 0.623 at the inner part of injector inlet.</p>

Table 5-5 (continued)

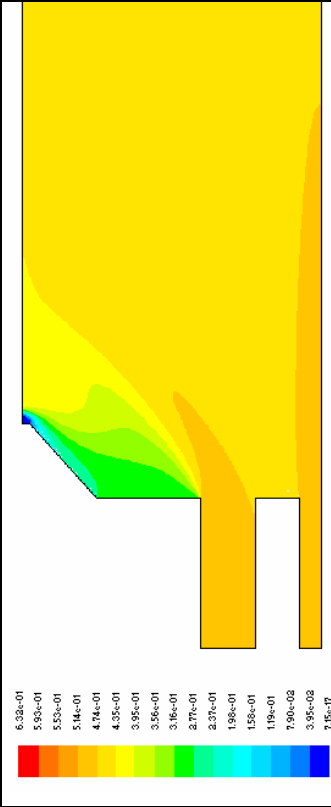


Figure 5-64. Contour of local fuel-air equivalence ratio for flat injector profile, for the first half of the combustor (refined palette).

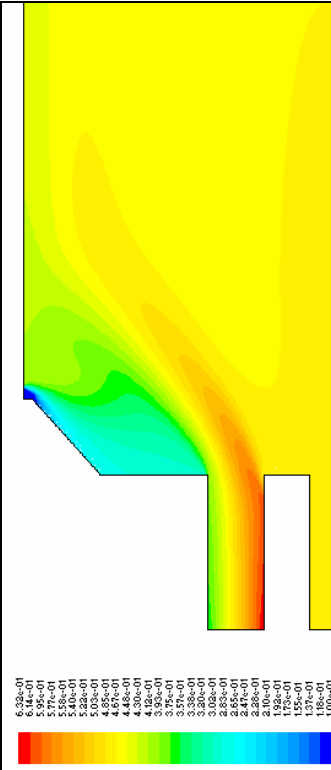


Figure 5-65. Contour of local fuel-air equivalence ratio for linear injector profile case, for the first half of the combustor (refined palette).

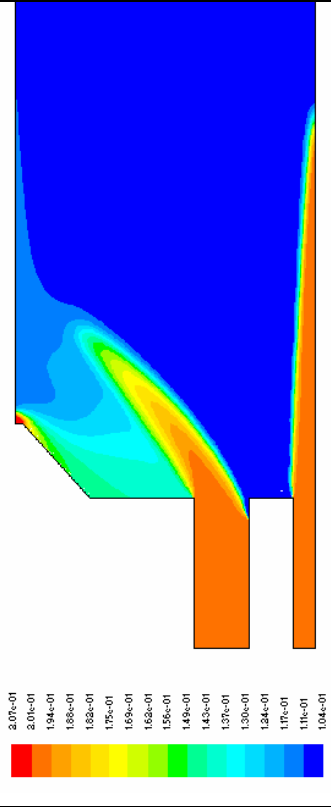


Figure 5-66. Mole fraction of O<sub>2</sub> for a flat injector mixing profile case for the first half of the combustor, minimum value is 0.104 kmolO<sub>2</sub>/kmol tot in the center recirculation zone and the post flame zone.

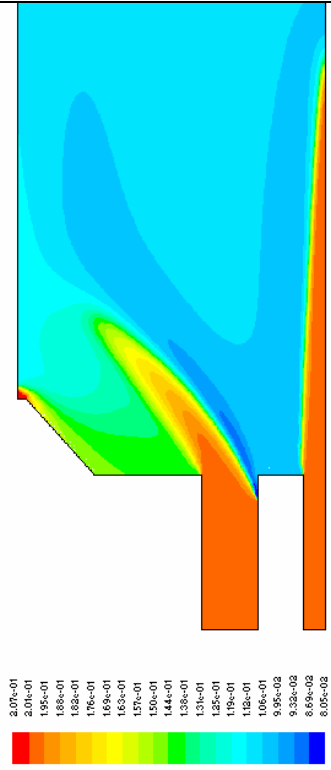


Figure 5-67. Mole fraction of O<sub>2</sub> for linear injector profile case for the first half of the combustor, minimum value is 0.08 kmolO<sub>2</sub>/kmol tot in the inner part of the main flame zone, the value in the center recirculation zone is 0.106 kmolO<sub>2</sub>/kmol tot.

Table 5-5 (continued)

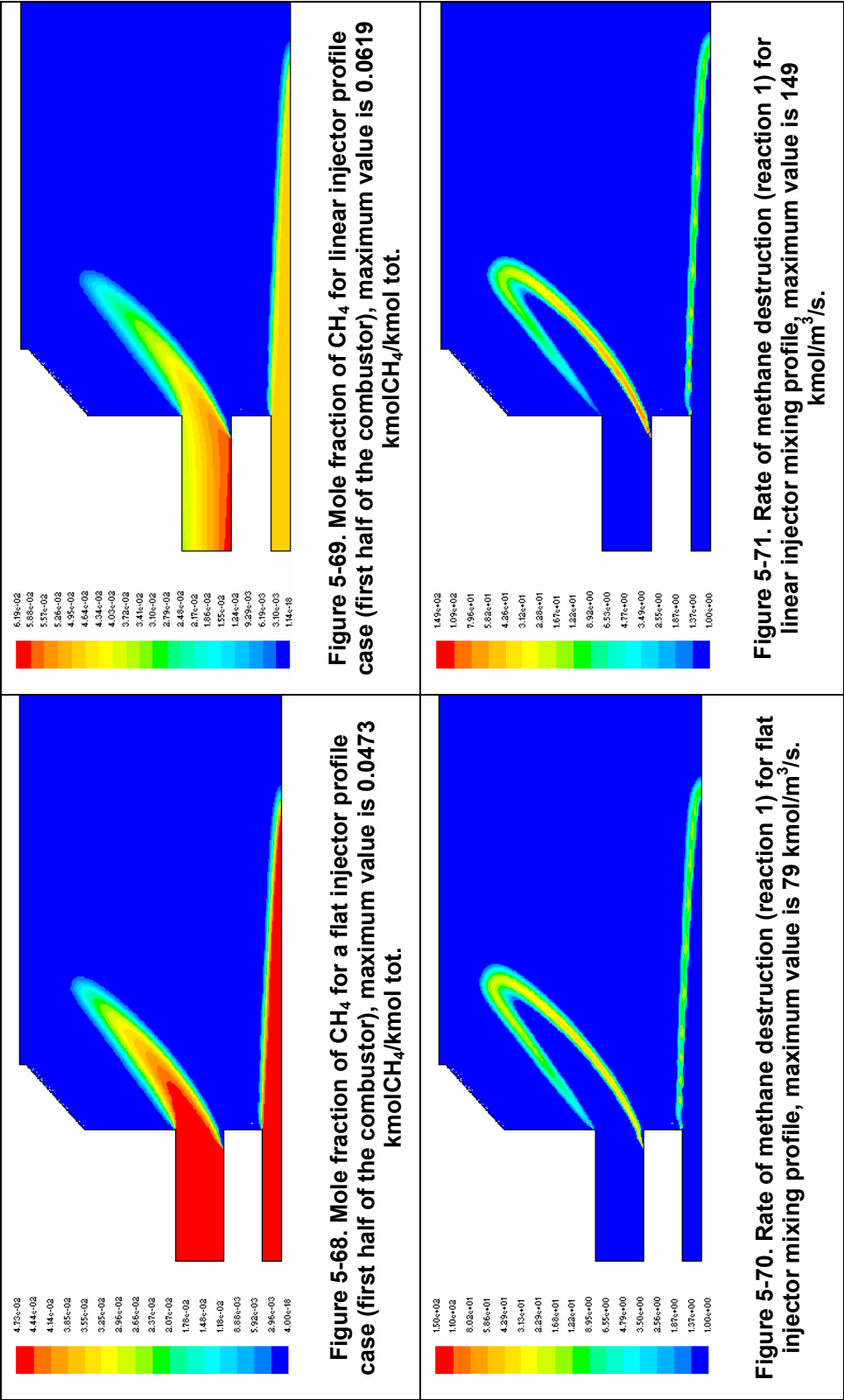


Table 5-5 (continued)

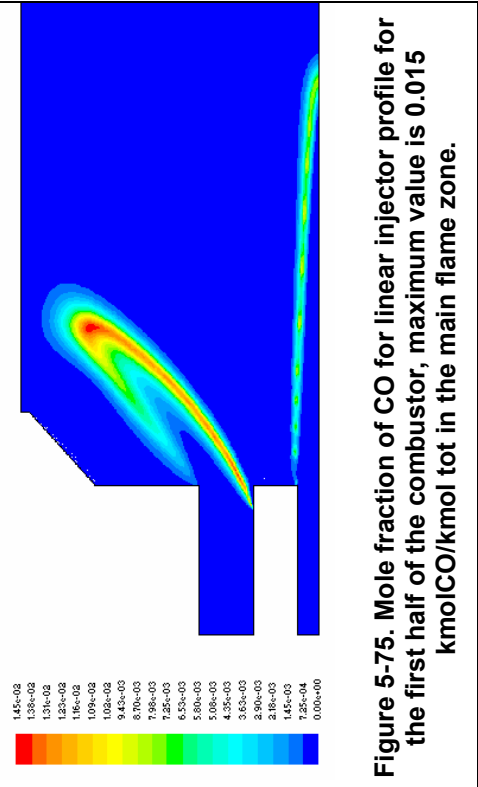
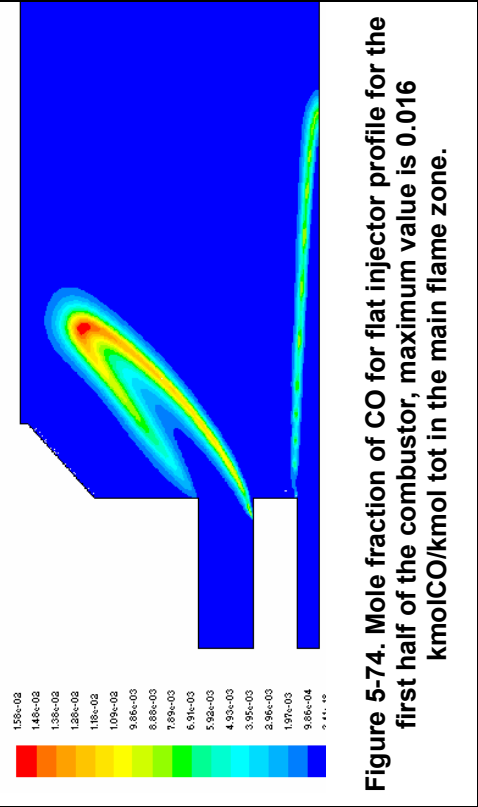
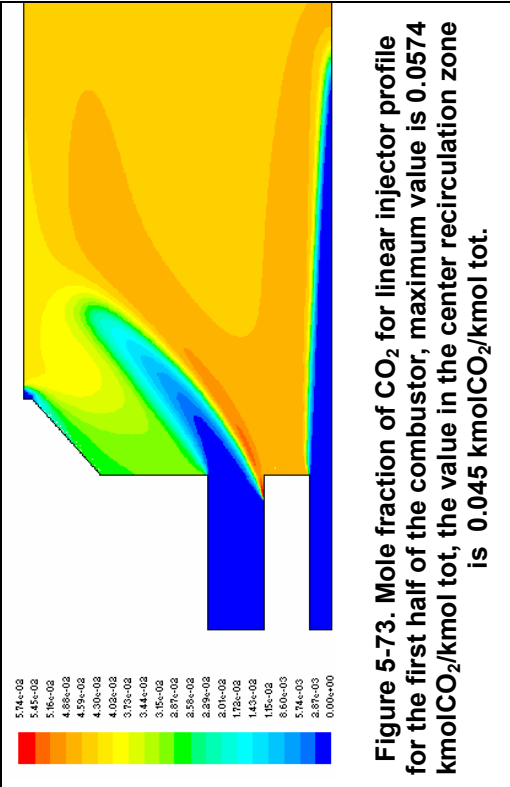
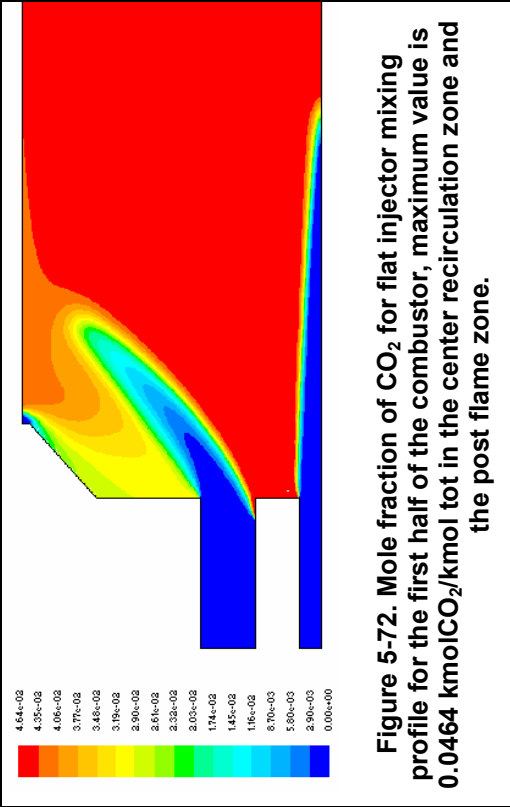


Table 5-5 (continued)

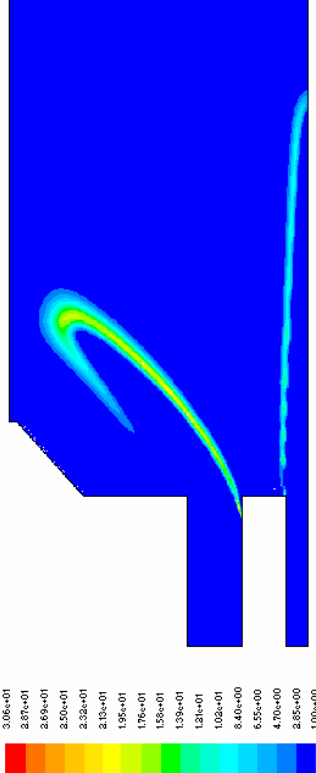
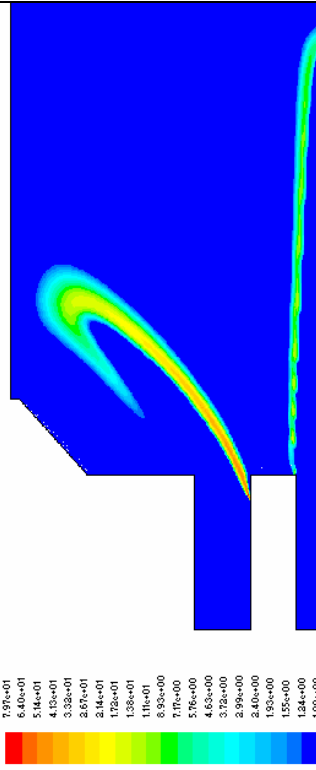
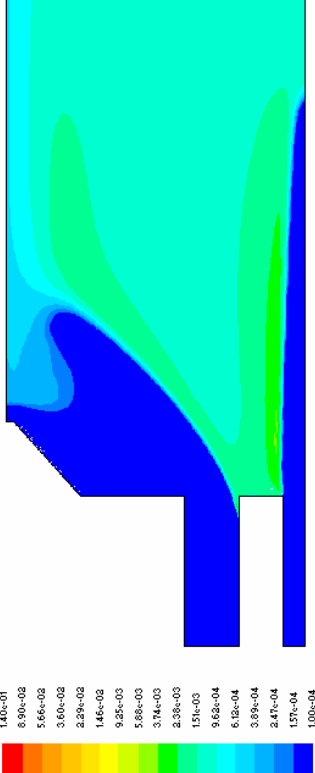
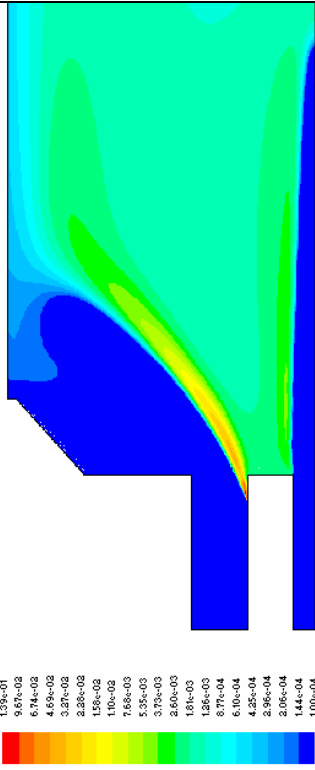
 <p>Figure 5-76. Rate of CO destruction (reaction 2) for flat injector mixing profile, maximum value is 31 kmol/m<sup>3</sup>/s.</p>	 <p>Figure 5-77. Rate of CO destruction (reaction 2) for linear injector mixing profile, maximum value is 80 kmol/m<sup>3</sup>/s.</p>
 <p>Figure 5-78. Rate of CO<sub>2</sub> dissociation (reaction 3) for flat injector mixing profile, maximum value is 0.004 kmol/m<sup>3</sup>/s.</p>	 <p>Figure 5-79. Rate of CO<sub>2</sub> dissociation (reaction 3) for linear injector mixing profile, maximum value is 0.14 kmol/m<sup>3</sup>/s.</p>

Table 5-5 (continued)

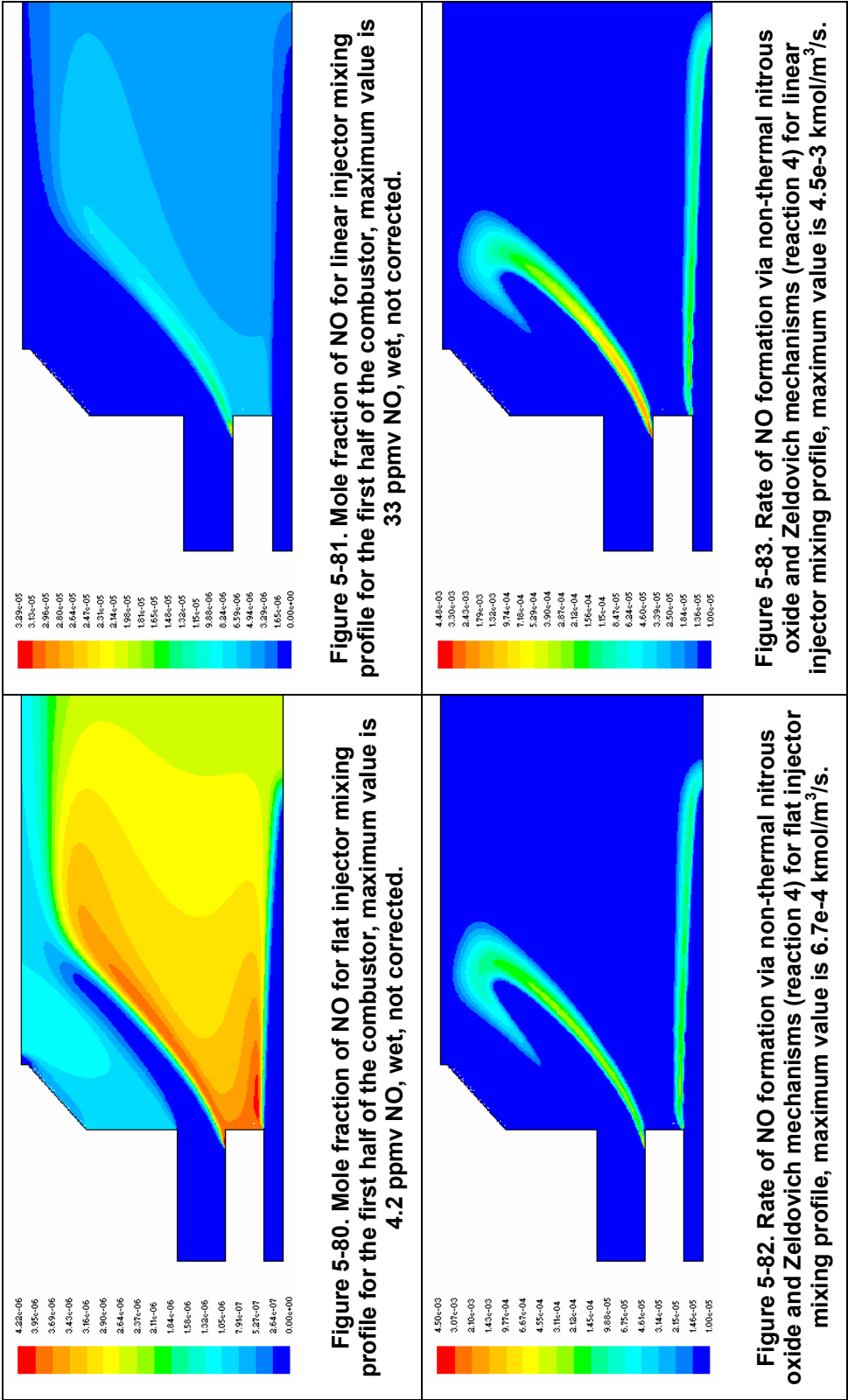


Table 5-5 (continued)

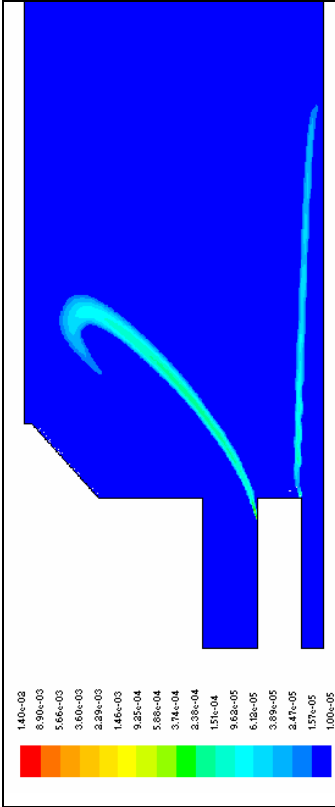


Figure 5-84. Rate of NO formation via prompt and NNH mechanisms (reaction 5) for flat injector profile, maximum value is 7.6e-4 kmol/m<sup>3</sup>/s.

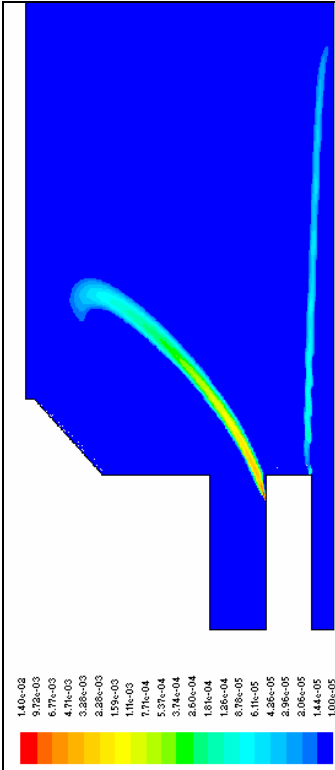


Figure 5-85. Rate of NO formation via prompt and NNH mechanisms (reaction 5) for linear injector profile, maximum value is 1.4e-2 kmol/m<sup>3</sup>/s.

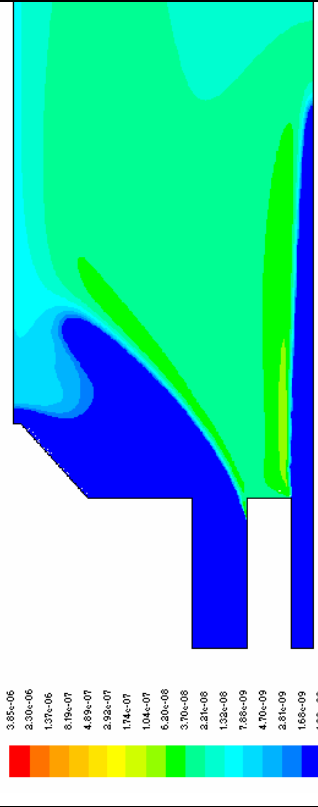


Figure 5-86. Rate of NO formation via thermal nitrous oxide mechanism assuming H-atom equilibrium (reaction 6) for flat injector mixing profile, maximum value is 8.6e-8 kmol/m<sup>3</sup>/s.

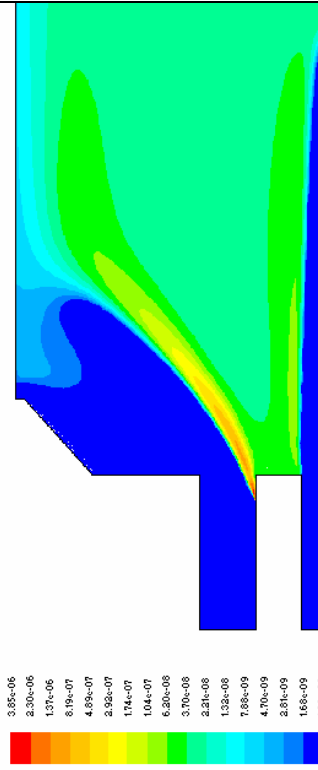


Figure 5-87. Rate of NO formation via thermal nitrous oxide mechanism assuming H-atom equilibrium (reaction 6) for linear injector mixing profile, maximum value is 3.85e-6 kmol/m<sup>3</sup>/s.

Table 5-5 (continued)

<p>Figure 5-88. Rate of NO formation via thermal nitrous oxide mechanism assuming O-atom equilibrium (reaction 7) for flat injector mixing profile, maximum value is 3.2e-6 kmol/m<sup>3</sup>/s.</p>	<p>Figure 5-89. Rate of NO formation via thermal nitrous oxide mechanism assuming O-atom equilibrium (reaction 7) for linear injector mixing profile, maximum value is 4.5e-4 kmol/m<sup>3</sup>/s.</p>
<p>Figure 5-90. Rate of NO formation via thermal Zeldovich mechanism (reaction 8) for flat injector mixing profile, maximum value is 1.7e-6 kmol/m<sup>3</sup>/s.</p>	<p>Figure 5-91. Rate of NO formation via thermal Zeldovich mechanism (reaction 8) for linear injector mixing profiles, maximum value is 6.61e-5 kmol/m<sup>3</sup>/s.</p>

## **6. Development of Chemical Reactor Network for the Gas Turbine Combustor**

### ***Introduction***

The development of the chemical reactor network (CRN) for the generic, lean-premixed, single-injector, can-type, gas-turbine combustor is discussed in this chapter. The description, operating and boundary conditions, and CFD modeling of this combustor have been addressed in Chapter 5. The fuel used in the modeling in this chapter is methane.

The University of Washington chemical reactor code, based on the CREK code (Pratt and Wormeck, 1976) is used in the development of the CRN. The development uses the insight gained from CFD modeling of the single-injector, can-type combustor. The CRN development rests on the following critical features:

- Fuel-air distribution in the premixer
- Injector velocity profile
- Turbulent mixing in the premixed stream issuing from the injector
- Pilot – main recirculation zone - main flame interaction
- Addition of dome cooling air

The CRN is constructed based on CFD-predicted flow patterns: flame shape and location, and entrainment of the dome air and gas from main recirculation zone into the flame. These flow patterns are CRN-treated by adjusting the flow splits between the corresponding elements of the network.

In order to develop the CRN, the first step is to think of the combustor volume as divided into the distinct regions or zones. Each of the zones is characterized by the particular physical properties of the flow and the flame behavior. Figures 6-1 and 6-2 show how the single-injector, can-type combustor can be divided into the zones based on the flow temperature, velocity, and chemical species concentrations. The CFD results used in this chapter have been generated for two cases: 1) the case of uniform fuel-air ratio at the injector outlet (i.e. flat fuel-air mixing profile, and 2) the case with linear fuel-air ratio variation at the outlet of the injector which allows the effect of cross-stream mixing in the injector outlet stream to be incorporated into the CRN.

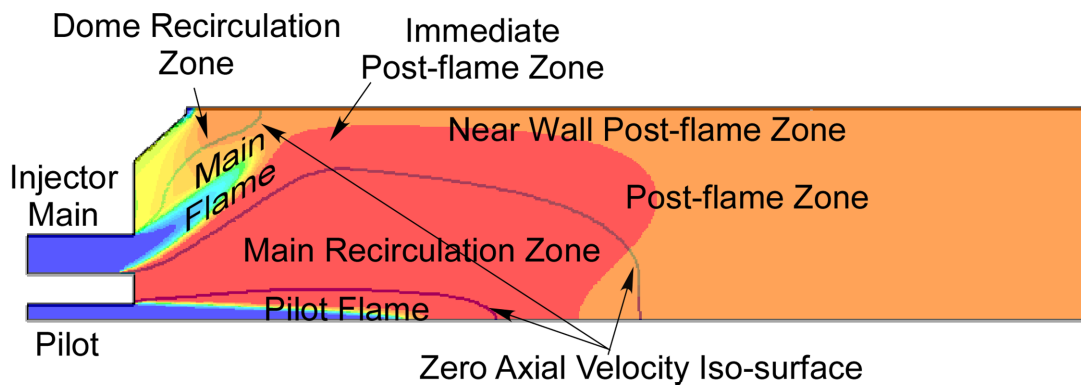


**Figure 6-1. Main zones of the generic GT combustor for the flat injector fuel-air ratio profile with neutral pilot case, overall injector  $\Phi = 0.475$ . Temperature contour plot is shown, maximum is 1750K, and minimum is 685K. Repeat of Figure 5-4.**

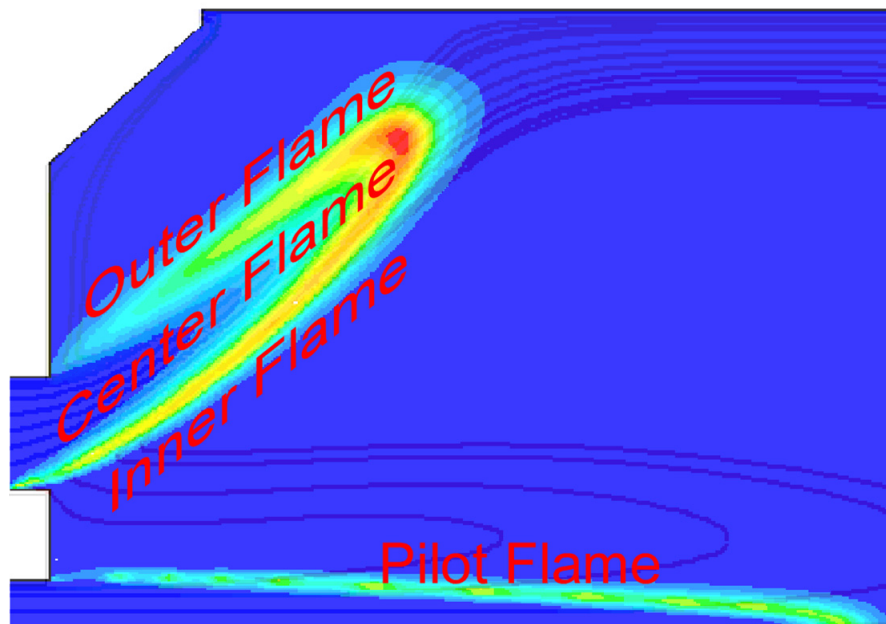


**Figure 6-2. Flame zone for the flat fuel-air ratio profile with neutral pilot case. Carbon monoxide profiles are shown; maximum value of CO is 1.58%. Overall injector  $\Phi = 0.475$ .**

Figure 6-3 shows the schematic layout of the 31 element CRN developed herein. The network consists of 31 PSR, PFR, and MIX elements, though in Figure 6-3 some of the MIX elements are not shown to avoid clutter. Each element type is described below:

- PSR stands for perfectly stirred reactor (i.e., a continuously stirred tank reactor), in which mixing to the molecular scale is assumed to happen instantaneously compared to chemical reaction. The chemical reaction occurs homogeneously in the reactor.
- PFR stands for plug flow reactor, in which the flow is assumed to move as a plug and the chemical reaction proceeds one-dimensionally, longitudinal mixing in the reactor is assumed to be zero.
- MIX stands for an element in which the entering streams are uniformly mixed without chemical reaction.

The elements are grouped according to the zones shown on Figures 6-1 and 6-2:

- Main flame zone (MFZ) consisting of the inner, middle and outer injector streams and flames as depicted in Figure 6-2.
- Pilot flame zone (PZ) consisting of the pilot flame input stream, as provided by the injector pilot circuit, and the pilot flame.
- Center (main) recirculation zone (CRZ) consisting of the back-mixed hot product gas flow.
- Dome recirculation zone (DRZ) consisting of the combustor dome air input stream.
- Post-flame zone (PFZ) consisting of the CO burnout zones.

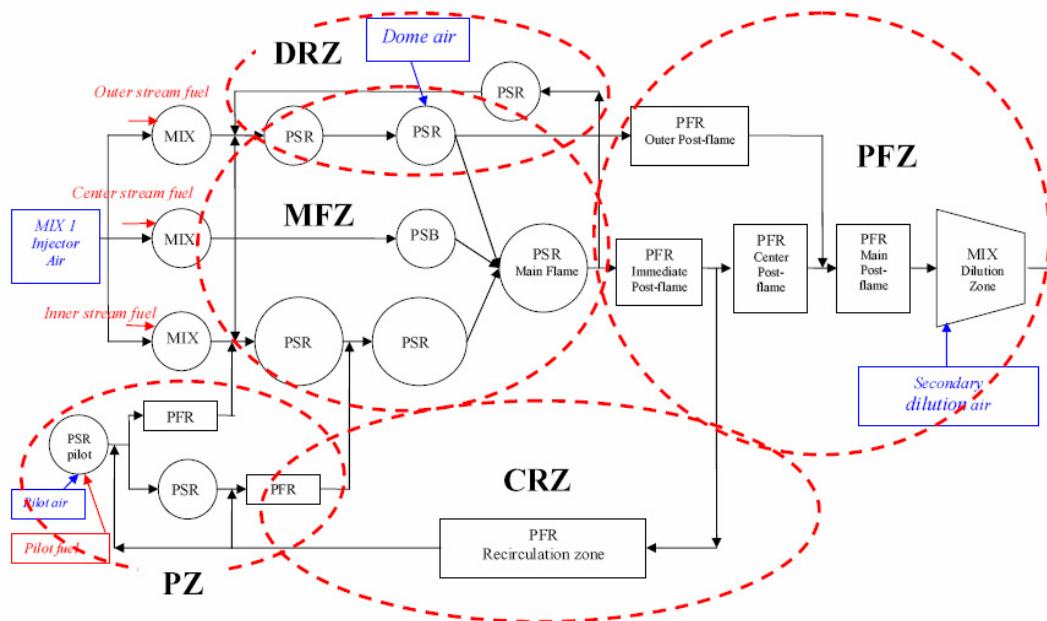
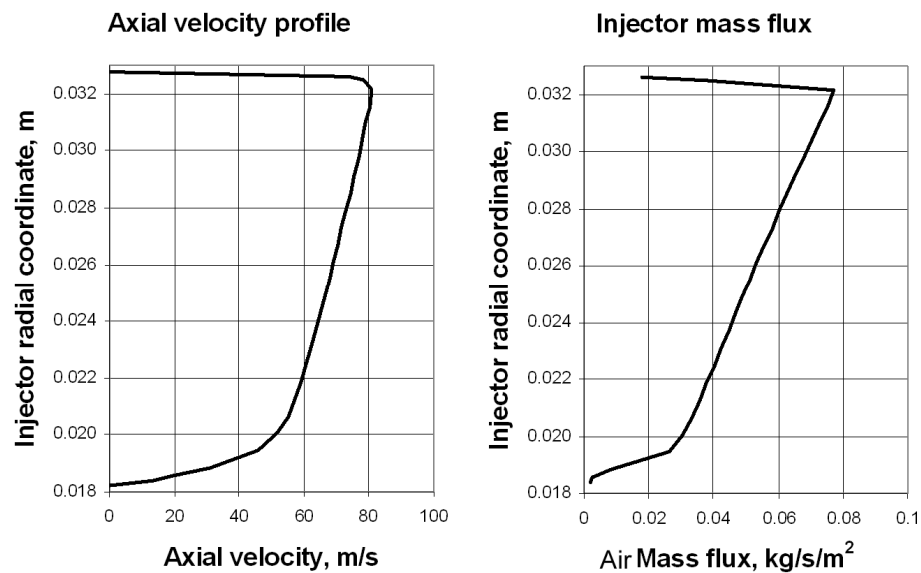


Figure 6-3. 31-element CRN for the single-injector, can-type, GT combustor.

Combustion is initiated in the center stream issuing from the injector and in the pilot stream by using PSR elements at the blow out condition (PSB). The inner and outer injector streams are ignited by entrainment of the hot gas from the recirculation zones. The flame is modeled using PSRs in series. The PFRs are added to complete the combustion allowing the carbon monoxide concentration to decrease and reach the local equilibrium value. The methodology of developing the CRN is discussed hereafter.

### ***Injector Modeling***

As seen in Chapter 5, the injector mass flow distribution and fuel-air rates profile can influence the formation of nitric oxide. Thus, one of the important tasks of the CRN development is to accurately represent the premixer air and fuel flow distribution in the injector outlet stream. The injector flow distribution is critical in determining the reaction zone structure. The velocity and mass flow profiles have been calculated in Chapter 5. Figure 6-4 shows the axial velocity at the injector outlet and the corresponding air mass flux.



**Figure 6-4. Axial velocity and air mass flux distribution at the injector outlet, repeat of Figure 5-2.**

The air and fuel flow rates of the injector are mapped into the CRN as three separate streams. This approach allows the treatment of variable velocities within the flame, as well as variable fuel-air ratios. The inner stream has the main recirculating and pilot gas mixing into it, while the outer stream is diluted by the dome air.

In the development of this CRN, the three streams are determined by the geometry of the injector. The height of each stream is taken as 1/3 of total injector height, see Equation 6-1.

$$h_{inner} = h_{center} = h_{outer} = 1/3 * (r_{inj,out} - r_{inj,inside}), \quad [6-1]$$

where:

$h_{inner}$	-	height corresponding to the inner stream
$h_{center}$	-	height corresponding to the center stream
$h_{outer}$	-	height corresponding to the outer stream
$r_{inj,out}$	-	injector outside radius
$r_{inj,inside}$	-	injector inside radius.

Figure 6-5 shows mapping of the injector mass flow rate and the fuel-air equivalence ratio for the premixer. The air mass flux profile is the same for all cases. The flat and linear injector fuel-air ratio profiles are shown on the figure. The flat profile has variable air flow rate as a function of injector radial coordinate, but the  $\Phi$  of the mixture stays the same (red line in the  $\Phi$  profile plot). In the case of the linear profile,  $\Phi$  changes as a function of the radial coordinate. Figure 6-6 shows the implementation of the flow division corresponding to these profiles in the CRN. The outer air stream includes 53% of the air flow due to the higher axial velocity in that region and larger

area associated with the larger radii, while the inner stream includes only 16% of the air flow. It is also apparent from the figure that when the linear injector profile is used, the fuel-air equivalence ratio of the outer stream is the lowest and that of the inner stream is the highest.

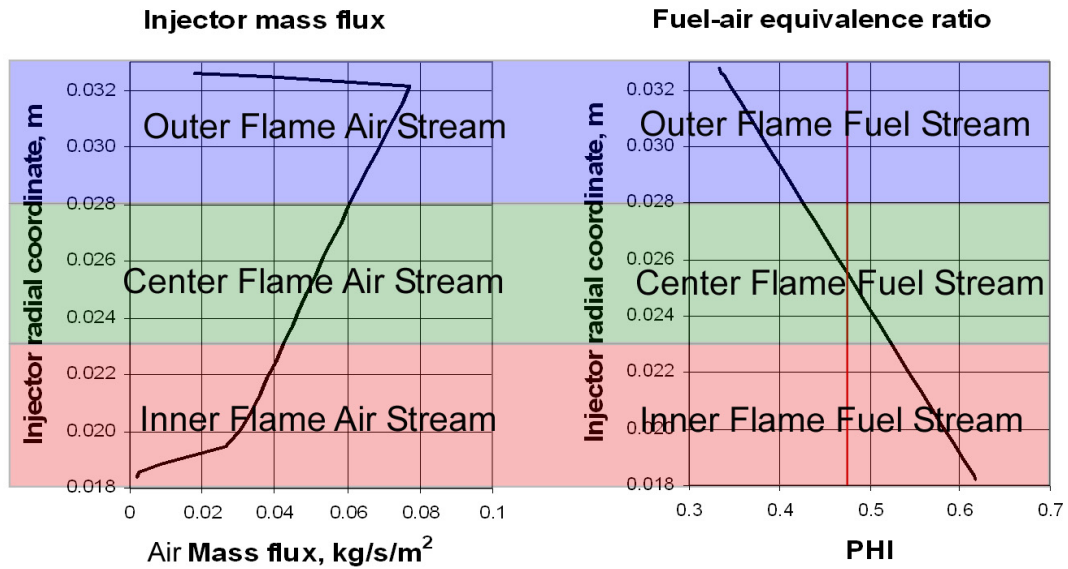


**Figure 6-5. Mapping of the air mass flow rates and the fuel air equivalence ratio onto CRN. Red line in the injector mixing profile plot corresponds to flat profile, black line corresponds to linear profile.**

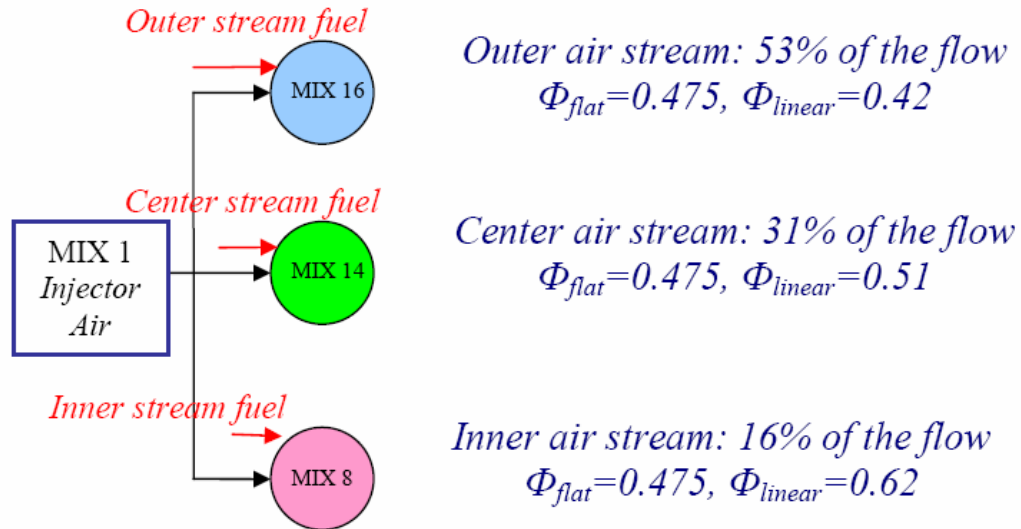


Figure 6-6. Injector flow splits for the can-type combustor CRN;  $\Phi_{flat}$  indicates the fuel-air equivalence ratio for the flat injector profile case;  $\Phi_{linear}$  indicates the fuel-air equivalence ratio for the linear injector mixing profile from Figure 6-5.

## Jet Cross Mixing

Cross-mixing between the streams is used to smooth out the fuel-air ratio as predicted by the CFD analysis. The fuel-air equivalence ratio in the overall stream and main flame becomes more uniform due to the effect of the turbulent mixing. The fuel-air equivalent ratio ( $\Phi$ ) field is calculated from the CFD results based on the C-H-O balance of the reactants and products in flow. The CFD calculated  $\Phi$  field is shown in Figure 6-7 for the case of the linear fuel-air rates profile in the injector. The effect of cross-mixing on the  $\Phi$  distribution between the streams is apparent. Adjusting the CRN  $\Phi$  profiles to match the contours obtained from the CFD modeling is achieved by introducing cross-stream mixing elements. Elements 11 and 18 in Figure 6-8 introduce the richer mixture to the outer stream and visa versa, the leaner mixture into the inner flame. This brings the fuel-air equivalence ratio of each

stream closer to the mean value. The  $\Phi$  of the center fuel-air stream is very close to the mean value to begin with, so adding and subtracting fuel or air to this stream would be meaningless. The flow splits between the elements are shown in Figure 6-8. The exchange rates in elements 11 and 18 are very close to each other.

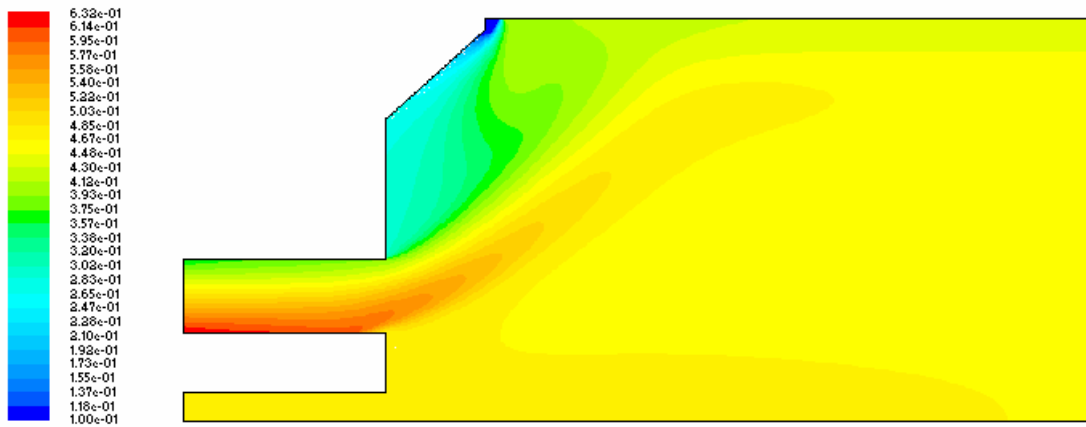


Figure 6-7. Relative  $\Phi$  distribution in can-type combustor with linear fuel-air ratio in injector, repeat of Figure 5-64.

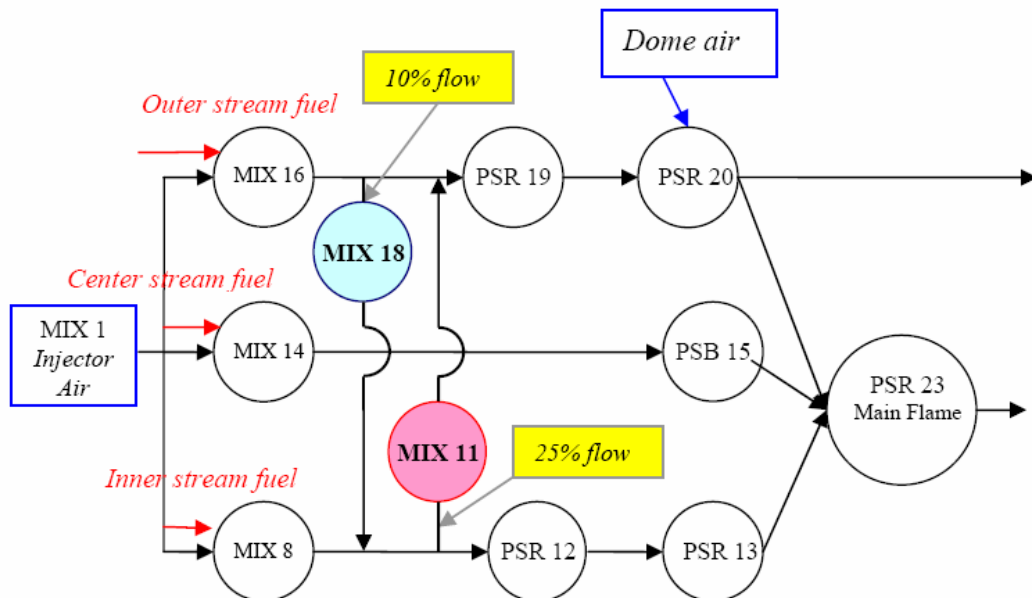


Figure 6-8. Cross-stream mixing sub-model in CRN.

## ***Flame Modeling***

### **Introduction**

In the early literature as discussed in Chapter 2, a single PSR was used to represent the flame. However, the use of several PSRs-in-series spreads out the flame, that is, it permits the flame to progress and produce intermediates and incomplete products of combustion, and then to consume these species and produce more heat as the final state of the combustion process is reached. Thus, a PSRs-in-series approach is used to model the flame in the CRN. Of interest in this regard is theory in the chemical reaction engineering text by Levenspiel (1972), which shows that the use of multiple PSRs-in-series yields a residence time distribution similar to that of a one dimensional chemical reactor with diffusion.

### **Main flame**

As shown above, the main flame is divided into three streams; each has a unique mass flow rate and fuel-air equivalence ratio. Each part of the flame is modeled as a series of PSRs. See Figure 6-9. The inner stream is ignited in PSR 12 due to entrainment of the hot gas from PFR 6. The flame propagates in the shear layer between the main recirculation zone and the fresh fuel-air mixture of the inner stream. More of the recirculation zone gas is added to PSR 13 representing entrainment of surrounding gas. The modeling approach is similar to the one used by Broadwell and Lutz (1998) in their two-stage Lagrangian model, see Chapter 2. The amount of entrained gas is calculated by taking a surface integral of the mass flux over the surface where the axial velocity equals zero.

$$\dot{m}_{entrained} = \int_{S, V_x=0} q''(S, V_x = 0) dS, V_x = 0, \quad [6-2]$$

where:

- $q''$  - mass flux  
 $S, V_x=0$  - surface with zero axial velocity

The example of such integration for Combustor A (Mellor, 1996) by Novosselov (2002) is shown in Figure 6-10. The solid line in the figure represents the injector flow (i.e. jet), while the dotted lines are the reverse flow rate in the recirculation zones. As the dashed lines end the recirculation flow becomes entrained in the main stream flow. The plot shows the increase of the main stream flow rate as a function of axial coordinate. The graph extends only to 0.22 m (about a half of the Combustor A length), since that is where the main recirculation zone ends. The size of the main recirculation zone of the modeled single-injector, can-type combustor is also about one half of the total length (see Fig. 6-1). Since the main recirculation zone size and geometry of the modeled combustor in this study is a scaled version of Combustor A, the overall percentages of flow in the recirculation zones are taken as those of the previous study.

The outer flame zone is modeled using a series of two PSRs. PSR 19 is ignited upon entraining some of the hot gas from the dome recirculation zone. The dome cooling air enters the outer flame zone in PSR 20, bringing the temperature of this element down.

The center flame zone is ignited in PSB 15. The volume of this element corresponds to a PSR at blowout residence time plus one percent. PSR 23 represents the main flame, where most of the flow from the flame PSRs is

mixed together and combustion is nearly completed. The residence time of this element is about 1ms. Some flow from the outer flame region bypasses the main flame zone and is directed to the near-wall post flame zone; this is discussed later in the post flame zone modeling section.

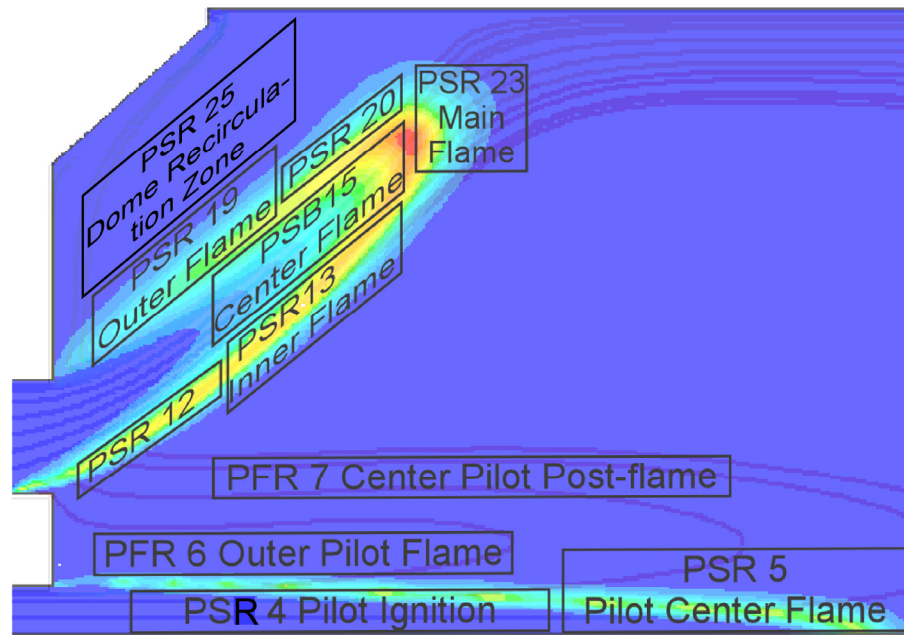


Figure 6-9. Flame zone mapping onto the CRN. Carbon monoxide mole fraction contours are shown. Maximum value is 1.58% by volume.

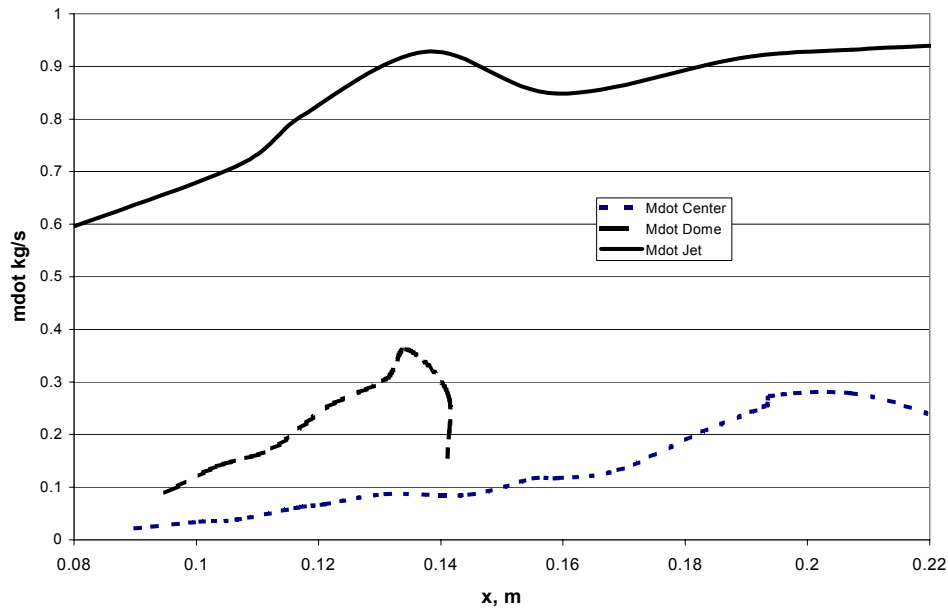
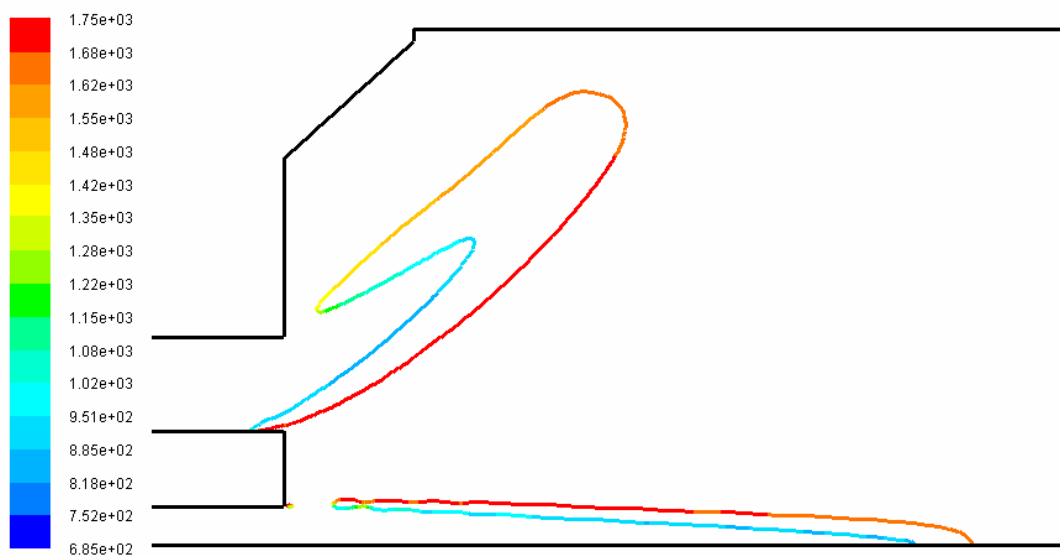


Figure 6-10. Flow rates in the center recirculation zone, dome recirculation zone, and the stream from the injector ("jet") for Combustor A (single-injector, can-type-type) operated with  $\Phi=0.49$ . The distance from the front of the combustor =  $x$ , (from Novosselov 2002).

## CRN Element Volume Considerations

The total main flame volume in the CFD simulation can be estimated by calculating the volume confined by iso-CO surfaces. For example, if the highest CO level in the flame is 1.5% by volume, one could define the iso-surface where CO is 0.3% (the value is 5% of the maximum CO concentration) as a reasonable limit to the main flame. This is shown in Figure 6-11.



**Figure 6-11. Iso-CO lines (CO=0.3%) colored by temperature, neutral pilot case with flat injector profile.**

Within the flame volume, the carbon monoxide is produced by the destruction of methane and is consumed by reaction with oxygen. Either rate can be controlled by the turbulent mixing or by chemical kinetics, depending on their respective rates. However, in the CRN model, the CO formation and consumption are kinetically controlled. Thus, if the CO formation and destruction in the combustor are actually controlled by the mixing rate, CO would be produced, reach its peak value, and be destructed slower -- in a larger volume.

In a situation where the chemical kinetic rates become the limiting rates, the flame zone volume CFD post-processing would be similar to the element volume in the CRN.

However, there are additional considerations. The combined volume of the flame PSRs used in the CRN is selected by considering the free radical concentrations in the elements. The first PSR of the series is normally associated with high free radical and CO concentrations, and if it is made too large, the free radical concentrations and CO decrease. The second PSR can involve the entrainment of outside gas (see PSR 13 and PSR 20). Generally, volumes of these flame PSRs are found to give best results if they are smaller than estimated by the CFD due to the absence of diffusion control reactions in the CRN as discussed above. The last element in the series (PSR 23) combines the three flame streams. This element does not have high free radical count or high CO level. The chemical reactions in this element are normally kinetically controlled due to the relatively uniform mixture (both temperature and species) and the size of the element can be estimated from the CFD simulation. The residence time in this element is about one millisecond.

### **Pilot Flame**

The air-fuel ratio of the pilot injector is assumed to be uniform; there is no radial or circumferential variability in the fuel-air mixture. As seen in the Figure 6-12, the pilot stream mixes with the gas of the main recirculation zone. The streamlines from the pilot stream penetrate the combustion chamber with very little interaction with the main stream. The additional recirculation zone (pilot recirculation zone) forms between the main flame and the pilot stream due to

the backward facing step at the pilot inlet into the combustor. Similar to the bluff body combustor, this recirculating gas ignites the pilot mixture.

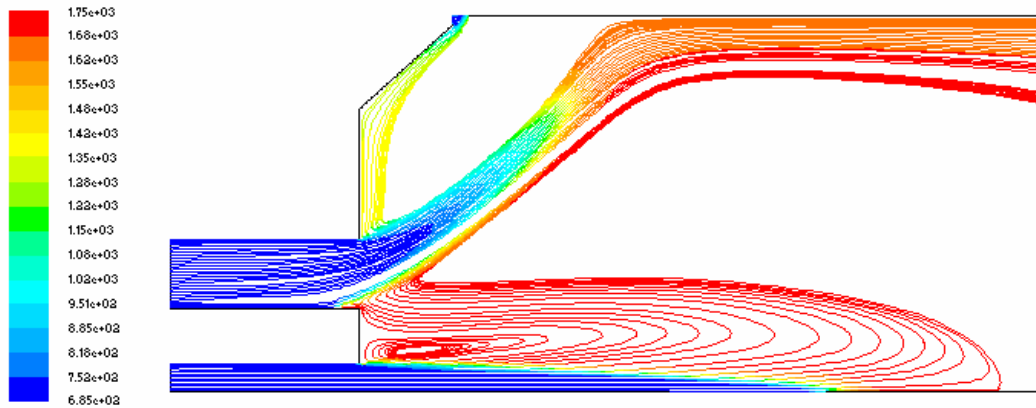


**Figure 6-12. Streamlines colored by temperature for flat injector mixing profile and neutral pilot, repeat of Figure 5-58.**

At a low fuel-air equivalence ratio of the pilot (below about 0.4), the pilot mixture cannot be ignited on its own. In this case the pilot fuel-air mixture mixes with the hot gas of the main recirculation zone where the pilot fuel becomes oxidized at the slow rate. For the cases with neutral or richer pilot, the fuel can be ignited by the pilot recirculation zone, forming a distinct flame sheet. Figures 6-13 and 6-14 show both: lean ( $\Phi=0.24$ ) and rich ( $\Phi=0.71$ ) pilot scenarios.

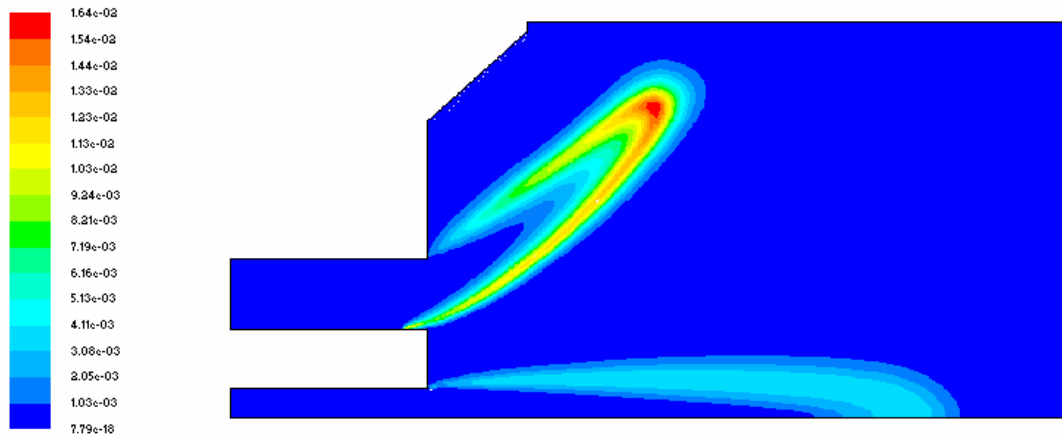


**Figure 6-13. Mole fraction of CO for the 50% pilot case (pilot  $\Phi$  is 0.24); maximum value is 0.016 kmolCO/kmol tot in the main flame zone. Low levels of CO indicate that well defined pilot flame does not exist. Repeat of Figure 5-30.**

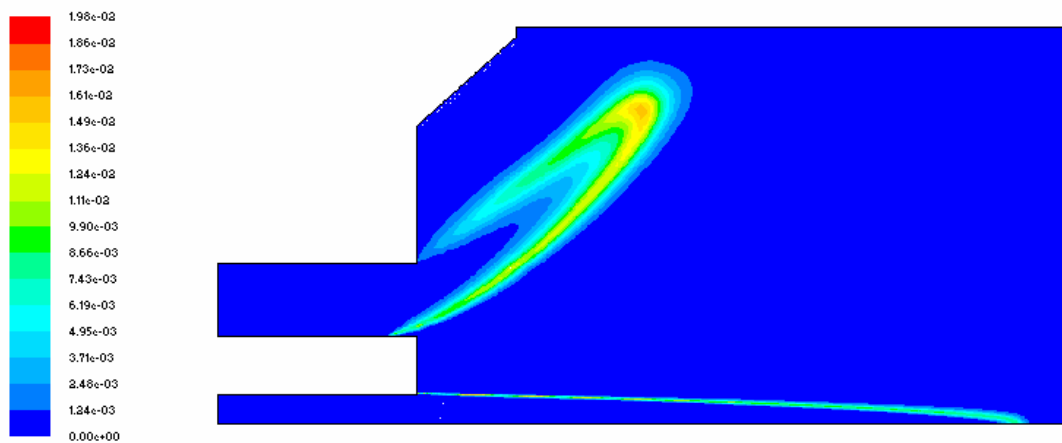


**Figure 6-14. Mole fraction of CO for the 150% pilot case (pilot  $\Phi$  is 0.71), maximum value is 0.02 kmolCO/kmol tot in the pilot flame zone, the value in the main flame zone is 0.015 kmolO<sub>2</sub>/kmol tot. Repeat of Figure 5-31.**

In the rich pilot cases, the pilot recirculation zone becomes hot and has a relatively long residence time of up to 25ms. Upon mixing with the main recirculation gas, the rich pilot increases the temperature of the main recirculation zone. The gas in this region can reach temperatures of 1900-2000K and also have long residence time (15-20ms). The combination of the hot pilot flame and the high main recirculation zone temperature trigger the

increase of all of the  $\text{NO}_x$  pathways and roughly double the  $\text{NO}_x$  emission compared to the neutral pilot case. See Figures 5-4 through 5-8.

In the CRN, the ignition of the pilot happens in PSR 4 before mixing with the recirculation zone gas. See Figures 6-15 and 6-16. This element represents a very thin inner surface of the pilot flame where the free radical concentration is high. The residence time in the element is about 0.5 millisecond. This is determined by matching the PSR temperature to the flame temperature from the CFD. In those cases for which the  $\Phi$  in element 4 is too low to ignite on its own, the element is modeled as a MIX element.

After PSR 4, the pilot stream is divided into the two parallel streams. See Figure 6-16. The first elements of each stream have the addition of the main recirculation zone gas that changes the fuel-air equivalence ratio. The pilot center stream (90 % of flow) represents the core of the stream that penetrates into the recirculation zone (to 1/3 of the combustor length). Then the flow turns around and follows the pattern of the main recirculation zone gas. This stream is modeled as PSR 5 followed by PFR 7. The outer stream (10% of flow) of the pilot flame and the pilot recirculation zone are modeled as a single PFR 6 with relatively long residence time (15-20ms).

The sizes of the PFR elements and flow splits in the pilot are found as follows:

- The sizes of the PFR elements are calculated based on the geometrical volumes (areas in 2D) that correspond to the flow patterns from the CFD model.

- The residence times in the elements are found from the CFD results by matching the gas residence time along the streamlines passing through the previously determined volumes.
- The CRN flow splits are found based on the flow rate through the volume of the PFR element. The flow splits may be adjusted to match the CFD  $\text{NO}_x$  prediction.

Figures 6-15 and 6-16 show the CFD predicted flow patterns and the CRN flow splits of the pilot model. As shown in Chapter 5, the  $\text{NO}_x$  levels stay nearly constant until the pilot  $\Phi$  becomes greater than the injector  $\Phi$ . The pilot modeling appears to be important in predicting the  $\text{NO}_x$  emissions for the higher than neutral cases. Figure 6-16 shows the CRN module that is activated when the temperature in the pilot zone is sufficient to form a relatively large amount of  $\text{NO}_x$ .

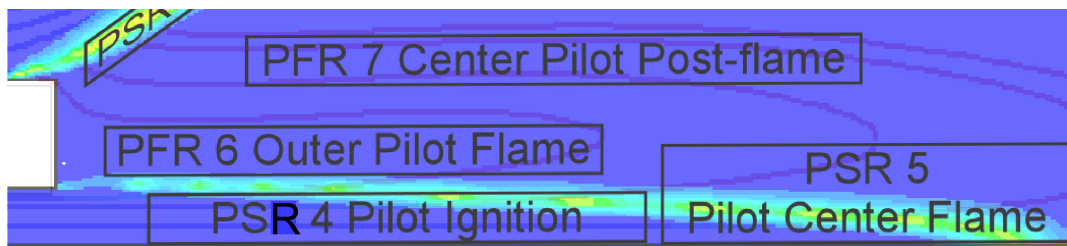


**Figure 6-15. Pilot flame zone mapping onto the CRN. Carbon monoxide mole fraction contours are shown. Maximum value is 1.5% by volume. Flat injector profile with 50% pilot case is shown.**

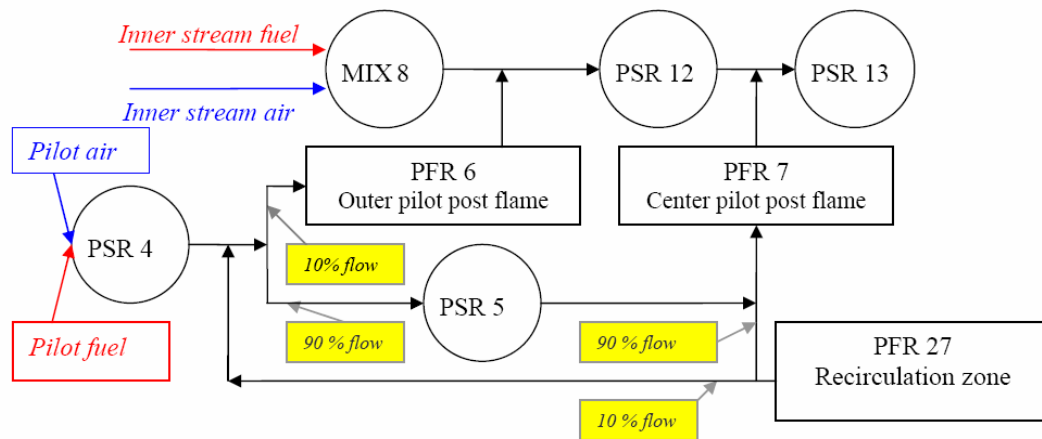
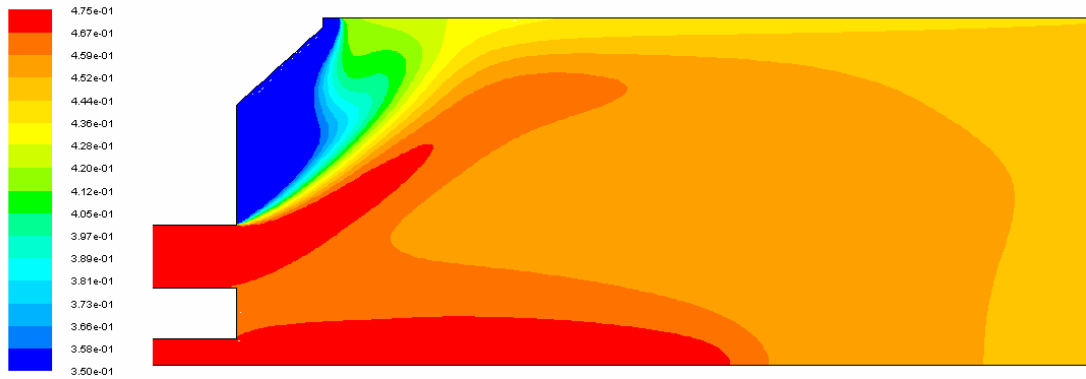


Figure 6-16. CRN flow split diagram for the pilot sub-model.

### Post Flame Zone Modeling

Figures 6-17 and 6-18 show that radial fuel-air equivalence ratio and temperature gradients exist in the post flame near the wall. The most obvious explanation for this is that a part of the dome cooling air does not mix with the main flame; this creates an additional dilution effect of the post-flame gases near the wall. This suggests the post-flame zone needs to be split in two streams. The flow split between the two streams (PSR 23 and PFR 21) is based on the CFD temperature and the fuel-air equivalence ratio in the near-wall post flame region and the center post flame zone. The streams are combined in PFR 30 where the local  $\Phi$  and temperature distribution is more uniform and not as critical for  $\text{NO}_x$  prediction. See Figures 6-19 and 6-20.

The typical backside cooled gas turbine combustor also has a dilution zone, where dilution air is introduced into the post-flame zone to reduce the gas temperature prior to entering the turbine. Though the can-type combustor CRN does not have any secondary dilution addition, element 31 could be used for this purpose.



**Figure 6-17.** Local fuel-air equivalence ratio in the can-type combustor, neutral pilot case with flat injector mixing profile is shown, maximum value is 0.475, blue - below 0.35.

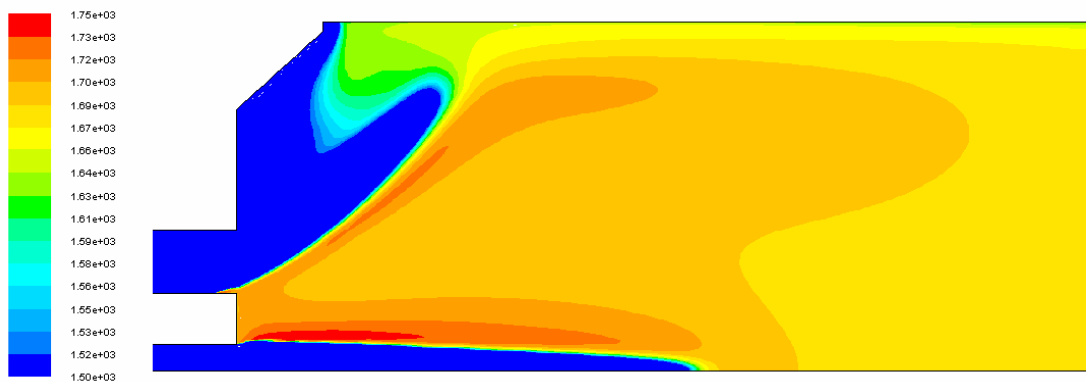


**Figure 6-18.** Temperature in the can-type combustor, the neutral pilot case with flat injector mixing profile case is shown, maximum value is 1750K, blue – below 1500K.

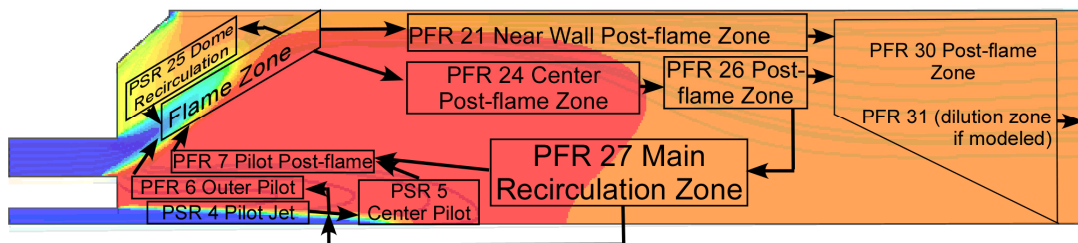


**Figure 6-19.** Flow field mapping onto the CRN for post flame and recirculation zones, temperature field for flat injector profile simulation is shown, neutral pilot.

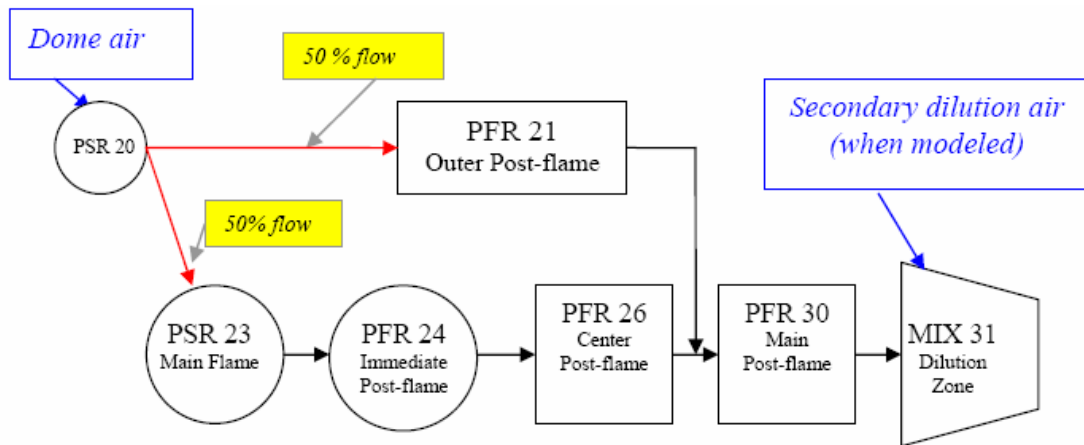


Figure 6-20. CRN post-flame zone sub-model.

## Recirculation Zones Modeling

### Main Recirculation Zone

The two major parameters of the recirculation zones that require modeling are: mass flow rate of the recirculation zone element and the gas temperature in the zone. Information about the flow rate and the temperature is obtained from the analysis of the CFD solution. The mass flow rate can be found by the integration over the zero axial velocity iso-surface (iso-line in 2D, Fig. 6-21). Figure 6-10, above, shows an example of such integration. Based on this figure, the main recirculation zone flow rate is about 20-25% of the main stream. The temperature of the main recirculation zone can be matched in the CRN by allowing some of the dome air to mix into the main flame and eventually enter the center recirculation zone.

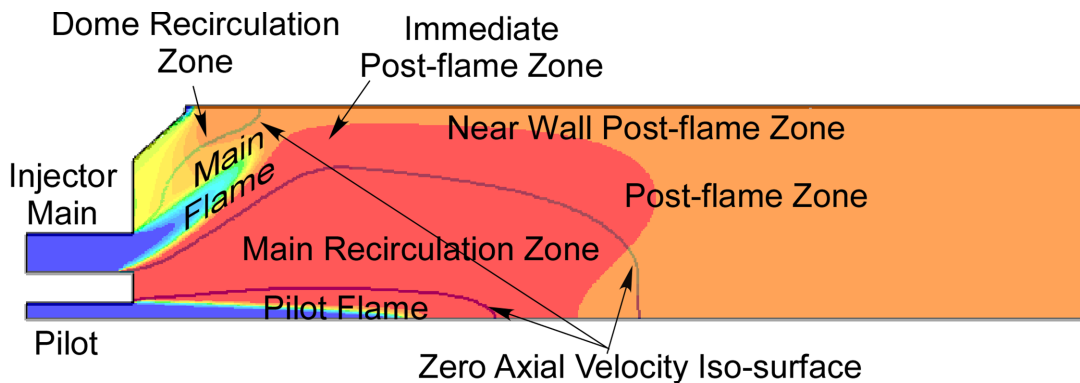


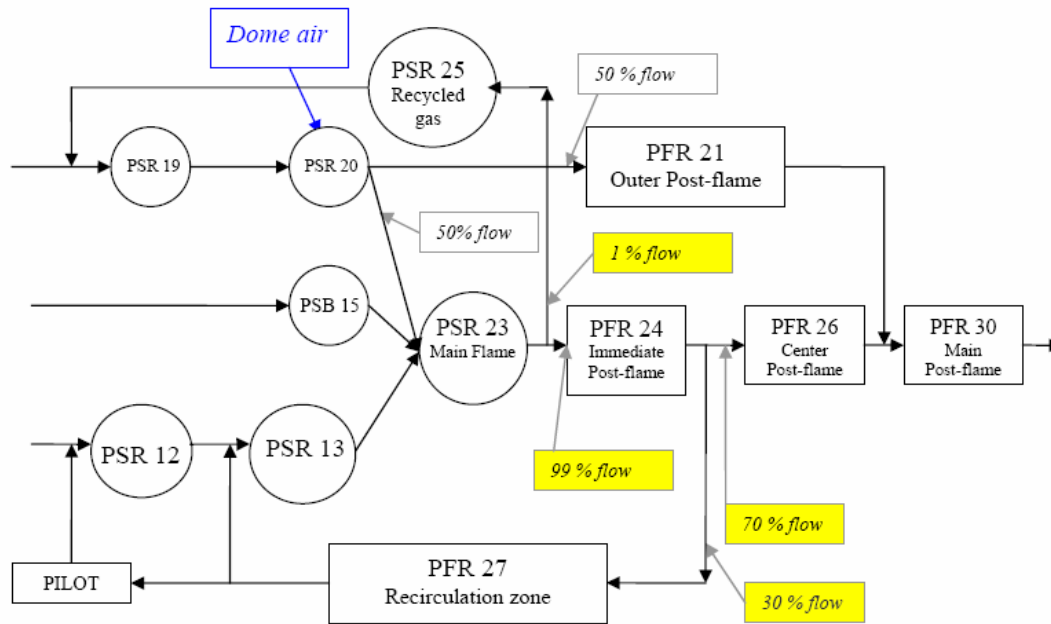
Figure 6-21. Recirculation region defined by  $V_x=0$  m/s iso-surface, repeat of the Figure 5-4.

Figure 6-22 shows the implementation of the recirculation zone sub-model. The combustion gases from the immediate post-flame zone enter the main recirculation zone driven by a pressure gradient created by a swirling of the premixer jet. Based on the CFD calculations, the gas in the recirculation zone has relatively slow velocity and low turbulent dissipation, which would argue for the use of the plug flow element in the recirculation zone modeling. The flow splits between elements PFR and PSR 23 are found by matching main recirculation zone temperature by allowing some of the dome cooling air to enter the recirculation zone.

### Dome Recirculation Zone

The dome recirculation zone brings additional air into the flame. The mixture from the outer stream mixes with the dome air and burns at the relatively low temperature due to the reduced fuel-air equivalence ratio in PSR 20. In the CFD modeling of the modeled combustor, it has been found that a very small amount of gas from the main flame (PSR 23) enters the dome recirculation zone. One percent of main flame gas has been assigned to be recycled into the dome recirculation zone (PSR 25). This percentage can change when a

different combustor setup is used. Figure 6-22 shows the recirculation zone flow splits in the CRN.



**Figure 6-22. CRN Recirculation flow splits for recirculation zone sub-model.**

Figure 6-23 shows the full CRN layout with all elements flow splits. The element numbers and the flow splits are shown on the figure. MIX elements denoted by a letter “M”, for example M1 stands for MIX1. Figure 6-24 shows the CRN diagram with node numbers; the flow splits are not shown to avoid clutter. The discussion about numbering approach is found in Appendix 1. The example of output of the 31- element CRN is found in Appendix 3.

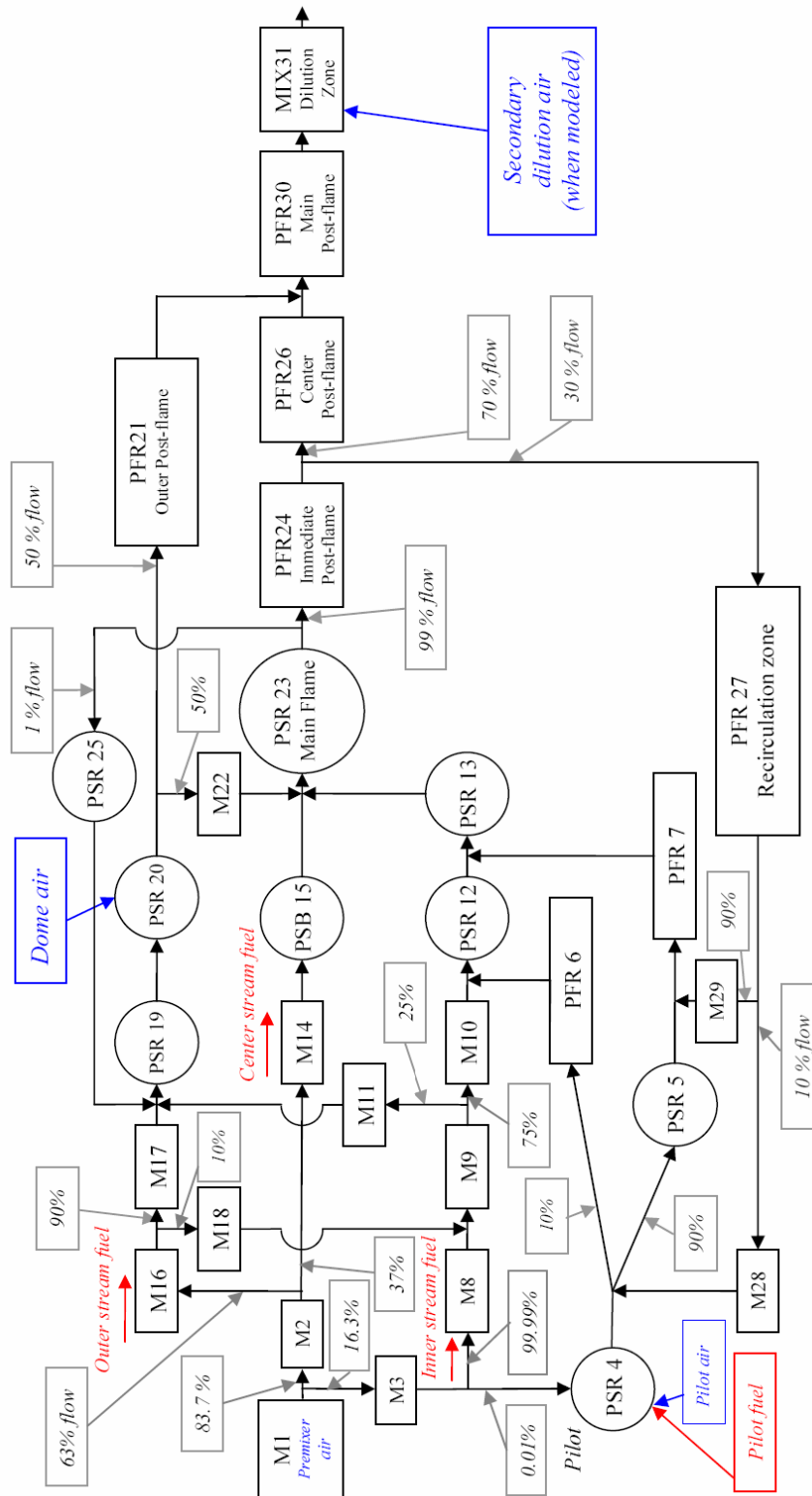


Figure 6-23. 31-element chemical reactor network for single-injector, can-type GT combustor.

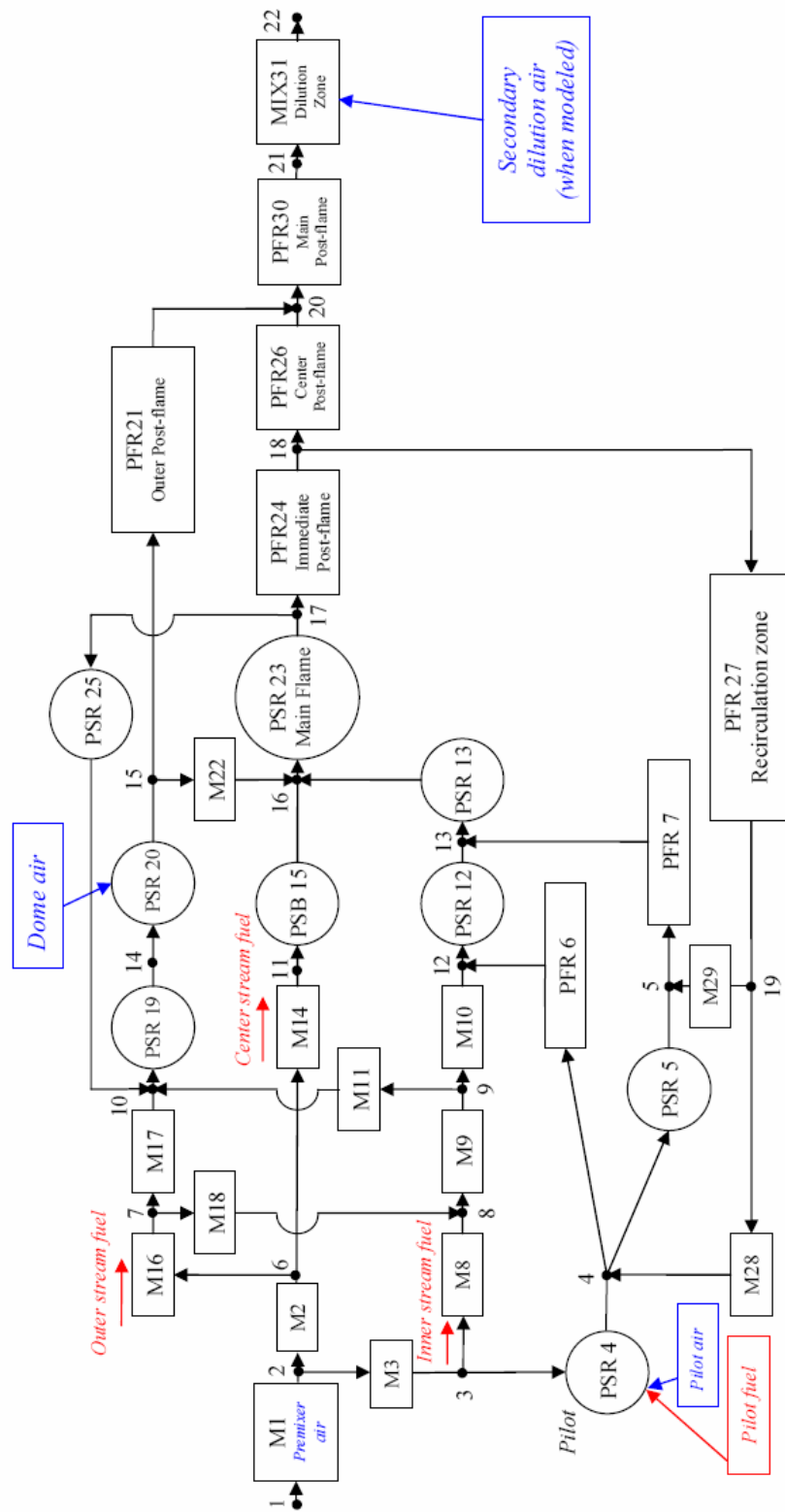


Figure 6-24. Nodal diagram of the 31-element chemical reactor network for single-injector, can-type GT combustor.

### ***Results of the Can-type Combustor CRN Modeling***

The 31-element CRN has been developed based on the CFD results for the can-type combustor. The fine tuning of the CRN flow splits and element sizes has been performed using the NO emissions predicted by the CFD for the combustor. All CRN calculations now shown are performed using the detailed chemical kinetic mechanism GRI 3.0. Methane diluted with 2.35% of nitrogen is used as the fuel in the CRN calculations; this is the same fuel as used in the CFD modeling in Chapter 5. Similar to the CFD modeling, uniform and linear fuel-air ratio injector profiles are considered. All operating and boundary conditions for the CRN model match those of the CFD runs for the respective cases; see Tables 5-1 and 5-4. The CO and the NO emissions are predicted using the CRN, and compared to the CFD results.

Carbon monoxide emissions for the uniform injector profile are shown in Table 6-1, and the emissions for the linear profile are shown in Table 6-2. The CO levels predicted by CFD and CRN are low in all cases, and represent the equilibrium CO concentrations in the post flame zone. Generally the CFD shows lower CO emissions than CRN. Although the difference in the emissions is less than 1ppmvd, there are two main reasons for it:

- The carbon monoxide in the CRN calculations is determined using the GRI3.0 mechanism for an assumed adiabatic combustor. In the case of the CFD calculation, the CO concentration is predicted by the eight-step global mechanism for the combustor outlet temperature, assuming heat loss through the combustor liner. This heat loss results in a lower combustor outlet temperature, and thus, in a lower CO level as CO attains local equilibrium. If the heat loss is assigned to the CRN post-flame zone, the outlet temperature

reaches that of the CFD solution, and the carbon monoxide levels become very close to the CFD results.

- The reaction rates of the eight-step global mechanism are tuned to the GRI 3.0 mechanism and are able to predict very close agreement over the range of the CO concentrations, temperatures, and fuel-air equivalence ratios. The global mechanism does not include free radicals, as does GRI 3.0, and thus its equilibrium CO concentration may be slightly off for some conditions. The difference between the global and GRI3.0 mechanisms for equivalent temperatures in this case is 0.2-0.3 ppmvd corrected to 15%O<sub>2</sub>.

**Table 6-1. Comparison of predicted carbon monoxide emissions between CFD and CRN models for single injector, can-type combustor with uniform injector fuel-air equivalence ratio.**

Pilot % of neutral	50	100	125	150
CO, ppmvd, 15% O <sub>2</sub> , CFD	0.96	0.93	0.93	0.93
CRN, ppmvd, 15% O <sub>2</sub> , adiabatic post-flame	1.77	1.79	1.78	1.81
CRN, ppmvd, 15% O <sub>2</sub> , at assigned post-flame temp	1.16	1.18	1.17	1.19

**Table 6-2. Comparison of predicted carbon monoxide emissions between CFD and CRN models for single injector, can-type combustor with linear injector fuel-air equivalence ratio.**

Pilot % of neutral	50	100	125	150
CO, ppmvd, 15% O <sub>2</sub> , CFD	0.80	0.93	1.04	1.04
CRN, ppmvd, 15% O <sub>2</sub> , adiabatic post-flame	1.53	1.74	1.93	2.06
CRN, ppmvd, 15% O <sub>2</sub> , with assigned post-flame temp	1.01	1.14	1.27	1.36

The nitrogen oxide emissions are predicted for both the flat and linear injector profiles. Overall, excellent agreement is obtained between the CRM and CFD calculated NO emissions. Figure 6-25 shows the comparison between the CFD and the 31-element CRN NO predictions for the uniform injector fuel-air

ratio profile as a function of the pilot fuel percentage. The emissions levels for the neutral and sub-neutral pilot cases are constant with respect to the pilot fuel rate. The NO level increases exponentially as the pilot fuel-air ratio increases producing high temperatures in the pilot flame. See Tables 5-3 and 5-7. The cases with the local pilot fuel-air equivalence ratio above 0.72 (above 150% pilot) are not considered because of the eight-step global mechanism limitation ( $\Phi=0.45-0.75$ ). The computations for the can-type combustor with linear injector profile are shown on Figure 6-26. Similar to the uniform injector profile, the pilot percentage range is 50-150 % of neutral pilot. The NO emission trend is different from the uniform injector profile case. There is a twenty percent nitrogen oxide emission increase from 50% to 100% pilot case. This is mainly due to the increased temperature in the inner part of the flame. While for the low pilot cases, the relatively rich inner flame zone becomes cooled by the leaner pilot mixture, as the pilot  $\Phi$  increases this effect diminishes. The absolute NO values for the linear injector profile cases are 20-40% higher than for the uniform profile; this is mainly due to the increase of local  $\Phi$  in the inner flame zone.

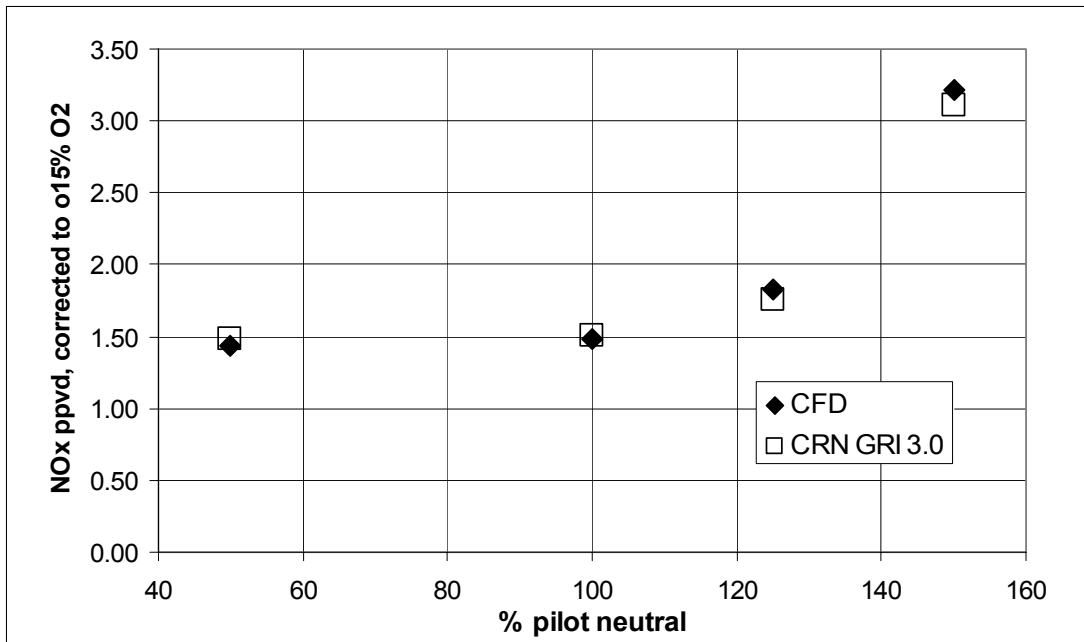


Figure 6-25. Comparison of predicted NO<sub>x</sub> emissions between CFD and CRN models for single injector, can-type combustor with uniform injector fuel-air equivalence ratio.

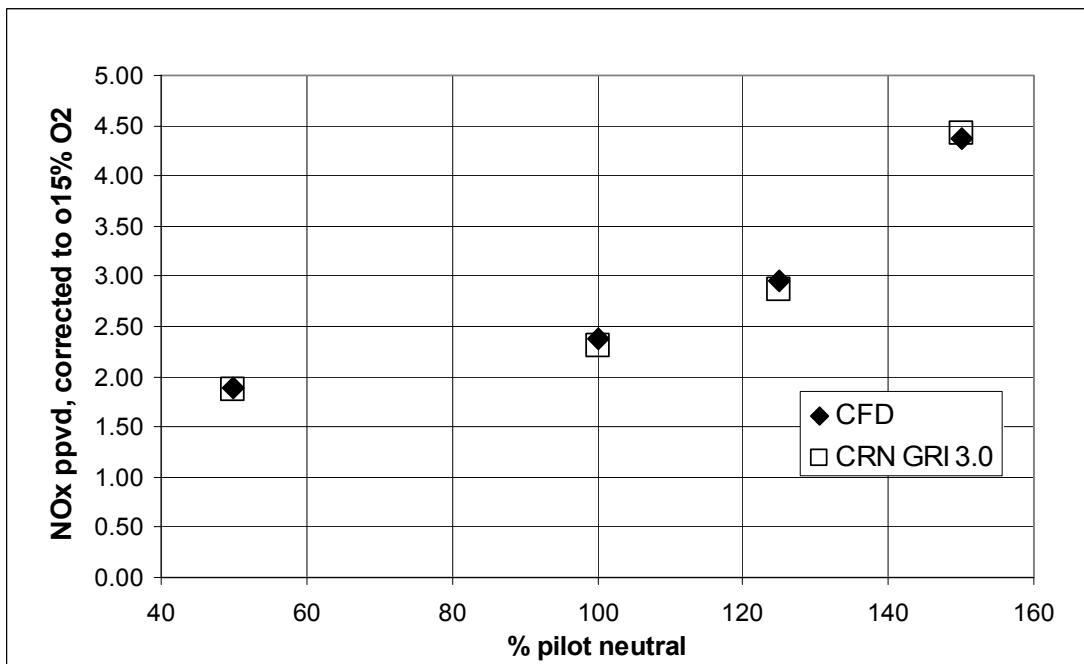


Figure 6-26. Comparison of predicted NO<sub>x</sub> emissions between CFD and CRN models for single injector, can-type combustor with linear injector fuel-air equivalence ratio.

It should be noted that the CRN modeling in this case does not include the added effect of turbulent fluctuations on the NO formation, since it is not a part of the steady state CFD solution. However, in the next chapter the CRN is applied to experimental industrial combustor, and the effect of turbulent fluctuations is included.

## **7. Application of CRN to Industrial Gas Turbine Combustor**

### ***Introduction***

In the previous chapter, the chemical reactor network model (CRN) was developed and applied to the generic, lean-premixed, single-injector, gas turbine combustor. Now in this chapter, the task is to adapt and apply the CRN to industrial, lean-premixed, multi-injector, gas turbine combustors for which engine test rig data are available. The data include the combustor liner geometry, boundary conditions for engine running conditions, and engine test rig emissions data. The data have been provided by the engine manufacturer; additionally the manufacturer has provided 3D CFD modeling results for one of the combustors. The manufacturer's data are shown herein normalized and non-dimensionalized.

Two engine test rig combustors are modeled using the CRN approach. The power output for the engines is in the 5-15 MWe range. The combustion systems are lean premixed and the flames are swirl stabilized. Annular augmented backside cooled (ABC) combustors are used. The premixing and swirl stabilization are provided by multiple fuel injectors in each case. Each injector consists of a "main" (i.e., premixer) and a "pilot" circuit. At equal fuel-air equivalence ratio, the pilot is said to be neutral. The emission results presented are normalized using the engine test rig data for natural gas fuel and neutral pilot.

The engine test rig is operated on natural gas at several low emission load conditions. The primary focus for this study is emissions prediction at full load

operating conditions. The two engine configurations are evaluated with one CRN layout:

1. Engine test rig combustor 1 with injector 1
2. Engine test rig combustor 2 with injector 2

Engine 2 is different from engine 1 in terms of power output, number of injectors, and flow rates for the injector, pilot, and cooling air. Additionally the design of the pilot in injector 2 is different from that of injector 1. While injector 2 has a relatively uniform fuel-air ratio profile at its outlet, injector 1 has a skewed profile with a higher fuel air equivalence ratio towards the inside of the injector. This is shown later in Figure 7-3.

As in the case with the generic, single-injector, can-type combustor, the University of Washington chemical reactor code is used in the CRN application. The CRN for the industrial combustor uses additional insight gained from 3D CFD modeling. The methodology for using CFD to guide the development of the CRN for lean-premixed gas turbine combustors has been discussed in Chapter 6. The number of reactor elements and layout of the CRN for the industrial annular gas turbine combustor are the same as in the generic can-type combustor. However, modifications are made to account for the differences in the flow and temperature fields.

The industrial gas turbine CRN considers the following effects, including those required for the generic can-type combustor, and those added for the industrial combustor (denoted *new*):

- Fuel-air distribution in the premixer/injector main circuit.

- Velocity profile in the premixer/injector main circuit.
- Entrainment of the main recirculation zone and dome recirculation zone gases into the main flame.
- Cross-flow turbulent mixing within the injector main circuit outlet stream and the resultant main flame.
- Interaction and mixing of the pilot gas with the main recirculation zone and the flame modeled.
- Mixing of gas from neighboring injectors/flames into the main flame (*new*).
- Temperatures, fuel-air ratios, and volumes of the main regions of the burning flow field.
- Fluctuations in flame temperature (*new*). [Although this would be required in general for any combustor, the development of the CRN for the generic, can-type combustor was based exclusively on the steady state CFD solution, and thus, the inclusion of the temperature fluctuation effect in that CRN was not appropriate.]

Figure 7-1 shows the CRN layout with the flow splits between the reactor elements. Some of the elements are changed from the can-type combustor CRN. PSB (i.e., PSR at incipient blowout) elements are eliminated from the network and recast as PSR elements. This is done because of an incompatibility between CHEMKIN and the UW chemical kinetic code, thereby allowing one to run the CRN in CHEMKIN. Some MIX elements are not shown on the figure in order to avoid clutter. The 31-element CRN is exercised for full load operating conditions with variable pilot fuel flows ranging from 35% to 180% of the neutral pilot.

Since both test rigs have more than one injector, the flames of the adjacent injectors can interact between each other. This interaction primarily happens in the region of the outer flame and dome recirculation region, and it is modeled as a part of the recirculation zone (PSR 25). All the reactor elements called out here are shown in Figure 6-24. The mixture in the outer part of the premixer stream/flame (PSR 19) mixes with gas from the neighboring injectors diluted by the dome cooling air. Since the CRN explicitly models only one injector, part of the main flame gas (PSR 23) represents mixture received or lost by the adjacent injector. This mixture is recycled through PSR 25 to the outer flame zone (PSR 19). The amount of gas entering PSR 25 is determined by the flow split between elements 24 and 25 and estimated based on the 3D CFD results for test rig combustor 1. This mechanism becomes important in the case of the lean outer flame zone as the hot gas from the neighboring injectors helps to ignite the outer flame.

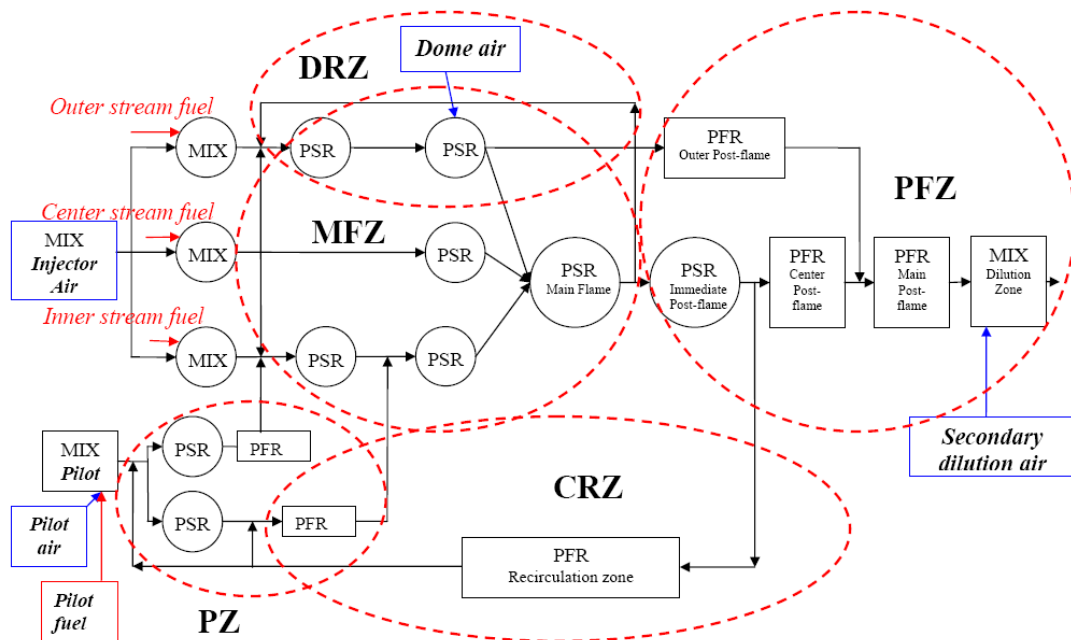


**Figure 7-1. 31-element CRN for evaluating the NO and CO emissions of engine test rig combustor.**

### ***Gas Turbine Combustor CFD***

The 3D CFD modeling of engine test rig combustor 1 has been performed by the manufacturer. In the CFD modeling of the test rig combustor, the manufacturer uses the commercial software package Star-CD version 3.24. A five million cell, sector geometry (i.e., one complete injector and sector of the annular combustor) with periodic boundary condition is used. The fuel used in the CFD modeling is methane diluted with 2.35% by volume of nitrogen, providing the same adiabatic equilibrium flame temperature as the actual natural gas used in the engine rig testing. Actual engine test rig pressure, temperature and flow rates are simulated. The k-epsilon turbulence closure model is used. Although the choice of the k-epsilon model for the high swirling flow application might not be fully appropriate, the simulation still offers valuable information about the flow field. The rate limiting, chemical kinetic versus eddy breakup rate approach as described in Chapter 4 is used in determining the reaction rates. The walls in the simulation are assumed adiabatic, so that heat transfer to the walls and from the walls is not modeled. This presents a difficulty in obtaining the correct temperature field at the injector outlet, resulting in the rate of methane destruction in the boundary layer at the injector outlet likely being over-predicted. The CFD simulation of the single-injector can-type combustor shows that the rate of methane destruction near the injector outlet is chemically controlled and low because of the wall cooling effect. That is, the wall temperature hinders the rate of the reaction in the boundary layer. This effect is not simulated in the 3D simulation. Fortunately the volume where this takes place is rather small, and thus, it does not severely effect the NO prediction. A representative CFD profile plot of the temperature field in the combustor is shown in Figure 7-2.

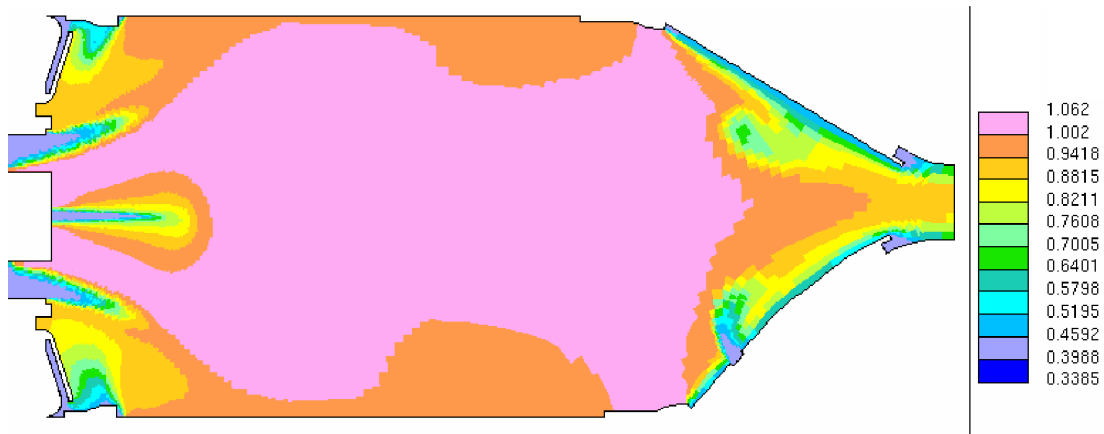


**Figure 7-2. Engine test rig combustor 1 configuration and typical CFD predicted temperature profile plot at full load condition. Temperature normalized by the adiabatic equilibrium temperature calculated for the mean fuel-air ratio of the premixer, from manufacturer**

### ***Effect of Temperature Fluctuations on NO Formation***

In order to incorporate the effect of temperature fluctuations on the NO formation into the industrial combustor CRN, the single-injector, can-type combustor CFD model of Chapter 5 is used. The combustor is modeled with Fluent 6.2, as discussed in Chapter 5, using the limiting reaction rate approach.

Nitrogen oxides emissions are calculated using the Fluent NO<sub>x</sub> post-processor chemistry in the time-averaged CFD simulation. Then, a joint fuel-temperature probability density function (PDF) is added to the model to predict NO<sub>x</sub> emissions. The turbulent fluctuation correction is calculated as a ratio of NO<sub>x</sub> PDF / NO<sub>x</sub> time averaged. This correction accounts for a 10-25 percent increase in NO formation depending on the fuel-air ratio. The higher value corresponds to leaner cases and to cases with low pilot fuel flow rates. In the cases where the combustor temperature is above 1800K, the effect of the temperature fluctuations on the nitrogen oxides formation diminishes due to

the increased contribution of post-flame thermal NO. The likelihood of temperature fluctuations is less in the post-flame zones than in the flame zones.

### ***Injector 1 Profiles***

If a radial and circumferentially uniform fuel-air ratio injector mixing profile is assumed, the predicted NO emissions are significantly lower than the engine test rig emission levels. It is clear that the degree of uniformity has significant impact on the NO emission output.

**Radial Profile:** The radial fuel-air ratio profile of the injector is mapped into the CRN as three separate streams with their unique values of mass flow and fuel mass fraction. This approach, as described in Chapter 6, allows for the existence of locally high fuel-air ratios (though lean) and variable velocities in the flame. Introduction of cross-mixing between the premixer outlet streams in the CRN model helps in maintaining the local flame temperatures in the range as predicted by the CFD modeling. The inner stream has the main recirculating gas mixing into it; while the outer stream is diluted by the dome cooling air and the hot gases from the neighboring injectors. Figure 7-3 shows the example of fuel-air ratio profile of the injector in engine test rig1.

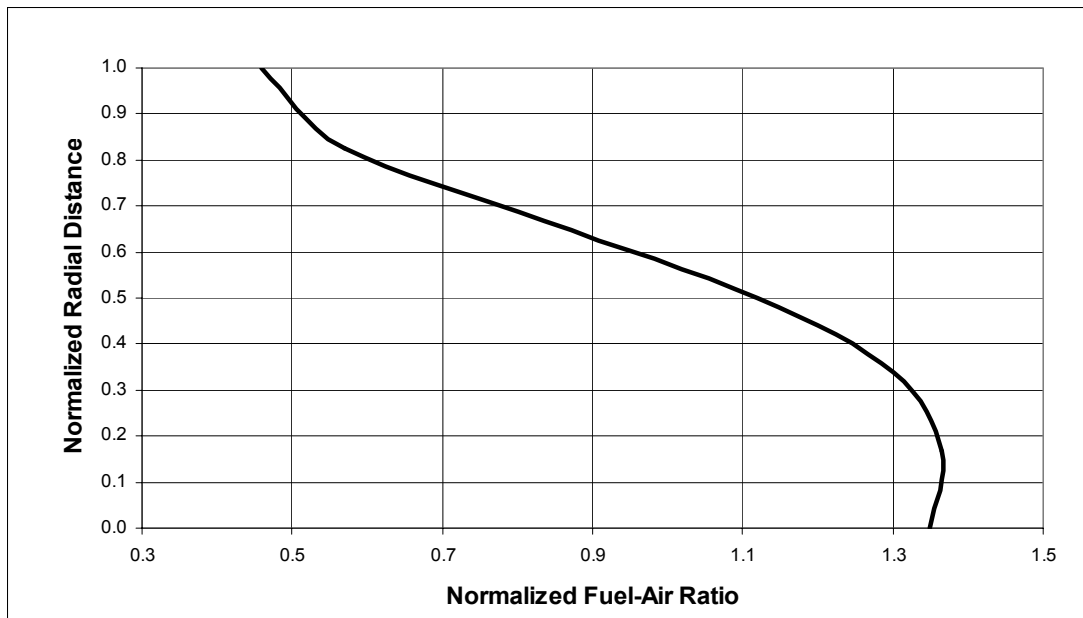


**Figure 7-3. Fuel-air ratio profile at the premixer outlet, i.e., main circuit of injector, for engine test rig 1. The fuel-air ratio is normalized by its mean value. The radial distance shown is the distance outward from the inner radius of premixer divided by the outer to inner radius difference, from manufacturer.**

**Circumferential Profile:** The injector also exhibits a circumferential variability in fuel-air ratio. In order to find the effect of the circumferential fuel-air variation, NO emissions are evaluated in the CRN for several radial profiles corresponding to the different angle positions (i.e., circumferential positions) of the injector. The NO predictions for the angular locations are divided by the mean value. This yields a correction factor that accounts for the circumferential non-uniformity of the fuel-air ratio. This correction is a function of the pilot fuel rate and is equal to a 10-20% increase of the NO predicted emission. The 10 percent correction corresponds to the high pilot cases, since in these cases the pilot flame produces relatively high levels of NO and the emissions are not affected as much by the circumferential injector non-uniformity. Table 7-1 shows the circumferential non-uniformity correction for the injector as a function of pilot percentage.

**Table 7-1. Correction of premixer circumferential fuel-air mixture non-uniformity on NO<sub>x</sub> prediction in CRN.**

Pilot % of neutral	50%	100%	180%
Circumferential correction for NO <sub>x</sub>	1.2	1.18	1.1

### ***Engine Test Rig Combustor 1 with Injector 1: CRN Predictions***

The full GRI 3.0 mechanism is used for CRN model development and validation. Figure 7-4 shows NO predictions with variable pilot and for natural gas as the fuel. The composition of the natural gas, consisting mainly of methane, with small amounts of ethane, propane, butane, carbon dioxide, and nitrogen, is modeled, except for the substitution of propane for the small amount of butane in the actual fuel. This is done because GRI 3.0 does not contain alkanes higher than C<sub>3</sub>. The NO emission results presented are normalized to the near neutral (95%) pilot NO and compared to the engine test rig data. Also shown in Figure 7-4 are calculated NO emissions based on the work of Leonard and Stegmaier (1994) (L&S). The higher L&S value represents a “no cross-mixing scenario” or worst case condition where the premixer flow is split into three distinct segments without any cross-mixing for an equivalence ratio/temperature smoothing effect. The calculated NO emission is performed for each stream separately and then weighted according to the mass flow for each stream. The L&S calculation is also performed for a uniform premixer leading to the lower L&S curve. The L&S curves do not include the pilot effect.

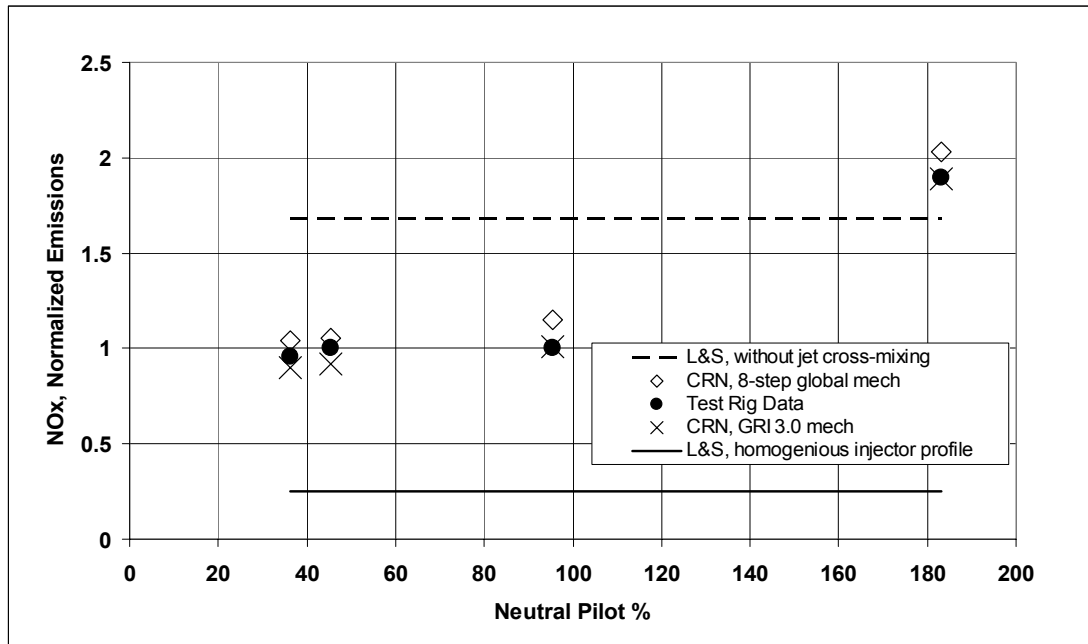


**Figure 7-4. Comparison of measured and predicted  $\text{NO}_x$  emissions for engine test rig1 with injector 1.**

As can be seen in Figure 7-4, very close agreement is obtained between the CRN predictions and the engine test rig NO data. The engine test rig I data and the CRN predictions of nitrogen oxides emissions fall in between the two Leonard and Stegmaier curves showing both the impact of radial fuel-air non-uniformities and the cross stream mixing. While the radial profile of the fuel-air ratio creates the local zones in the combustor, and thus, keeps the NO levels above the lower L&S line, the cross-stream mixing prevents the NO emission from rising above to higher L&S curve. The rise of nitrogen oxides emissions at the high pilot case is attributed to the increase of the local temperature in the pilot flame and consequently to the increase of No formation rate in pilot (see Tables 7-3 and 7-4 discussed below). The calculations for the sub-neutral pilot agree with the engine test rig data and do not show any significant change in the No emissions with respect of the pilot fuel flow rate. The high pilot case also shows good CRN to measurements agreement.

The full GRI 3.0 mechanism is used for model development and validation. A companion set of calculations is performed using the UW eight-step global mechanism. The results obtained with the UW eight-step global mechanism in the CRN generally show an increase of about 5-10% in NO emission when compared with the full GRI 3.0 mechanism. The CRN computations using the global mechanism predict temperatures in the flame zone that are slightly higher (by 3-8 degrees C) than in GRI 3.0. This difference occurs because of the lack of endothermic reactions that produce radical species in the flame, and explains the greater NO. Post-flame temperatures for both mechanisms are the same. This agreement gives further validation of the eight-step global mechanism for lean-premixed GT combustion.

The CRN modeled CO emissions stay relatively flat for all of the modeled cases (see Table 7-2). This agrees with the experimental data as well. The predicted CO emissions for both the eight-step global mechanism and full GRI 3.0 are about 2 ppm. The level of CO is at the chemical equilibrium condition before the injection of the secondary cooling air into the combustor. The secondary air tends to freeze the CO. Engine test rig carbon monoxide measurements are within a few parts per million of the predicted emissions. The difference between the measured and predicted values is small and can be attributed to lack of measurement instrument resolution or to a slight CO wall quenching effect in the test rig, which is not modeled in this CRN.

**Table 7-2. CO predictions in the CRN.**

Pilot Level	35%	45%	95%	185%
GRI 3.0, CO ppmvd, 15%O <sub>2</sub>	1.79	1.83	1.82	1.84
Eight-Step Global CO ppmvd, 15%O <sub>2</sub>	1.93	1.99	1.97	1.99

### ***NO Formation Mechanisms and Zones of Formation***

CRN modeling helps to understand the zones and pathways that contribute to the NO emissions in the gas turbine combustor. Both zonal and mechanism pathway contributions may change with modifications to the combustion liner and injector setups or boundary conditions (such as fuel-air equivalence ratio, pressure and load).

Table 7-3 shows relative contributions of different NO formation mechanisms for the modeled combustor (i.e., using the NO chemistry from GRI3.0). The cases with the pilot at less than neutral (not listed) are very similar to the neutral pilot case. The different NO formation pathways have been discussed in Chapter 3.

The five pathways are:

1. Fenimore prompt NO
2. NO formed from NNH chemistry
3. NO formed from the  $N_2O$  pathway
4. NO formed from the Zeldovich chemistry influenced by super-equilibrium O-atom (flame Zeldovich)
5. NO formed from the Zeldovich chemistry influenced by equilibrium O-atom (thermal Zeldovich)

Prompt and NNH nitrogen oxide form in the early part of the flame and then their rates fall off quickly as the flame continues to completion. The  $N_2O$  and flame Zeldovich routes are very active in the heart of the flame and persist into the near post-flame zone. Thermal Zeldovich is primarily a post-flame zone effect. Table 7-4 shows the contributions of the different combustion zones to the NO emissions. At the neutral pilot, the main flame zone is the

greatest contributor to the NO production, while pilot flame production accounts only for 2 percent of total NO. At the high pilot case, the NO production shifts to the pilot flame region due to the increased temperature of the pilot flame.

**Table 7-3. NO Formation Pathways.**

Pilot Level	Prompt	NNH	N <sub>2</sub> O	Flame Zeldovich	Thermal Zeldovich
Neutral Pilot	8%	4%	45%	19%	25%
High Pilot	5%	2%	33%	18%	42%

**Table 7-4. NO Formation Zones.**

Pilot Level	Main flame	Pilot flame	Recirculation zone	Post flame
Neutral pilot	72%	2%	9%	17%
High pilot	37%	46%	6%	11%

### ***Engine Test Rig 2 with Injector 2: CRN***

The lay out of the engine test rig combustor 2 with injector 2 is similar to that engine test rig 1. The main difference is the uniform fuel-air ratio at the outlets of the main circuits of the injectors. Additionally, the number of injectors is reduced and the pilot circuit set up is modified. There are a number of fuels used in engine test rig 2 and in the CRN model for this engine; however, the only fuel considered in this chapter is natural gas. The CRN predictions are corrected for turbulent fluctuation and circumferential profile non-uniformity as described in the engine test rig 1 case. The circumferential fuel-air ratio injector distribution has been provided by the gas turbine manufacturer.

The CFD simulation for engine test rig 2 has not been performed, thus the CFD computed flow, temperature, and species fields cannot be used as a guide for the CRN development. The CRN for the engine test rig 2 is a scaled version of the CRN for engine test rig 1. The scaling is performed by adjusting the volumes of the reactor elements in the CRN model to match the velocities and mean gas residence times predicted by CFD for engine test rig 1 using the boundary conditions of engine test rig 2. The flow splits between the elements are not varied from the engine test rig 1 CRN.

The pilot circuit of injector 2 has a different configuration from injector 1. This presents a difficulty in modeling the pilot flame, because of the different flow rates and the fuel-air distribution in the pilot. This discrepancy is most noticeable for pilot percentages near and greater than neutral. In injector 2, a hot region is produced within the pilot flame, which leads to relatively large NO formation. For the cases when the pilot flame is not a large contributor to overall nitrogen oxide formation, the scaling approach to the CRN works rather well.

Figure 7-5 shows the comparison between the NO emissions for engine test rig 2 with injector 2 and the 31-element CRN. The NO emissions are normalized to the engine test rig NO emissions at 104% of neutral pilot. Figure 7-5 also shows the Leonard and Stegmaier (1994) calculations for the primary flame zone fuel-air equivalence ratio. Overall, good agreement between CRN, engine test rig data, and L&S calculations is reached for the cases of 70% of neutral pilot and below. Because of the flatness of the premixer fuel-air ratio profile the L&S prediction falls close to the data and CRN prediction.

As pointed out, the injector 2 pilot is different from that of injector 1. Because of the different characteristics of this pilot flame, the NO emissions near and greater than neutral pilot are rather high when compared to the low pilot cases. This pilot behavior could be modeled by the CRN approach; however, first additional CFD modeling of the pilot flame would be required.

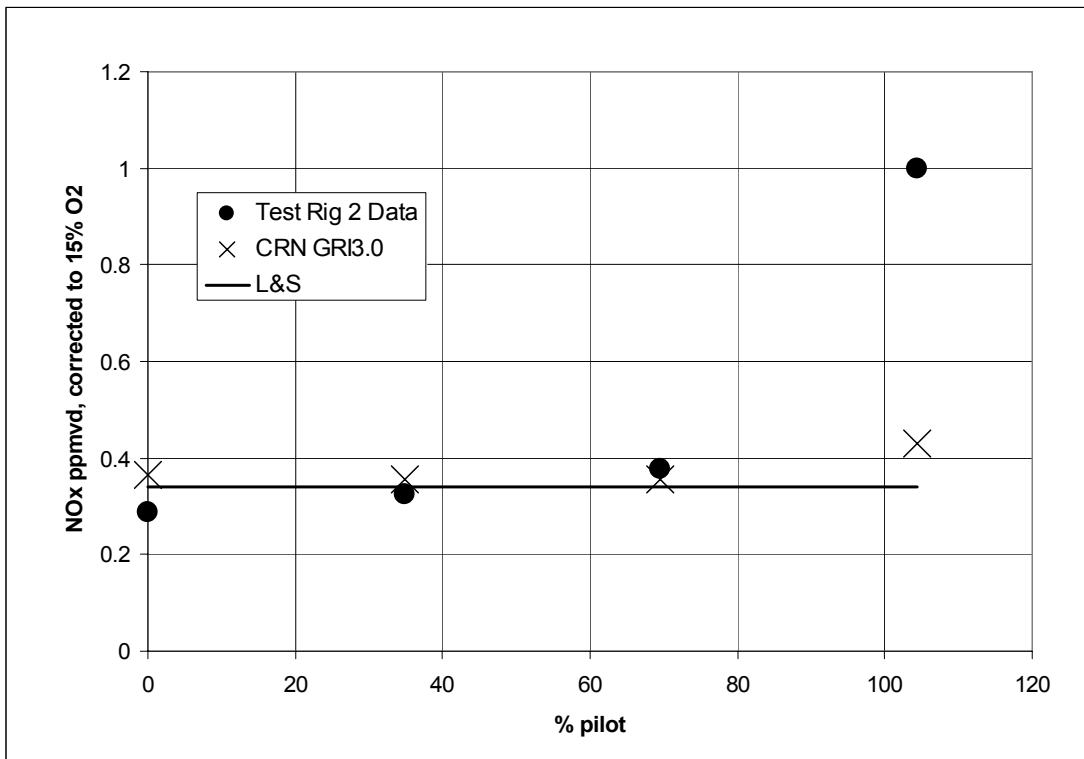


**Figure 7-5. Comparison of measured and predicted NO emissions for engine test rig combustor 2 with injector 2.**

***Conclusion***

Notwithstanding the rich pilot case for test rig 2; the CRN shows very good capability for prediction the NO, and CO emission of the lean-premixed industrial GT combustors.

## 8. Modeling the Combustion of Hydrocarbon Fuel Blends

The 31-element CRN model can handle mixtures of gaseous and prevaporized hydrocarbon fuels, assuming that the appropriate chemical kinetic mechanism is available. The GRI 3.0 mechanism and the eight-step global mechanism are used herein for modeling the combustion of fuel blends. This modeling is performed for both the generic single-injector, can-type combustor and the industrial annular combustor (i.e., engine test rig combustor 2 with injector 2). The CRN model of the can-type combustor is compared with the CFD results for various fuel blends. The CRN modeling results for engine test rig 2 are compared with test rig emissions data.

### ***Hydrocarbon Fuel Blends Combustion in Can-type Combustor***

#### **CFD modeling**

CFD calculations are performed for the can-type combustor for three different fuel blends in addition to methane combustion. The detailed description of the computational domain and boundary conditions is provided in Chapter 5. A uniform injector fuel-air ratio profile is used for simulations of the blended fuel combustion. Propane is chosen as a second component in the mixture stream mainly because of two reasons:

1. Global chemical rate data for propane oxidation are available in the literature (Westbrook and Dryer, 1981).
2. Propane chemical kinetic rate data are incorporated in the GRI 3.0 mechanism. Although the  $C_3$  chemistry in GRI 3.0 is limited and does not comprise a full propane mechanism, the modeling of data from a

laboratory jet stirred reactor fired on propane has shown good agreement with the experimental data, see Appendix 4.

Propane volumetric percentage in the fuel blend is varied from 20 to 70%. Table 8-1 shows the fuels used in the modeling. The overall fuel flow rates are adjusted to achieve the same combustor exit temperature as in the methane combustion cases.

**Table 8-1. Fuel composition for the hydrocarbon blends used in modeling.**

	Methane %	Propane %	C/H ratio
Blend 1	80	20	0.275
Blend 2	60	40	0.300
Blend 3	30	70	0.338

As in the CFD modeling of methane combustion, the limiting chemical kinetic/turbulent mixing reaction rate approach is used for the fuel blends. Additionally, the chemical kinetic rates of methane and CO oxidation as well as the CO<sub>2</sub> dissociation rate are taken from the eight-step global mechanism. The global kinetic rate of propane oxidation ( $\text{C}_3\text{H}_8 + 3.5\text{O}_2 \Rightarrow 3\text{CO} + 4\text{H}_2\text{O}$ ) of Westbrook and Dryer (1981) is used in the modeling:

$$d[\text{C}_3\text{H}_8]/dt = -8.6\text{e}+11 [\text{C}_3\text{H}_8]^{0.1} [\text{O}_2]^{1.65} \exp(-15098/T),$$

where the units are: gmol/cm<sup>3</sup>, K, and seconds.

Table 8-2, containing Figures 8-1 through 8-24, shows the comparison between the CFD results for methane and blend 3. As seen in the figures, the addition of propane to the fuel increases the carbon monoxide concentration in the flame due to the higher C/H ratio of the fuel – see Figures 8-9 and 8-10. Additionally, as propane is added, the flame becomes shorter because of

increased heat release in the early part of the flame. The flame brush also appears thicker than for the methane combustion. Since the combustor outlet temperature for both cases is the same, the chemical energy entering the premixer is the same. The thin flame in the methane case implies that the chemical energy is released into the smaller volume, which corresponds to the creation of the higher local temperature. On the other hand, presence of the greater concentration of carbon monoxide (substitute for free radicals) in the blended case increases the volume of heat release, enabling heat transfer from the flame area. These factors determine the local temperature. Due to the thicker flame, the flame temperature in the blended fuel case is about 10K lower than in the methane combustion.

This has dual effects on the NO formation in the flame. While the greater peak flame temperature creates regions with higher NO formation rate due to the exponential temperature dependency in the rate, the thicker flame leads to a larger volume where the flame NO formation chemistry is active. Figures 8-14 and 8-15 show the NO concentrations for the two respective cases. The propane fuel blend has slightly higher peak NO. Figures 8-16 through 8-19 show the CFD contour plots with flame NO formation rates.

Table 8-2.CFD simulation of methane and blend 3 (30%CH<sub>4</sub>, 70%C<sub>3</sub>H<sub>8</sub>) combustion in the single-injector, can-type combustor with uniform injector fuel-air ratio and neutral pilot.

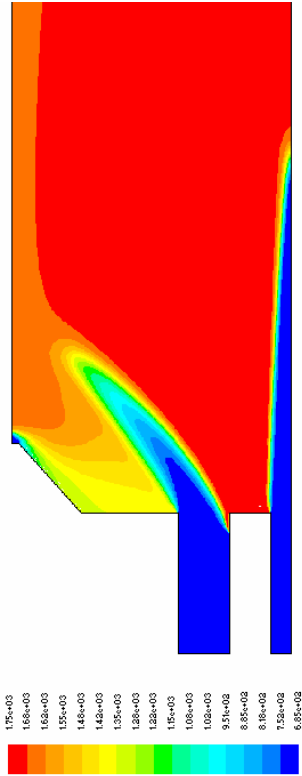
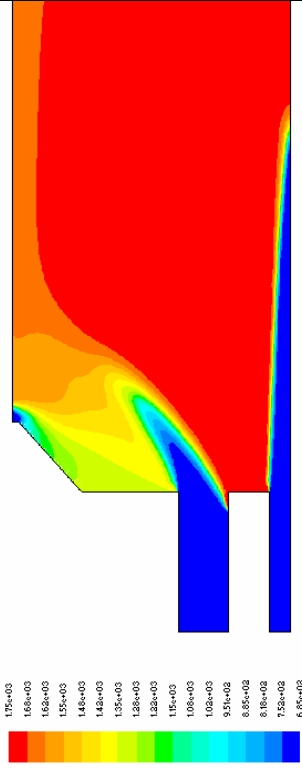
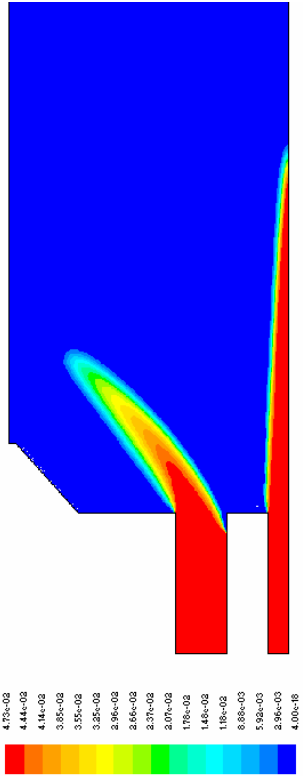
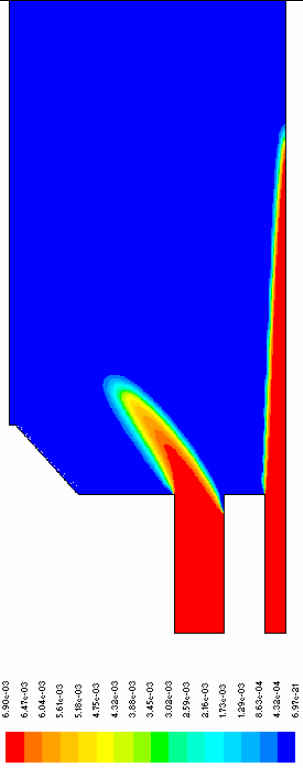
<p>Methane combustion, uniform injector mixing profile, neutral pilot case</p>  <p>Figure 8-1. Temperature contour plot for methane combustion, max. value is 1750 K, the first half of the combustor is shown, repeat of Figure 5-53.</p>	<p>Blend 3 (30%CH<sub>4</sub>, 70%C<sub>3</sub>H<sub>8</sub>) combustion, uniform injector mixing profile, neutral pilot case</p>  <p>Figure 8-2. Temperature contour plot for combustion of blend 3, max. value is 1740 K, the first half of the combustor is shown.</p>
 <p>Figure 8-3. Mole fraction of CH<sub>4</sub> for methane combustion (first half of the combustor), maximum value is 0.0473 kmolCH<sub>4</sub>/kmol total, repeat of Figure 5-69.</p>	 <p>Figure 8-4. Mole fraction of CH<sub>4</sub> for combustion of blend 3 (first half of the combustor), maximum value is 0.007 kmolCH<sub>4</sub>/kmol total.</p>

Table 8-2 (continued)

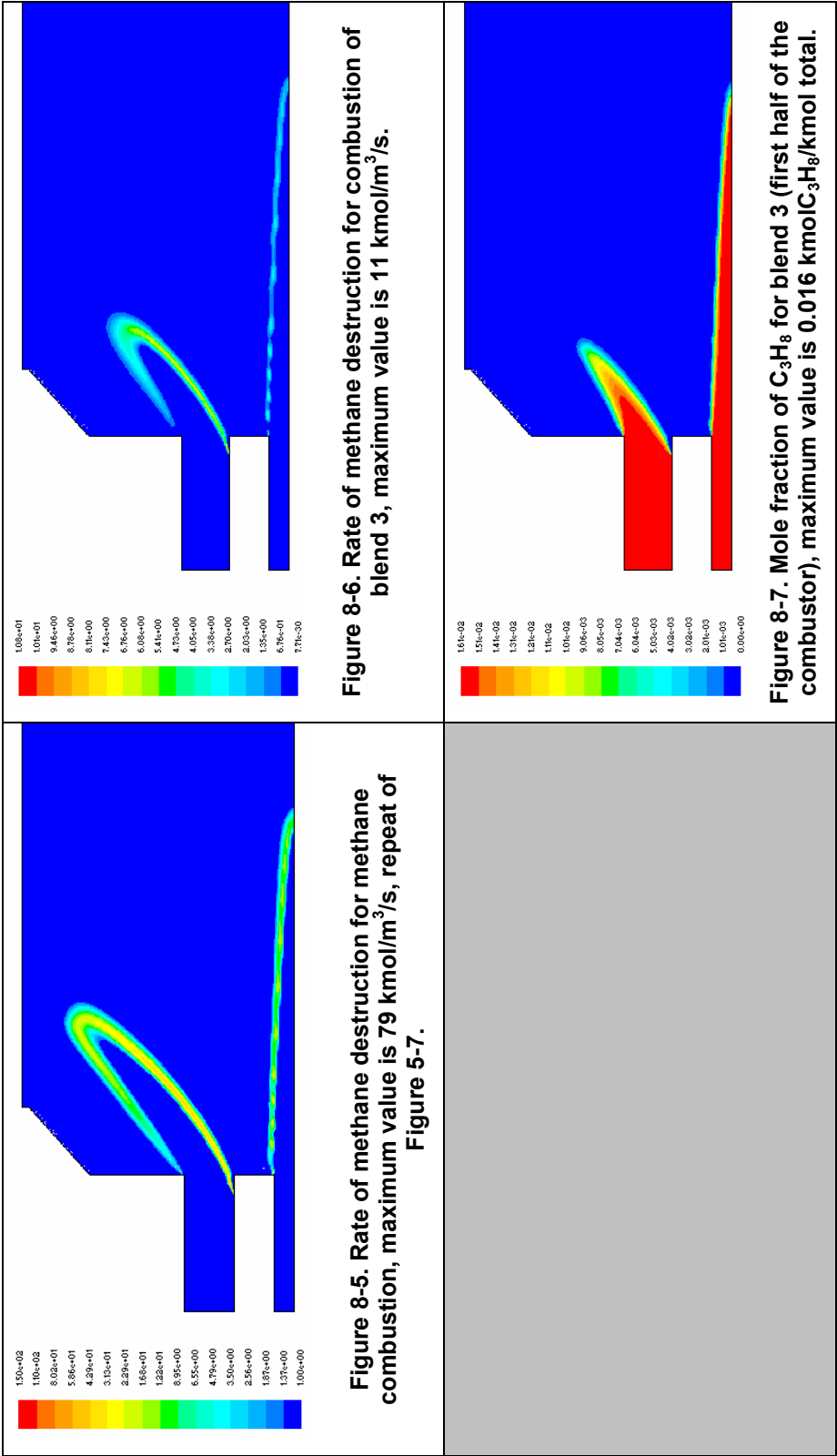


Table 8-2 (continued)

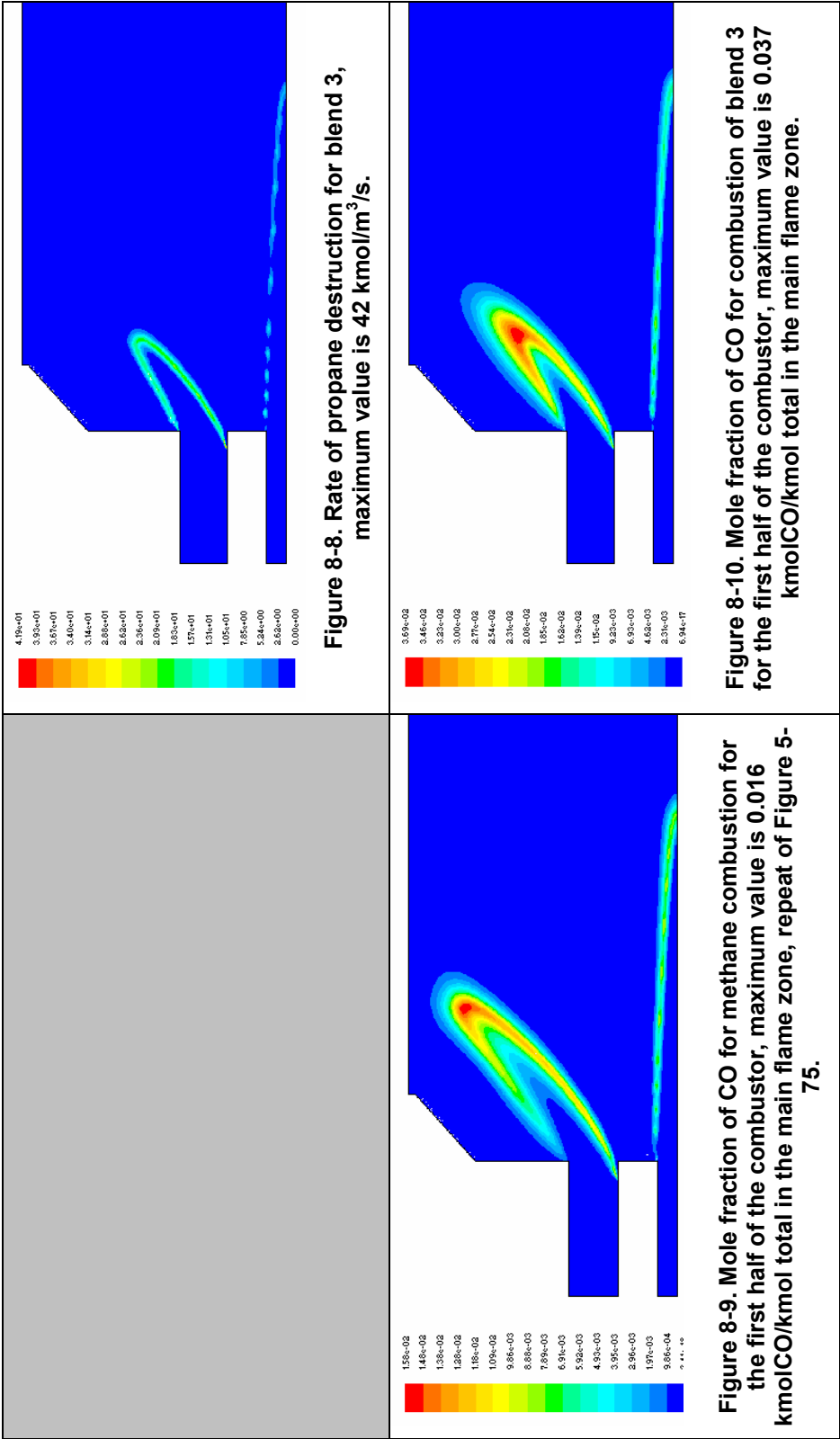


Table 8-2 (continued)

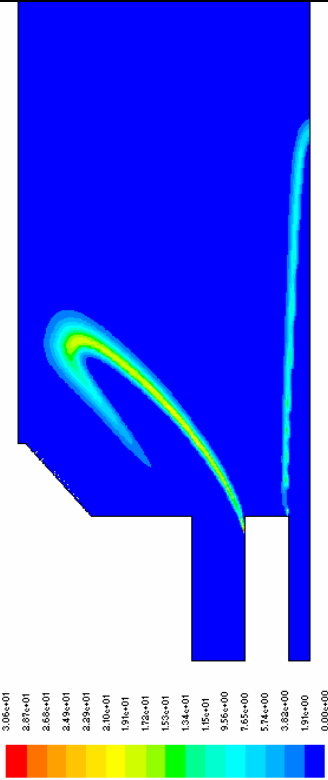
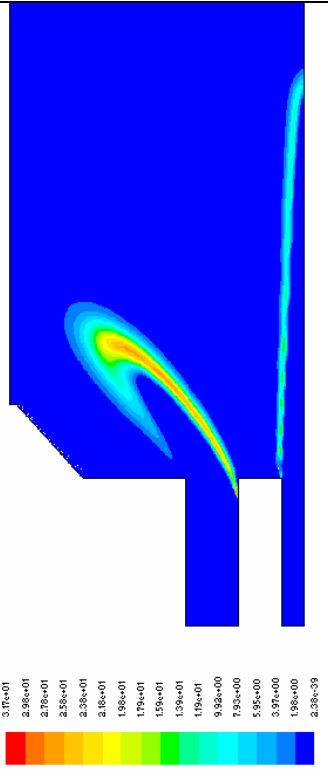
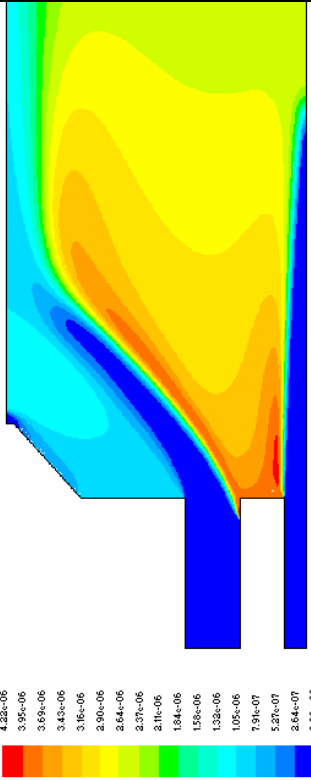
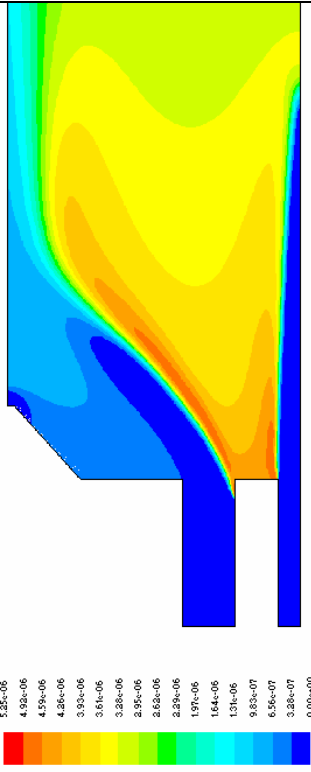
 <p>Figure 8-11. Rate of CO destruction for methane combustion, maximum value is 31 kmol/m<sup>3</sup>/s repeat of Figure 5-77.</p>	 <p>Figure 8-12. Rate of CO destruction for combustion of blend 3, maximum value is 31 kmol/m<sup>3</sup>/s.</p>
 <p>Figure 8-13. Mole fraction of NO for methane combustion for the first half of the combustor, maximum value is 4.2 ppmv NO, at the combustor exit the NO is 2.0 ppmv, wet, not corrected, repeat of Figure 5-81.</p>	 <p>Figure 8-14. Mole fraction of NO for combustion of blend 3 for the first half of the combustor, maximum value is 5.3 ppmv NO, at the combustor exit NO is 2.6 ppmv, wet, not corrected.</p>

Table 8-2 (continued)

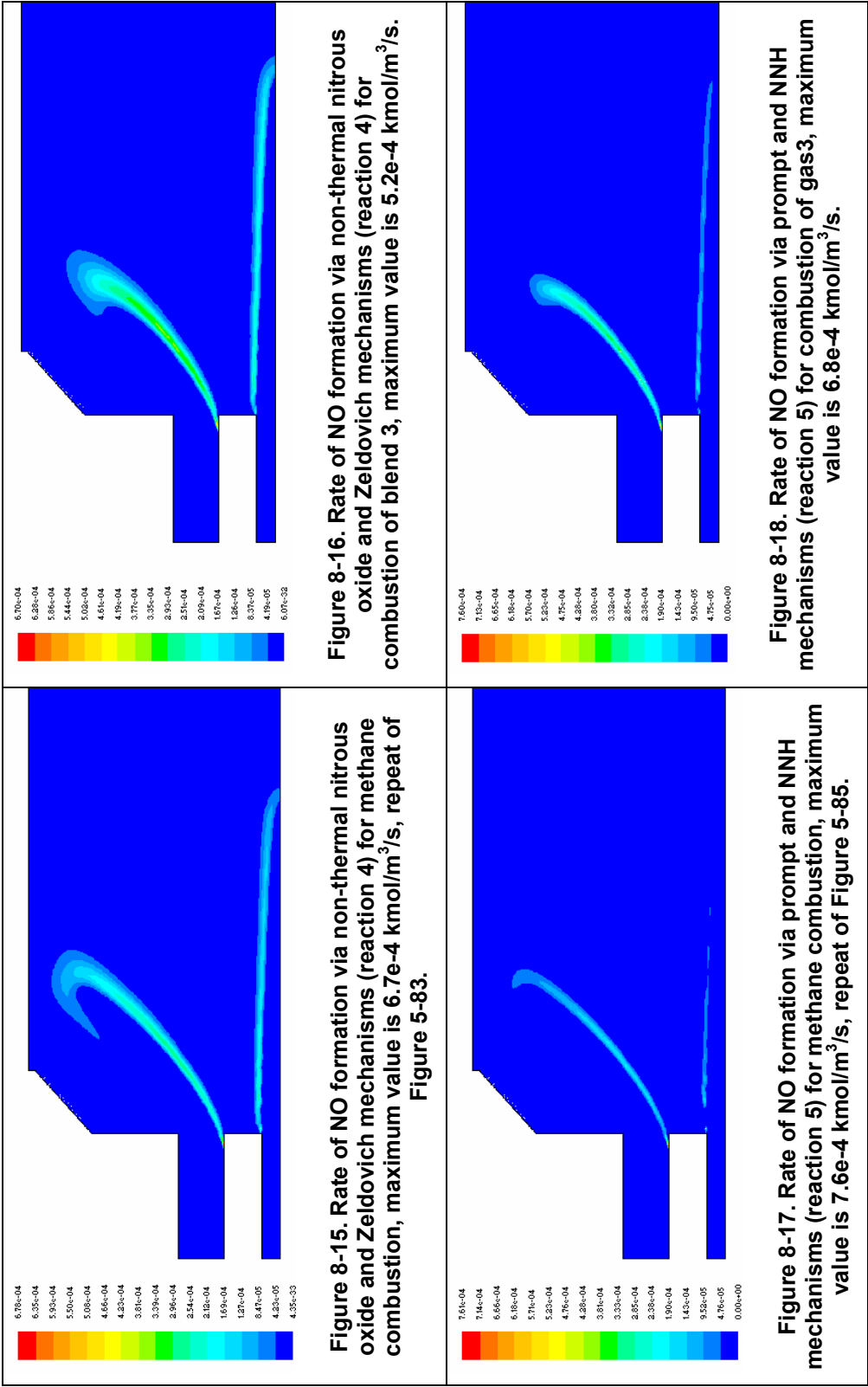


Table 8-2 (continued)

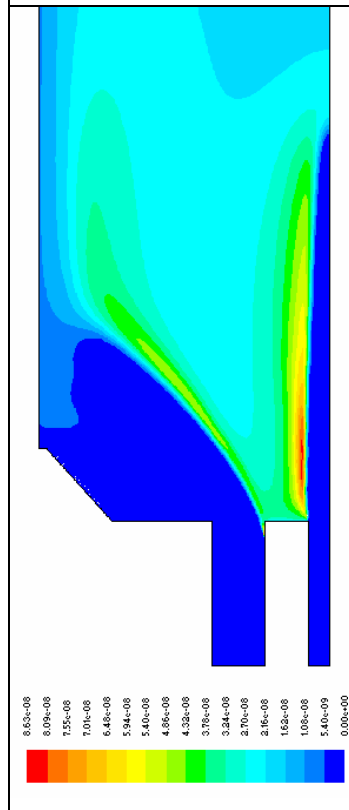


Figure 8-19. Rate of NO formation via thermal nitrous oxide mechanism assuming H-atom equilibrium (reaction 6) for methane combustion, maximum value is 8.6e-8 kmol/m<sup>3</sup>/s.

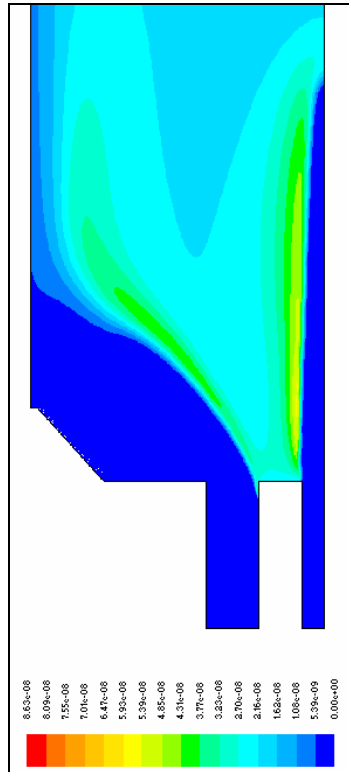


Figure 8-20. Rate of NO formation via thermal nitrous oxide mechanism assuming H-atom equilibrium (reaction 6) for combustion of blend 3, maximum value is 5.85e-8 kmol/m<sup>3</sup>/s.

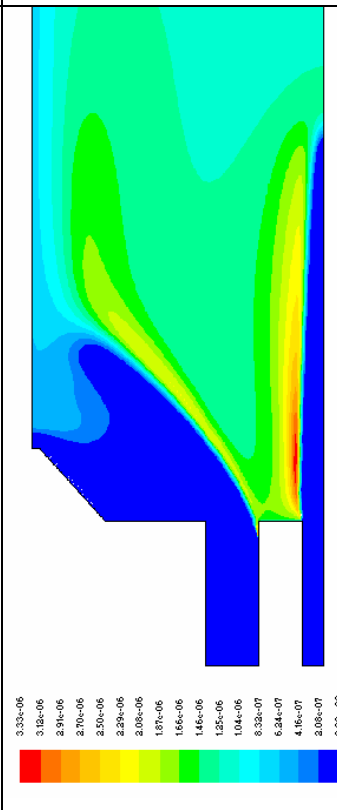


Figure 8-21. Rate of NO formation via thermal nitrous oxide mechanism assuming O-atom equilibrium (reaction 7) for methane combustion, maximum value is 3.2e-6 kmol/m<sup>3</sup>/s.

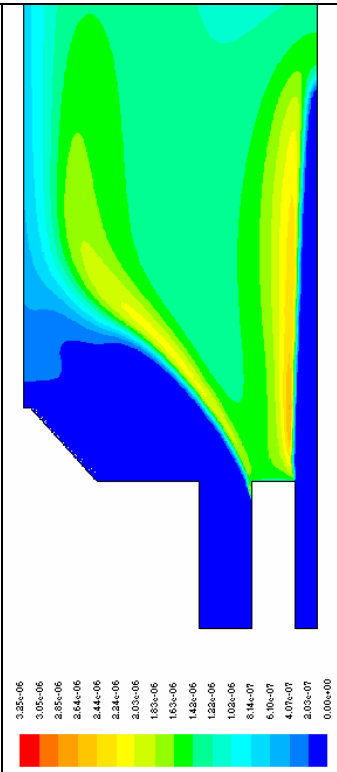
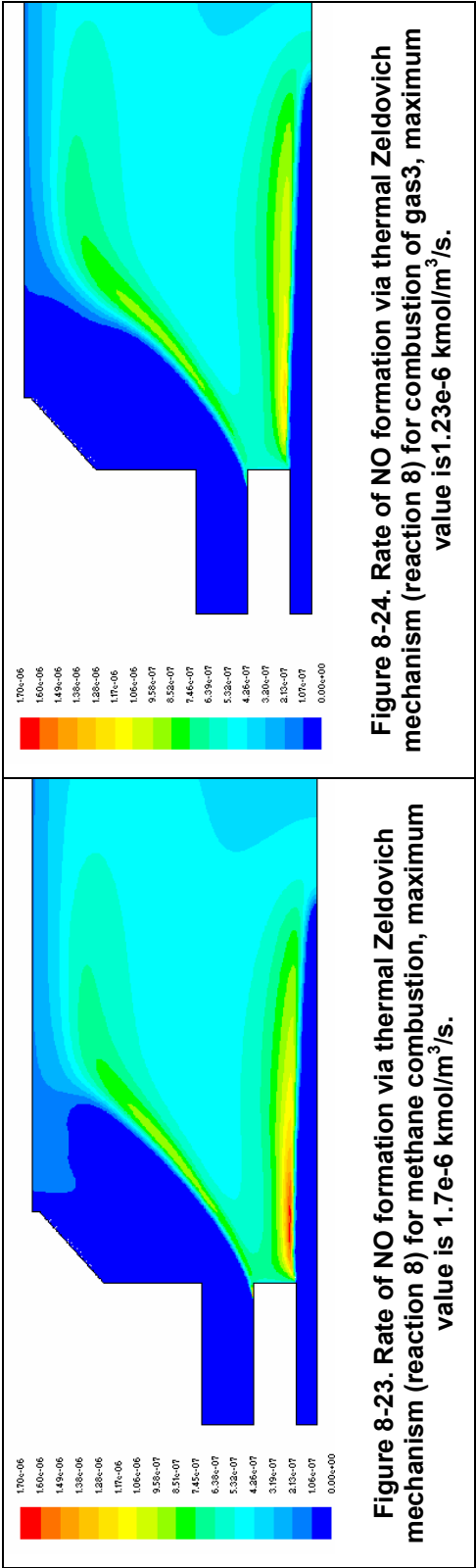


Figure 8-22. Rate of NO formation via thermal nitrous oxide mechanism assuming O-atom equilibrium (reaction 7) for combustion of blend 3, maximum value is 2.8e-8 kmol/m<sup>3</sup>/s.

Table 8-2 (continued)



### CRN modeling: results and discussion

The 31-element CRN for the can-type combustor is now used to evaluate the  $\text{NO}_x$  emissions for the blended fuels. The CRN is not changed from the methane combustion application. GRI 3.0 is used for the methane-propane fuel blends. The results of the CRN modeling are compared with the CFD computations. Figures 8-25 and 8-26 compare the CRN and CFD results for  $\text{NO}_x$  emission for the pilot set at 50 to 150% of neutral pilot; the figures show good agreement between the CFD and CRN prediction for blend 1 (80%  $\text{CH}_4$  – 20%  $\text{C}_3\text{H}_8$ ). For blends 2 and 3 (60%  $\text{CH}_4$  – 40%  $\text{C}_3\text{H}_8$ , and 30%  $\text{CH}_4$  – 70%  $\text{C}_3\text{H}_8$ , respectively) the maximum discrepancy between the CFD and CRN results for NO emission is 20% (relative). In general, the agreement between the CFD and the CRN results weakens as the volumetric fraction of propane in the fuel increases. There are a number of possible explanations for this:

1. As seen in Table 8-2, the flame length and position in the CFD simulations changes as the propane is added to the fuel. Since the CRN element volumes and the flow splits between elements are tuned to the methane combustion, the flame volume and flame position for high propane fuels might not be adequately represented by the CRN.
2. The CFD simulation uses a global kinetic rate of propane oxidation that is not optimized for the lean-premixed combustion regime. Although this rate is used in combination with the turbulent mixing rate and only is effective in the flame regions with very intense turbulence, it might lead to faulty temperature and species concentrations near boundary layers and in shear layers with strong turbulent dissipation. An example of this possible flow field misrepresentation is flame anchoring at the outer injector location in the blend 3 case. This is seen by

comparing Figure 8-9 and Figure 8-10. Figure 8-9, for methane combustion, suggests weak anchoring at top relative to Figure 8-10, which shows stronger flame anchoring.

3. The 31-element CRN of the can-type combustor employs PSB and PSR elements with very short residence times. The formation and destruction of free radicals under the blowout condition determine the residence time and the temperature in these elements. Since GRI 3.0 has very limited propane chemistry, the temperature predictions in the short PSR and PSB elements might be affected by lack of propane-related free radicals. This could also affect the NO formation routes that are active in the early part of the flame.

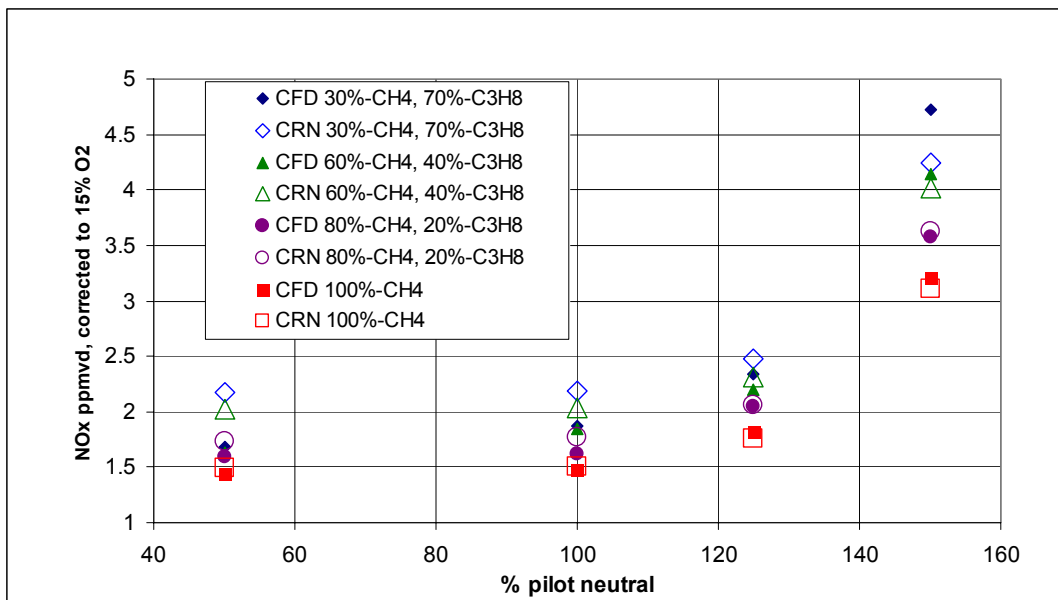


**Figure 8-25. Comparison of the CFD and CRN NO predictions for methane and the hydrocarbon fuel blends as a function of the percentage of neutral pilot for the can-type combustor.**

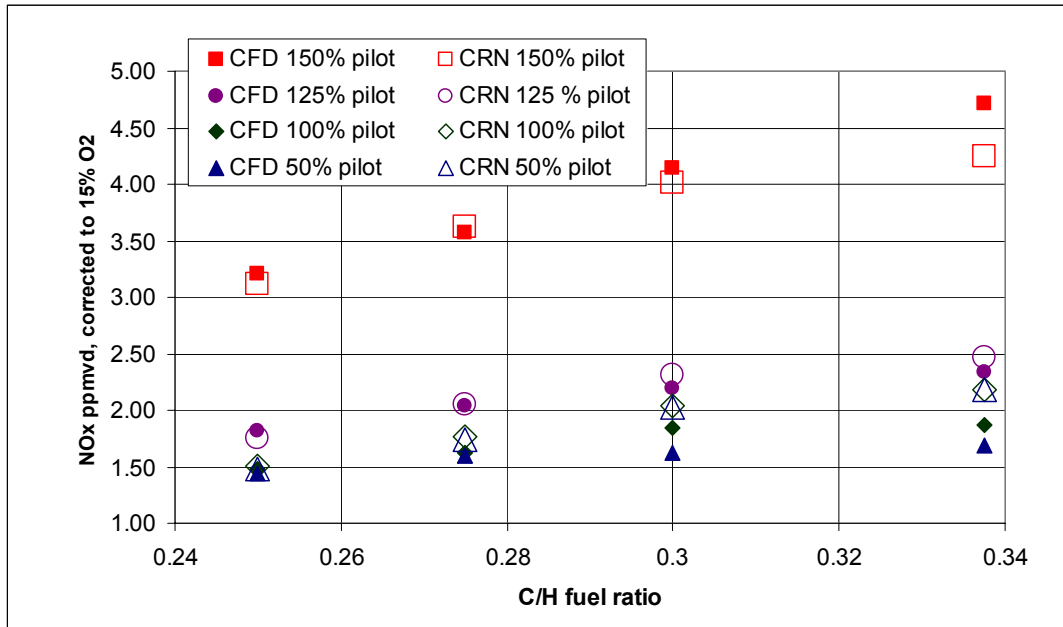


Figure 8-26. Comparison of the CFD and CRN NO prediction for methane and the hydrocarbon fuel blends as a function C/H fuel ratio for can-type combustor.

### ***Hydrocarbon Fuel Blend Combustion in Engine Test Rig 2***

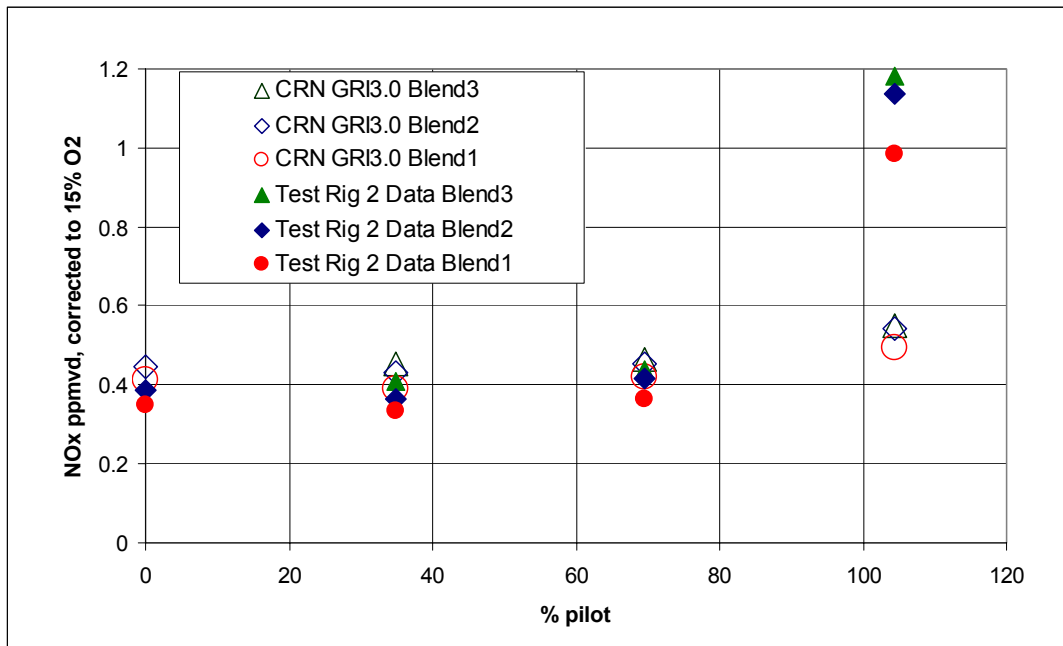
There are three fuel compositions of different C/H ratio considered for engine test rig 2: blend 1 with C/H=0.292; blend 2 with C/H = 0.31; and blend 3 with C/H = 0.336. These three blends are different than those used in modeling of the can-type combustor. These blends contain C<sub>1</sub> to C<sub>4</sub> alkanes, except for blend 1 that does not have hydrocarbons higher in order than C<sub>3</sub>. The combustion of blend 1 can be modeled using the GRI 3.0 mechanism without modification to the fuel composition. Since the mechanism does not contain rates for hydrocarbons heavier than propane, butane in blends 2 and 3 is treated as propane on the following carbon-conservation basis:

$$\%C_3H_8 \text{ for GRI} = \%C_3H_8 + 4/3 (\%C_4H_{10})$$

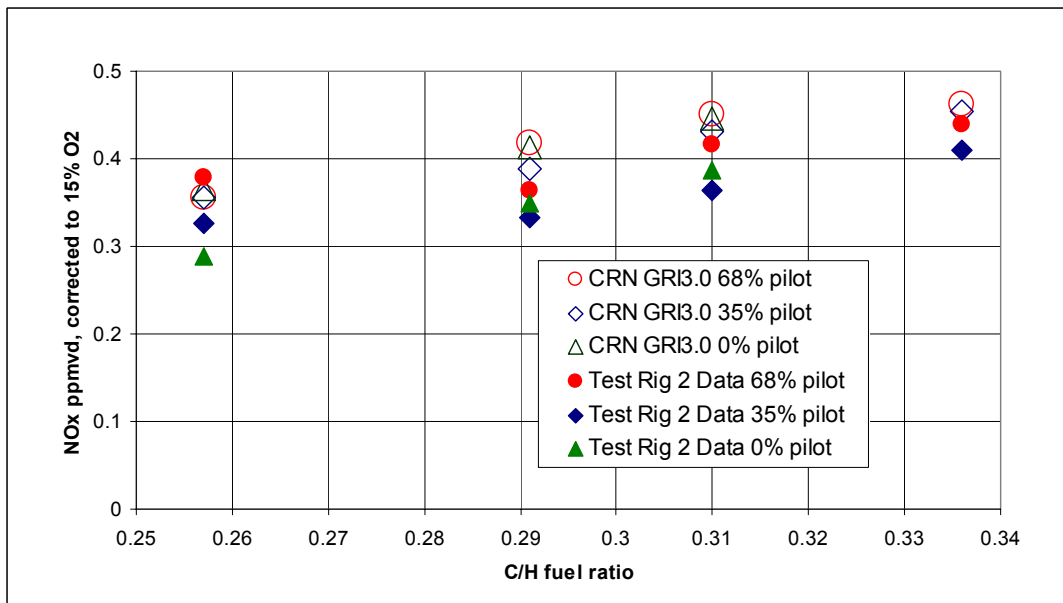
The fuel flow rates in the CRN are adjusted to achieve the same combustor exit temperature as measured in the engine rig test. This explains some scatter in both the engine testing rig data and the CRN predictions. The example of such scatter is the test rig emissions for natural gas at 68% pilot. The emissions in this case are higher than the NO<sub>x</sub> emissions for the blend 1 for the case pilot, see Figure 8-27. This is due to slightly higher combustor outlet and flame temperatures in the natural gas case. The CRN predictions of NO are corrected for the effects of temperature fluctuation and circumferential injector profile, as described in Chapter 7.

Figure 8-27 compares the NO emissions for the fuel blends as a function of the % pilot. Since any NO<sub>2</sub> in the test rig exhaust would have to come from NO formed in the flame, predicted NO mole fraction is the same as NO test rig emissions. Similar to the results presented in Chapter 7, the data are normalized to the NO<sub>x</sub> emission for natural gas combustion, 104% pilot case. Both the engine test rig data and the CRN model show that the emission levels do not change significantly with respect to pilot fuel flow rate up to 70% of neutral pilot. The engine test rig data for the richest pilot case is a factor 2.5-3 higher than the base level. This behavior is also seen in Chapter 7.

Figure 8-28 shows the effect of the fuel C/H ratio on the NO emissions. The high pilot case is not plotted to increase the graph resolution at the lower end. The plot shows a weak linear NO<sub>x</sub> dependency on the C/H fuel ratio for both the engine test rig data and the CRN predictions. This linear trend is reported by Malte et al. (2003) for combustion of hydrocarbon fuels in the atmospheric jet stirred reactor. See Appendix 4.



**Figure 8-27. Engine test rig 2 NO<sub>x</sub> emissions for hydrocarbon blends with uniform fuel-air ratio injector profile and CRN predictions with GRI 3.0 mechanism as a function of percent pilot.**



**Figure 8-28. Engine test rig 2 NO<sub>x</sub> emissions for hydrocarbon blends with uniform fuel-air ratio injector profile and CRN predictions with GRI 3.0 mechanism as a function C/H fuel ratio.**

### ***CRN with Mixing Control Rate for Hydrocarbon Fuel Blends***

An alternative way to model combustion of hydrocarbon fuel blends in the absence of a detailed chemical kinetic mechanism for the heavier hydrocarbons is to use a global chemical mechanism. From CFD modeling of the generic, can-type combustor one finds that the turbulent mixing rate of the initial fuel break down is in most cases smaller than the chemical kinetic rate. Using the rate limiting approach in the CRN, the global chemical rate of the initial fuel oxidation can be replaced with a mixing reaction rate for this reaction. The details of the methodology of global mixing control rate in the CRN are discussed in Appendix 2.

The mixing controlled reaction rate allows the use of any fuel in the CRN model. In this case, for fuel blends 2 and 3, n-butane is used in the gas composition. The CRN layout and the flow splits are not changed when global mixing controlled reaction is used in the initial fuel oxidation. However, the volumes of self-ignited elements (PSR 15 and PSR 19) are adjusted. These volumes are increased in order to account for the difference between the kinetic and mixing times. The reactor volume is chosen to match the NO concentration in the element calculated using the full kinetic mechanism.

Figure 8-29 shows the comparison between the CRN model in kinetic control using the GRI 3.0 mechanism and using the global mechanism with the mixing control reaction for initial fuel oxidation. These simulations serve as an important example for the use of the global mechanism approach in the chemical reactor network for the fuel blends. The difference between two simulations is less than 5%. Figures 8-30 and 8-31 compare the CRN modeling results with the engine test rig 2 emission data for nitrogen oxides. The CRN predictions are very close to the engine test rig data. The mixing

CRN comparison with test rig data is very similar to the results in Figures 8-27 and 8-28 (CRN with GRI3.0).

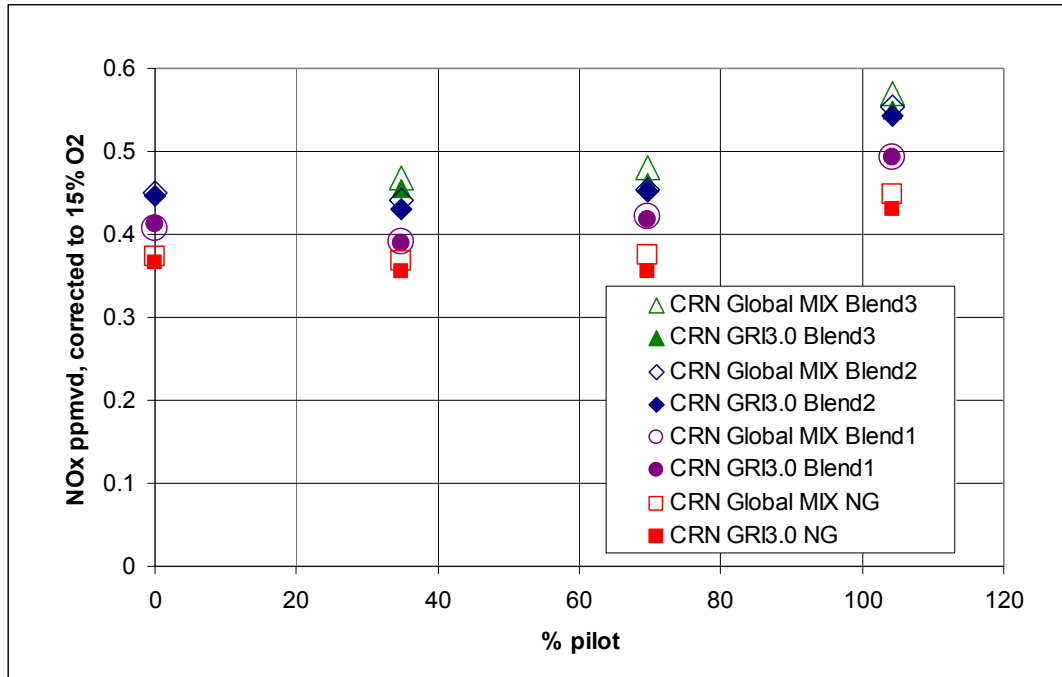


**Figure 8-29. Predicted NO<sub>x</sub> emissions for CRN using detailed chemical kinetic mechanism GRI3.0 and global mechanism with mixing controlled reaction for fuel oxidation.**

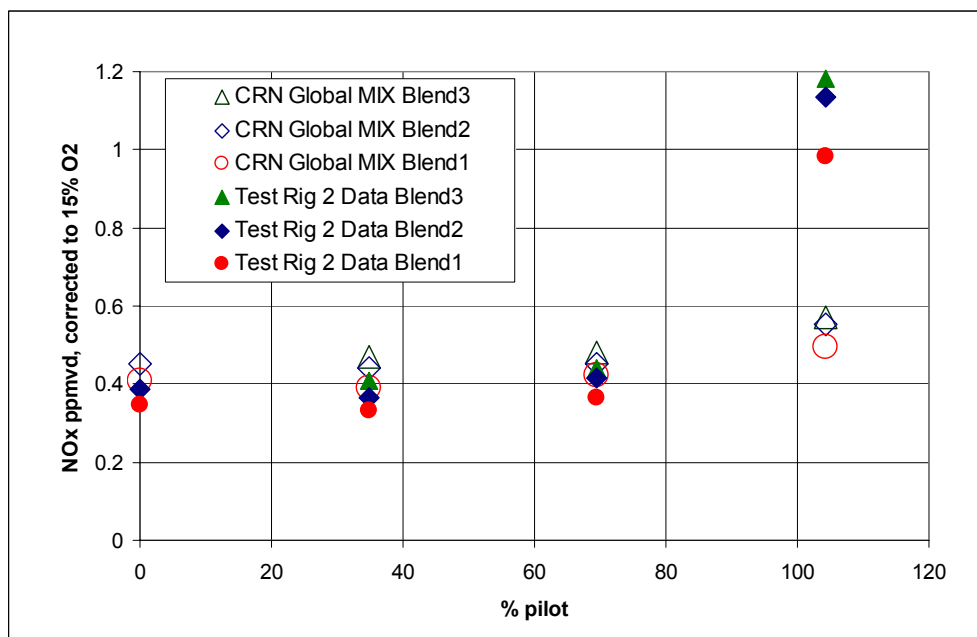


Figure 8-30. Engine test rig 2 NOx emissions for hydrocarbon blends with uniform fuel-air ratio injector profile and CRN predictions with global mechanism with mixing control as a function of percent pilot.

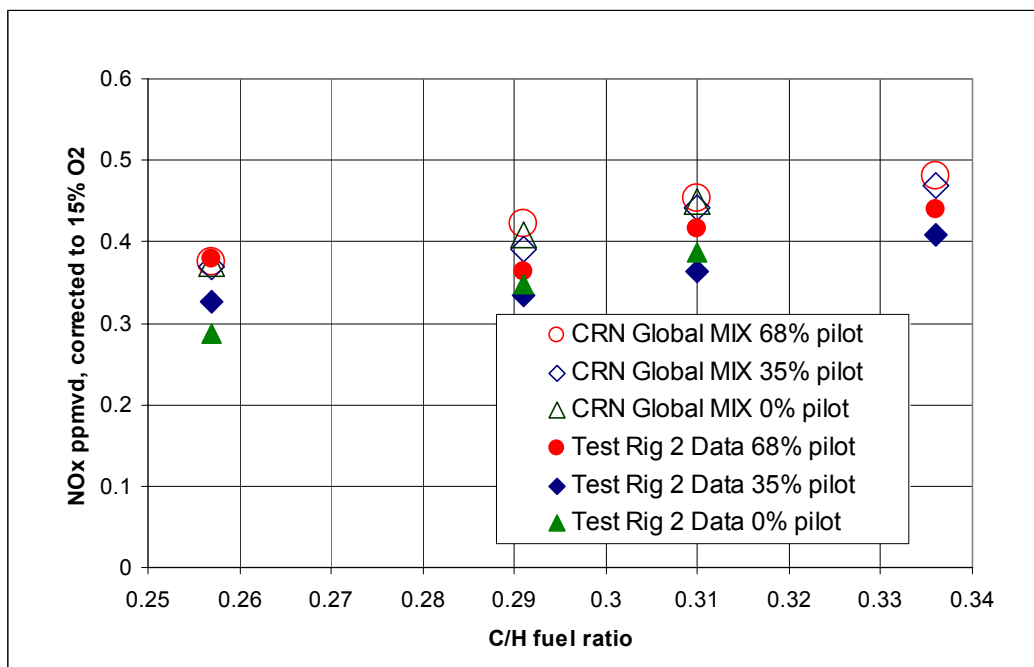


Figure 8-31. Engine test rig 2 NOx emissions for hydrocarbon blends with uniform fuel-air ratio injector profile and CRN predictions with global mechanism with mixing control as a function of C/H fuel ratio.

## 9. Chemical Reactor Modeling of Jet Stirred Reactor

In this section, modeling of the jet stirred reactor (JSR) using the chemical reactor network (CRN) approach is considered. The prediction of NO<sub>x</sub> and CO by the CRN approach is compared to experiments conducted by P.C. Malte using the 64 cm<sup>3</sup> atmospheric-pressure jet-stirred reactor. These experimental data have not been previously published and are presented here (Appendix 4) with the permission of P.C. Malte. The fuels are pure and blended hydrocarbons and pure hydrogen. The CRN approach is also compared to data contained in the MSME Thesis of Horning (1996). Horning obtained NO<sub>x</sub> and CO data using a 2 cm<sup>3</sup> JSR operated at 6.5 atm on fuel mixtures of H<sub>2</sub> and CO. For both JSRs, the fuel-air mixture enters the reactor as a strong jet and is well premixed.

The hydrocarbon fuels tested by Malte are: methane, propane, ethane, ethylene, and mixtures (blends) of C<sub>1</sub>-C<sub>4</sub> alkanes, but only the C<sub>1</sub>-C<sub>3</sub> fuels are modeled herein due to the chemical mechanism restriction. The combustion temperature in the JSR based on the corrected thermocouple measurement is 1792±3 K, and the inlet fuel air temperature is 573 K. The combustion temperature is measured in the recirculation zone of the reactor, which comprises about 90% of the reactor volume and exhibits very nearly uniform temperature and measured composition. NO<sub>x</sub>, CO, CO<sub>2</sub>, and O<sub>2</sub> are measured in the recirculation zone. The JSR residence time of the combustion cavity is 3.7±0.1 ms, based on the mean temperature of the reactor. The table below summarizes the conditions of the JSR experiments modeled.

**Table 9-1. JSR cases modeled.**

Case	P (atm)	JSR vol (cm <sup>3</sup> )	Inlet T (K)	Recirc zone T (K, corrected)	Res time (ms)
Malte: HC fuels	1	64	583	1792±3	3.7±0.1
Malte: H <sub>2</sub>	1	64	315-327	1300-1790	3.5-5.5
Horning: CO/H <sub>2</sub>	6.5	2	385±5	1785	4.0 nominal

### ***Modeling Approach***

The University of Washington chemical reactor code with the detailed chemical kinetic mechanism GRI 3.0 is used for the HC fuels modeling. Two arrangements of chemical reactor elements are examined: 3-element scheme and 13-element CRN.

The 3-element model consists of three perfectly stirred reactors (PSRs) in series. The methodology and justification of using this reactor arrangement can be found in Lee et al. (2003). The first reactor in the series is a PSB. The second reactor is an adiabatic PSR with 5% of the total JSR volume. The third reactor is a PSR at the assigned temperature. The temperature in PSR 3 is assigned the measured temperature corrected for the radiation thermocouple heat loss. The volume of the PSR 3 is the remaining 92-93% of the JSR cavity.

The PSB exhibits a high concentration of free radicals and occupies a very small volume of the reactor -- from 1.3 to 2.3% (the largest volume corresponds to methane and the smallest to ethylene combustion). The reactor represents the turbulent flame front in the JSR. The NO formation rate is relatively small due to the low (blowout) temperature in this element. The second element is 5% of the total JSR volume. It represents the main

flame, with free radicals at super-equilibrium concentration. PSR 2 has a high NO production rate due to its high temperature and free radical concentrations. The third element represents the post-flame and recirculation zone of the JSR. With most of the species in this zone relaxing towards equilibrium concentrations, the NO formation rate is relatively low. The temperature in the element is not high enough (1792K) to trigger significant amounts of thermal NO.

The 13-element model is a more elegant representation of the combustion process in the JSR. Figure 9-1 shows the schematic representation and the elements corresponding to the different regions of the JSR. In order to represent the flame that surrounds the incoming jet, the domain is divided into three streams and sets of PSB-PSR. These two reactors are assumed adiabatic. Each stream receives fresh fuel-air mixture in the first element (PSB) and the recirculation zone gas entrained by the jet action in the second element (PSR). The ignition of the fresh fuel air mixture occurs in the flame front which is modeled using PSB elements 3, 6 and 7. After entraining some of the recirculating gas from the recirculation zone the combustion continues in the PSR elements 4, 5 and 8 at the super-equilibrium levels of free radicals and at higher temperature. Similar to the 3-element model described above, the recirculation zone of the JSR is represented by a PSR element assigned the measured combustion temperature (this is termed a PST). The exhaust flow of the reactor is modeled as a PFR element.

Although CFD calculations have not been performed for the JSR geometry, flow splits between the elements in the 13-element CRN are chosen partly based on the CFD results for the can-type combustor (of Chapter 5) and the relation for axisymmetric jet entrainment (Ricou and Spalding, 1961). The CRN flow splits are tuned to obtain the best agreement with the experimental

data for methane combustion. Figure 9-2 shows the 13-element CRN with the flow splits between the elements. The model assumes that the ignition happens in the flame front represented by the PSB elements, the front is divided into three zones depending on their geometric position in the jet: the furthest from the center (PSB 3), the intermediate (PSB 6), and the center (near the tip of the flame front – PSB 8). The outer jet stream (PSB 3-PSR 4) receives 50% of the total jet fuel-air mixture due to larger area associated with the greater radius. The rest of the flow is divided in half between the two other streams PSB 6-PSR 5 and PSB 7-PSR 8, which are located closer to the center of the jet. The second element in each series treats the combustion of the mixture of ignited fresh mixture from the PSB element and entrained recirculating gas. PSR 4, PSR 5, and PSR 8 represent all of the upward moving burning gas in the JSR. Then, PST 9 treats all of downward moving gas in the JSR (as depicted in Figure 9.1).

The total jet entrainment defines the flow split between element MIX 10 and PFR 13. The flow fraction that is entrained by the jet passes through MIX 10. It is determined based on the jet entrainment relation applied to the jet-stirred reactor by Thornton et al. (1987) and calculated to be 80% of the jet mass flow. Consequently 20% of the recirculation zone mass flow is exhausted (PFR 13). The probe for emissions measurement is inserted into the recirculation zone. The flow conditions and the species concentrations inside of the probe are similar to those of the exhaust ports. Thus, in this modeling, it is assumed that the sampled gas is the same as the exhaust gas, PFR 13 also represents the interior of the hot sample probe section through which the gases are pulled from the JSR. PFR 13 has a short residence time and thus has little effect on the NO<sub>x</sub> emissions (typically 0.1-0.2 ppm). Its function is mainly to help with carbon monoxide conversion to CO<sub>2</sub>.

The recirculation gas is entrained by the jet in two different locations of the CRN. First, a small part (3%) is entrained near the bottom of JSR into PSR 4, the rest of the recirculating gas is entrained by the half length distance of the JSR into PSR 5, see Figure 9-1. PSR 4 is modeled as adiabatic element, the local temperature in this element is 10-20 K higher than the temperature measured in the recirculation zone. The gas from the PSR 4 enters PSR 5 along with the majority of the recirculating gas. The temperature in this element is only slightly higher than in the recirculation zone. Finally, the gas from the PSR 5 mixes with the freshly ignited mixture from PSB 7 and enters PSR 8. The temperatures in the PSR elements are determined by adiabatic combustion diluted with recirculating gas at the measured corrected temperature.

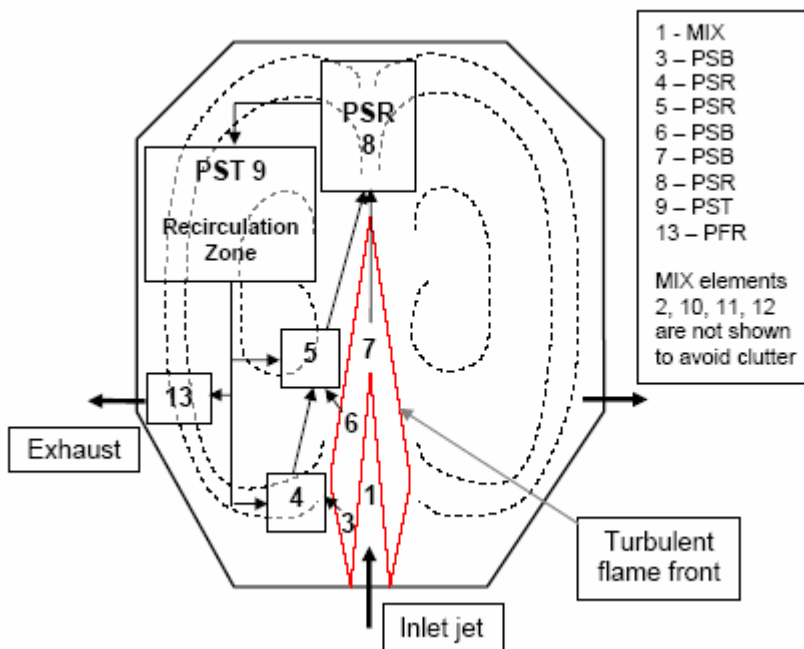


Figure 9-1. Schematic representation of the jet-stirred reactor.

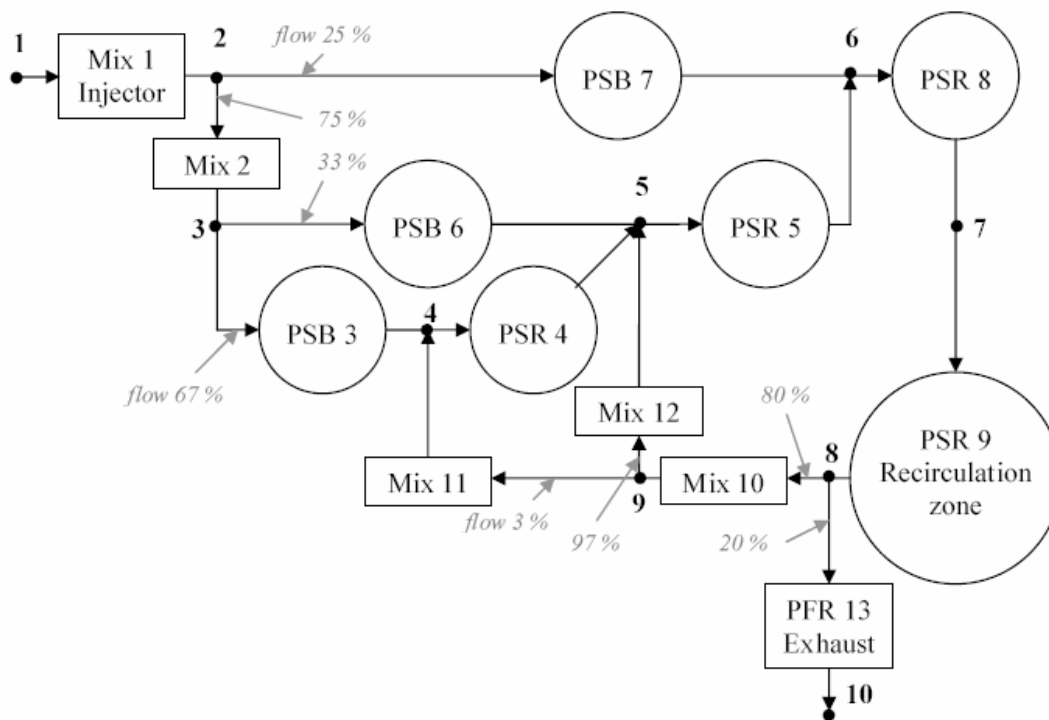


Figure 9-2. 13-element CRN for evaluating NO<sub>x</sub> and CO behavior of the JSR.

### Hydrocarbon Combustion Modeling

The NO formation routes vary depending on the position in the flame. Since, the flame front is modeled as PSB, the temperatures in these elements are not high enough to form significant amounts of NO via the prompt, N<sub>2</sub>O, or Zeldovich mechanisms due to the exponential temperature dependency in the rate expressions. However, the NNH formation route in GRI3.0 mechanism (modified Bozzelli and Dean, 1995) does not have temperature dependency in the NO formation rate. The NNH mechanism becomes active at the low temperature condition in the PSB element and contributes up to 2 ppmvd NO corrected to 15% O<sub>2</sub> (30% of total NO for the JSR). PSR 4 is the largest NO

producer due to its high temperature and high free radical concentrations. Elements PSR 5 and PSR 8 have a large amount of recirculation gas entrained, that reduces the temperature in these elements as well as their free radical counts. The NO formation in elements PSR 5 and PSR 8 is due to the relatively active  $N_2O$  pathway; the NNH and prompt pathways contributions are small due to the small concentration of relative free radical species.

Figure 9-3 shows the  $NO_x$  results of modeling for both the 3-element and 13-element models applied to the hydrocarbon fuels experiments of Malte. Generally, both models show very good agreement with the data. The 13-element CRN can be further tuned to obtain better agreement with the data; however, in this study this has not been done due to the lack of detailed flow field information. Figure 9-4 shows the CO results.

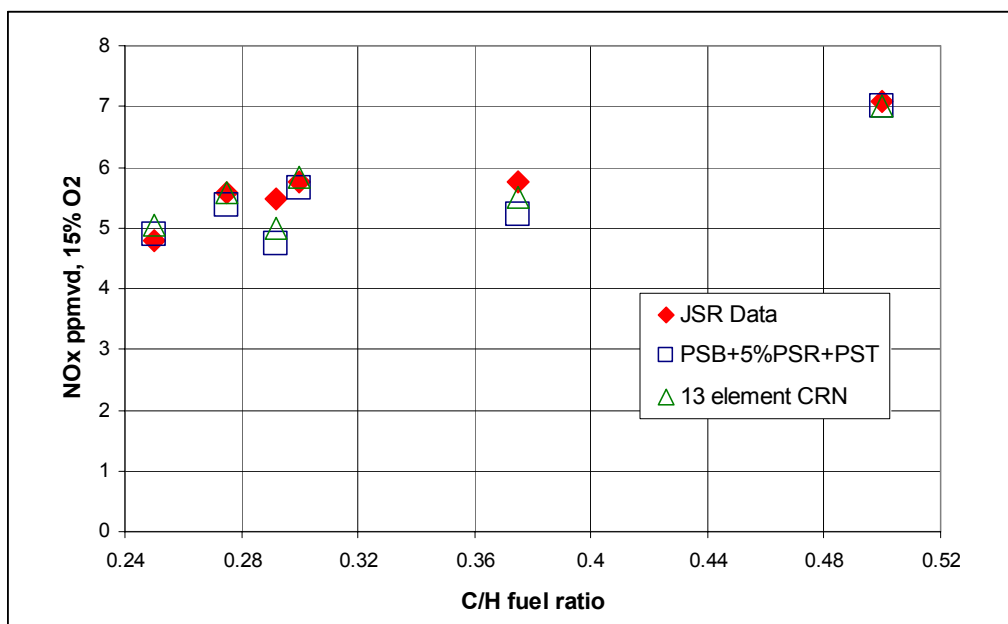


**Figure 9-3. Modeled and measured  $NO_x$  for the hydrocarbon-fuels experiments of Malte for the 64 cm<sup>3</sup> JSR.**

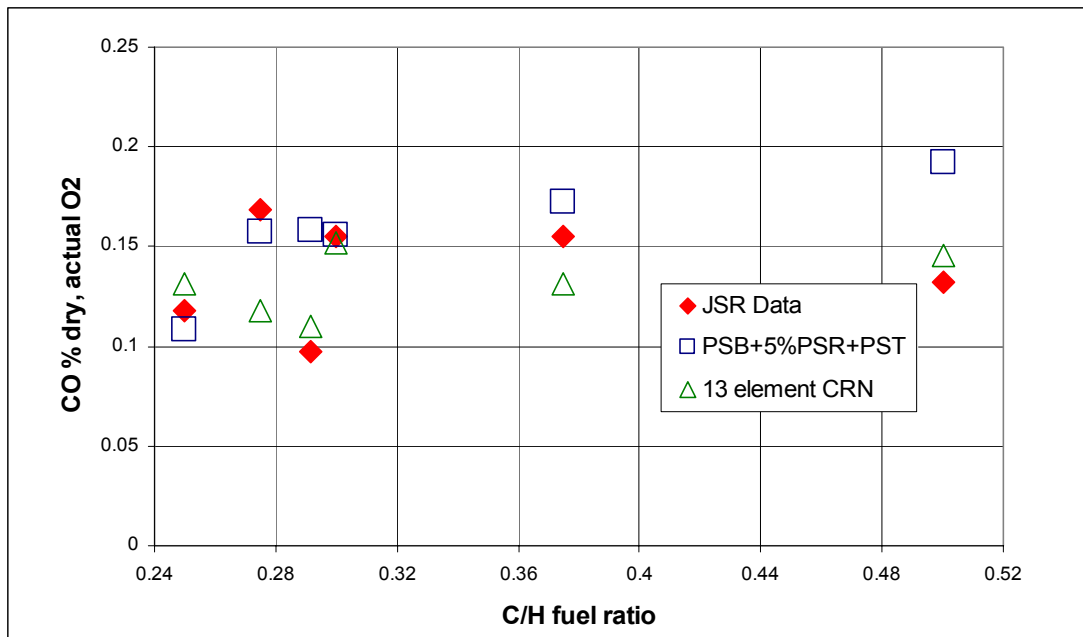


**Figure 9-4. Modeled and measured CO for the hydrocarbon-fuels experiments of Malte for the 64 cm<sup>3</sup> JSR.**

### ***Hydrogen Combustion Modeling***

The 64 cm<sup>3</sup> reactor is used for the hydrogen combustion experiment. See Appendix 4. The results are modeled using the modified GRI 3.0 mechanism and the 3-element model and 13-element CRN. The 13-element CRN results show reasonably close agreement to the measurements. As shown on Figure 9-5, the modeled NO<sub>x</sub> (adjusted to 15% O<sub>2</sub>) is within 0.4 part per million of the measurements for the 13-element CRN. However, the 3-element model is somewhat off for this case, over predicting the NO<sub>x</sub> by about 3 parts per million at the highest temperature run.

The kinetic mechanism used is a modified version of GRI 3.0. The modification is conducted by substituting the Konnov and de Ruyck (2001)

temperature-dependent rate constant for the reaction:  $\text{NNH} + \text{O} \rightarrow \text{NH} + \text{NO}$ . In the unmodified GRI 3.0 mechanism, this rate constant (modified Bozzeli and Dean, 1995) has zero activation energy, which causes the reaction rate to remain high at the reduced temperature levels of interest in lean-premixed, low-NO<sub>x</sub> combustion. This leads to over prediction of the NO<sub>x</sub> formation. The problem is most severe at low pressure for H<sub>2</sub> combustion, because of the high levels of super equilibrium H and O generated, which give rise to increased NO<sub>x</sub> formed from the NNH chemistry.

By making this single change to GRI 3.0, good agreement is obtained between the NO<sub>x</sub> predictions and measurements for the hydrogen atmospheric combustion and for 6.5 atm combustion of H<sub>2</sub>-CO blends (discussed in the next section). The activation energy of  $\text{NNH} + \text{O} \rightarrow \text{NH} + \text{NO}$  is taken as 16.8 kJ/mol (4 kcal/mol), which is in the center of the suggested range and the pre-exponential constant is taken as  $10^{14} \text{ cm}^3/\text{mol/s}$ , which is at the minimum of the range recommended by Konnov and de Ruyck.

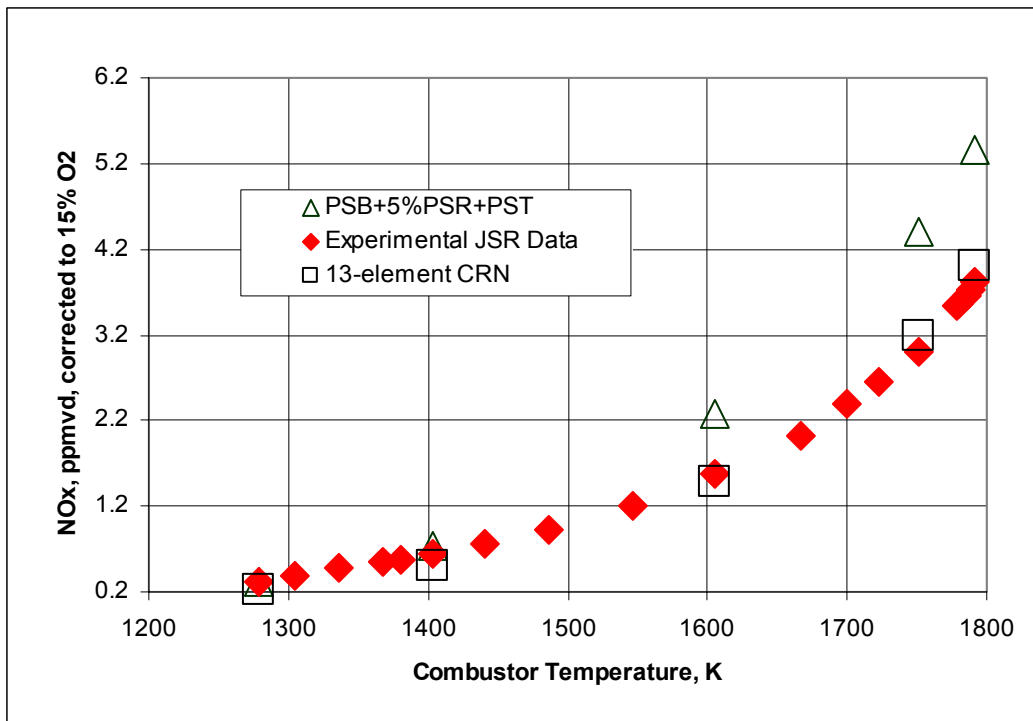


Figure 9-5. Modeled and measured NO<sub>x</sub> for the hydrogen combustion experiments of Malte for the 64 cm<sup>3</sup> JSR.

### ***H<sub>2</sub>-CO Fuel Blend Combustion Modeling***

The H<sub>2</sub>-CO experimental data of Horning (1996) for 6.5 atm 2cm<sup>3</sup> JSR is modeled in this section. Modified GRI 3.0 (described in previous section) is used in the modeling. Comparison of the modeling results to measurements is shown in Figures 9-6 and 9-7. In these experiments, Horning (1996) held the CO/H<sub>2</sub> molar ratio at a constant value and varied the fuel-air ratio (from  $\Phi = 0.47$  to 0.59). The nominal residence time is 4 ms. In Figure 9-6, the CO/H<sub>2</sub> ratio is 0.5, and in Figure 9-7 it is 1.0. The combustion temperature is that measured and corrected for the JSR recirculation zone. The air and fuel are not preheated. However, in order to account for recuperation of heat to the inflowing reactants, the temperature of the reactants entering the JSR is

increased. The increase has been determined by heat transfer modeling of the reactor, nozzle block, and injector, and is found to result in a jet inlet temperature of 380-395K for Horning's experiments.

Conclusion: Generally a good agreement is obtained between the modeling and the experiments. For  $H_2$  fuels this requires modification of the rate for  $NNH+O=NH+NO$ .

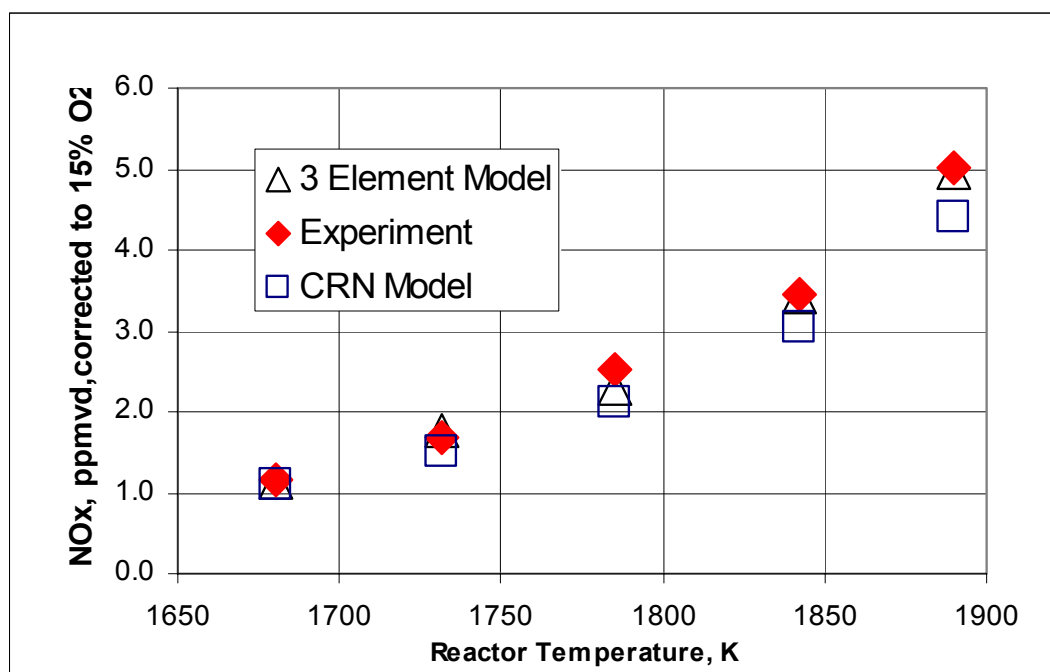
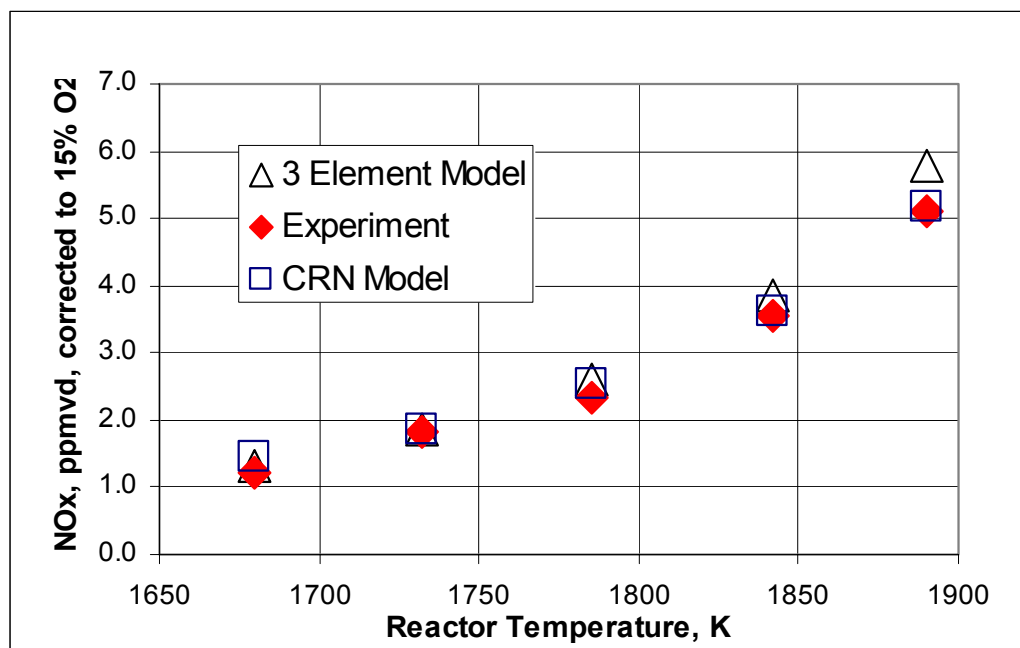


Figure 9-6. Modeled and measured NO for the  $H_2$ -CO fuels blend experiments of Horning for the  $2\text{ cm}^3$  JSR.  $CO/H_2 = 0.5$ .



**Figure 9-7. Modeled and measured NO for the H<sub>2</sub>-CO fuels blend experiments of Horning for the 2 cm<sup>3</sup> JSR. CO/H<sub>2</sub> = 1.0.**

## 10. Conclusions

This research has shown that the use of the combined CFD and CRN approach has the ability to accurately predict  $\text{NO}_x$  and CO emissions for lean-premixed gas turbine combustion applications: single-injector, can-type combustor and industrial, multi-injector, annular combustor. Additionally, the CRN approach is shown to accurately predict the  $\text{NO}_x$  and CO of the experimental jet-stirred reactor for different fuels.

In the process of the CRN development, the eight-step global chemical mechanism for methane oxidation with NO formation has been updated and verified for use in CFD code. CFD modeling with the updated eight step global mechanism has been performed for a bluff body burner and yielded good agreement with the experimental data for both  $\text{NO}_x$  and CO emissions.

The global eight-step mechanism has been applied for CFD modeling of the generic single-injector, can-type combustor in order to obtain insight on the flow, temperature, and species fields. The flow field information from the can-type combustor CFD has been analyzed to determine combustion zones in the combustor. These zones are modeled as chemical reactor elements in the CRN. The methodology of CRN development is determined based on the agreement between CFD and CRN models. Nitrogen oxide emissions predicted by both models are in good agreement over the range of different pilot fuel flows for the industrial GT. The CRN utilizes the detailed chemical kinetic mechanism GRI 3.0 taking advantage of the minimal computational time requirements for convergence.

The methodology of the CRN development for the generic, single-injector, can-type combustor is applied to the industrial combustor. The resulting CRN incorporates important flow features and boundary conditions such as: fuel-air distribution in the premixer, velocity profile in the premixer, entrainment of the main recirculation zone and dome recirculation zone gases into the main flame, turbulent mixing within the premixer jet, interaction of the pilot with the main recirculation zone and the main flame, and mixing of gas from neighboring injectors/flames into the main flame. The CRN emission predictions for the industrial gas turbine combustor show very good agreement with the test rig engine data over a range of pilot flows for two different engines. Comparison of CRN emission prediction using both the GRI 3.0 mechanism and the eight-step global mechanism to the engine test rig data provides additional validation of the eight-step mechanism.

A parametric study using CFD and CRN is performed to determine the influence of the fuel type on the NO<sub>x</sub> emissions for the single-injector, can-type combustor as well as for the industrial test rig engine. The study shows a nearly linear dependency of NO<sub>x</sub> emissions as a function of the C/H fuel ratio. These results agree with experimental data obtained from two experimental jet-stirred reactors and from the engine test rig combustor.

The use of the CRN provides significant insight into the pollutant formation behavior. The CRN can handle the most complex chemical mechanisms with relative ease – something that cannot be done with CFD. It can be used as a means for parametric analyses and be conveniently integrated into combustor design, because of its small computational time requirement. The CRN can also be used for evaluating truncated and global chemical mechanisms for use in CFD.

Among the recommendations for future work in the CRN development and application are:

- Evaluation of combustion of other fuels: hydrocarbon blends, hydrogen, hydrogen blends with hydrocarbons and carbon monoxide, also various prevaporized liquid fuels.
- Development of an automated CFD-CRN translation tool. Such a tool would convert a CFD output into a chemical reactor network with minimum input of the modeler. This approach would minimize human error in analyzing the flow fields and significantly speed up the analysis time.

## References

- Antifora, A, Faravelli, T, Kandamby, N, Ranzi, E., Sala, M., Vigevano, L.  
 “Comparison between two complementary approaches for predicting NOX emissions in the furnaces of utility boilers” *Fifth International Conference on Technologies and Combustion Technologies for a Clean Environment*, Lisbon, Portugal, pp. 377–384, 1999.
- Ballal, D.R., Vangsness, M.D., Heneghan, S.P., Sturgess, G.J. “Studies of Lean Blowout in a Research Combustor,” *AGARD Conference Proceedings* 536, 1993.
- Benedetto, D.; Pasini, S.; Falcitelli, M.; La Marca, C.; Tognotti, L., “NO<sub>x</sub> emission prediction from 3-D complete modelling to reactor network analysis,” *Combustion Science and Technology*, v153, n1, pp. 279-294, 2000.
- Bengtsson K.U.M., Benz, P., Schareren, R., and Frouzakis, C.E. “N<sub>y</sub>O<sub>x</sub> Formation in Lean Premixed Combustion of Methane in a High Pressure Jet-Stirred Reactor,” *Twenty-Seventh Symposium (International) on Combustion*, *The combustion institute*, pp. 1393-1401, 1998.
- Bragg, S.L. “Application of Reaction Rate Theory to Combustion Chamber Analysis,” *Aeronautical Research Council Pub. ARC 16170*, Ministry of Defense, London, England, pp. 1629-1633, 1953.
- Bray, K. N. C. and Libby, P. A. “Recent development in the BML model of premixed combustion,” in P. A. Libby and F. A. Williams, editors, *Turbulent reacting flows*, pages 115-151, Academic press, London, 1994.

Broadwell, J. E. and Lutz, A. E. *Combust. Flame* 114, p.319, 1998.

Bryden, K.M. and Hagge, M.J. "Modeling the combined impact of moisture and char shrinkage on the pyrolysis of a biomass particle," *Fuel*, 82(13), pp. 1633-1644, 2003.

Chan, W.-C.R, Kelbon, M., and Krieger, B.B. "Modelling and experimental verification of physical and chemical processes during pyrolysis of a large biomass particle," *Fuel*, 64(11): pp. 1505-1513, 1985.

Chen, J.C. and Lin, C. A. "Computations of strongly swirling flows with second-moment closures," *Int. J. Numer. Meth. Fl.*, 30 (5), (1999): 493-508.  
Dryer, F. L., and Glassman I. *Fourteenth Symposium International on Combustion*, The Combustion Institute, Pittsburg, PA, p. 987, 1973.

Correa, S. M., and Pope, S. B., "Comparison of a Monte Carlo/Finite Volume Mean Flow Model with Bluff-Body Raman Data," *Twenty-Fourth Symposium (International) on Combustion*, The Combustion Institute, Pittsburgh, PA, pp. 279-285, 1992.

DuPont, V., Pourkashanian, M., and Williams, A., *Journal of the Institute Of Energy*, 66:20, 1993.

Ehrhardt, K.R., "Development of a hybrid model for the prediction of nitric oxides emissions of furnaces," MIT, Energy Laboratory Report, 1993

Falcitelli, M., Pasini, S., Rossi, N., Tognotti, L. "CFD + reactor network analysis: an integrated methodology for the modeling and optimization of

industrial systems for energy saving and pollution reduction," *Applied Thermal Engineering* 22, pp. 971–979, 2002.

Falcitelli, M., Pasini, S., Tognotti, L. "Modeling practical combustion systems and predicting NO<sub>x</sub> emissions with an integrated CFD based approach," *Computers and Chemical Engineering* 26, pp. 1171–1183, 2002.

Fry, M. "NO<sub>x</sub> in the panel Board Industry," Coen Co, Burlington CA, *Internal Report*, 1993.

Faravelli, T., Bua, L.; Frassoldati, A.; Antifora, A.; Tognotti, L.; Ranzi, E. "A new procedure for predicting NO<sub>x</sub> emissions from furnaces," *Computers & Chemical Engineering*, v 25, n4-6, pp. 613-18, 2001.

Feitelberg, A.S., Tangirala, V.E.; Elliott, R.A.; Pavri, R.E.; Schiefer, R.B. "Reduced NO<sub>x</sub> Diffusion Flame Combustors for Industrial Gas Turbines," *ASME Journal of Engineering for Gas Turbines and Power*, 123, n4, pp. 757-765, 2001.

Field, M. A., Gill, D. W., Morgan, B. B., and Hawksley, P. G. W. "Combustion of Pulverized Coal," *The British Coal Utilization Board, Leatherhead, UK*, 1967.

Front, R. "Kinetics of the pyrolysis of almond shells and almond shells integrated with CoCl in a fluidized bed reactor and in Pyroprobe 100," *Industrial & engineering Chemistry Research*, 29(9), pp. 1846-1855, 1990.

Gibson, M.M., and Launder, B.E. "Ground Effects on Pressure Fluctuations in the Atmospheric Boundary Layer," *J. Fluid Mech.*, 86, pp. 491-511, 1978.

Glassman, I., *Combustion*, Academic Press, 1996.

GRI MECH 3.0. *World Wide Web Site* [http://www.me.berkeley.edu/gri\\_mech/](http://www.me.berkeley.edu/gri_mech/), accessed 2005.

Leonard, G. and Stegmaier, J. "Development of an Aeroderivative Gas Turbine Dry Low Emissions Combustion System," *ASME Journal of Engineering for Gas Turbines and Power*, vol. 116, pp. 542-546, 1994.

Haworth, Naomi L.; Mackie, John C.; Bacskey, George B. "An ab initio quantum chemical and kinetic study of the NNH + O reaction potential energy surface: How important is this route to NO in combustion?," *Journal of Physical Chemistry A*, v 107, n 35, pp. 6792-6803, 2003.

Hogg, S. and M. A. Leschziner. "Computation of highly swirling confined flow with a Reynolds stress turbulence model," *AIAA J.* 27 (1), pp. 57-63, 1989.

Jones, W. P., and Lindstedt, R.P., *Combustion and Flame*, 73, pp. 233, 1988.

Kee, R.J., G. Dixon-Lewis, J. Warnatz, M.E. Coltrin, J.A. Miller, "A Fortran computer code package for the evaluation of gas-phase multi-component transport properties," *Technical Report SAND86-8246*, Sandia National Laboratories, 1986.

A.A. Konnov, J. De Ruyck, *Combust. Sci. Technol.*, 168, 2001.

A.A. Konnov, J. De Ruyck, *Combust. Flame*, 125, pp. 1258, 2001.

Koufopoulos, C.A. "Modelling of the Pyrolysis of Biomass Particles. Studies on Kinetics, Thermal and Heat Transfer Effects," *The Canadian Journal of Chemical Engineering*, 69, pp. 907-915, 1991.

B. E. Launder. "Second-Moment Closure: Present... and Future?," *Inter. J. Heat Fluid Flow*, 10(4), pp. 282-300, 1989.

Launder, B.E., Reece, G. J. and Rodi, W. "Progress in the Development of a Reynolds-Stress Turbulence Closure," *J. Fluid Mech.*, 68(3), pp. 537-566, April 1975

Lee, J.C.Y., Malte, P.C., Benjamin, M.A., *J. Eng. Gas Turbine Power* 125 (4), pp. 761-771, 2003.

Lee, J.C.Y. "Reduction of NO<sub>x</sub> Emission for Lean Prevaporized-Premixed Combustors," *PhD Thesis*, University of Washington, Seattle, WA, 2000.

Levenspiel, O. "Chemical Reaction Engineering," Second Edition, *John Wiley & Sons, Inc.*, pp. 253-325, 1972.

Liden, C.K., F. Berruti, and D.S. Scott, "A kinetic model for the production of liquids from the flash pyrolysis of biomass," *Chemical Engineering Communications*, 65: pp. 207-221, 1988.

Lien F. S., and Leschziner M. A. "Assessment of Turbulent Transport Models Including Non-Linear RNG Eddy-Viscosity Formulation and Second-Moment Closure," *Computers and Fluids*, 23(8):983-1004, 1994.

Longwell, J. P., and Weiss, M. A., "High Temperature Reaction Rates in Hydrocarbon Combustion," *Industrial and Engineering Chemistry*, 47(8), pp.1634-1643, 1955.

Magnussen, B. F. and Hjetager, B. H., "On Mathematical Models of Turbulent Combustion with Special Emphasis on Soot Formation and Combustion," *Sixteen Symposium (International) on Combustion*, pages 719-729, The Combustion Institute, Pittsburgh, PA, 1977.

Malte P.C., Pratt D.T., Nicol, D.G., Tonouchi J.H., and Steele R.C., "The Chemical Reactor Modeling: Subtask 1.3," Section 4.0 in Mellor, A.M., Editor. "NO<sub>x</sub> and CO Emissions Models for Gas-Fired, Lean Premixed Combustion Turbine: Semi-Annual Report 2," Vanderbilt University, Nashville, TN, 1995.

Malte, P.C., Nicol, D.G. "CFD Modeling of Combustor A with Evaluation of the Five-Step Mechanism for Methane Oxidation with Nitric Oxide Formation." *Report to Solar Turbine, Inc., San Diego, California*, 2000.

Malte P.C., Nicol D.G. and Rutar T., "Development of a Model for Predicting the NO<sub>x</sub> Emissions of Burners Fired with Sawdust and Sanderdust High in Nitrogen," *Report for Weyerhaeuser Technology Center* (1996).

Malte P.C., Nicol D.G., "Engineering Analysis of NO<sub>x</sub> Formation in Wood Dust Burner: Application to the Marshfield Plant," *Report for Weyerhaeuser Technology Center*, 1997.

Malte P.C., Lee J.C.Y, and Benjamin M.A., "Low NO<sub>x</sub> Combustion for Liquid Fuels: Atmospheric Pressure Experiments Using a Staged Prevaporizer-

Premixer,” *Transactions of the ASME, Journal of Engineering for Gas Turbines and Power*, Vol. 125, pp. 861-871, 2003.

Mellor, A.M., Editor. “NO<sub>x</sub> and CO Emissions Models for Gas-Fired, Lean Premixed Combustion Turbine: Final Report,” Vanderbilt University, Nashville, TN, 1996.

Miller, J.A. and Bowman, C.T., *Prog. In Energy and Combust. Science*, 15:287, 1989.

Nichols, K., Weyerhaeuser Technology Center, *Personal communication*, 2004.

Nicol, D.G. “A Chemical and Numerical Study of NO<sub>x</sub> and Pollutant Formation in Low-Emission Combustion,” *Ph.D. Dissertation, University of Washington*, Seattle, WA, 1995.

Nicol, D.G., “The Chemical Reactor Model Combustion Code,” Section 4.6 in Mellor, A.M., Editor. “NO<sub>x</sub> and CO Emissions Models for Gas-Fired, Lean Premixed Combustion Turbine: Final Report,” Vanderbilt University, Nashville, TN, 1996.

Niksa, S. and Liu G.-S., *Fuel*, 81(18), 2371-85, 2002.

Niksa S, Liu G-S. “Advanced CFD post-processing for pulverized fuel flame structure and emissions,” *International Joint Power Generation Conference*, Phoenix, AZ: ASME; paper No. IJPGC2002–26136, 2002.

Niksa, S.; Liu, G.-S.; Felix, L. G.; Bush, P. V.; and Boylan, D. M. "Predicting NOX Emissions from Biomass Cofiring," *28th Int. Technical Conf. on Coal Utilization and Fuel Systems*, Coal Technology Assoc., Clearwater, FL, March, 2003.

Novosselov, I.V. "Eight-Step Global Kinetic Mechanism of Methane Oxidation with Nitric Oxide Formation for Lean Premixed Combustion Turbines." *MSME Thesis, University of Washington*, Seattle, WA, 2002.

Novosselov, I.V. and Malte, P.C., <http://faculty.washington.edu/malte/pubs/8-step.pdf>, 2005.

Parish M., NOx Conversion of Wood Dust High in Nitrogen Content *Master Thesis, University of Washington*, Seattle, WA, 1998.

Peters, N., *Turbulent Combustion*, Cambridge University Press, 2000.

Pedersen LS, Glarborg P, et al. "A chemical engineering model for predicting NO emissions and burnout from pulverized coal flames," *Combustion Science and Technology*; pp.132:251–314, 1998.

Pope, S. "PDF methods for turbulent reactive flows," *Progress in Energy and Combustion Science* 11, 1985.

Pratt, D.T. "Calculation of Chemically Reactive Flows with Complex chemistry," in *Studies in Convection*, Vol. 2, B.E. Launder, Editor, Academic Press, 1997.

Pratt, D.T. and Wormeck, J.D., "CREK, Combustion Reaction Equilibrium and Kinetics in Laminar and Turbulent Flows," *Report TEL-76-1*, Department of Mechanical Engineering, Washington State University, Pullman, WA, 1976.

Pratt, D. T., and Radhakrishnan, K. "CREK1D: A COMPUTER CODE FOR TRANSIENT, GAS-PHASE COMBUSTION KINETICS," *NASA Technical Memorandum*, Oct, 1984.

Radhakrishnan, K. and Pratt, D. T. "Fast Algorithm for Calculating Chemical Kinetics in Turbulent Reacting Flows", *Comb. Sci. Tech.*, pp. 155-176, 1988.

Robertus, R.J.; Nielsen, K.L.; Crowe, C.T.; Pratt, D.T. "ATTEMPT TO REDUCE NO<sub>x</sub> EMISSIONS FROM PULVERIZED COAL FURNACES," *Environmental Science and Technology*, v9, n9, pp. 859-862, 1975.

Roby R. J.; Klassen M.S.; Vashistat D.; Joklik R.; Marshall A. "High Fuel-Air Ratio (FAR) Combustor Modeling," *Report to Naval Air Warfare Center*, 2003.

Rubins, P. M. and Pratt, D. T. "Zone Combustion Model Development and Use: Application to Emissions Control," *American Society of Mechanical Engineers*, 91-JPGC-FACT-25, 1991.

Rutar, T., Malte, P. C., and Kramlich, J. C. "Investigation of NO<sub>x</sub> and CO Formation in Lean Premixed, Methane-Air, High-Intensity, Confined Flames at Elevated Pressures," *Proc. Combust. Inst.*, 28, pp. 2435–2441, 2000.

Rutar, T. and Malte, P.C. "NO<sub>x</sub> Formation in High-Pressure Jet-Stirred Reactors with Significance to Lean-Premixed Combustion Turbines," *ASME Journal of Engineering for Gas Turbines and Power*, 124, pp. 776-783, 2002.

Rutar-Shuman, T. "NO<sub>x</sub> and CO Formation for Lean-Premixed Methane-Air Combustion in a Jet-Stirred Reactor Operated at Elevated Pressure," *Ph.D. Dissertation, University of Washington, Seattle, WA*, 2000.

Scharfe, F. "Laboratory Sanderdust Burner Measurements for High and Low Nitrogen Fuels," *Thesis, University of Stuttgart, Stuttgart, Germany*, 1998.

Schlegel, A.; Benz, P.; Griffin, T.; Weisenstein, W.; Bockhorn, H. "Catalytic Stabilization of Lean Premixed Combustion: Method for Improving NO<sub>x</sub> Emissions," *Combustion and Flame*, 105, no. 3, pp. 332-340, 1996.

Smith, T. F, Shen, Z. F. and Friedman, J. N. "Evaluation of Coefficients for the Weighted Sum of Gray Gases Model," *J. Heat Transfer*, 104:602-608, 1982.

Spalart, P.R. and Allmaras, S.R., *Rech. Aerospatiale* 1, pp. 5–21, 1994.

Speziale, C.G., Sarkar, S., and Gatski, T.B. "Modelling the Pressure-Strain Correlation of Turbulence: An Invariant Dynamical Systems Approach," *J. Fluid Mech.*, 227, pp. 245-272, 1991.

Steele R.C. "NO<sub>x</sub> and N<sub>2</sub>O in Lean-Premixed Jet Stirred Reactors Operated from 1 to 7 atm," *Ph.D. Dissertation, University of Washington, Seattle, WA*, 1995.

Steele, Robert C. Tonouchi, Jon H.; Nicol, David G.; Horning, David C.; Malte, Philip C.; Pratt, David T. "Characterization of NO<sub>x</sub>, N<sub>2</sub>O, and CO for lean-premixed combustion in a high-pressure jet-stirred reactor," *American Society of Mechanical Engineers (Paper)*, 96-GT-128, 1996.

Sturgess, G.J.; Heneghan, S.P.; Vangsness, M.D.; Ballal, D.R.; Lesmerises, A.L., "Lean Blowout in a Research Combustor at Simulated Low Pressures," *American Society of Mechanical Engineers (Paper)*, 91-GT-359, 1991.

Sturgess, G.. and Shouse, D.T. "A Hybrid Model for Calculating Lean Blow-outs in Practical Combustors," *AIAA Paper No. 96-3125*, 1996.

Sturgess, G.J. "Assessment of an Abbreviated Jet-A/JP-5/JP-8 Reaction Mechanism for Modeling Gas Turbine Engine Gaseous Emissions," *AIAA Paper No. 97-2709*, 1997.

Swithenbank, J. "Combustion Fundamentals," *AFOSR 70-2110 TR*, 1970.

Taylor, P. B. and Foster, P. J. "Some Gray Weighting Coefficients for CO<sub>2</sub>-H<sub>2</sub>O-Soot Mixtures," *Int. J. Heat Transfer*, 18, pp. 1331-1332, 1974.

Tomeczek, J., Gradon, P. J. "The role of N<sub>2</sub>O and NNH in the formation of NO via HCN in hydrocarbon flames," *Combustion and Flame*, v133, n3, pp. 311-322, 2003.

Tonouchi, J.H. "Macromixing in Lean Premixed Combustion," *PhD Thesis*, University of Washington, Seattle, WA, 1996.

Tonouchi, J.H. and Pratt D.T., "A Finite-Rate Macromixing Model for Premixed Combustion," *Paper No 95F-167 presented at the Fall Meeting of the Western States Section of the Combustion Institute*, Stanford, CA, 1995.

Thurner, F., and Mann "Kinetic investigation of wood pyrolysis," *Industrial & engineering Chemistry Research*, 20(3), pp.482-488, 1981.

Turns, S.R. "An Introduction to Combustion," *McGraw-Hill*, 2000.

Westbrook, C.K., and Dryer, F.L., *Prog. Progress in Energy and Combustion Science*, 10:1, 1984.

Wilcox, D. C. "Turbulence Modeling for CFD," *DCW Industries, Inc*, 1993.

Wormeck, J.J. "Computer Modeling of Turbulent Combustion in a Longwell Jet-Stirred Reactor," *PhD Thesis, Washington State University*, 1976.

## **Appendix 1: University of Washington Chemical Kinetic Code**

### ***Introduction***

The present form of the UW chemical kinetic code has evolved from the work of Pratt and Wormeck (1976), and Pratt (1977), who developed a computer program designated for Combustion Reaction Equilibrium and Kinetics (CREK). Later work by Pratt and Radhakrishnan, (1984) and Radhakrishnan and Pratt, (1988) updated the convergence algorithms used in the CREK code. Nicol, (1996) added additional capabilities to the code, namely:

- Non-adiabatic PSR and PFR capability
- Ability to use pressure dependent reactions in formats of Lindermann (1992), Troe (Gilbert et al., 1983), SRI (Stewart et al., 1989) and Tsang-Herron (1991)
- Increased maximum allowable number of reactors (up to 25)
- Ability to use chemical kinetic rates in the global format, where the reaction rates may have non-integer species dependence
- Multiple independent fuel composition and temperature input in each element.

In order to perform the calculations described in this work a few other changes to the code are made:

- Modification in the subroutine calculating global chemical reaction rates allowing the use of the eight-step global mechanism, including the global mechanism with mixing controlled initial rate
- Increased maximum number of reactors (up to 100).

The UW chemical kinetic code uses three main types of elements: PSR, PFR, and MIX. Each element type is described below:

- PSR stands for perfectly stirred reactor (i.e., a continuously stirred tank reactor), in which mixing to the molecular scale is assumed to happen instantaneously compared to chemical reaction. The chemical reaction occurs homogeneously in the reactor.
- PFR stands for plug flow reactor, in which the flow is assumed to move as a plug and the chemical reaction proceeds one-dimensionally; longitudinal mixing in the reactor is assumed to be zero.
- MIX stands for an element in which the entering streams are uniformly mixed without chemical reaction.

The solution of the steady state PSR is obtained by balancing the Arrhenius source term of net production of each chemical species with the convective removal of that species from the control volume. The resulting matrix of non-linear algebraic equations is solved iteratively by a method of under-relaxed Newton iteration. The detailed description of the convergence algorithms can be found in Pratt and Wormeck (1976), and Pratt (1977), Pratt and Radhakrishnan, (1984), and Radhakrishnan and Pratt, (1988). The mathematical model for the PFR reactor is described in Radhakrishnan and Pratt (1988).

Five types of PRS and four types of PFR elements can be used in the code. Detailed mathematical models and solution algorithms used in the code for these elements can be found in Nicol (1995). These elements are:

- PSR – adiabatic perfectly stirred reactor with residence time based on the input of the mass flows, volume, and calculated temperature
- PSB - adiabatic perfectly stirred reactor operated at blowout plus 1% percent of volume
- PSX – adiabatic perfectly stirred reactor with the input of the mass flows and with the assigned residence time
- PST – non-adiabatic perfectly stirred reactor with the input of the mass flows and volume and with the assigned temperature
- PSZ - non-adiabatic perfectly stirred reactor with the input of the mass flows and with the assigned temperature and residence time
- PFR – adiabatic plug flow reactor with residence time based on the input of the mass flows and volume, and calculated temperature
- PFX – adiabatic plug flow reactor with the input of the mass flows and with the assigned residence time
- PFT – non-adiabatic plug flow reactor with the input of the mass flows and volume and with the assigned temperature
- PFZ - non-adiabatic plug flow reactor with the input of the mass flows and with the assigned temperature and residence time

### ***Code Networking Capabilities***

The UW chemical kinetic code finds the steady state solution for a complex network of chemical reactor elements. Arrangement of the flow reactors in the code is based on the nodal network configuration. Each reactor has an inlet and outlet node. In a case of the elements connected in series, the outlet node of the first element becomes in the inlet node of the second element. Figure A1-1 shows the arrangement for a simple two PSR in-series model. In

the solution procedure for multiple reactors, the code finds an iterative solution for one reactor at a time, and then this solution becomes an input for the second reactor. The second element can have the addition of fuel and air into it. This approach has a great advantage over “solve everything at once” scenario when a large network of elements is considered. The solving everything at once approach is used in some commercially available codes, and normally results in a slow convergence time. For example, the execution time for 31 element CRN using CHEMKIN 4.0 software is 50 -100 times slower than using UW chemical kinetic code.

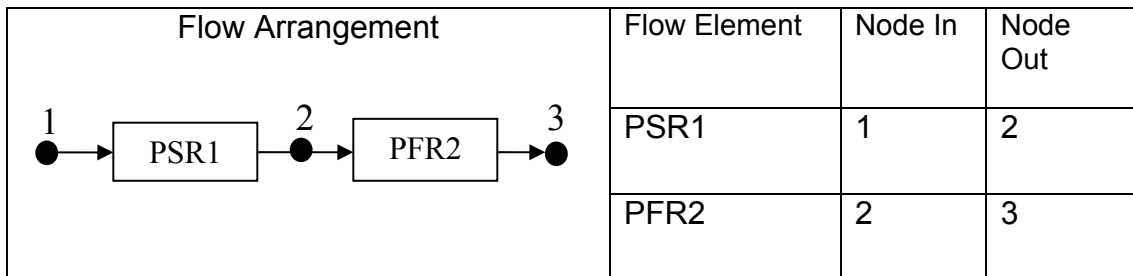


**Figure A1-0-1 Nodal diagram for two reactor in series arrangement**

The flow elements can also be arranged as parallel streams as shown in figure A1-2. The flow fractions entering each element must be specified in this case. The sum of the flow fractions should between elements 1 and 2 must be equal to unity.

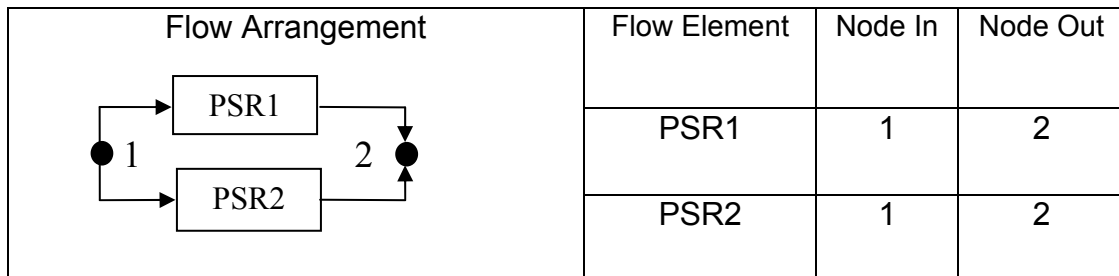


**Figure A1-0-2 Nodal diagram for two reactor in series arrangement**

The other important building block for the CRN is the recycle (back-mixed) element. This element can be MIX, PSR, or PFR. The recycle element's inlet node has a higher number than its outlet node. The flow fraction entering the recycle element must be specified similarly to the parallel flow scenario.

Figure A1-3 shows an example of the reactor arrangement with a recycle element.

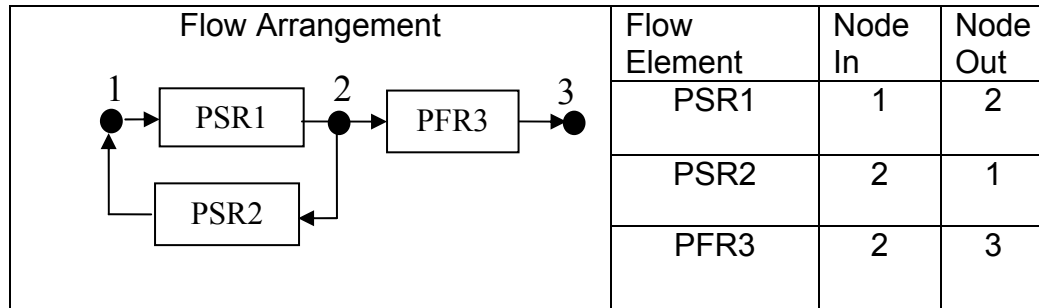


Figure A1-0-3 Nodal diagram for three reactor arrangement including a recycle element

### ***Input Data File***

Information about the number and types of elements, nodal configuration, and flow fractions in each element is specified in the input data file. In addition to the flow element arrangement, the data file must contain the following inputs:

- Elemental composition of the species
- Thermo-chemical species data
- Chemical kinetic mechanism
- Operating pressure
- Inlet fuel temperature
- Inlet air temperature
- Mass flow rates of fuel
- Mass flow rates of air

The detailed description about the formats and the input parameters to the UW chemical kinetic code can be found Malte et al. (1995)

## Appendix 2: Turbulent Mixing Rate for Use in Global Mechanism and Limiting Rate Approach

In the context of the GT combustor, the oxidation rate of the initial fuel is controlled by the Arrhenius reaction rate but most likely by the turbulent mixing rate. This approach was employed by Magnussen and Hjertager, 1976 in their Eddy Break-Up (EBU) approach. In this case, the two competing rates are:

$$R_{\text{CH}_4 \text{ destruction EBU}} - \text{turbulent mixing rate}$$

$$R_{\text{CH}_4 \text{ destruction kinetic}} - \text{Arrhenius reaction rate}$$

In the limiting reaction rate situation:

$$1 / R_{\text{CH}_4 \text{ destruction}} = 1 / R_{\text{CH}_4 \text{ destruction EBU}} + 1 / R_{\text{CH}_4 \text{ destruction kinetic}} \quad [\text{A2-1}]$$

$$R_{\text{CH}_4 \text{ destruction}} = (R_{\text{CH}_4 \text{ destruction EBU}} + R_{\text{CH}_4 \text{ destruction kin}}) / (R_{\text{CH}_4 \text{ destruction EBU}} R_{\text{CH}_4 \text{ destruction kin}}) \quad [\text{A2-2}]$$

When the turbulent mixing rate is orders of magnitude smaller than the chemical kinetic rate:

$$R_{\text{CH}_4 \text{ destruction EBU}} = A_{\text{EBU}} \epsilon / k [\text{CH}_4] \ll R_{\text{CH}_4 \text{ destruction kinetic}} = 10^{13.354-0.004628 \times P} [\text{CH}_4]^{1.3-0.01148 \times P} [\text{O}_2]^{0.01426} [\text{CO}]^{0.1987} \exp(-(21932+269.4 \times P)/T), \quad [\text{A2-3}]$$

where:

$$\begin{aligned}\varepsilon &= \text{turbulent dissipation rate, m}^2/\text{s}^3 \\ k &= \text{turbulent kinetic energy, m}^2/\text{s}^2\end{aligned}$$

$$R_{\text{CH}_4 \text{ destruction}} = R_{\text{CH}_4 \text{ destruction EBU}} \cdot \quad [\text{A2-4}]$$

In this case, the global reaction rate can be expressed in terms of EBU rate. In general, the global chemical kinetic mechanism reaction rates are written as:

$$R_i = d[X]/dt = 10^{a_j} T^m e^{-E_a/RT} [X]^x [Y]^y, \quad [\text{A2-5}]$$

where:

$$\begin{aligned}10^{a_j} &= \text{pre-exponential factor} \\ T &= \text{temperature} \\ E_a &= \text{activation energy of the reaction} \\ [X] &= \text{concentration of species X} \\ [Y] &= \text{concentration of species Y}\end{aligned}$$

The eddy break-up rate explicitly depends only on the concentration of the limiting species to the first power and the turbulent mixing coefficient. Thus, the global rate of the reaction is simplified as:

$$R_1 = d[X]/dt = A_j [X] = 10^{a_1} [\text{CH}_4], \quad [\text{A2-6}]$$

where:

$$\begin{aligned}A_j &= \text{pre-exponential factor} \\ [X] &= \text{limiting species concentration}\end{aligned}$$

In order to obtain the pre-exponential term, one needs to analyze the average parameters of the flow field in the region of flame front. The data ( $k$ ,  $\epsilon$ , and the reaction rate) for calculating the pre-exponential term should be obtained from the CFD solution. Based on the CFD computation for the generic, can-type combustor, the coefficient  $A$  does not change significantly in the flame zone. The pre-exponential factor for the reaction is in the range  $A=10^{(3.5-4.5)}$ . In this study the pre-exponential factor is estimated based on the generic, can-type combustor CFD solution: the recommended value for use in the global reaction format is taken to be  $A=10^4$ . Then the methane oxidation rate becomes:

$$R_1=10^4 \times [\text{CH}_4]. \quad [\text{A2-7}]$$

This approach can be used for the any hydrocarbon fuel as an initial fuel break down step to CO and H<sub>2</sub>O, when global rates are applied in the chemical reactor code.

## Appendix 3: CRN Sample Calculation

### *Generic, Single-Injector, Can-type Combustor*

The calculations are performed using the 31-element chemical reactor network for the single-injector can-type combustor as described in Chapter 6.

This sample shows the input and output of the UW chemical reactor code.

The boundary conditions for this run correspond to methane combustion with uniform fuel-air injector distribution and neutral pilot.

**Table A3-1. Input for the UW chemical kinetic code for 31-element CRN.**

*** INPUT DATA ***								
ELEM	NODE	NODE	ELEM	AREA	LENGTH	IN AIR	IN FUEL1	IN FLOW
#	IN	OUT	TYPE	(SQ.IN)	(INCHES)	(LBM/S)	(LBM/S)	FRACTION
1	1	2	MIX	4.00E+00	1.00E+00	2.41E+00	0.00E+00	1.00E+00
2	2	6	PSR	1.00E+00	1.00E+00	0.00E+00	0.00E+00	8.37E-01
3	2	3	PSR	1.00E+00	1.00E+00	0.00E+00	0.00E+00	1.63E-01
4	3	4	PSR	2.00E+00	2.00E-01	7.46E-02	2.06E-03	1.00E-03
5	4	5	PSR	4.00E+00	1.00E-01	0.00E+00	0.00E+00	9.00E-01
6	4	12	PFR	1.50E+00	2.00E+00	0.00E+00	0.00E+00	1.00E-01
7	5	13	PFR	2.50E+01	4.50E+00	0.00E+00	0.00E+00	1.00E+00
8	3	8	MIX	1.00E+00	2.00E+00	0.00E+00	1.09E-02	9.99E-01
9	8	9	MIX	1.00E+00	1.00E+00	0.00E+00	0.00E+00	1.00E+00
10	9	12	MIX	1.50E+00	4.00E-01	0.00E+00	0.00E+00	7.50E-01
11	9	10	MIX	1.00E+00	1.00E+00	0.00E+00	0.00E+00	2.50E-01
12	12	13	PSR	6.00E+00	1.00E+00	0.00E+00	0.00E+00	1.00E+00
13	13	16	PSR	1.40E+01	1.60E+00	0.00E+00	0.00E+00	1.00E+00
14	6	11	MIX	1.00E+00	1.00E+00	0.00E+00	2.07E-02	3.70E-01
15	11	16	PSB	3.60E+00	4.94E-01	0.00E+00	0.00E+00	1.00E+00
16	6	7	MIX	1.00E+00	1.00E+00	0.00E+00	3.52E-02	6.30E-01
17	7	10	MIX	1.00E+00	1.00E+00	0.00E+00	0.00E+00	9.00E-01
18	7	8	PSR	1.00E+00	1.00E+00	0.00E+00	0.00E+00	1.00E-01
19	10	14	PSR	1.40E+01	6.80E-01	0.00E+00	0.00E+00	1.00E+00
20	14	15	PSR	1.70E+01	3.00E+00	9.94E-02	0.00E+00	1.00E+00
21	15	20	PFR	6.60E+00	6.00E+00	0.00E+00	0.00E+00	5.00E-01
22	15	16	MIX	1.00E+00	1.00E+00	0.00E+00	0.00E+00	5.00E-01
23	16	17	PSR	2.50E+01	1.00E+00	0.00E+00	0.00E+00	1.00E+00
24	17	18	PFR	1.30E+01	2.30E+00	0.00E+00	0.00E+00	9.90E-01
25	17	10	PSR	3.50E+00	1.50E+00	0.00E+00	0.00E+00	1.00E-02
26	18	20	PFR	2.60E+01	1.50E+00	0.00E+00	0.00E+00	7.00E-01
27	18	19	PFR	1.00E+01	4.00E+00	0.00E+00	0.00E+00	3.00E-01
28	19	4	MIX	1.00E+00	1.00E+00	0.00E+00	0.00E+00	1.00E-01
29	19	5	MIX	1.00E+00	1.00E+00	0.00E+00	0.00E+00	9.00E-01
30	20	21	PFR	3.20E+01	1.50E+00	0.00E+00	0.00E+00	1.00E+00
31	21	22	MIX	1.70E+01	3.00E+00	0.00E+00	0.00E+00	1.00E+00

**Table A3-2 Output data from UW chemical kinetic code for 31-element CRN**

*** OUTPUT ***									
TEMP AND COMPOSITION FOR MARK-II MODEL:									
PRESSURE=1.6000E+01 ATM					OVERALL E.R.=4.5605E-01				
FUEL FLOW = 2.4784E+02 LBM/HR					AIR FLOW=2.5854E+00 LBM/SEC				
ELEMENT_NO.	1	2	3	4	5	6	7	8	
ELEMENT_TYPE	MIX	PSR	PSR	PSR	PSR	PFR	PFR	MIX	
EQUIV_RATIO	0.00E+00	0.00E+00	0.00E+00	4.72E-01	4.67E-01	4.67E-01	4.63E-01	4.75E-01	
RES_TIME,SEC	4.92E-04	1.47E-04	7.54E-04	6.06E-04	3.20E-04	2.16E-02	1.46E-02	1.44E-03	
AREA,SQ_IN	4.00E+00	1.00E+00	1.00E+00	2.00E+00	4.00E+00	1.50E+00	2.50E+01	1.00E+00	
VELO,FT/SEC	1.70E+02	5.68E+02	1.11E+02	2.75E+01	2.61E+01	7.73E+00	2.57E+01	1.16E+02	
FLOW,LBM/SEC	2.41E+00	2.02E+00	3.93E-01	7.70E-02	1.44E-01	1.60E-02	8.91E-01	4.04E-01	
LENGTH,IN	1.00E+00	1.00E+00	1.00E+00	2.00E-01	1.00E-01	2.00E+00	4.50E+00	2.00E+00	
ENTH,BTU/LBM	1.73E+02	1.73E+02	1.73E+02	1.28E+02	1.28E+02	1.28E+02	1.29E+02	1.28E+02	
TEMP_EFF	-3.87E-02	-3.87E-02	-3.87E-02	9.69E-01	1.00E+00	1.01E+00	1.01E+00	-5.62E-05	
TEMP,K	6.86E+02	6.86E+02	6.86E+02	1.70E+03	1.73E+03	1.73E+03	1.72E+03	6.86E+02	
MIN.REACTION	9.90E-16	6.01E-13	6.01E-13	9.90E-16	9.90E-16	9.90E-16	9.90E-16	6.01E-13	
ELEMENT_NO.	9	10	11	12	13	14	15	16	
ELEMENT_TYPE	MIX	MIX	MIX	PSR	PSR	MIX	PSB	MIX	
EQUIV_RATIO	4.74E-01	4.74E-01	4.74E-01	4.74E-01	4.66E-01	4.75E-01	4.75E-01	4.74E-01	
RES_TIME,SEC	3.90E-04	3.12E-04	1.56E-03	1.65E-03	1.97E-03	3.78E-04	2.86E-04	2.22E-04	
AREA,SQ_IN	1.00E+00	1.50E+00	1.00E+00	6.00E+00	1.40E+01	1.00E+00	3.60E+00	1.00E+00	
VELO,FT/SEC	2.14E+02	1.07E+02	5.34E+01	5.05E+01	6.77E+01	2.20E+02	1.44E+02	3.75E+02	
FLOW,LBM/SEC	5.34E-01	4.01E-01	1.34E-01	4.17E-01	1.31E+00	7.68E-01	7.68E-01	1.31E+00	
LENGTH,IN	1.00E+00	4.00E-01	1.00E+00	1.00E+00	1.60E+00	1.00E+00	4.94E-01	1.00E+00	
ENTH,BTU/LBM	1.28E+02	1.28E+02	1.28E+02	1.28E+02	1.28E+02	1.28E+02	1.28E+02	1.28E+02	
TEMP_EFF	2.55E-01	2.55E-01	2.55E-01	9.95E-01	1.01E+00	-5.62E-05	8.70E-01	-5.62E-05	
TEMP,K	9.55E+02	9.55E+02	9.55E+02	1.73E+03	1.73E+03	6.86E+02	1.60E+03	6.86E+02	
MIN.REACTION	9.90E-16	9.90E-16	9.90E-16	9.90E-16	9.90E-16	9.90E-16	9.90E-16	9.90E-16	
ELEMENT_NO.	17	18	19	20	21	22	23	24	
ELEMENT_TYPE	MIX	PSR	PSR	PSR	PFR	MIX	PSR	PFR	
EQUIV_RATIO	4.74E-01	4.74E-01	4.74E-01	4.40E-01	4.40E-01	4.40E-01	4.62E-01	4.62E-01	
RES_TIME,SEC	2.47E-04	8.84E-04	8.23E-04	4.21E-03	6.53E-03	1.65E-04	1.04E-03	1.25E-03	
AREA,SQ_IN	1.00E+00	1.00E+00	1.40E+01	1.70E+01	6.60E+00	1.00E+00	2.50E+01	1.30E+01	
VELO,FT/SEC	3.38E+02	9.43E+01	6.89E+01	5.94E+01	7.65E+01	5.05E+02	8.05E+01	1.53E+02	
FLOW,LBM/SEC	1.18E+00	1.31E-01	1.34E+00	1.44E+00	7.19E-01	7.19E-01	2.79E+00	2.77E+00	
LENGTH,IN	1.00E+00	1.00E+00	6.80E-01	3.00E+00	6.00E+00	1.00E+00	1.00E+00	2.30E+00	
ENTH,BTU/LBM	1.28E+02	1.28E+02	1.28E+02	1.31E+02	1.31E+02	1.31E+02	1.29E+02	1.29E+02	
TEMP_EFF	-5.61E-05	9.81E-01	1.01E+00	1.01E+00	1.01E+00	1.01E+00	1.01E+00	1.01E+00	
TEMP,K	6.86E+02	1.72E+03	1.72E+03	1.68E+03	1.68E+03	1.68E+03	1.72E+03	1.72E+03	
MIN.REACTION	9.90E-16	9.90E-16	9.90E-16	9.90E-16	9.90E-16	9.90E-16	9.90E-16	9.90E-16	
ELEMENT_NO.	25	26	27	28	29	30	31	EQL	
ELEMENT_TYPE	PSR	PFR	PFR	MIX	MIX	PFR	MIX	EQL	
EQUIV_RATIO	4.62E-01	4.62E-01	4.62E-01	4.62E-01	4.62E-01	4.56E-01	4.56E-01	4.56E-01	
RES_TIME,SEC	2.17E-02	2.33E-03	5.57E-03	1.39E-03	1.55E-04	2.10E-03	2.24E-03	0.00E+00	
AREA,SQ_IN	3.50E+00	2.60E+01	1.00E+01	1.00E+00	1.00E+00	3.20E+01	1.70E+01	0.00E+00	
VELO,FT/SEC	5.76E+00	5.37E+01	5.98E+01	5.98E+01	5.38E+02	5.94E+01	1.12E+02	0.00E+00	
FLOW,LBM/SEC	2.79E-02	1.94E+00	8.30E-01	8.30E-02	7.47E-01	2.65E+00	2.65E+00	2.65E+00	
LENGTH,IN	1.50E+00	1.50E+00	4.00E+00	1.00E+00	1.00E+00	1.50E+00	3.00E+00	0.00E+00	
ENTH,BTU/LBM	1.29E+02	1.29E+02	1.29E+02	1.29E+02	1.29E+02	1.29E+02	1.29E+02	1.29E+02	
TEMP_EFF	1.01E+00	1.01E+00	1.01E+00	1.01E+00	1.01E+00	1.01E+00	1.01E+00	1.44E+07	
TEMP,K	1.72E+03	1.72E+03	1.72E+03	1.72E+03	1.72E+03	1.71E+03	1.71E+03	1.71E+03	
MIN.REACTION	9.90E-16	9.90E-16	9.90E-16	9.90E-16	9.90E-16	9.90E-16	9.90E-16	1.00E+00	

Table A3-2 (continued)

MOLE FRACTIONS X(I)						
SPECIES_"I"	1	2	3	4	5	6
C	0.00E+00	2.89E-19	2.89E-19	3.66E-14	1.33E-17	2.83E-19
CH	0.00E+00	2.89E-19	2.89E-19	1.45E-10	8.74E-13	2.83E-19
CH2	0.00E+00	2.89E-19	2.89E-19	1.88E-07	1.76E-09	6.55E-17
CH2CHO	0.00E+00	2.89E-19	2.89E-19	5.72E-09	3.73E-11	2.83E-19
CH2CO	0.00E+00	2.89E-19	2.89E-19	2.46E-06	4.66E-08	2.12E-14
CH2O	0.00E+00	2.89E-19	2.89E-19	3.71E-05	4.32E-07	3.20E-15
CH2OH	0.00E+00	2.89E-19	2.89E-19	3.40E-08	3.09E-10	5.19E-19
CH2(S)	0.00E+00	2.89E-19	2.89E-19	1.82E-08	1.69E-10	1.56E-18
CH3	0.00E+00	2.89E-19	2.89E-19	4.37E-05	5.26E-07	7.74E-16
CH3CHO	0.00E+00	2.89E-19	2.89E-19	1.10E-07	7.40E-10	2.83E-19
CH3O	0.00E+00	2.89E-19	2.89E-19	6.66E-08	4.62E-10	7.34E-19
CH3OH	0.00E+00	2.89E-19	2.89E-19	1.26E-05	1.89E-07	4.88E-16
CH4	0.00E+00	2.89E-19	2.89E-19	3.19E-04	2.89E-06	1.10E-15
CN	0.00E+00	2.89E-19	2.89E-19	2.70E-12	4.43E-14	1.22E-16
CO	0.00E+00	2.89E-19	2.89E-19	3.68E-03	3.78E-04	3.50E-06
CO2	0.00E+00	2.89E-19	2.89E-19	4.30E-02	4.63E-02	4.67E-02
C2H	0.00E+00	2.89E-19	2.89E-19	1.45E-10	4.97E-12	2.39E-17
C2H2	0.00E+00	2.89E-19	2.89E-19	7.00E-07	2.89E-08	2.07E-13
C2H3	0.00E+00	2.89E-19	2.89E-19	1.18E-08	9.75E-11	2.83E-19
C2H4	0.00E+00	2.89E-19	2.89E-19	3.40E-06	3.58E-08	2.83E-19
C2H5	0.00E+00	2.89E-19	2.89E-19	6.37E-08	9.32E-11	2.83E-19
C2H6	0.00E+00	2.89E-19	2.89E-19	9.06E-07	2.08E-09	2.83E-19
C3H7	0.00E+00	2.89E-19	2.89E-19	1.03E-12	1.32E-16	2.83E-19
C3H8	0.00E+00	2.89E-19	2.89E-19	7.00E-14	2.06E-16	2.83E-19
H	0.00E+00	2.89E-19	2.89E-19	8.15E-06	4.80E-07	6.92E-08
HCCO	0.00E+00	2.89E-19	2.89E-19	1.63E-08	2.31E-10	1.52E-16
HCCOH	0.00E+00	2.89E-19	2.89E-19	1.23E-07	6.91E-08	2.27E-11
HCN	0.00E+00	2.89E-19	2.89E-19	2.87E-17	4.56E-19	2.83E-19
HCNN	0.00E+00	2.89E-19	2.89E-19	3.55E-12	1.99E-14	2.83E-19
HCNO	0.00E+00	2.89E-19	2.89E-19	1.03E-08	6.95E-09	2.37E-09
HCO	0.00E+00	2.89E-19	2.89E-19	1.48E-07	1.23E-09	2.85E-15
HNCO	0.00E+00	2.89E-19	2.89E-19	3.31E-08	6.90E-09	3.55E-11
HNO	0.00E+00	2.89E-19	2.89E-19	2.00E-10	1.56E-11	4.10E-12
HOCN	0.00E+00	2.89E-19	2.89E-19	1.07E-11	3.92E-12	1.66E-14
HO2	0.00E+00	2.89E-19	2.89E-19	3.40E-05	2.55E-06	9.47E-07
H2	0.00E+00	2.89E-19	2.89E-19	1.57E-04	1.03E-05	1.98E-06
H2CN	0.00E+00	2.89E-19	2.89E-19	5.39E-14	8.76E-16	2.83E-19
H2O	0.00E+00	2.89E-19	2.89E-19	9.30E-02	9.32E-02	9.33E-02
H2O2	0.00E+00	2.89E-19	2.89E-19	9.34E-07	1.69E-07	8.18E-08
N	0.00E+00	2.89E-19	2.89E-19	7.05E-12	1.23E-12	4.78E-13
NCO	0.00E+00	2.89E-19	2.89E-19	6.08E-10	8.36E-11	2.90E-13
NH	0.00E+00	2.89E-19	2.89E-19	7.02E-11	3.75E-12	1.27E-13
NH2	0.00E+00	2.89E-19	2.89E-19	3.38E-10	7.02E-11	4.35E-13
NH3	0.00E+00	2.89E-19	2.89E-19	1.80E-09	5.28E-10	4.88E-12
NNH	0.00E+00	2.89E-19	2.89E-19	1.84E-10	1.11E-11	1.63E-12
NO	0.00E+00	2.89E-19	2.89E-19	1.16E-06	1.80E-06	2.91E-06
NO2	0.00E+00	2.89E-19	2.89E-19	6.45E-08	2.87E-08	2.43E-08
N2	7.90E-01	7.90E-01	7.90E-01	7.51E-01	7.53E-01	7.53E-01
N2O	0.00E+00	2.89E-19	2.89E-19	2.62E-06	1.37E-06	5.19E-07
O	0.00E+00	2.89E-19	2.89E-19	4.60E-05	1.26E-05	5.05E-06
OH	0.00E+00	2.89E-19	2.89E-19	3.52E-04	2.73E-04	1.83E-04
O2	2.10E-01	2.10E-01	2.10E-01	1.08E-01	1.07E-01	1.07E-01

Table A3-2 (continued)

MOLE FRACTIONS X(I)						
SPECIES_"I"	7	8	9	10	11	12
C	2.83E-19	2.75E-19	5.37E-15	5.37E-15	5.37E-15	3.74E-15
CH	2.83E-19	2.75E-19	2.85E-11	2.85E-11	2.85E-11	4.53E-11
CH2	1.15E-16	2.75E-19	3.54E-08	3.54E-08	3.54E-08	6.36E-08
CH2CHO	2.83E-19	2.75E-19	6.38E-10	6.38E-10	6.38E-10	5.34E-10
CH2CO	1.01E-13	2.75E-19	2.75E-07	2.75E-07	2.75E-07	2.59E-07
CH2O	5.91E-15	2.75E-19	5.71E-06	5.71E-06	5.71E-06	9.69E-06
CH2OH	9.11E-19	2.75E-19	6.14E-09	6.14E-09	6.14E-09	1.04E-08
CH2(S)	2.64E-18	2.75E-19	3.42E-09	3.42E-09	3.42E-09	6.13E-09
CH3	1.49E-15	2.75E-19	7.54E-06	7.54E-06	7.54E-06	1.43E-05
CH3CHO	2.83E-19	2.75E-19	1.03E-08	1.03E-08	1.03E-08	6.18E-09
CH3O	1.34E-18	2.75E-19	9.97E-09	9.97E-09	9.97E-09	1.50E-08
CH3OH	9.18E-16	2.75E-19	2.12E-06	2.12E-06	2.12E-06	4.02E-06
CH4	2.16E-15	4.75E-02	3.59E-02	3.59E-02	3.59E-02	8.72E-05
CN	1.16E-16	2.75E-19	6.40E-13	6.40E-13	6.40E-13	1.47E-12
CO	3.19E-06	2.75E-19	5.93E-04	5.93E-04	5.93E-04	1.05E-03
CO2	4.63E-02	2.75E-19	1.09E-02	1.09E-02	1.09E-02	4.62E-02
C2H	1.06E-16	2.75E-19	2.33E-11	2.33E-11	2.33E-11	3.07E-11
C2H2	9.87E-13	2.75E-19	9.80E-08	9.80E-08	9.80E-08	1.32E-07
C2H3	2.83E-19	2.75E-19	1.49E-09	1.49E-09	1.49E-09	1.39E-09
C2H4	2.83E-19	2.75E-19	3.84E-07	3.84E-07	3.84E-07	3.76E-07
C2H5	2.83E-19	2.75E-19	7.13E-09	7.13E-09	7.13E-09	5.91E-09
C2H6	2.83E-19	2.75E-19	9.73E-08	9.73E-08	9.73E-08	8.93E-08
C3H7	2.83E-19	2.75E-19	7.83E-14	7.83E-14	7.83E-14	3.35E-14
C3H8	2.83E-19	2.75E-19	5.29E-15	5.29E-15	5.29E-15	2.57E-15
H	6.19E-08	2.75E-19	1.47E-06	1.47E-06	1.47E-06	2.61E-06
HCCO	6.66E-16	2.75E-19	2.02E-09	2.02E-09	2.02E-09	1.82E-09
HCCOH	1.14E-10	2.75E-19	2.67E-08	2.67E-08	2.67E-08	8.03E-08
HCN	2.83E-19	2.75E-19	6.90E-18	6.90E-18	6.90E-18	1.51E-17
HCNN	2.83E-19	2.75E-19	6.63E-13	6.63E-13	6.63E-13	1.01E-12
HCNO	2.54E-09	2.75E-19	3.19E-09	3.19E-09	3.19E-09	1.53E-08
HCO	2.42E-15	2.75E-19	2.42E-08	2.42E-08	2.42E-08	3.75E-08
HNCO	3.63E-11	2.75E-19	8.23E-09	8.23E-09	8.23E-09	2.53E-08
HNO	3.73E-12	2.75E-19	4.11E-11	4.11E-11	4.11E-11	8.40E-11
HOCN	2.00E-14	2.75E-19	2.86E-12	2.86E-12	2.86E-12	9.33E-12
HO2	9.12E-07	2.75E-19	5.55E-06	5.55E-06	5.55E-06	1.04E-05
H2	1.81E-06	2.75E-19	2.55E-05	2.55E-05	2.55E-05	4.60E-05
H2CN	2.83E-19	2.75E-19	1.17E-14	1.17E-14	1.17E-14	2.68E-14
H2O	9.26E-02	2.75E-19	2.30E-02	2.30E-02	2.30E-02	9.43E-02
H2O2	7.89E-08	2.75E-19	1.67E-07	1.67E-07	1.67E-07	3.96E-07
N	4.07E-13	2.75E-19	1.68E-12	1.68E-12	1.68E-12	4.12E-12
NCO	2.87E-13	2.75E-19	1.56E-10	1.56E-10	1.56E-10	4.35E-10
NH	1.10E-13	2.75E-19	1.37E-11	1.37E-11	1.37E-11	2.46E-11
NH2	4.34E-13	2.75E-19	8.18E-11	8.18E-11	8.18E-11	2.43E-10
NH3	5.02E-12	2.75E-19	4.19E-10	4.19E-10	4.19E-10	1.37E-09
NNH	1.45E-12	2.75E-19	3.37E-11	3.37E-11	3.37E-11	6.07E-11
NO	2.78E-06	2.75E-19	3.70E-07	3.70E-07	3.70E-07	1.93E-06
NO2	2.37E-08	2.75E-19	1.62E-08	1.62E-08	1.62E-08	5.83E-08
N2	7.53E-01	7.53E-01	7.52E-01	7.52E-01	7.52E-01	7.52E-01
N2O	5.08E-07	2.75E-19	6.35E-07	6.35E-07	6.35E-07	2.12E-06
O	4.70E-06	2.75E-19	1.02E-05	1.02E-05	1.02E-05	2.76E-05
OH	1.74E-04	2.75E-19	9.43E-05	9.43E-05	9.43E-05	3.64E-04
O2	1.08E-01	2.00E-01	1.77E-01	1.77E-01	1.77E-01	1.06E-01

Table A3-2 (continued)

MOLE FRACTIONS X(I)						
SPECIES_"I"	13	14	15	16	17	18
C	2.83E-19	2.75E-19	3.21E-14	2.75E-19	2.75E-19	2.19E-14
CH	1.80E-14	2.75E-19	8.64E-11	2.75E-19	2.75E-19	1.16E-10
CH2	5.32E-11	2.75E-19	1.89E-07	2.75E-19	2.75E-19	1.45E-07
CH2CHO	4.32E-13	2.75E-19	5.53E-08	2.75E-19	2.75E-19	2.61E-09
CH2CO	7.64E-10	2.75E-19	3.12E-05	2.75E-19	2.75E-19	1.12E-06
CH2O	1.97E-08	2.75E-19	1.94E-04	2.75E-19	2.75E-19	2.33E-05
CH2OH	9.22E-12	2.75E-19	4.41E-08	2.75E-19	2.75E-19	2.51E-08
CH2(S)	5.11E-12	2.75E-19	1.81E-08	2.75E-19	2.75E-19	1.40E-08
CH3	2.30E-08	2.75E-19	1.04E-04	2.75E-19	2.75E-19	3.08E-05
CH3CHO	6.39E-12	2.75E-19	1.70E-06	2.75E-19	2.75E-19	4.22E-08
CH3O	1.58E-11	2.75E-19	3.31E-07	2.75E-19	2.75E-19	4.07E-08
CH3OH	8.56E-09	2.75E-19	3.66E-05	2.75E-19	2.75E-19	8.66E-06
CH4	1.36E-07	4.75E-02	1.59E-03	4.74E-02	4.74E-02	2.03E-04
CN	2.73E-15	2.75E-19	8.10E-13	2.75E-19	2.75E-19	2.61E-12
CO	2.29E-05	2.75E-19	1.28E-02	2.75E-19	2.75E-19	2.42E-03
CO2	4.67E-02	2.75E-19	3.23E-02	2.75E-19	2.75E-19	4.47E-02
C2H	1.15E-13	2.75E-19	2.36E-10	2.75E-19	2.75E-19	9.53E-11
C2H2	9.63E-10	2.75E-19	3.74E-06	2.75E-19	2.75E-19	4.00E-07
C2H3	1.17E-12	2.75E-19	5.91E-08	2.75E-19	2.75E-19	6.07E-09
C2H4	6.20E-10	2.75E-19	4.51E-05	2.75E-19	2.75E-19	1.57E-06
C2H5	8.81E-13	2.75E-19	5.91E-07	2.75E-19	2.75E-19	2.91E-08
C2H6	2.93E-11	2.75E-19	1.50E-05	2.75E-19	2.75E-19	3.97E-07
C3H7	2.83E-19	2.75E-19	4.29E-11	2.75E-19	2.75E-19	3.20E-13
C3H8	1.17E-18	2.75E-19	5.08E-12	2.75E-19	2.75E-19	2.16E-14
H	8.46E-08	2.75E-19	1.25E-05	2.75E-19	2.75E-19	6.00E-06
HCCO	2.71E-12	2.75E-19	8.08E-08	2.75E-19	2.75E-19	8.27E-09
HCCOH	1.70E-08	2.75E-19	1.42E-07	2.75E-19	2.75E-19	1.09E-07
HCN	2.83E-19	2.75E-19	9.37E-18	2.75E-19	2.75E-19	2.73E-17
HCNN	4.06E-16	2.75E-19	2.87E-12	2.75E-19	2.75E-19	2.71E-12
HCNO	5.97E-09	2.75E-19	2.66E-09	2.75E-19	2.75E-19	1.30E-08
HCO	3.84E-11	2.75E-19	3.85E-07	2.75E-19	2.75E-19	9.87E-08
HNCO	1.28E-09	2.75E-19	1.31E-08	2.75E-19	2.75E-19	3.36E-08
HNO	4.68E-12	2.75E-19	1.35E-10	2.75E-19	2.75E-19	1.68E-10
HOCN	1.72E-12	2.75E-19	2.67E-12	2.75E-19	2.75E-19	1.17E-11
HO2	1.02E-06	2.75E-19	1.07E-04	2.75E-19	2.75E-19	2.27E-05
H2	2.39E-06	2.75E-19	6.49E-04	2.75E-19	2.75E-19	1.04E-04
H2CN	5.56E-17	2.75E-19	2.93E-14	2.75E-19	2.75E-19	4.78E-14
H2O	9.33E-02	2.75E-19	8.98E-02	2.75E-19	2.75E-19	9.39E-02
H2O2	8.67E-08	2.75E-19	3.91E-06	2.75E-19	2.75E-19	6.83E-07
N	5.17E-13	2.75E-19	2.31E-12	2.75E-19	2.75E-19	6.84E-12
NCO	1.08E-11	2.75E-19	1.48E-10	2.75E-19	2.75E-19	6.37E-10
NH	4.36E-13	2.75E-19	5.37E-11	2.75E-19	2.75E-19	5.61E-11
NH2	1.38E-11	2.75E-19	1.51E-10	2.75E-19	2.75E-19	3.34E-10
NH3	1.51E-10	2.75E-19	1.45E-09	2.75E-19	2.75E-19	1.71E-09
NNH	1.99E-12	2.75E-19	2.54E-10	2.75E-19	2.75E-19	1.38E-10
NO	2.65E-06	2.75E-19	2.41E-07	2.75E-19	2.75E-19	1.51E-06
NO2	2.34E-08	2.75E-19	3.57E-08	2.75E-19	2.75E-19	6.62E-08
N2	7.53E-01	7.53E-01	7.47E-01	7.53E-01	7.53E-01	7.52E-01
N2O	6.15E-07	2.75E-19	1.71E-06	2.75E-19	2.75E-19	2.59E-06
O	5.44E-06	2.75E-19	3.61E-05	2.75E-19	2.75E-19	4.15E-05
OH	1.89E-04	2.75E-19	1.46E-04	2.75E-19	2.75E-19	3.85E-04
O2	1.07E-01	2.00E-01	1.15E-01	2.00E-01	2.00E-01	1.07E-01

Table A3-2 (continued)

MOLE FRACTIONS X(I)						
SPECIES_"I"	19	20	21	22	23	24
C	2.27E-14	2.83E-19	2.83E-19	2.83E-19	7.45E-18	2.83E-19
CH	1.18E-10	3.83E-14	1.95E-18	3.83E-14	6.54E-13	3.11E-17
CH2	1.47E-07	1.59E-10	4.56E-15	1.59E-10	1.48E-09	4.80E-14
CH2CHO	2.75E-09	3.35E-12	2.61E-18	3.35E-12	9.49E-11	2.35E-17
CH2CO	1.18E-06	6.24E-09	1.11E-11	6.24E-09	1.22E-07	7.24E-11
CH2O	2.40E-05	8.10E-08	3.30E-13	8.10E-08	4.09E-07	2.51E-12
CH2OH	2.56E-08	2.86E-11	3.42E-17	2.86E-11	2.47E-10	3.90E-16
CH2(S)	1.42E-08	1.56E-11	9.54E-17	1.56E-11	1.41E-10	1.08E-15
CH3	3.16E-05	8.70E-08	7.81E-14	8.70E-08	4.85E-07	6.78E-13
CH3CHO	4.49E-08	7.67E-11	2.83E-19	7.67E-11	2.24E-09	2.83E-19
CH3O	4.20E-08	5.71E-11	6.10E-17	5.71E-11	3.87E-10	5.86E-16
CH3OH	8.88E-06	3.74E-08	5.26E-14	3.74E-08	1.68E-07	3.98E-13
CH4	2.09E-04	5.74E-07	1.31E-13	5.74E-07	2.90E-06	9.88E-13
CN	2.65E-12	4.67E-15	1.90E-16	4.67E-15	3.84E-14	2.60E-16
CO	2.49E-03	8.21E-05	1.81E-06	8.21E-05	3.09E-04	3.16E-06
CO2	4.46E-02	4.41E-02	4.42E-02	4.41E-02	4.59E-02	4.63E-02
C2H	9.82E-11	4.63E-13	7.75E-15	4.63E-13	9.15E-12	7.53E-14
C2H2	4.16E-07	5.61E-09	1.10E-10	5.61E-09	6.06E-08	7.09E-10
C2H3	6.35E-09	7.04E-12	3.67E-18	7.04E-12	2.39E-10	3.98E-17
C2H4	1.65E-06	5.03E-09	2.05E-17	5.03E-09	9.89E-08	1.84E-16
C2H5	3.07E-08	7.05E-12	2.83E-19	7.05E-12	2.56E-10	2.83E-19
C2H6	4.20E-07	2.61E-10	2.83E-19	2.61E-10	6.47E-09	2.83E-19
C3H7	3.46E-13	4.41E-18	2.83E-19	4.41E-18	5.14E-16	2.83E-19
C3H8	2.33E-14	1.89E-17	2.83E-19	1.89E-17	2.85E-15	2.83E-19
H	6.12E-06	8.02E-08	3.20E-08	8.02E-08	3.65E-07	6.06E-08
HCCO	8.66E-09	1.59E-11	4.69E-14	1.59E-11	5.18E-10	4.70E-13
HCCOH	1.10E-07	6.09E-08	1.73E-08	6.09E-08	1.46E-07	8.28E-08
HCN	2.78E-17	2.83E-19	2.83E-19	2.83E-19	4.02E-19	2.83E-19
HCNN	2.76E-12	9.96E-16	2.83E-19	9.96E-16	1.52E-14	7.16E-19
HCNO	1.30E-08	1.00E-08	8.55E-09	1.00E-08	6.19E-09	5.77E-09
HCO	1.02E-07	1.29E-10	5.62E-15	1.29E-10	1.07E-09	4.61E-14
HNCO	3.40E-08	3.24E-09	9.30E-11	3.24E-09	2.10E-09	1.44E-10
HNO	1.71E-10	4.02E-12	1.81E-12	4.02E-12	1.08E-11	2.71E-12
HOCN	1.17E-11	4.34E-12	1.33E-12	4.34E-12	1.33E-12	8.42E-13
HO2	2.33E-05	1.07E-06	7.25E-07	1.07E-06	2.24E-06	9.05E-07
H2	1.07E-04	2.55E-06	1.08E-06	2.55E-06	8.58E-06	1.78E-06
H2CN	4.89E-14	1.25E-16	2.83E-19	1.25E-16	8.36E-16	2.83E-19
H2O	9.38E-02	8.83E-02	8.83E-02	8.83E-02	9.24E-02	9.24E-02
H2O2	6.97E-07	8.54E-08	6.33E-08	8.54E-08	1.52E-07	7.83E-08
N	6.87E-12	2.34E-13	1.56E-13	2.34E-13	8.93E-13	3.94E-13
NCO	6.44E-10	2.47E-11	6.06E-13	2.47E-11	2.45E-11	1.12E-12
NH	5.71E-11	7.29E-13	5.52E-14	7.29E-13	1.57E-12	1.32E-13
NH2	3.38E-10	3.32E-11	9.90E-13	3.32E-11	2.19E-11	1.70E-12
NH3	1.73E-09	3.89E-10	1.36E-11	3.89E-10	1.79E-10	2.00E-11
NNH	1.40E-10	1.79E-12	7.24E-13	1.79E-12	8.42E-12	1.42E-12
NO	1.51E-06	1.64E-06	1.78E-06	1.64E-06	1.89E-06	1.97E-06
NO2	6.71E-08	2.07E-08	1.71E-08	2.07E-08	2.88E-08	1.69E-08
N2	7.52E-01	7.55E-01	7.55E-01	7.55E-01	7.53E-01	7.53E-01
N2O	2.59E-06	8.04E-07	4.46E-07	8.04E-07	1.08E-06	5.23E-07
O	4.18E-05	4.42E-06	3.05E-06	4.42E-06	1.05E-05	4.64E-06
OH	3.83E-04	1.51E-04	1.28E-04	1.51E-04	2.46E-04	1.72E-04
O2	1.07E-01	1.12E-01	1.12E-01	1.12E-01	1.08E-01	1.08E-01

Table A3-2 (continued)

MOLE_FRACTIONS_X(I)								
SPECIES_"I"	25	26	27	28	29	30	31	EQL
C	2.83E-19	2.83E-19	2.83E-19	2.83E-19	2.83E-19	2.83E-19	2.83E-19	2.83E-19
CH	1.69E-16	1.30E-17	4.05E-18	4.05E-18	4.05E-18	4.24E-18	4.24E-18	2.83E-19
CH2	5.24E-13	2.01E-14	6.29E-15	6.29E-15	6.29E-15	7.32E-15	7.32E-15	2.83E-19
CH2CHO	2.90E-14	9.84E-18	3.05E-18	3.05E-18	3.05E-18	3.72E-18	3.72E-18	2.83E-19
CH2CO	9.75E-11	3.03E-11	9.39E-12	9.39E-12	9.39E-12	1.25E-11	1.25E-11	2.83E-19
CH2O	2.20E-10	1.05E-12	3.29E-13	3.29E-13	3.29E-13	4.17E-13	4.17E-13	2.61E-17
CH2OH	8.95E-14	1.64E-16	5.11E-17	5.11E-17	5.11E-17	5.83E-17	5.83E-17	2.83E-19
CH2(S)	4.85E-14	4.53E-16	1.42E-16	1.42E-16	1.42E-16	1.62E-16	1.62E-16	2.83E-19
CH3	2.36E-10	2.84E-13	8.87E-14	8.87E-14	8.87E-14	1.09E-13	1.09E-13	2.83E-19
CH3CHO	6.86E-13	2.83E-19	2.83E-19	2.83E-19	2.83E-19	2.83E-19	2.83E-19	2.83E-19
CH3O	1.60E-13	2.46E-16	7.68E-17	7.68E-17	7.68E-17	9.16E-17	9.16E-17	2.83E-19
CH3OH	9.49E-11	1.67E-13	5.21E-14	5.21E-14	5.21E-14	6.63E-14	6.63E-14	2.83E-19
CH4	1.44E-09	4.15E-13	1.29E-13	1.29E-13	1.29E-13	1.64E-13	1.64E-13	2.83E-19
CN	1.67E-16	2.33E-16	2.01E-16	2.01E-16	2.01E-16	2.09E-16	2.09E-16	2.83E-19
CO	4.83E-06	3.13E-06	3.13E-06	3.13E-06	3.13E-06	2.71E-06	2.71E-06	2.56E-06
CO2	4.63E-02	4.63E-02	4.63E-02	4.63E-02	4.63E-02	4.57E-02	4.57E-02	4.57E-02
C2H	2.50E-14	3.15E-14	9.77E-15	9.77E-15	9.77E-15	1.17E-14	1.17E-14	2.83E-19
C2H2	2.34E-10	2.97E-10	9.20E-11	9.20E-11	9.20E-11	1.23E-10	1.23E-10	2.83E-19
C2H3	7.58E-14	1.66E-17	5.16E-18	5.16E-18	5.16E-18	5.99E-18	5.99E-18	2.83E-19
C2H4	4.45E-11	7.69E-17	2.39E-17	2.39E-17	2.39E-17	2.92E-17	2.92E-17	2.83E-19
C2H5	1.78E-14	2.83E-19	2.83E-19	2.83E-19	2.83E-19	2.83E-19	2.83E-19	2.83E-19
C2H6	6.57E-13	2.83E-19	2.83E-19	2.83E-19	2.83E-19	2.83E-19	2.83E-19	2.83E-19
C3H7	2.83E-19	2.83E-19	2.83E-19	2.83E-19	2.83E-19	2.83E-19	2.83E-19	2.83E-19
C3H8	3.98E-19	2.83E-19	2.83E-19	2.83E-19	2.83E-19	2.83E-19	2.83E-19	2.83E-19
H	6.17E-08	6.06E-08	6.06E-08	6.06E-08	6.06E-08	5.11E-08	5.11E-08	4.77E-08
HCCO	3.53E-13	1.97E-13	6.10E-14	6.10E-14	6.10E-14	7.23E-14	7.23E-14	2.83E-19
HCCOH	1.66E-08	3.47E-08	1.07E-08	1.07E-08	1.07E-08	1.55E-08	1.55E-08	2.83E-19
HCN	2.83E-19	2.83E-19	2.83E-19	2.83E-19	2.83E-19	2.83E-19	2.83E-19	1.69E-18
HCNN	3.90E-18	3.00E-19	2.83E-19	2.83E-19	2.83E-19	2.83E-19	2.83E-19	2.83E-19
HCNO	3.14E-09	5.20E-09	4.51E-09	4.51E-09	4.51E-09	5.64E-09	5.64E-09	2.83E-19
HCO	4.14E-13	2.06E-14	7.96E-15	7.96E-15	7.96E-15	8.64E-15	8.64E-15	1.54E-15
HNCO	7.81E-11	7.40E-11	6.39E-11	6.39E-11	6.39E-11	7.46E-11	7.46E-11	3.84E-14
HNO	3.82E-12	2.80E-12	2.97E-12	2.98E-12	2.98E-12	2.58E-12	2.58E-12	2.41E-09
HOCN	1.71E-13	3.79E-13	1.38E-13	1.38E-13	1.38E-13	3.48E-13	3.48E-13	2.10E-17
HO2	9.10E-07	9.05E-07	9.05E-07	9.05E-07	9.05E-07	8.54E-07	8.54E-07	8.24E-07
H2	1.81E-06	1.78E-06	1.78E-06	1.78E-06	1.78E-06	1.56E-06	1.56E-06	1.49E-06
H2CN	6.06E-19	2.83E-19	2.83E-19	2.83E-19	2.83E-19	2.83E-19	2.83E-19	2.83E-19
H2O	9.24E-02	9.24E-02	9.24E-02	9.24E-02	9.24E-02	9.13E-02	9.13E-02	9.13E-02
H2O2	7.88E-08	7.83E-08	7.83E-08	7.83E-08	7.83E-08	7.40E-08	7.40E-08	7.20E-08
N	3.97E-13	3.94E-13	3.94E-13	3.94E-13	3.94E-13	3.08E-13	3.08E-13	1.37E-12
NCO	6.12E-13	5.80E-13	5.01E-13	5.01E-13	5.01E-13	5.57E-13	5.57E-13	2.94E-16
NH	1.19E-13	1.14E-13	1.12E-13	1.12E-13	1.12E-13	9.25E-14	9.25E-14	1.39E-13
NH2	9.03E-13	8.35E-13	7.28E-13	7.28E-13	7.28E-13	8.28E-13	8.28E-13	7.37E-14
NH3	1.05E-11	9.71E-12	8.46E-12	8.46E-12	8.46E-12	1.01E-11	1.01E-11	9.20E-13
NNH	1.45E-12	1.42E-12	1.42E-12	1.42E-12	1.42E-12	1.19E-12	1.19E-12	1.10E-12
NO	2.84E-06	2.07E-06	2.21E-06	2.21E-06	2.21E-06	2.06E-06	2.06E-06	2.09E-03
NO2	2.44E-08	1.77E-08	1.89E-08	1.89E-08	1.89E-08	1.82E-08	1.82E-08	1.86E-05
N2	7.53E-01	7.53E-01	7.53E-01	7.53E-01	7.53E-01	7.54E-01	7.54E-01	7.53E-01
N2O	5.17E-07	5.06E-07	5.06E-07	5.06E-07	5.06E-07	4.89E-07	4.89E-07	4.80E-07
O	4.67E-06	4.63E-06	4.63E-06	4.63E-06	4.63E-06	4.15E-06	4.15E-06	3.92E-06
OH	1.72E-04	1.72E-04	1.72E-04	1.72E-04	1.72E-04	1.59E-04	1.59E-04	1.53E-04
O2	1.08E-01	1.08E-01	1.08E-01	1.08E-01	1.08E-01	1.09E-01	1.09E-01	1.08E-01

***13-element CRN for JSR***

This sample calculation is for methane combustion in the 64 cm<sup>3</sup> JSR. The input and output of the UW chemical reactor code are shown. The boundary conditions for this run correspond to methane combustion with uniform fuel-air injector distribution and neutral pilot case.

**Table A3-3 Input for the UW chemical kinetic code for 13-element CRN.**

***INPUT DATA***								
ELEM #	NODE IN	NODE OUT	ELEM TYPE	AREA (SQ.IN)	LENGTH (INCHES)	INLET AIR (LBM/S)	INLET FUEL1 (LBM/S)	INLET FLOW FRACTION
1	1	2	MIX	8.30E-02	1.00E-01	7.10E-03	2.67E-04	1.00E+00
2	2	3	MIX	1.00E-01	1.00E-01	0.00E+00	0.00E+00	7.50E-01
3	3	4	PSB	1.00E-01	4.33E-01	0.00E+00	0.00E+00	6.70E-01
4	4	5	PSR	7.00E-01	5.00E-01	0.00E+00	0.00E+00	1.00E+00
5	5	6	PSR	2.00E+00	3.00E-01	0.00E+00	0.00E+00	1.00E+00
6	3	5	PSB	1.00E-01	2.13E-01	0.00E+00	0.00E+00	3.30E-01
7	2	6	PSB	2.00E-01	1.08E-01	0.00E+00	0.00E+00	2.50E-01
8	6	7	PSR	1.90E+00	2.00E-01	0.00E+00	0.00E+00	1.00E+00
9	7	8	PST	2.00E+00	1.00E+00	0.00E+00	0.00E+00	1.00E+00
10	8	9	MIX	1.00E-01	1.00E-01	0.00E+00	0.00E+00	8.00E-01
11	9	4	MIX	1.00E-01	1.00E-01	0.00E+00	0.00E+00	3.00E-02
12	9	5	MIX	1.00E-01	1.00E-01	0.00E+00	0.00E+00	9.70E-01
13	8	10	PFR	3.90E+00	5.00E-02	0.00E+00	0.00E+00	2.00E-01

**Table A3-4 Output data from the UW chemical kinetic code for 13-element CRN**

[illegible]

Table A3-4 (continued)

MOLE FRACTIONS X(I)							
SPECIES "I"	1	2	3	4	5	6	7
C	0.00E+00	0.00E+00	5.83E-08	2.35E-10	1.21E-11	5.83E-08	5.79E-08
CH	0.00E+00	0.00E+00	6.14E-07	5.35E-09	9.37E-10	6.14E-07	6.13E-07
CH2	0.00E+00	0.00E+00	9.53E-06	1.31E-07	5.98E-08	9.53E-06	9.56E-06
CH2CHO	0.00E+00	0.00E+00	5.75E-08	1.33E-10	4.31E-11	5.75E-08	5.83E-08
CH2CO	0.00E+00	0.00E+00	3.01E-06	3.27E-08	1.82E-08	3.01E-06	3.06E-06
CH2O	0.00E+00	0.00E+00	2.33E-04	1.99E-06	1.05E-06	2.33E-04	2.34E-04
CH2OH	0.00E+00	0.00E+00	1.29E-06	1.49E-08	5.39E-09	1.29E-06	1.29E-06
CH2(S)	0.00E+00	0.00E+00	1.28E-06	1.44E-08	5.32E-09	1.28E-06	1.29E-06
CH3	0.00E+00	0.00E+00	3.06E-04	2.48E-06	1.45E-06	3.06E-04	3.08E-04
CH3CHO	0.00E+00	0.00E+00	9.67E-07	5.80E-09	2.80E-09	9.66E-07	9.84E-07
CH3O	0.00E+00	0.00E+00	7.32E-07	2.20E-09	1.05E-09	7.32E-07	7.40E-07
CH3OH	0.00E+00	0.00E+00	9.18E-06	4.88E-08	4.02E-08	9.17E-06	9.27E-06
CH4	6.33E-02	6.33E-02	2.62E-03	1.12E-05	6.34E-06	2.62E-03	2.64E-03
CN	0.00E+00	0.00E+00	1.87E-09	4.98E-11	1.14E-11	1.87E-09	1.86E-09
CO	0.00E+00	0.00E+00	2.98E-02	5.89E-03	2.44E-03	2.98E-02	2.99E-02
CO2	0.00E+00	0.00E+00	2.89E-02	5.70E-02	6.07E-02	2.89E-02	2.88E-02
C2H	0.00E+00	0.00E+00	9.18E-10	2.44E-11	1.08E-11	9.18E-10	9.24E-10
C2H2	0.00E+00	0.00E+00	6.89E-07	6.16E-09	4.90E-09	6.88E-07	6.99E-07
C2H3	0.00E+00	0.00E+00	1.65E-07	8.64E-10	3.26E-10	1.65E-07	1.67E-07
C2H4	0.00E+00	0.00E+00	4.73E-06	1.75E-08	1.14E-08	4.72E-06	4.80E-06
C2H5	0.00E+00	0.00E+00	2.24E-07	4.43E-10	2.02E-10	2.24E-07	2.28E-07
C2H6	0.00E+00	0.00E+00	1.39E-06	1.53E-09	8.93E-10	1.39E-06	1.42E-06
C3H7	0.00E+00	0.00E+00	1.57E-12	3.42E-16	1.06E-16	1.57E-12	1.61E-12
C3H8	0.00E+00	0.00E+00	2.01E-14	2.59E-17	1.58E-17	2.01E-14	2.07E-14
H	0.00E+00	0.00E+00	2.65E-03	9.91E-04	2.59E-04	2.65E-03	2.63E-03
HCCO	0.00E+00	0.00E+00	1.53E-07	2.72E-09	1.33E-09	1.53E-07	1.55E-07
HCCOH	0.00E+00	0.00E+00	2.87E-09	1.76E-10	2.82E-10	2.87E-09	2.91E-09
HCN	0.00E+00	0.00E+00	2.63E-14	6.04E-16	1.06E-16	2.63E-14	2.62E-14
HCNN	0.00E+00	0.00E+00	1.53E-09	6.16E-12	1.32E-12	1.53E-09	1.53E-09
HCNO	0.00E+00	0.00E+00	3.92E-09	5.54E-10	6.97E-10	3.92E-09	3.92E-09
HCO	0.00E+00	0.00E+00	1.94E-05	1.53E-07	4.29E-08	1.94E-05	1.94E-05
HNCO	0.00E+00	0.00E+00	4.28E-08	3.33E-09	2.89E-09	4.28E-08	4.29E-08
HNO	0.00E+00	0.00E+00	1.59E-09	8.72E-10	4.81E-10	1.59E-09	1.59E-09
HOCN	0.00E+00	0.00E+00	8.03E-12	1.89E-12	1.39E-12	8.03E-12	8.02E-12
HO2	0.00E+00	0.00E+00	7.81E-05	8.62E-06	5.09E-06	7.81E-05	7.85E-05
H2	0.00E+00	0.00E+00	6.33E-03	1.76E-03	7.24E-04	6.32E-03	6.34E-03
H2CN	0.00E+00	0.00E+00	1.07E-10	7.92E-14	2.27E-14	1.07E-10	1.08E-10
H2O	0.00E+00	0.00E+00	1.08E-01	1.21E-01	1.24E-01	1.08E-01	1.08E-01
H2O2	0.00E+00	0.00E+00	1.06E-06	2.81E-07	2.00E-07	1.06E-06	1.07E-06
N	0.00E+00	0.00E+00	8.55E-09	9.96E-10	2.57E-10	8.55E-09	8.51E-09
NCO	0.00E+00	0.00E+00	7.02E-09	3.62E-10	2.20E-10	7.02E-09	7.03E-09
NH	0.00E+00	0.00E+00	5.00E-09	1.04E-09	2.88E-10	5.00E-09	4.99E-09
NH2	0.00E+00	0.00E+00	1.44E-09	9.58E-11	5.39E-11	1.44E-09	1.44E-09
NH3	0.00E+00	0.00E+00	7.84E-10	6.55E-11	5.62E-11	7.84E-10	7.89E-10
NNH	0.00E+00	0.00E+00	3.18E-09	1.54E-09	3.94E-10	3.19E-09	3.17E-09
NO	0.00E+00	0.00E+00	2.76E-06	8.45E-06	9.10E-06	2.76E-06	2.74E-06
NO2	0.00E+00	0.00E+00	2.43E-09	5.50E-09	9.31E-09	2.43E-09	2.43E-09
N2	7.40E-01	7.40E-01	7.24E-01	7.35E-01	7.38E-01	7.24E-01	7.24E-01
N2O	0.00E+00	0.00E+00	1.44E-07	4.21E-07	5.47E-07	1.44E-07	1.44E-07
O	0.00E+00	0.00E+00	2.37E-03	2.22E-03	8.65E-04	2.37E-03	2.36E-03
OH	0.00E+00	0.00E+00	3.46E-03	4.95E-03	2.99E-03	3.46E-03	3.44E-03
O2	1.97E-01	1.97E-01	9.12E-02	7.14E-02	7.04E-02	9.12E-02	9.13E-02

Table A3-4 (continued)

MOLE_FRACTIONS_X(I)							
SPECIES_"I"	8	9	10	11	12	13	EQL
C	2.51E-11	1.21E-13	1.21E-13	1.21E-13	1.21E-13	2.80E-19	2.80E-19
CH	1.62E-09	1.83E-11	1.83E-11	1.83E-11	1.83E-11	4.04E-17	2.80E-19
CH2	9.07E-08	1.70E-09	1.70E-09	1.70E-09	1.70E-09	5.04E-15	2.80E-19
CH2CHO	7.06E-11	8.17E-13	8.17E-13	8.17E-13	8.17E-13	2.80E-19	2.80E-19
CH2CO	2.74E-08	9.60E-10	9.60E-10	9.60E-10	9.60E-10	1.11E-14	2.80E-19
CH2O	1.57E-06	3.54E-08	3.54E-08	3.54E-08	3.54E-08	1.10E-13	6.87E-16
CH2OH	8.41E-09	1.45E-10	1.45E-10	1.45E-10	1.45E-10	4.19E-17	2.80E-19
CH2(S)	8.23E-09	1.42E-10	1.42E-10	1.42E-10	1.42E-10	1.49E-16	2.80E-19
CH3	2.11E-06	4.67E-08	4.67E-08	4.67E-08	4.67E-08	1.04E-14	2.80E-19
CH3CHO	4.29E-09	7.85E-11	7.85E-11	7.85E-11	7.85E-11	1.29E-18	2.80E-19
CH3O	1.60E-09	3.19E-11	3.19E-11	3.19E-11	3.19E-11	8.39E-18	2.80E-19
CH3OH	5.72E-08	1.57E-09	1.57E-09	1.57E-09	1.57E-09	5.29E-16	2.80E-19
CH4	9.39E-06	1.81E-07	1.81E-07	1.81E-07	1.81E-07	1.31E-14	2.80E-19
CN	1.86E-11	3.23E-13	3.23E-13	3.23E-13	3.23E-13	1.42E-14	2.80E-19
CO	2.96E-03	1.42E-03	1.42E-03	1.42E-03	1.42E-03	9.13E-04	5.63E-05
CO2	6.01E-02	6.18E-02	6.18E-02	6.18E-02	6.18E-02	6.23E-02	6.32E-02
C2H	1.63E-11	3.98E-13	3.98E-13	3.98E-13	3.98E-13	1.57E-17	2.80E-19
C2H2	6.93E-09	2.24E-10	2.24E-10	2.24E-10	2.24E-10	1.03E-14	2.80E-19
C2H3	5.16E-10	6.64E-12	6.64E-12	6.64E-12	6.64E-12	2.80E-19	2.80E-19
C2H4	1.68E-08	2.89E-10	2.89E-10	2.89E-10	2.89E-10	2.85E-18	2.80E-19
C2H5	3.19E-10	1.38E-12	1.38E-12	1.38E-12	1.38E-12	2.80E-19	2.80E-19
C2H6	1.35E-09	6.64E-12	6.64E-12	6.64E-12	6.64E-12	2.80E-19	2.80E-19
C3H7	1.80E-16	2.80E-19	2.80E-19	2.80E-19	2.80E-19	2.80E-19	2.80E-19
C3H8	2.37E-17	2.80E-19	2.80E-19	2.80E-19	2.80E-19	2.80E-19	2.80E-19
H	3.19E-04	1.40E-04	1.40E-04	1.40E-04	1.40E-04	8.09E-05	2.14E-06
HCCO	2.04E-09	6.05E-11	6.05E-11	6.05E-11	6.05E-11	9.94E-16	2.80E-19
HCCOH	3.57E-10	3.26E-11	3.26E-11	3.26E-11	3.26E-11	2.62E-14	2.80E-19
HCN	1.78E-16	2.64E-18	2.64E-18	2.64E-18	2.64E-18	2.80E-19	1.39E-16
HCNN	2.27E-12	2.65E-14	2.65E-14	2.65E-14	2.65E-14	2.80E-19	2.80E-19
HCNO	9.26E-10	3.09E-10	3.09E-10	3.09E-10	3.09E-10	1.33E-10	2.80E-19
HCO	6.98E-08	1.19E-09	1.19E-09	1.19E-09	1.19E-09	2.97E-11	6.96E-14
HNCO	4.04E-09	8.81E-10	8.81E-10	8.81E-10	8.81E-10	1.88E-10	2.27E-13
HNO	5.46E-10	3.30E-10	3.30E-10	3.30E-10	3.30E-10	2.25E-10	3.23E-09
HOCN	1.95E-12	4.88E-13	4.88E-13	4.89E-13	4.89E-13	1.16E-13	1.90E-16
HO2	5.76E-06	3.64E-06	3.64E-06	3.64E-06	3.64E-06	2.64E-06	6.00E-07
H2	8.34E-04	4.74E-04	4.74E-04	4.74E-04	4.74E-04	3.30E-04	2.91E-05
H2CN	3.57E-14	5.35E-16	5.35E-16	5.36E-16	5.36E-16	2.80E-19	2.80E-19
H2O	1.24E-01	1.25E-01	1.25E-01	1.25E-01	1.25E-01	1.25E-01	1.26E-01
H2O2	2.16E-07	1.64E-07	1.64E-07	1.64E-07	1.64E-07	1.29E-07	3.12E-08
N	3.12E-10	1.40E-10	1.40E-10	1.40E-10	1.40E-10	1.04E-10	3.93E-11
NCO	3.17E-10	4.26E-11	4.26E-11	4.27E-11	4.27E-11	8.12E-12	4.47E-15
NH	3.58E-10	1.52E-10	1.52E-10	1.52E-10	1.52E-10	9.12E-11	2.66E-12
NH2	7.68E-11	1.81E-11	1.81E-11	1.81E-11	1.81E-11	6.74E-12	7.71E-13
NH3	7.53E-11	2.39E-11	2.39E-11	2.39E-11	2.39E-11	1.04E-11	3.91E-12
NNH	4.85E-10	2.13E-10	2.13E-10	2.13E-10	2.13E-10	1.24E-10	3.32E-12
NO	8.94E-06	9.33E-06	9.33E-06	9.34E-06	9.34E-06	9.48E-06	2.41E-03
NO2	8.67E-09	1.11E-08	1.11E-08	1.11E-08	1.11E-08	1.24E-08	3.39E-06
N2	7.37E-01	7.39E-01	7.39E-01	7.39E-01	7.39E-01	7.39E-01	7.39E-01
N2O	5.34E-07	5.76E-07	5.76E-07	5.76E-07	5.76E-07	5.87E-07	1.35E-07
O	9.91E-04	5.77E-04	5.77E-04	5.77E-04	5.77E-04	4.02E-04	3.58E-05
OH	3.18E-03	2.43E-03	2.43E-03	2.43E-03	2.43E-03	2.06E-03	6.31E-04
O2	7.06E-02	7.00E-02	7.00E-02	7.00E-02	7.00E-02	6.99E-02	6.87E-02

## **Appendix 4: Atmospheric Pressure Jet–Stirred Reactor Measurements**

### **Hydrocarbon Fuel Experiments**

The data and discussion presented herein have not been previously published and are included with the permission of P.C. Malte. The hydrocarbon fuel experiments were conducted in 2003. The experimental data were gathered for the 64 cm<sup>3</sup> ceramic jet-stirred reactor operated at 1 atm pressure. The reactor is geometrically similar to the 16 cm<sup>3</sup> of Lee (2000), depicted below in Figure A4-1. The gases enter the axisymmetrical JSR through a nozzle at the bottom, creating a strong jet. A temperature-staged prevaporizer-premixer (SPP) and an air-heater lie upstream of the nozzle (Lee, 2000).

The 64 cm<sup>3</sup> JSR has a maximum height and width (diameter) of 71 mm and 40 mm, respectively. The nozzle diameter used for these experiments is 5.6 mm. The measured, corrected combustion temperature is 1792±3 K, the SPP outlet temperature (JSR inlet temperature) is 573 K, the air mass flow rate is 11.7 kg/hr, and the resultant mean residence time of the combustion cavity is 3.7±0.1 ms. The fuels tested are methane, propane, ethane, and mixtures of C<sub>1</sub>-C<sub>4</sub> alkanes.

The 64 cm<sup>3</sup> JSR data are in close agreement with data published by J.C.Y. Lee (2000). The geometrically similar Lee - JSR had a volume of 16 cm<sup>3</sup> and a maximum height and width (diameter) of 45 mm and 25 mm, respectively. The nozzle diameter for Lee's experiments is 4.0 mm. The combustion temperature is 1790 K, the SPP outlet temperature is 623 K, the fuel flow rate

is adjusted to maintain temperature constant, resulting in a fuel-air equivalence ratio of  $0.61 \pm 0.04$  over the range of fuels run. The mean residence time of the JSR is held nearly constant at  $2.3 \pm 0.1$  ms. The fuels are: methanol, natural gas (93% methane), ethane, propane, n-pentane, n-hexane, n-heptane, n-dodecane, n-hexadecane, two light naphthas, four number two diesel fuels, benzene and toluene. For more details, see Lee (2000) and Lee et al. (2003).

The premixing of fuel and air in this experimental system was examined by A.C. Lee (2003), where laser Rayleigh scattering was used to examine the outlet stream of the SPP operated on number two diesel fuel. The measurements indicated no droplets exiting the SPP and a well mixed diesel vapor-air mixture exiting the SPP. This was inferred by noting that the standard deviation in the scattered light signal (collected at 90 degrees to the laser beam) was no more than about 10% of the mean scattered light signal. Thus, for the purposes of the present research, it is assumed that the stream exiting the SPP and entering the JSR is fully vaporized (when liquid fuels are used) and well premixed.

The reported combustion temperature is 30-40 K higher than the temperature measured with a thermocouple (type R with alumina coating) placed in the recirculation zone of the JSR at  $2/3^{\text{rd}}$  reactor height. The temperature correction accounts for calculated radiation heat loss from the thermocouple. Gas sampling is conducted using a small quartz probe inserted into the recirculation zone of the JSR at  $2/3^{\text{rd}}$  reactor height – though through a different port than the thermocouple. The sample probe is warm-water cooled, except for the probe tip that enters the recirculation zone and become very hot. The sampled gas is maintained warm in the sample line until the water of combustion is removed by impingers surrounded by ice water bath.

The dried sample gas is then drawn into an analyzer cart by a metal bellows pump and distributed into four gas analyzers placed in parallel: O<sub>2</sub> analyzer, non-dispersive infrared (NDIR) CO<sub>2</sub> analyzer, NDIR CO analyzer, and chemiluminescent NO-NO<sub>x</sub> analyzer. The analyzers are calibrated with standard gases frequently throughout the experiments. Gaseous fuels and air are metered through mass flow controllers and liquid fuels are metered through rotometers.

The 64 cm<sup>3</sup> JSR experimental results for the hydrocarbon fuels are plotted in Figure A4-2 superimposed on J.C.Y. Lee's data for the 16 cm<sup>3</sup> JSR. As noted, the linear curve fit to the 64 cm<sup>3</sup> JSR alkane data ( $0.25 \leq C/H \leq 0.375$ ) is essentially identical to the curve fit for the 16 cm<sup>3</sup> JSR alkane data ( $0.25 \leq C/H \leq 0.47$ ). This close agreement, obtained in different sized JSRs, by different individuals, and four years apart, helps to provide confidence in the experimental results. The linear curve fit is seen to extrapolate well to the blended fuels data of Lee's 16 cm<sup>3</sup> JSR. The two light naphthas are located at  $0.44 \leq C/H \leq 0.52$  and the four number two diesels are located at  $C/H = 0.57-0.58$ . Data for the diesel fuels are shown with the fuel bound NO<sub>x</sub> subtracted. This is done by assuming complete conversion of the small amount of fuel bound nitrogen to NO<sub>x</sub>, and subtracting this small amount of NO<sub>x</sub> from the total measured NO<sub>x</sub> (Lee, 2000 and Lee et al., 2003).

Figure A4-2 also shows 64 cm<sup>3</sup> JSR ethene data ( $C/H = 0.5$ ) falling slightly below the level estimated by extrapolating the alkane linear curve fit. Methanol NO<sub>x</sub> falls well below the alkane curve. Aromatics NO<sub>x</sub> data are not plotted in Fig. A4-2. These are 7.2 ppmvd (15% O<sub>2</sub>) for toluene ( $C/H = 0.875$ ) and 7.1 ppmvd (15% O<sub>2</sub>) for benzene ( $C/H = 1.0$ ) (Lee, 2000 and Lee et al., 2003).

## Hydrogen Experiments

In 2005 the same experimental setup was used to study the combustion of premixed hydrogen and air. These results were obtained by P.C. Malte and are included with his permission. The JSR was operated without preheat, so that the inlet temperature is 300K (nominal). The measured, corrected combustion temperature was varied from the “standard” temperature of 1790K to about 1300K. This was done by increasing the air flow rate of the JSR. Over the 1790 to 1300K temperature range, the residence time of the JSR increased from 3.7 to about 5.5 ms. The NO<sub>x</sub> data obtained over this range have been shown above in Chapter 9, Figure 9-5.

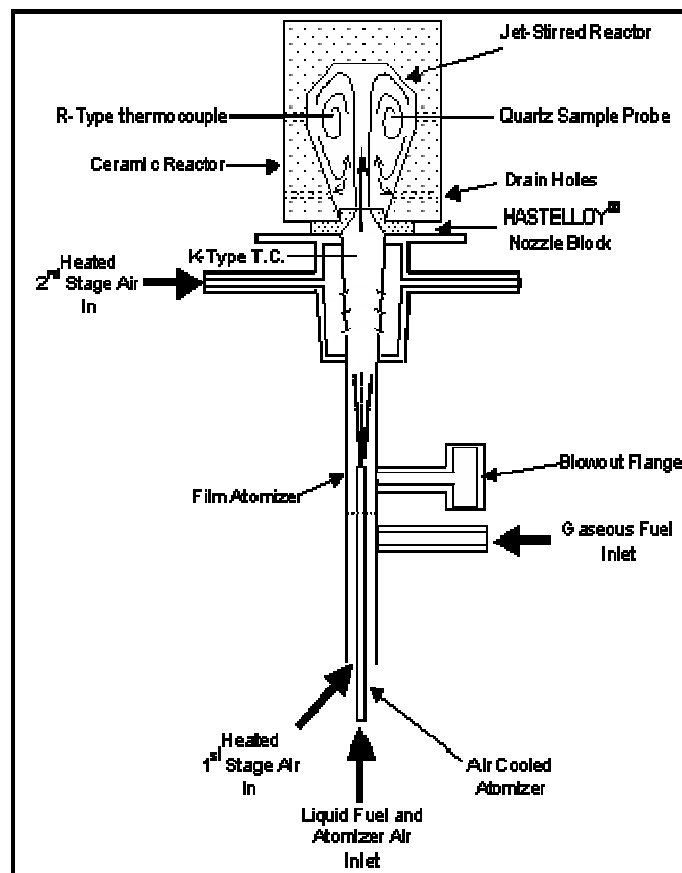


Figure A4-0-1 Schematic drawing of the experimental setup from Lee (2000).

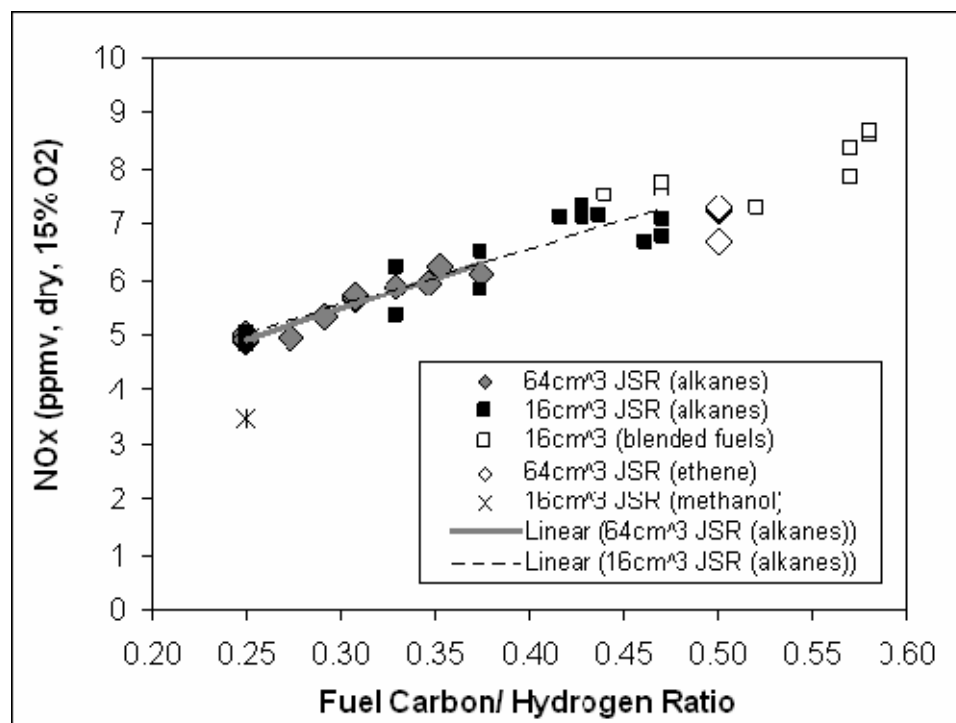


Figure A4-0-2. Experimental data for 16cm<sup>3</sup> and 64cm<sup>3</sup> JSRs.

## **Appendix 5: Modeling the Emissions of Wood Dust Burners**

### ***Introduction***

Commercial wood dust burners are widely used by the wood products industry. There are about 700 of these units in North America. Among the challenges presented by this burner design are high levels of nitrogen oxides and particulate emissions. The most cost effective way to reduce the emissions is to modify the combustion process in the burner. However measuring flow, temperature, and species concentrations for this type of combustor is not a trivial task. Further, optimization of the combustion process by trial and error becomes very expensive.

The alternative approach for this problem is to model the combustion process using CFD and CRN modeling. Reliable flow field information is needed to develop the CRN. This has been done by applying CFD in two wood dust burners: (1) the UW laboratory wood dust burner, and (2) an industrial cyclone dust burner. One of the most challenging parts in CFD is finding the appropriate modeling approach for species transport. In this regard, two different modeling techniques are: (1) finite rate global reactions; and (2) probability density functions (PDF). The PDF method might be possible in this work if time allowed. However, because of time constraints on the study, the global reaction approach is used. Once the CFD solutions for the flow field are available, and the CRN is in place, parametric analysis of NO<sub>x</sub> formation can be performed.

### ***Development of Finite Rate Global Chemistry for Wood Dust Combustion***

The objective of this task is to develop a global kinetic mechanism that can be applied to wood dust combustion. A number of assumptions have to be made in the development of the mechanism. To further understand the kind of modeling that is required one needs to look at the physical and chemical description of the processes involved in wood particle combustion.

As a wood particle enters the combustor it experiences heating by radiative and convective heat transfer. As the particle heats up its moisture evaporates. The water in the wood particle can be divided in two categories, free water and bound water. The analysis for wood dust sample, see Table A5-1, shows low moisture content (3.7-6.5%) by weight, placing the moisture in the bound regime. The bound water comes out prior to pyrolysis of the wood. As the wood undergoes pyrolysis, the tars and light gases escape from the particle by means of advection and diffusion. The tars are subjected to secondary pyrolysis, which yields production of more light gases. Figure A5-1 shows the diagram of wood pyrolysis and combustion. The yields of pyrolysis and the rates of devolatilization and combustion are discussed hereafter. The rates are:  $R_1$  for pyrolysis of the wood,  $R_2$  for pyrolysis of the tars,  $R_3$  for oxidation of the char particle, and  $R_4$  for vaporization of the bound water. Additionally, there are rates of the oxidation of the light gases.

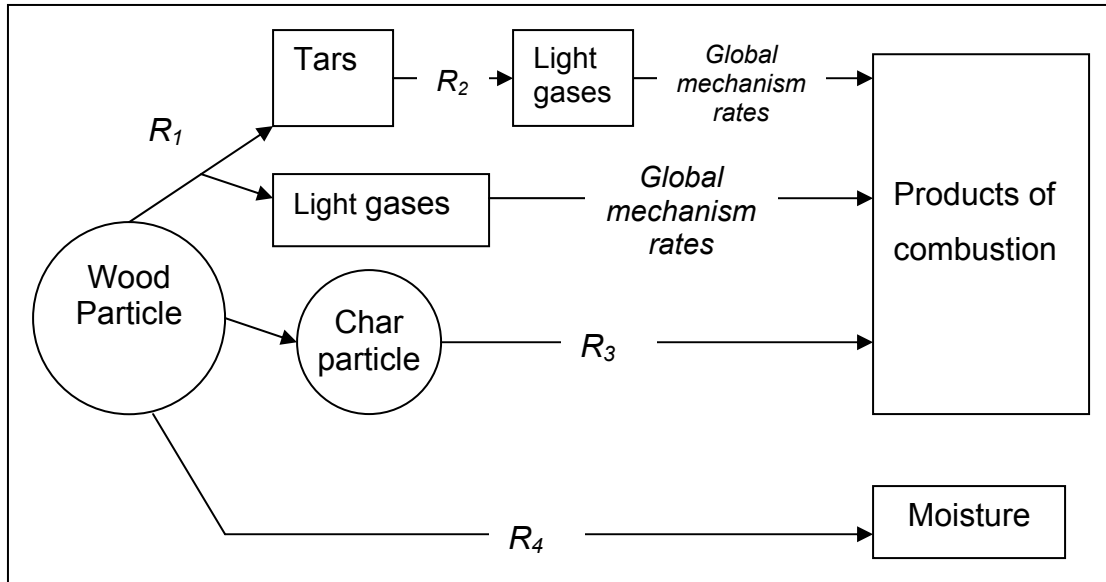


Figure A5-1. Diagram of devolatilization and combustion for a wood particle.

### Wood Composition

The chemical formula of the wood considered is based on the results of ultimate analyses of wood dusts from Weyerhaeuser data (Malte et al., 1996). Table A5-1 shows the analysis of wood from the Weyerhaeuser samples. The analysis is performed for urea-formaldehyde resin containing samples. The resin is assumed to have formula  $C_{2.5}H_5O_{1.5}N_2$  as an average of two forms of urea formaldehyde cured resin. After subtracting the resin, the ash and resin free wood formula for the Marshfield sample is  $C_6H_{9.844}O_{3.97}N_{0.0106}S_{0.00234}$ . Since, the sulfur chemistry is not considered in this study, the formula is simplified to  $C_6H_{9.844}O_{3.97}N_{0.0106}$ .

Table A5-1. Results of ultimate analysis of Weyerhaeuser sawdust samples

	Moisture	C	H	O	N	S	Ash	HHV
Sample	105C as recorded %mass	OD basis %mass	OD basis %mass	OD basis %mass	OD basis %mass	OD basis %mass	OD basis %mass	Btu/lb OD basis
Elkin	5.5	50.5	6.6	42.0	0.41	0	0.58	N/A
Grayling	4.0	48.7	5.9	42.9	0.43	0	2.12	N/A
Moncure (MDF)	3.7	46.4	6.2	42.8	3.4	0.03	1.12	N/A
Moncure (MB)	3.8	46.85	6.35	40.8	5.2	0.03	0.86	N/A
Marshfield	6.5	45.85	6.45	39.95	5.65	0.15	2.08	8160

Malte et al. (1996) applied the rates and the yields of pyrolysis of Nunn et al (1985) to the Marshfield wood. In this approach, when a wood particle is heated up, the volatile gases escape from the particle leaving 7% of char by mass. For modeling purposes the char is assumed as carbon (for determining the nitrogen oxides in post-processing the char may contain some of the fuel nitrogen). The composition of volatile gases released in primary pyrolysis is shown in Table A5-2. Nunn et al. also have reported other species present in the pyrolysis such as: methanol, butane, acetone, with total yield of 5.2% on a mass basis.

**Table A5-2. Yield data for primary pyrolysis of wood based on Nunn et al. (1995)**

Specie	based on Nunn et al.			simplified		
	% mass	Moles	Mole fraction	% mass	Moles	Mole fraction
WOOD TO CHAR	7.00	0.5833	0.1229	7.00	0.583	0.1199
WOOD TO TAR(C1 H1.473 O0.529)	67.80	3.0907	0.6514	67.80	3.091	0.6355
WOOD TO H2O	12.25	0.6806	0.1434	12.25	0.681	0.1399
WOOD TO CH2O	2.00	0.0667	0.0141	0.00	0.000	0.0000
WOOD TO CH3CHO	1.40	0.0318	0.0067	0.00	0.000	0.0000
WOOD TO C3H6	0.40	0.0095	0.0020	0.00	0.000	0.0000
WOOD TO CO2	4.25	0.0966	0.0204	4.25	0.097	0.0199
WOOD TO CO	4.25	0.1518	0.0320	4.25	0.152	0.0312
WOOD TO CH4	0.40	0.025	0.0053	3.80	0.238	0.0488
WOOD TO C2H4	0.25	0.0089	0.0019	0.65	0.023	0.0048
total	100.00	4.74	1.00	100.00	4.864	1.00

Simplification in the yields of pyrolysis is required in order to reduce the amount of computational time in the CFD simulation. Since some of the species are present in small amounts, they are eliminated from the pyrolysis reaction. In order to maintain the C, H, and O atom balances, some adjustments are made in the yields. Table A5-2 shows the increase in CH<sub>4</sub> and C<sub>2</sub>H<sub>4</sub> mole fraction, while CH<sub>2</sub>O, CH<sub>3</sub>CHO, and C<sub>3</sub>H<sub>6</sub> are not participating in the simplified pyrolysis reaction. A similar adjustment is performed for the tar pyrolysis. The formula for tar is back calculated based on the products of secondary pyrolysis. The yields for the tar pyrolysis are taken from Boroson et al. (1989) and adjusted to the Marshfield wood sample by Malte et al (1996). The products of the secondary pyrolysis are simplified for CFD modeling. The summary of the tar pyrolysis yields is presented in Table A5-3.

**Table A5-3. Yield data for tar pyrolysis of wood based on Boroson et al. (1989)**

Specie	based on Boroson et al.			Simplified	
	% mass of wood	Moles	Mole fraction	Moles	Mole fraction
TAR TO CO	36.60	1.30714	0.4833	0.4254	0.4833
TAR TO CO2	7.00	0.15909	0.0588	0.0518	0.0588
TAR TO CH4	10.50	0.65625	0.2426	0.2136	0.2426
TAR TO C2H4	13.30	0.475	0.1756	0.1546	0.1756
TAR TO H2	0.20	0.1	0.0370	0.0000	0.0000
TAR TO HCN	0.20	0.00741	0.0027	0.0000	0.0000

### Thermo-Chemical Properties

In order to model the combustion process one needs to know the thermo-chemical data of all the species considered. The data for gaseous species are readily available from GRI 3.0. However the data for wood, resin, char, and tar have to be determined. The elemental composition of wood, resin and tar are determined above. The methodology of finding the thermo-chemical information of these species is developed in Malte et al. (1996).

The enthalpy of formation of wood is based on the empirical equation given by Reed (1979):

$$h_{f-298K} = 3342 \text{ H/C} - 346.6 = 3342 \times 9.844/6 - 346.6 = -5830 \text{ kJ/kg} \quad [\text{A5-1}]$$

Assuming the ash content of 2.08% (oven dry, mass basis), the molecular weight of resin and ash free wood is 145.6 kg/kmol, This gives the higher heating value for dry, resin free wood with ash as:

$$\begin{aligned} \text{HHV} &= (h_{f-298K \text{ wood}} - 6 h_{f-298K \text{ CO}_2} - 4.922 h_{f-298K \text{ H}_2\text{O(L)}}) / \text{MW}_{\text{wood with ash}} \\ &= (-5830 \times 145.6 - 6 (-393522) - 4.922 (-285838)) / 148.9 = \\ &19604 \text{ kJ/kg} = 8435 \text{ BTU/lbm} \end{aligned} \quad [\text{A5-2}]$$

The HHV for the cured resin is taken to be 6000 BTU/lbm (Nichols, 2004); this gives  $h_{f-298K \text{ resin}} = -455138 \text{ kJ/kmol}$ .

The HHV for the Marshfield wood sample has been measured in the ultimate wood analysis, and it is equal to 8160 BTU/lb. This value corresponds to 4.6% resin content in the Marshfield wood sample. This is consistent with the

information given by Nichols (2004), who indicates that the Marshfield sample contains 4-6% of resin on a mass basis.

In determining the higher heating value for tar, a number of investigators, including Hastaoglu et al. (1989), Solomon and Colket (1978), and Lewellen et al. (1977), argue that for wood and coal pyrolysis the thermo-chemical properties of tar are essentially the same as for the original wood or coal. However, based on the enthalpies of the species participating in tar pyrolysis, the tar enthalpy of formation can be derived. Table A5-4 shows the values of the enthalpies and the higher heating values for the species considered. The calculations show the HHV of tar is 12% lower than that of wood, mostly due to absence of the more energetic char in the products of pyrolysis.

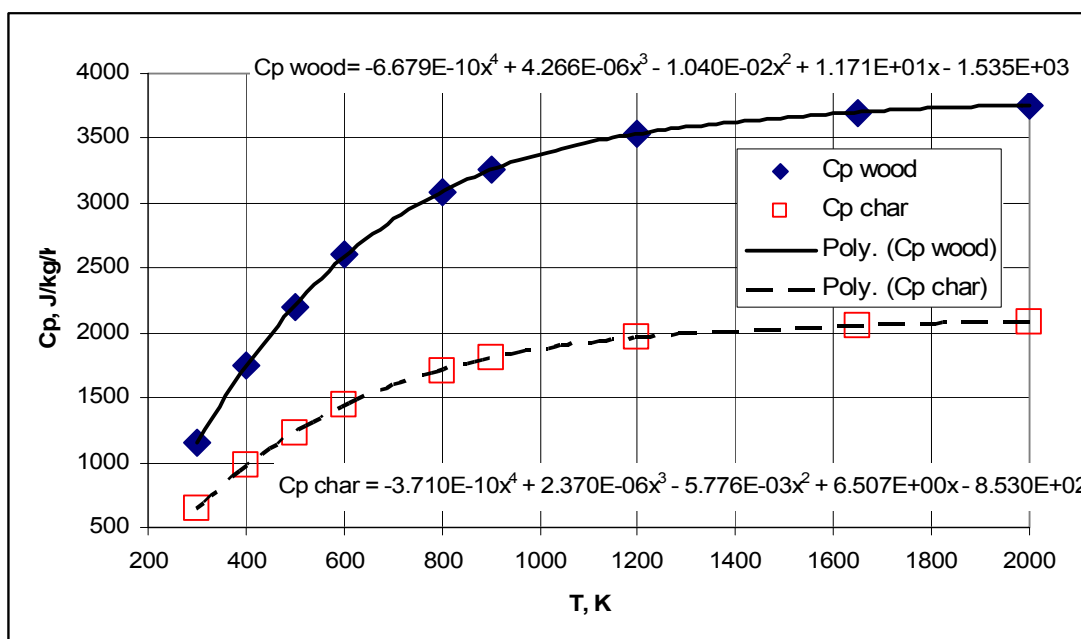
**Table A5-4. Enthalpy of formation and HHV for wood, char, tar, and resin. The wood and tar compositions are normalized to C<sub>1</sub> basis.**

	wood	total volatiles	char	tar	resin
Molecular Weight	24.15	22.46	12.00	21.94	87.00
Heat of reaction, kJ/kg species		-449.47		46.23	-116.03
Heat of reaction, kJ/kmol species		-10094.70		1014.30	-10094.70
HHV Btu/lb	8435			7447	6000
HHV kJ/kg	1.960E+04	1.731E+04	3.280E+04	1.731E+04	1.395E+04
HHV kJ/kmol	4.735E+05	3.988E+05	3.935E+05	4.458E+05	1.223E+06
Enthalpy of form. products, kJ/kmol	-5.822E+05	5.267E+05	3.935E+05	-5.716E+05	-1.588E+06
Enthalpy of formation, kJ/kmol	-1.087E+05	1.279E+05	0.000E+00	-1.259E+05	-3.651E+05
Enthalpy of formation, kJ/kg	-4.502E+03	5.694E+03	0.000E+00	-5.737E+03	-4.197E+03

The values for the specific heats and the entropy at 298 K for these species are developed in Malte et al. (1996) and summarized in Table A5-5. The values of the heat capacity of wood and char are plotted in Figure A5-2. Since cured resin is bonded with the wood cellulose structure, the resin properties are taken to be equal to the wood properties.

**Table A5-5. Heat capacity and entropy of wood, char, tar, and resin.**

Species	Heat capacity, J/kg/K	$S_{298\text{ K}}$ , J/kg/K
Wood	$C_{p\text{ wood}} =$ $-6.679\text{E-}10\text{ T}^4 + 4.266\text{E-}6\text{ T}^3 - 1.04\text{E-}2\text{ T}^2 + 11.71\text{ T} - 1535$	859
Char	$C_{p\text{ char}} =$ $-3.71\text{E-}10\text{ T}^4 + 2.37\text{E-}6\text{ T}^3 - 5.776\text{E-}3\text{ T}^2 + 6.507\text{ T} - 853$	477.25
Tar	Same as wood	859
Resin	Same as wood	859

**Figure A5-2.** Polynomial fits for heat capacity of wood and char.

## Rates of Pyrolysis

An extensive literature search is conducted to find the appropriate rates of wood particle pyrolysis. Most of the rates are reported for temperatures below 800K and for large particle size. The kinetic rates for wood pyrolysis of Nunn

et al. (1985) and Front et al. (1991) are reported for the temperature range of 500-1400K. The rates in these two data bases are comparable. Lu et al. (2004) show good agreement of their model with experimental data for the sawdust size particles using the rates of Front et al. Thus, in the present work, the rates of Front et al. (1991) are used. Table A5-6 summarizes the kinetic rates and the heats of reaction used for modeling of wood pyrolysis.

**Table A5-6. Kinetic rates and the heats of reaction used for modeling of wood pyrolysis.**

Rate	Pre-exponential factor, 1/s	Activation energy, kJ/Mol	Reference	Heat of Reaction, kJ/kg	Reference
R <sub>1</sub>	5.85e+6	119	Front et al (1991)	-418	Chan et al. (1985)
R <sub>2</sub>	4.28e+6	107.5	Liden et al. (1988),	42	Koufopoulos et al. (1991)
R <sub>3</sub>	0.002	79	Field et al (1967)	3.28e+4	Field et al (1967)
R <sub>4</sub>	5.13e+5	88	Bryden et al. (2003)	-2440	Bryden et al. (2003)

## **Development of the Global Kinetic Mechanism for Wood Combustion**

There are a number of global chemical kinetic mechanisms available for methane combustion at atmospheric pressure. Most of the mechanisms are limited to a certain range of fuel-air equivalence ratio. The global mechanism of Nicol (1995) has been evaluated in the laboratory wood burner simulation. The mechanism had difficulty predicting the high levels of carbon monoxide in the fuel rich case. This is expected, because the mechanism was developed for methane combustion for fuel-air equivalence ratios between 0.5-0.8. This prompted the development of a new global chemical kinetic mechanism suitable for the fuel gases and the conditions of the wood dust combustor.

Wood dust combustors often operate in the fuel rich regime followed by a fuel lean burnout zone. The operating pressure of these combustion systems nominally is one atmosphere. By large, these are diffusion flame burners where the flame front is located in the region of stoichiometric fuel-air equivalence ratio. Often the post-flame zone is fuel lean to facilitate carbon oxidation. This dictates the optimization parameters for the global mechanism for wood volatiles combustion.

A regression analysis of the detailed chemical kinetic mechanism GRI 3.0 is performed as described in Novosselov (2002). The main objective of the new mechanism is to capture the correct behavior of CO oxidation in the flame and the post-flame zones. The reactor arrangements used in the development of the mechanism and the range of the fuel-air equivalence ratio are shown in Table A5-7. These reactor schemes are designed to capture the rates and species concentrations in the near stoichiometric flame zone; the post flame in these arrangements can be fuel lean or rich.

**Table A5-7. Reactor arrangements and fuel-air equivalence ratios ( $\phi$ ) used in the development of the global chemical kinetic mechanism.**

Reactor arrangement	$\phi$ in element 1	$\phi$ in element 2
Single PSR (blowout – 3 ms)	0.8-1.2	N/A
PSR (2 ms) followed by a PSR (1 - 4 ms)	0.8-1.2	0.8-1.2
PSR followed by a short (2-10 ms) PFR at assigned temperature (1200K –adiabatic)	0.8-1.2	0.8-1.2
PSR followed by a long (50 ms) PFR at assigned temperature (900K -adiabatic)	0.8–1.2	0.4-1.2

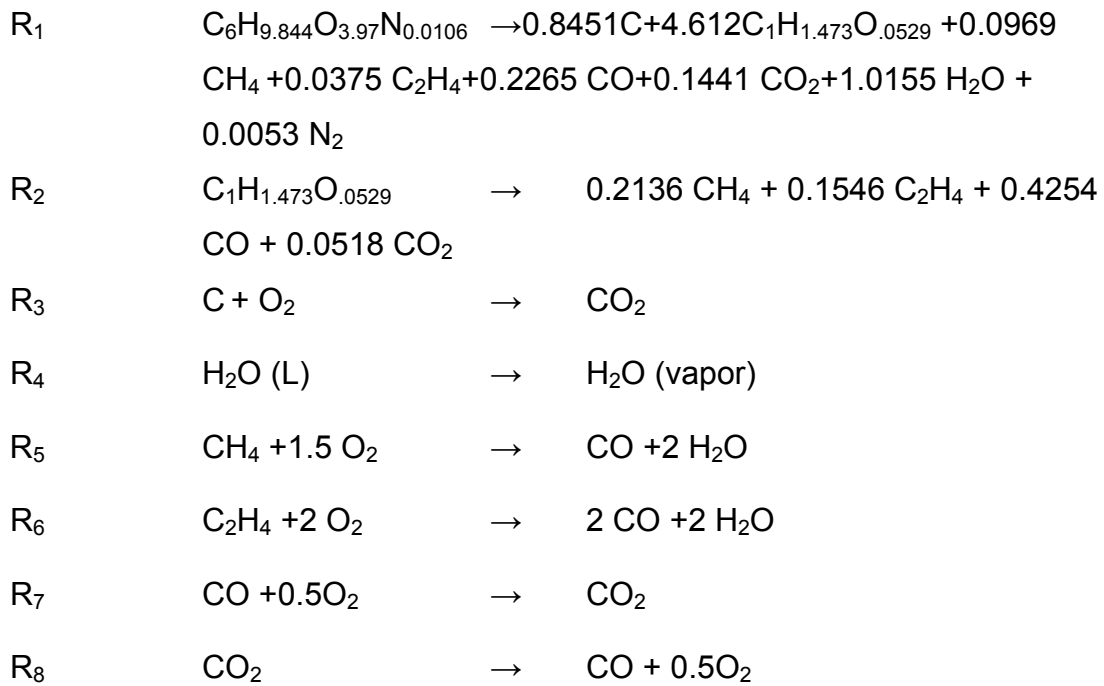
The fuel-air equivalence ratio in the first element is always near stoichiometric, which corresponds to the flame front position in the diffusion flame. The fuel-air equivalence ratio ( $\phi$ ) of the second element is the same as in the first element, except for the long PFR at assigned temperature. This

element represents the post-flame zone with the addition of the dilution air. Including the single PSR element in the regression analysis database is important for capturing the dynamics in the early part of the flame. The PSR-PSR scheme is conceptually analogous to the arrangement that is used in the chemical reactor modeling of the gas turbine combustors and jet-stirred reactors. The residence time of the first PSR is set to 2 ms. The PSR- PFR system at assigned temperature introduces the possible heat loss by the reactor if a large temperature gradient is present. The fuel-air equivalence ratio stays constant throughout the scheme. The PFR temperature is varied from 1200K to adiabatic. The residence time in the PFR is varied from 3 to 10ms. This longer residence time assures that the CO-CO<sub>2</sub> chemistry approaches local equilibrium. The last scheme is a PSR – long PFR. In this case the PSR residence time remains 2 ms, but it is 50 ms in the PFR. Also, additional air is added to the PFR. The temperature in the PFR is in the range from 900K to the adiabatic equilibrium temperature for a given  $\phi$ . The reactor arrangement represents the flame front followed by the post-flame zone with the secondary air addition to the combustor, which is the case in most combustion systems.

It is found that the initial oxidation step of the hydrocarbons in the diffusion flame is not governed by the chemical kinetic rate. The mixing time in this system is orders of magnitude larger than the chemical time. Although the chemical kinetic rates of hydrocarbon destruction are calculated, it is not practical to use these rates in the CFD simulation. The mixing rate of the hydrocarbon oxidation is a function of the flow parameters. The EBU rates of Magnussen et al. (1976) are used. The global reactions and their rates are presented below. These rates are used in the CFD code to solve the species transport equations. Generally, the use of the global kinetic rates creates a

number of uncertainties; the major one is prediction of the adiabatic flame temperature. The combustion temperature depends on the presence of the radicals and the endothermic reactions that are associated with their formation. In the development of the global mechanism this task is handled by the reaction of CO<sub>2</sub> dissociation to CO, which keeps the flame temperature from rising above adiabatic.

The combined rates of wood and tar pyrolysis and the global mechanism rates for wood volatiles oxidation are listed below:



The global rates for these reactions are:

$$R_1 = 10^{6.767} [C_6H_{9.844}O_{3.97}N_{0.0106}] \exp(-9.894e+5/T)$$

$$R_2 = 10^{6.6314} [C_1H_{1.473}O_{.0529}] \exp(-8.938e+5/T)$$

$$R_3 = 10^{-2.699} [C] \exp(-6.568e+5/T)$$

$$R_4 = 10^{5.71} [\text{H}_2\text{O (L)}] \exp(-7.316 \times 10^5/T)$$

$$R_5 = R_{\text{EBU}}$$

$$R_6 = R_{\text{EBU}}$$

$$R_7 = 10^{10.4056} [\text{CO}]^{1.1418} [\text{H}_2\text{O}]^{0.5} [\text{O}_2]^{0.25} \exp(-15658/T)$$

$$R_8 = 10^{6.1} [\text{CO}_2]^{1.0} \exp(-18135/T)$$

The units used in the rate expressions are: activation temperature ( $E_a/R$ ) = K, concentration = kmol/m<sup>3</sup>, and reaction rate = kmol/(m<sup>3</sup>-s).

## **Global Chemistry Modeling Approach in the Laboratory Wood Dust Combustor**

The University of Washington laboratory wood dust burner is modeled with CFD using the global chemistry approach. The wood burner was developed at the UW Combustion Laboratory as part of a research contract with the Weyerhaeuser Company entitled, "Control of Exhaust Emissions from Sawdust and Sander Dust Burners". The detailed description of the experimental setup and presentation of initial emissions data can be found in Parish (1998). The schematic drawing of the burner is shown in Figures A5-3 and A5-4.

The geometry of the experimental wood combustor is symmetric with respect to the yz-plane; thus, for the simulation of the flow inside of the burner this symmetry is used. In meshing the geometry, the rotational periodic boundary conditions are applied. The burner consists of four main zones (see Figure A5-5): (1) primary combustion zone, (2) flame holding nozzle (throat), (3) main burner section, and (4) burner extension. The burner is set up vertical in the laboratory.

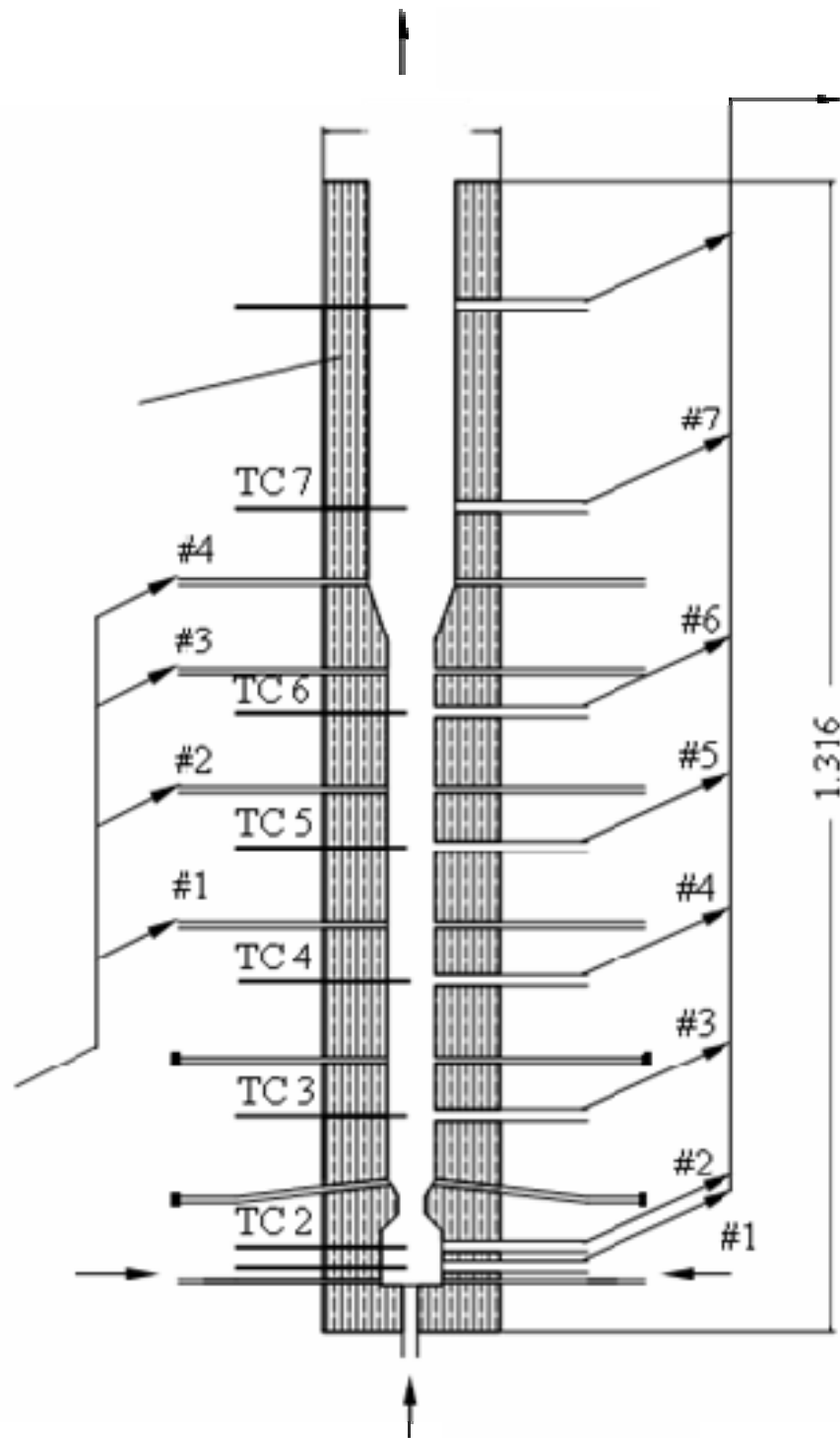


Figure A5-3. Schematic drawing of the laboratory wood dust burner, the dimension is in meters.

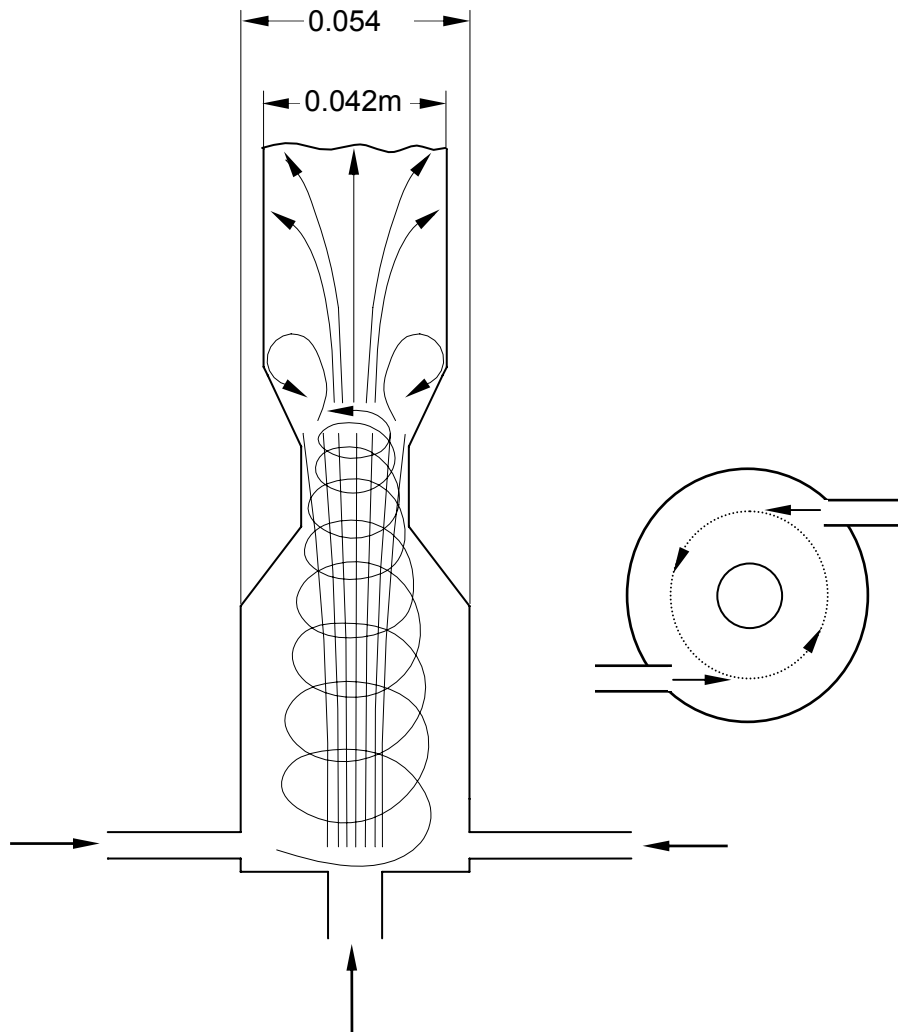
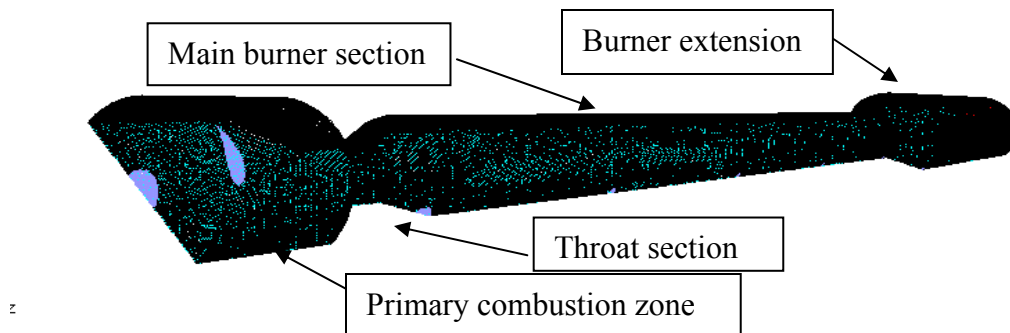


Figure A5-4. Schematic diagram of the flow pattern in the lower part of the burner.



**Figure A5-5. Wood dust burner for computational grid.**

The primary air and the gaseous fuel (when used) enter the primary combustor zone tangentially through the two opposed openings as seen on Figure A5-4. The sawdust is injected axially and upward at the bottom of the combustor. The primary combustion zone serves for flame stabilization. In a number of cases gaseous fuel as propane or methane is used to stabilize the flame. However, the present modeling is done for the case where wood dust is the only fuel. The throat section separates the primary combustor zone from the main burner section. It also serves to enhance the ignition of the sawdust due to the presence of the recirculation zone created by the diverging part of the throat.

Figures A5-6 to A5-9 show the burner sections for the CFD grid. As Figure A5-7 shows, the first out of six secondary air inlet ports are also located in the downstream part of the throat section. The main burner section (Fig. A5-8) of the combustor is 24 inches long and 1 21/32 inches in diameter; it has four inlets for secondary air and is equipped with thermocouples, sampling probe ports, and viewing windows. The burner extension section (Fig. A5-9) provides the additional residence time for the combustion process. It has a

larger diameter (3 inches) and is 18 inches long. The burner extension also has one secondary air inlet and sampling ports.

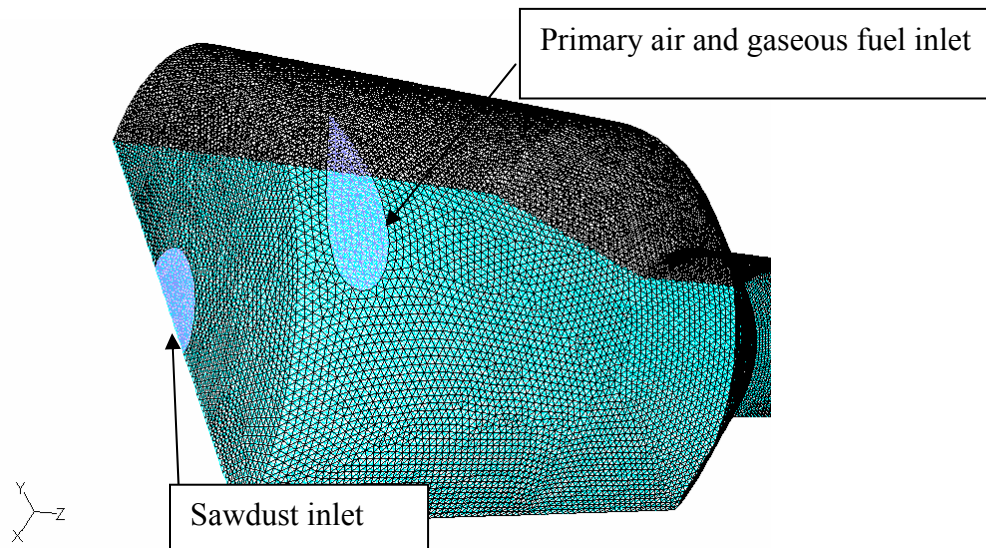


**Figure A5-6. Primary combustion zone.**

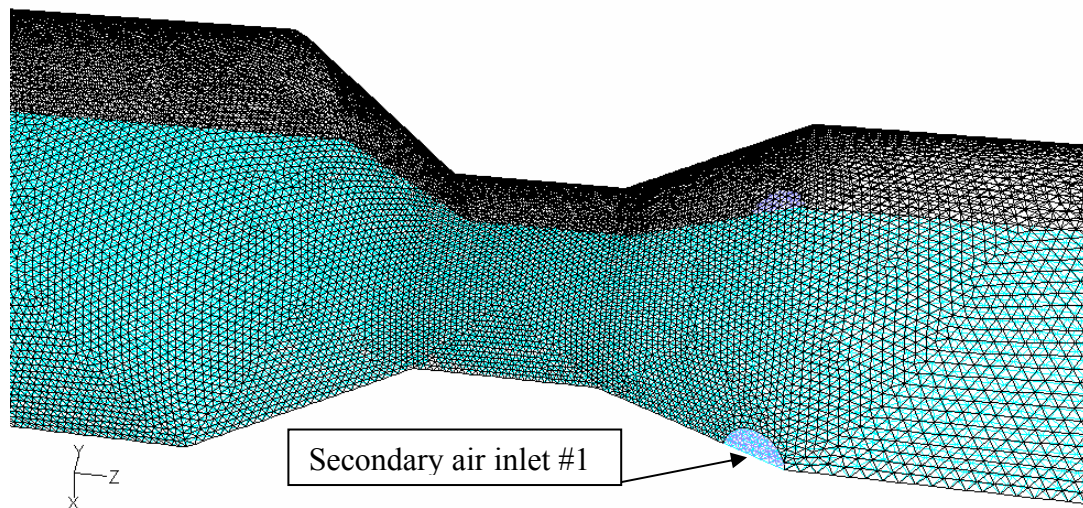


**Figure A5-7. Throat section.**

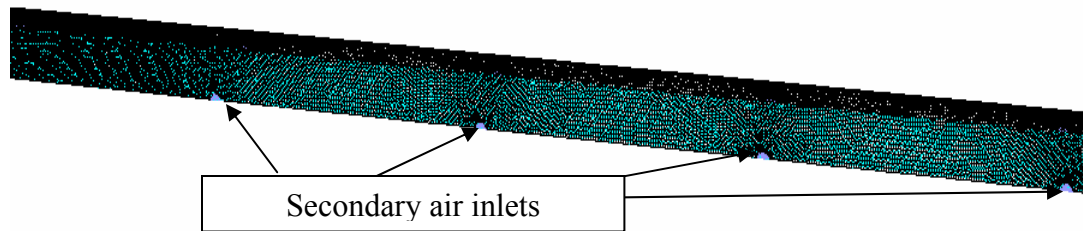


**Figure A5-8. Main burner section.**

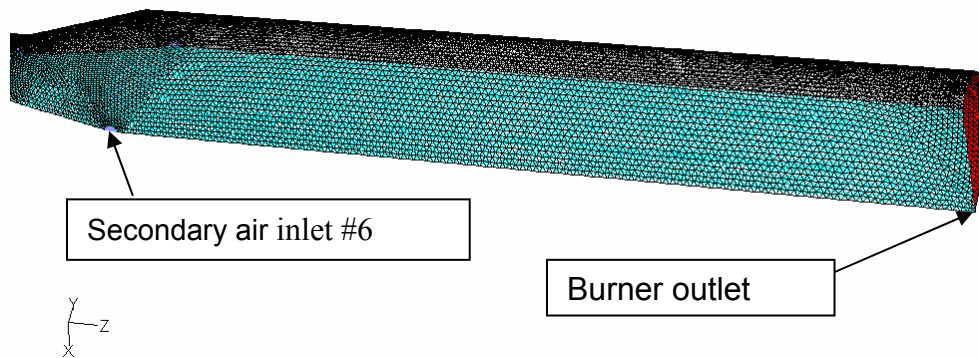


**Figure A5-9. Burner extension.**

### ***CFD Simulation of the Laboratory Wood Dust Burner***

A non-structured tetrahedral grid is used for meshing the geometry. Grid spacing is varied throughout the burner. The primary zone and the throat use the most fine spacing (0.025 inches). The grid spacing on the main burner is between 0.06 inch, close to the throat, and up to 0.1 inch at the extension. The grid spacing on the extension section is 0.1 inch. The total number of cells is about 800,000.

The flow field is solved with the Navier-Stokes equations using the Reynolds stress turbulence closure model. Species transport with volumetric reaction

and the energy equation are solved. The burner wall heat transfer rate is determined by the thickness of the wall and its material properties. The heat transfer equations for the combustor wall are solved for both radiative and convective components. The convective heat transfer coefficient is assigned to the outside wall of the combustor. The discrete ordinates radiation model is used to model the radiative component of the heat transfer by the combustion gas. It is found that for the laboratory wood burner the radiative heat transfer accounts for about a third of the total heat loss.

The dust combustion is modeled as two phase combustion. The diagram of the combustion model for the wood particle has been shown in Figure A5-1. A wood particle receives heat via radiative and convective heat transfer from the mean flow and the surrounding walls. As the particle heats up, water evaporates. In the CFD model, water is injected separately and the wood particle is assumed dry. This simplification allows assigning a different rate from the pyrolysis rate to the evaporation of water from the particle. The rate of evaporation is much higher than the rate of pyrolysis, so all of the water is evaporated before the pyrolysis of wood begins. The wood particle undergoes pyrolysis at the controlling diffusion/kinetic rate. The products of the pyrolysis then react. The volumetric reaction rates for the species are described above.

The remaining char particles are treated as burning particles and tracked through the domain. The char surface oxidation is kinetic/diffusion limited; the rates for char oxidation developed in Field (1969) are used. The particle energy equation is coupled with the bulk flow energy equation. This permits both convective and radiative heat exchange with the mean flow.

### **Effect of Soot on the Combustion Temperature**

It was found in the experiments that the burner produces significant amounts of soot. The soot can play a large role in the radiative heat transfer in the burner, and thus, in the temperature solution. For this reason, a soot model is explored for coupling with the temperature/species calculations. A single step soot formation reaction from Khan and Greeves (1974) is examined. The rate for the soot oxidation reaction is taken from Magnussen and Hjertager (1976). The effect of soot radiation on the temperature field can be calculated using the soot model. The model estimates the effect of the soot on the radiative heat transfer by determining an effective absorption coefficient for soot. The absorption coefficient for a mixture of soot and an absorbing (radiating) gas is then calculated as the sum of the absorption coefficients of pure gas and pure soot. The absorption coefficient for the gas is based on the weighted sum of gray gases (WSGGM) from Taylor and Foster (1974) and Smith et al. (1982). It is found in test simulations that the presence of soot radiation effectively reduces the combustion temperature due to additional radiative heat transfer from the gas to the wall. However, there are many uncertainties in the soot modeling, and further development and evaluation is needed. Thus, for the computational results presented herein, a soot model is not incorporated.

### **CFD Results for the Laboratory Wood Dust Burner**

The plots for the CFD computations of the laboratory wood dust burner are presented in Figures A5-10 through A5-34. The dust particle size range is 20 to 600 micrometers; i.e., the size distribution given in Malte et al. (1996) is assumed. The assumptions and the modeling approach are as discussed

above. The overall fuel-air equivalence ratio ( $\phi$ ) is 0.65 and the primary  $\phi$  is 1.35. About 28% of the total air flow enters the combustor tangentially through the tangentially opposed openings in the primary combustion zone. The secondary air enters the burner through the air ports 5 and 6 and roughly accounts for half of the total air flow; the rest of the air comes in as the wood transport air. The sawdust is carried by the transport air stream through the bottom opening. The tangential air is preheated to a temperature of 673K prior to entering the burner. The transport air and dust enter at the ambient temperature.

To determine the location of the particles at the inlet of the combustor, the injection of the dust is modeled separately. The wood feeder in the experimental setup had a 90-degree bend six inches before entering the combustor. The tube is modeled in a 2D CFD simulation. It is found that at the exit of the wood dust feeder tube the distribution of particles is highly asymmetrical. The bigger particles stay near the wall of the tube on the side furthest from the wood feeder.

Figures A5-10 through A5-13 show the data obtained from the experiment and the results from the CFD computation. The plots show two CFD points at each axial location. One point corresponds to the CFD cross-sectional area averaged value at the probe or thermocouple axial location; the other point shows the value corresponding to the radial location of the probe/thermocouple tip. The experimental temperature data, see Figure A5-10, are corrected using the heat transfer calculations for the thermocouple based on the balance between the convective and radiative heat fluxes for the thermocouple, as  $Q_{\text{conv.gained}} = Q_{\text{rad.lost}}$ . The wall temperatures and the gas temperature at the thermocouple location are obtained from the CFD

simulation. The location of thermocouple in the primary combustion zone is estimated based on Parish (1998). CFD shows that the first two thermocouple positions are near the temperature high gradient region, so a slight shift in their locations yields a significant change in the probe temperature reading. The thermocouple readings can also be influenced by flame radiation and by heat conduction in the thermocouple sheath.

The axial species profiles are shown in Figures A5-11, A5-12, and A5-13. Although the overall agreement is reasonable, discrepancies exist for the concentrations of CO and CO<sub>2</sub>. The CFD results indicate a faster CO to CO<sub>2</sub> conversion in the main burner region than measured. A number of factors should be looked at to determine inconsistencies; the most likely one is the turbulent mixing model empirical coefficients that determine the EBU rate.

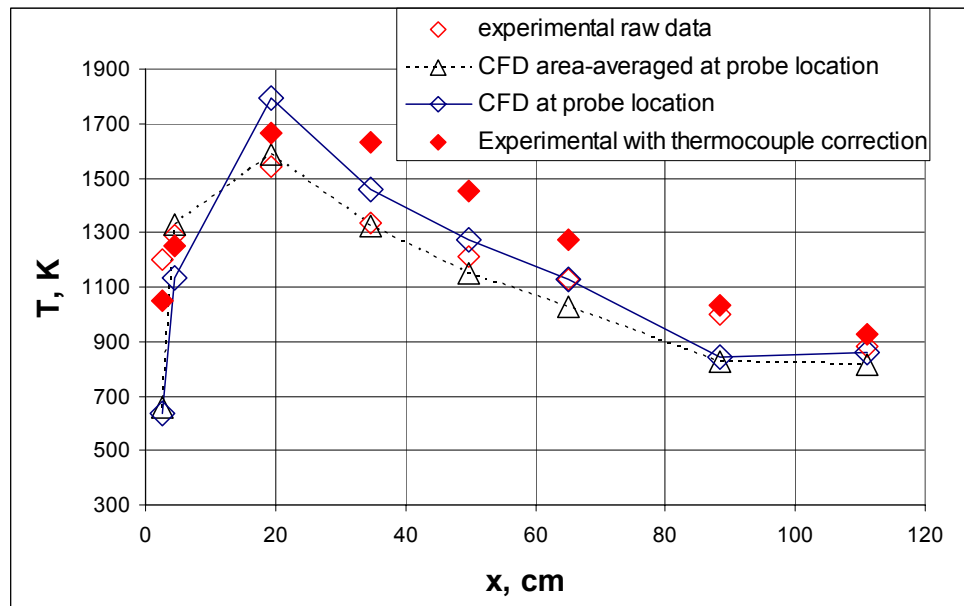


**Figure A5-10 Axial temperature profile for UW laboratory wood dust burner. The CFD calculations are shown at the probe location and as the cross-sectional, area-averaged values at the probe axial coordinate. At the first two locations the wall temperature is higher than the gas temperature, thus the thermocouple corrected value is less than the raw data.**

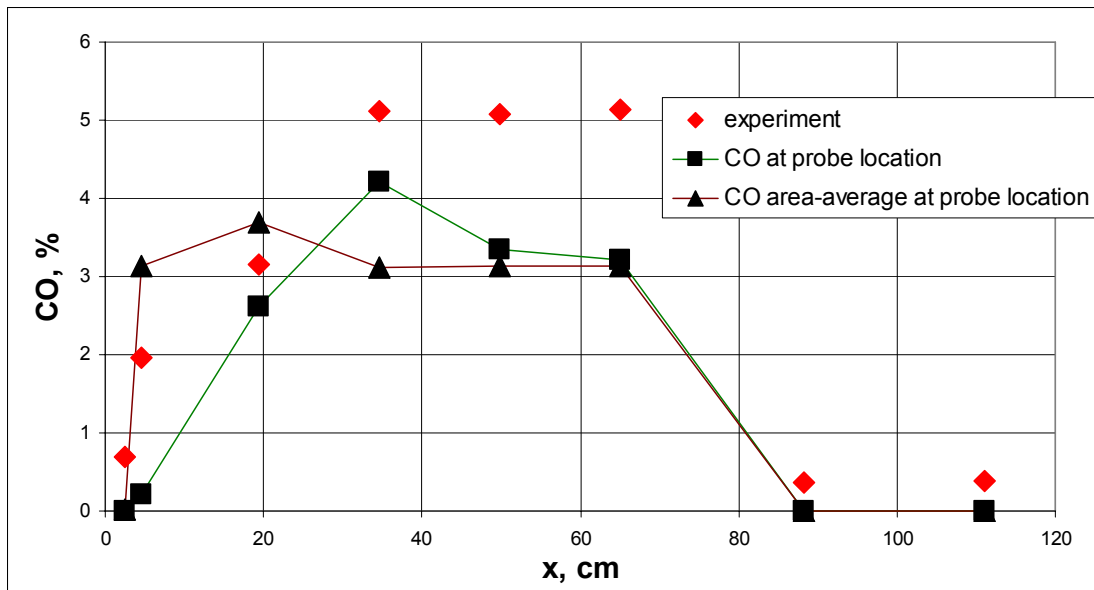


Figure A5-11. Axial CO profile for UW laboratory wood dust burner. The maximum resolution for the experimental sampling equipment is 5%.

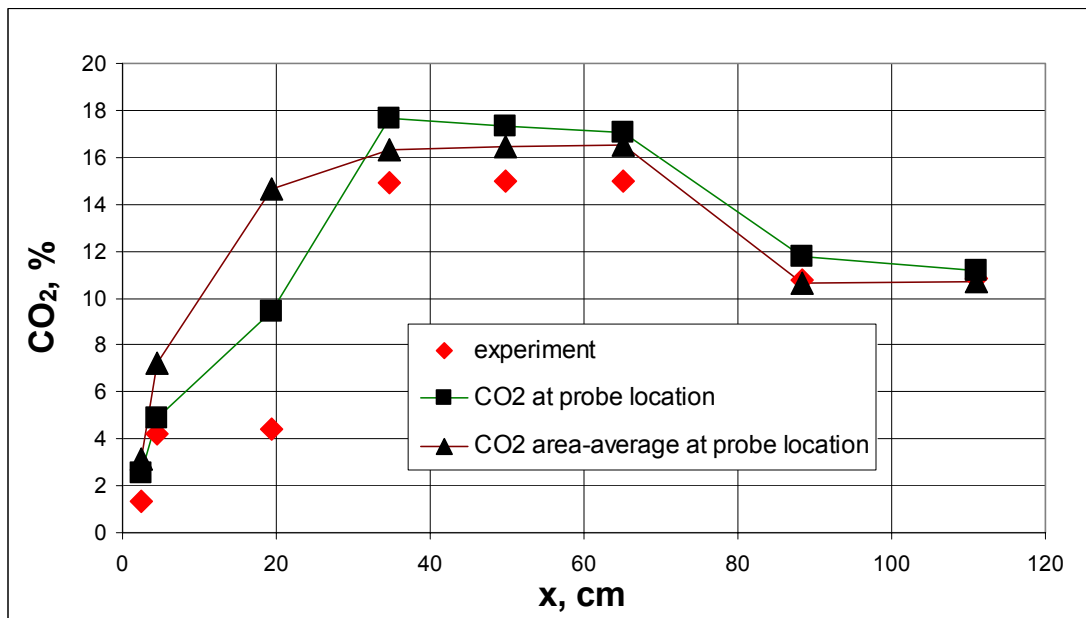
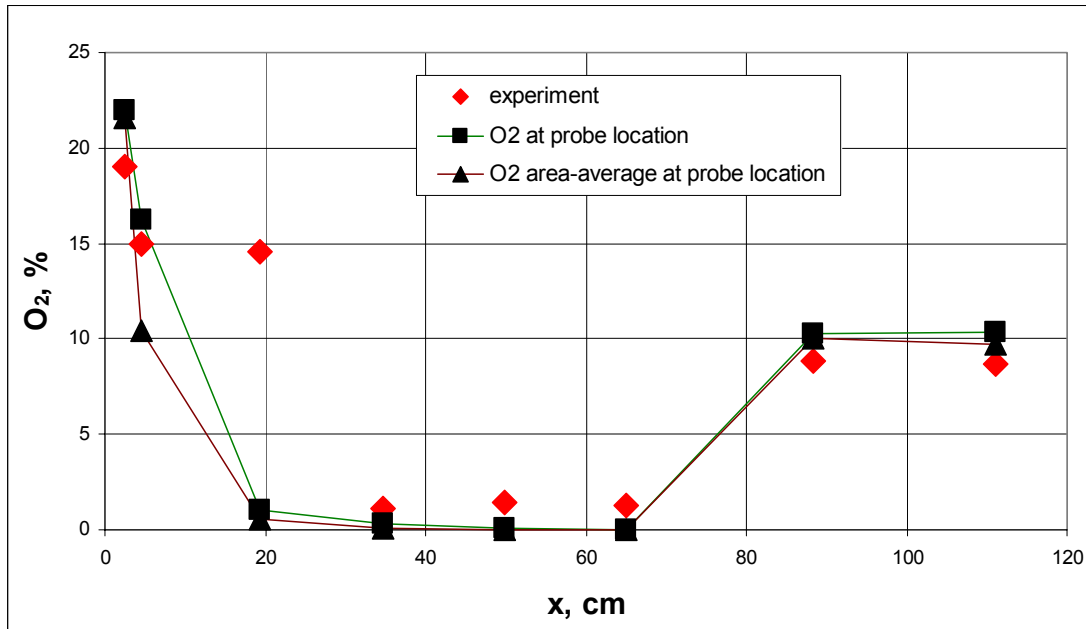
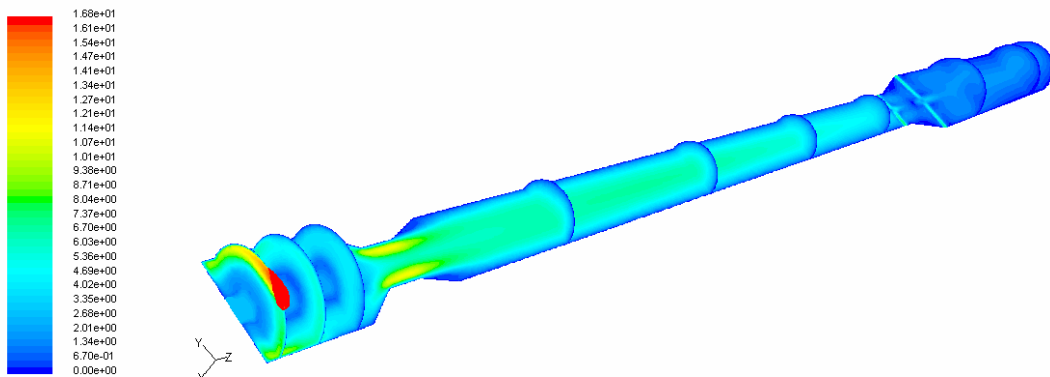


Figure A5-12. Axial CO<sub>2</sub> profile for UW laboratory wood dust burner.



**Figure A5-13. Axial O<sub>2</sub> profile for UW laboratory wood dust burner.**

Figures A5-14 through A5-24 show the CFD contour plots for the laboratory combustor. The species contour plots are shown on a wet basis. The particle tracks are shown in Figures A5-25 through A5-34. The results suggest that most of the larger particles do not burnout completely. The char does not have a chance to oxidize in the rich combustion zone due to the lack of oxygen. By the time the secondary air is injected into the combustor the temperature is low enough (1000K) to quench the chemistry. This leaves much of the black carbon in the exhaust gas. There is far less black carbon when the primary zone is lean.



**Figure A5-14. Velocity magnitude plot, maximum value is about 17 m/s.**

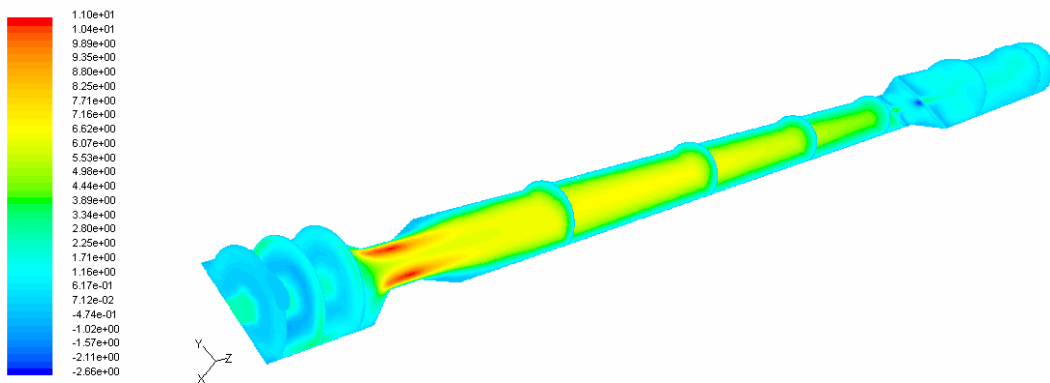


**Figure A5-15. Axial velocity, maximum value is 11 m/s.**

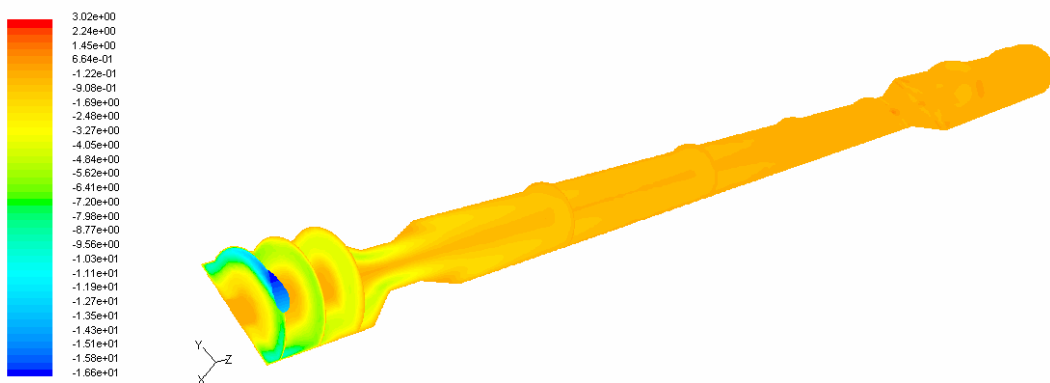


**Figure A5-16. Tangential velocity, maximum value is 16.5 m/s.**

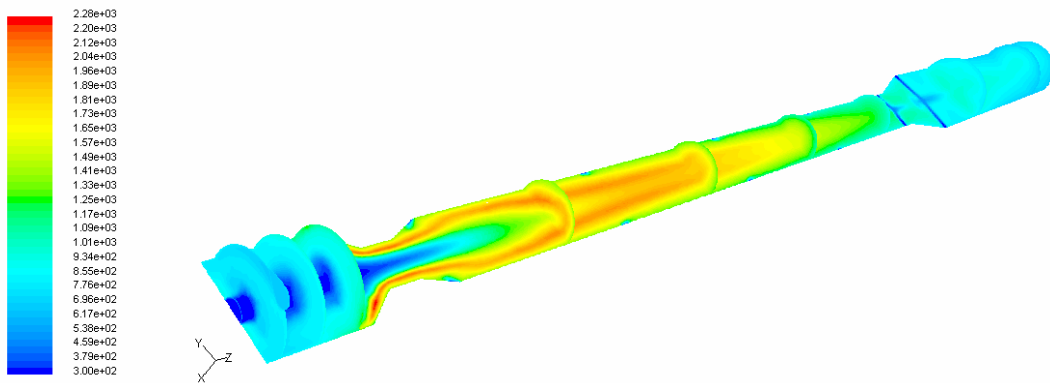


Figure A5-17. Gas temperature in the combustor, maximum value is 2260 K.

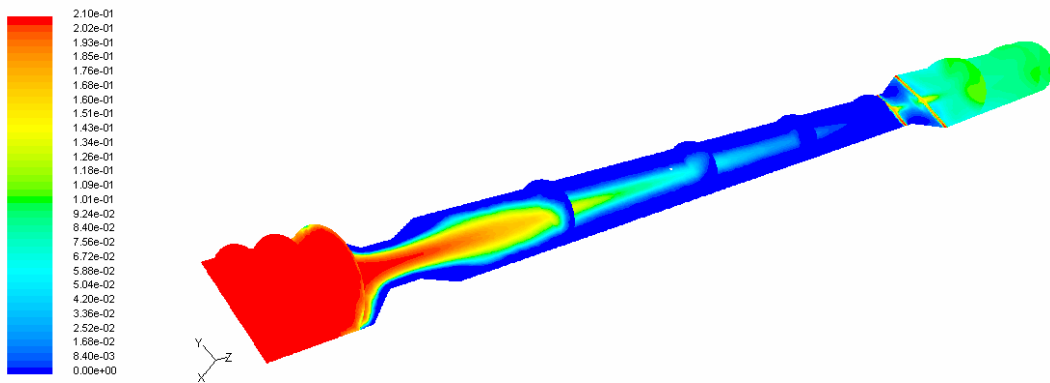


Figure A5-18. Mole fraction of  $O_2$ .

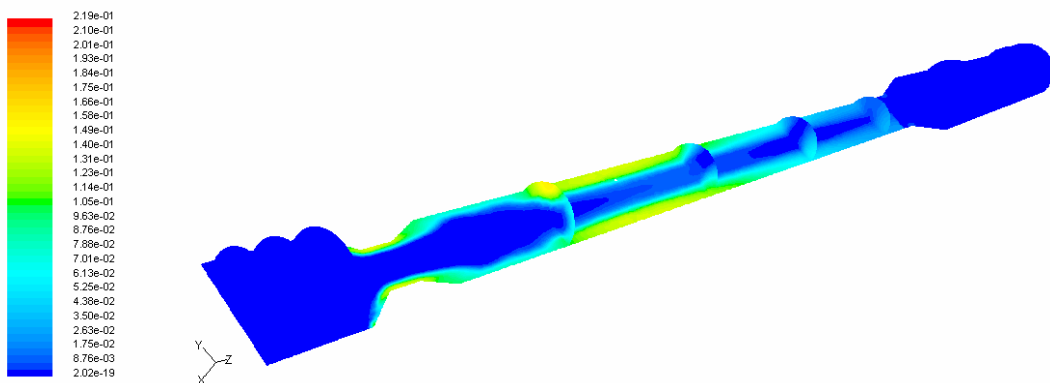


Figure A5-19. Mole fraction of carbon monoxide, maximum value is about 22%.

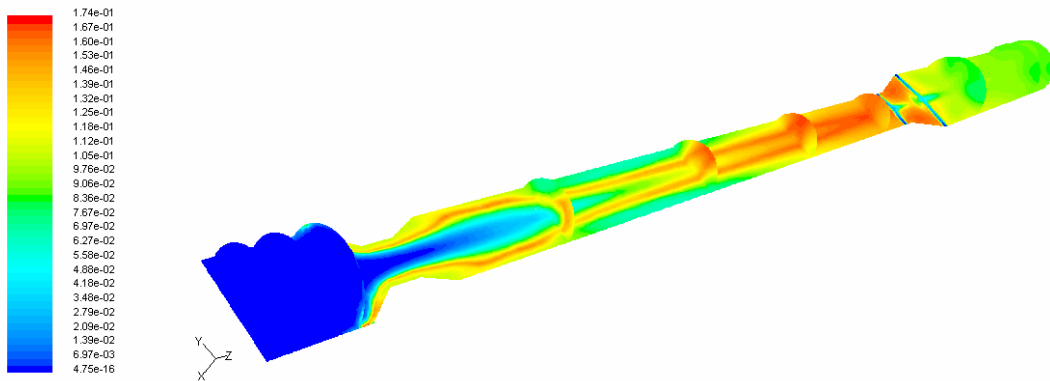


Figure A5-20. Mole fraction  $\text{CO}_2$ , maximum value is about 17%.

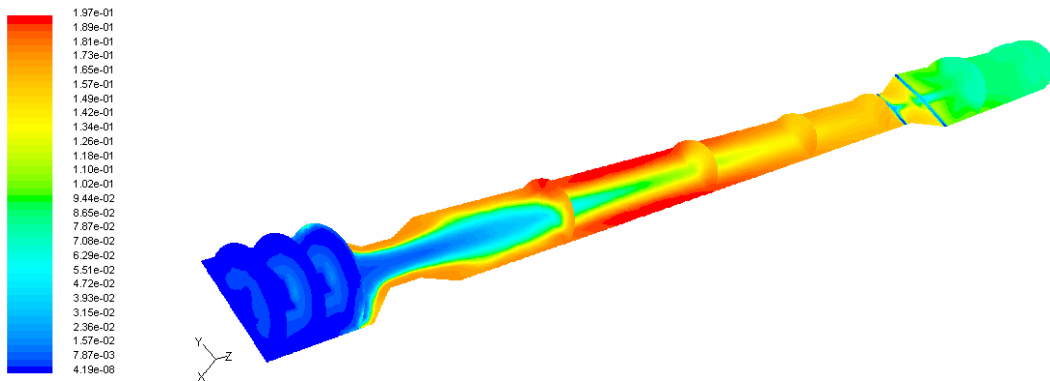


Figure A5-21. Mole fraction of  $\text{H}_2\text{O}$ , maximum is about 20%.

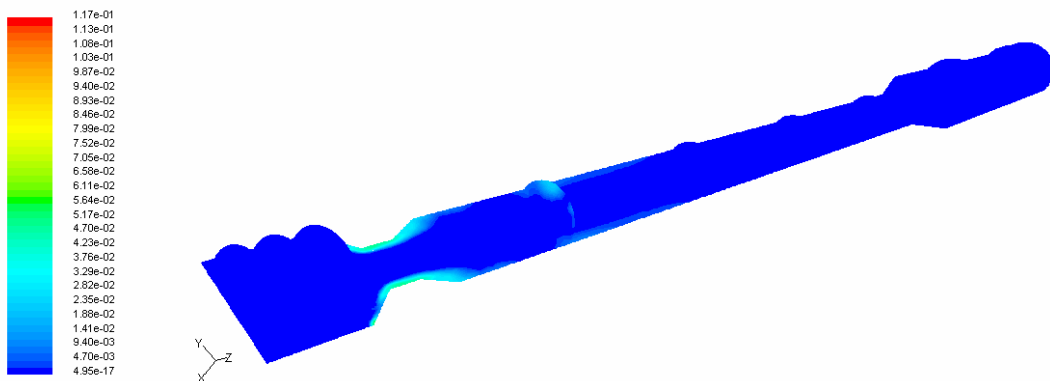
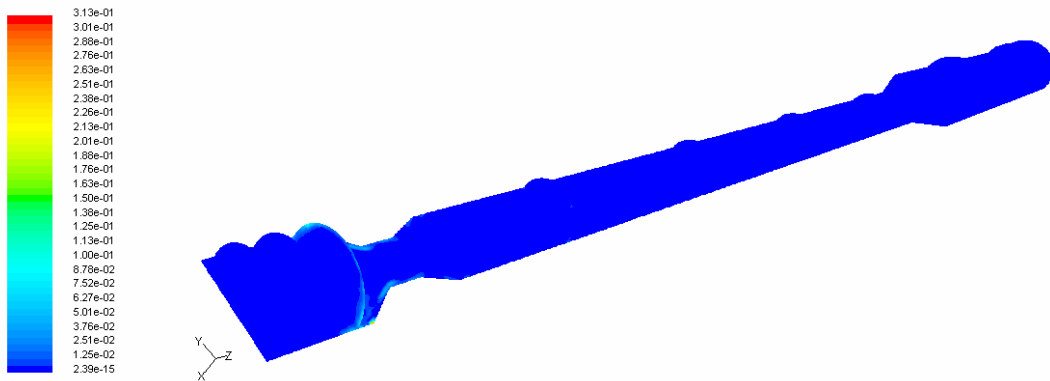
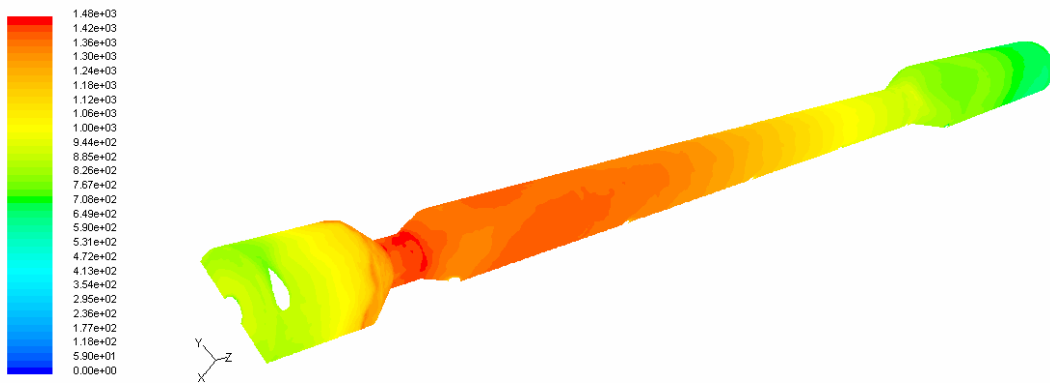


Figure A5-22. Mole fraction of methane, maximum value is about 12%.



**Figure A5-23. Mole fraction of tar, maximum value is about 30%, typical concentration near the throat is 5%.**



**Figure A5-24. Inside wall temperature, maximum value is 1480K.**

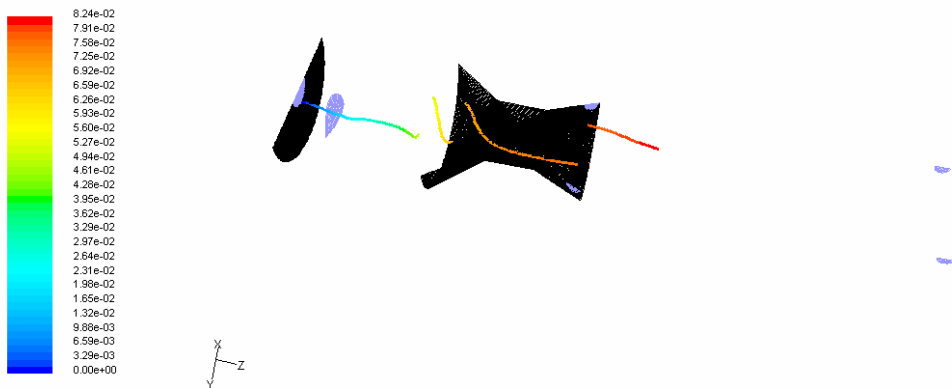


**Figure A5-25. 20 micron particle that burns out, particle track colored by the particle residence time.**

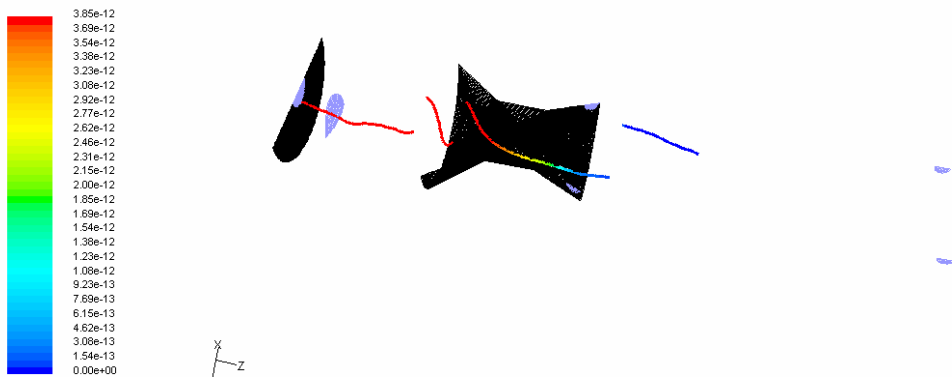


**Figure A5-26. 20 micron particle that burns out, particle track colored by the mass of the particle.**

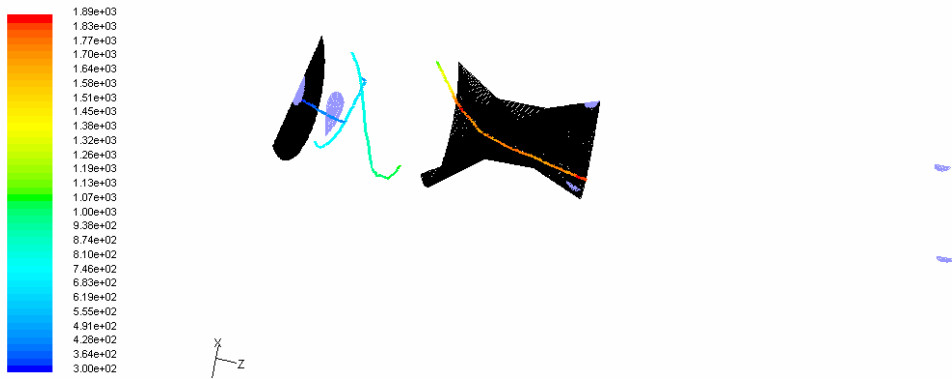


**Figure A5-27. 20 micron particle that burns out, particle track colored by the particle temperature.**

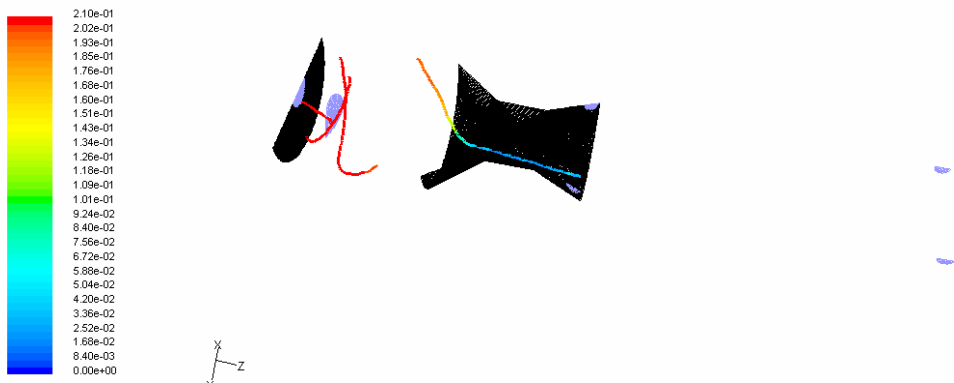


**Figure A5-28.** 20 micron particle that burns out, particle track colored by  $O_2$  mole fraction in the vicinity of the particle. The  $O_2$  concentration at the end of the particle track is 2%.

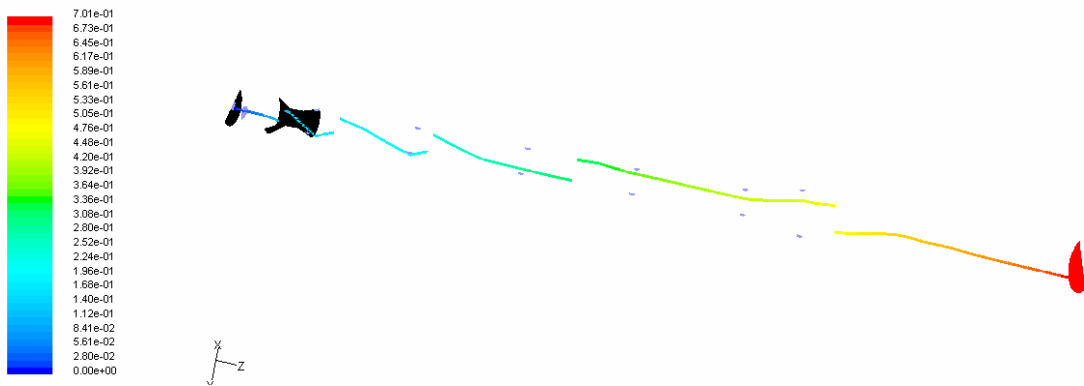


**Figure A5-29.** 600 micron particle that does not burn out, particle track colored by the particle residence time.

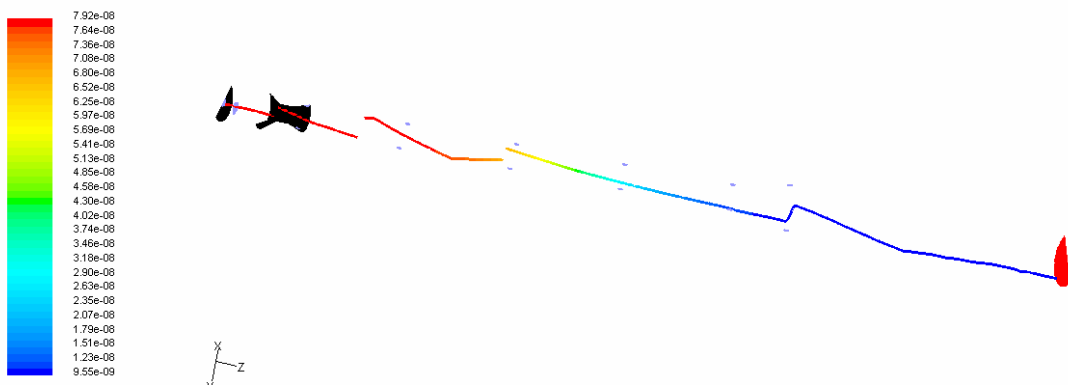


**Figure A5-30.** 600 micron particle that does not burn out, particle track colored by the mass of the particle.

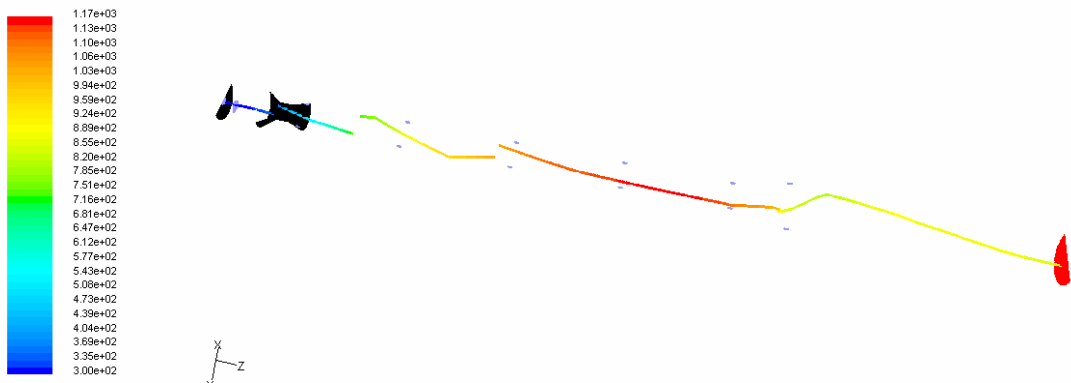


**Figure A5-31. 600 micron particle that does not burn out, particle track colored by the particle temperature.**

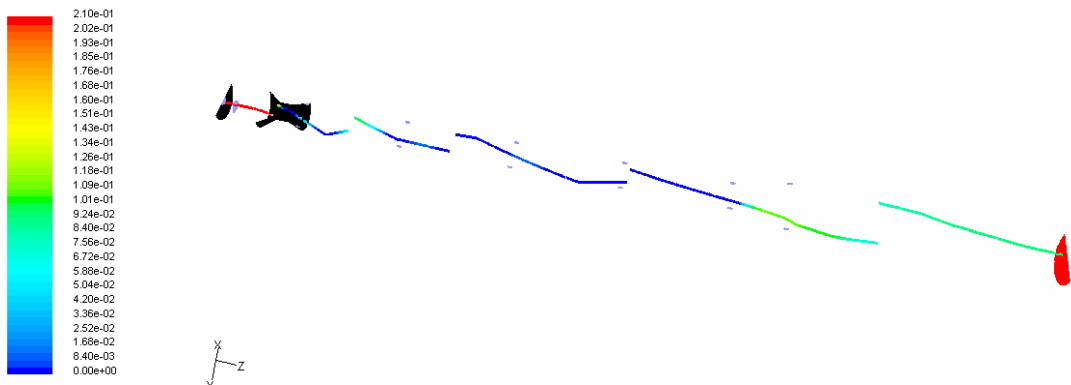


**Figure A5-32. 600 micron particle that does not burn out, particle track colored by  $O_2$  mole fraction in the vicinity of the particle.**

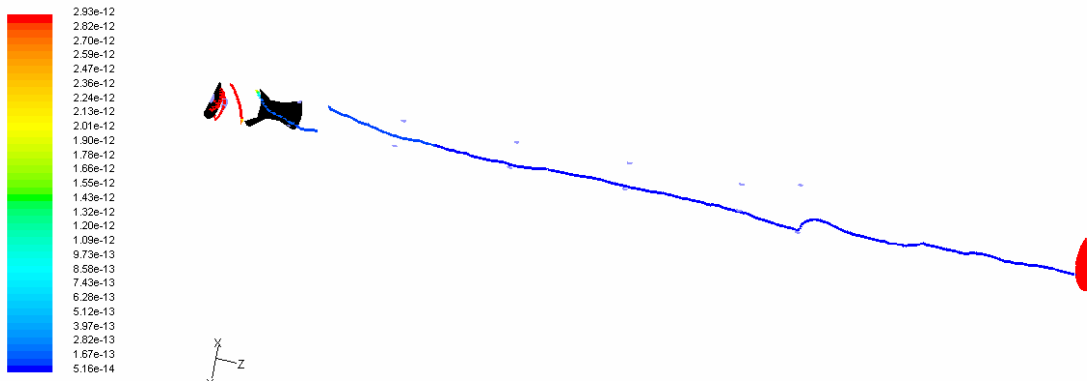


**Figure A5-33. 20 micron particle that does not burn out, particle track colored by the mass of the particle.**

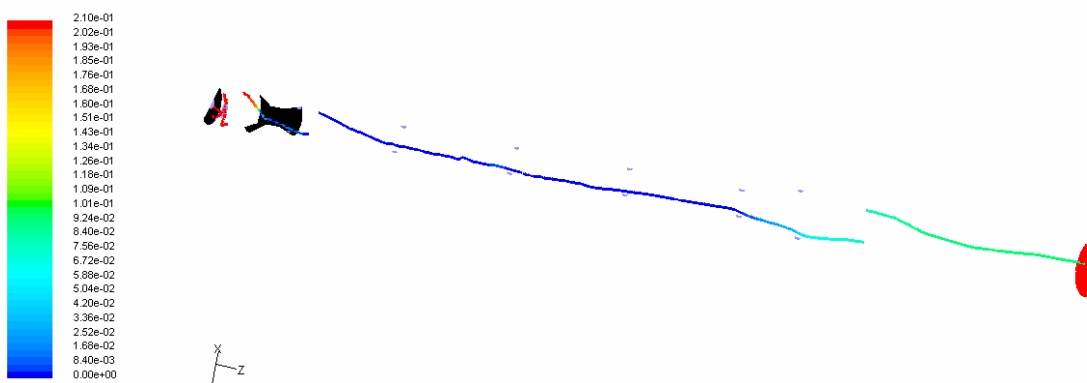


**Figure A5-34. 20 micron particle that does not burn out, particle track colored by  $O_2$  mole fraction in the vicinity of the particle.**

### ***Chemical Reactor Network for UW Laboratory Wood Dust Burner***

The chemical reactor network is based on the results of the CFD simulation of the laboratory wood dust burner. The University of Washington chemical reactor code is used. The modeling approach for wood dust combustion in the code is discussed in Malte et al. (1996), and Malte and Nicol (1997).

The CFD simulation shows that strong diffusion flame characteristics exist in the laboratory wood dust combustor for all fuel air equivalence ratios. The flame sheet is located at the interface between the locally rich and lean mixtures. This dictates that two streams with different fuel-air equivalence ratios should be modeled. The diagram of the CRN is shown in Figure A5-36. The zone near the wall is rich and does not have oxygen available for combustion. Ignition occurs in the PSR at  $\phi$  near unity. After the secondary air enters the burner the gases are mixed in the PFR. All of the elements following the ignition PSR are at the assigned temperature, with the assigned temperature provided from the CFD modeling. Simulation for rich-lean and lean-lean combustion are analyzed to obtain axial and radial temperature profiles. These temperatures are mapped onto the CRN. Effectively, the CRN acts as the post-processor for the CFD simulations. This post-processor is able to apply a complex chemical kinetic mechanism to the previously obtained CFD solution.

Chemical kinetic mechanism and rate data for primary and secondary wood pyrolysis reactions from Nunn et al. (1985) and Boroson et al. (1989) are used. This reaction scheme has been used by Malte et al. (1996). The rates are expressed by the equation:

$$dV_i/dt = (V_i^* - V_i) 10^{A_i} \exp(-E_i/RT), \quad [A5-1]$$

where  $V_i$  is the weight % yield of species “i” on the basis of the original fuel,  $V_i^*$  is asymptotic species yield. Table A5-8 shows the final yield of species and the kinetic rates of the reactions. Table A5-9 shows the yield of resin pyrolysis and the kinetic rates. The species nomenclature is:

Wxx – wood component

Txx - tar component

WTxx - wood component that undergoes primary pyrolysis to tar

The Miller and Bowman (1989) chemical kinetic mechanism is used in the UW chemical kinetic code to describe the hydrocarbon and nitrogen chemistry after the initial wood tar and resin pyrolysis to the light gases as described in Tables A5-8 and A5-9. Chemical species  $\text{CH}_3\text{CHO}$  and  $\text{C}_3\text{H}_6$  participate in the wood pyrolysis but they are not included in the Miller and Bowman mechanism. These species are substituted by the simpler species ( $\text{HCHO}$  and  $\text{C}_2\text{H}_4$ ).

**Table A5-8 Yield and rate data for wood and tar pyrolysis (from Malte et al., 1996)**

Reaction	Final yield	$10^{A_i}$	$E_i/R$
	(% wt of original wood)	1/s	K
$WH_2O \rightarrow H_2O$	11.0	$10^{4.53}$	5788
$WH_2 \rightarrow H_2$	1.0	$10^{4.53}$	5788
$WOH \rightarrow OH$	0.25	$10^{4.53}$	5788
$WA1 \rightarrow HCHO$	2.0	$10^{3.31}$	6492
$WA1 \rightarrow CH_3CHO$	1.4	$10^{3.51}$	10720
$WC3 \rightarrow C_3H_6$	0.4	$10^{5.80}$	21540
$WCO_2 \rightarrow CO_2$	4.25	$10^{4.53}$	8304
$WCO \rightarrow CO$	4.25	$10^{4.53}$	8304
$WCH_4 \rightarrow CH_4$	0.4	$10^{4.53}$	8304
$WC_2H_4 \rightarrow C_2H_4$	0.25	$10^{4.53}$	8304
$WC \rightarrow C_{(c)} \text{ (char)}$	7.0	$10^{4.53}$	8304
$WTCO \rightarrow TCO$	36.6	$10^{4.53}$	8304
$WTCO_2 \rightarrow TCO_2$	7.0	$10^{4.53}$	8304
$WTC1 \rightarrow TC1$	10.5	$10^{4.53}$	8304
$WTC2 \rightarrow TC2$	13.3	$10^{4.53}$	8304
$WTH_2 \rightarrow TH_2$	0.2	$10^{4.53}$	8304
$WTHCN \rightarrow THCN$	0.2	$10^{4.53}$	8304
$TCO \rightarrow CO$		$10^{4.66}$	10583
$TCO_2 \rightarrow CO_2$		$10^{2.55}$	5900
$TC1 \rightarrow CH_4$		$10^{4.89}$	11342
$TC2 \rightarrow C_2H_4$		$10^{5.88}$	13364
$TH_2 \rightarrow H_2$		$10^{6.64}$	15532
$THCN \rightarrow HCN$		$10^{4.98}$	11233

**Table A5-9 Yield and rate data for resin pyrolysis (from Malte et al., 1996)**

Reaction	Final yield	$10^{A_i}$	$E_i/R$
	(% wt. of original wood)	1/s	K
$RH_2O \rightarrow H_2O$	20.7	$10^{4.53}$	8304
$RHCHO \rightarrow HCHO$	17.2	$10^{4.53}$	8304
$RHCN \rightarrow HCN$	62.1	$10^{4.53}$	8304

Char oxidation rates are fitted to the modified Arrhenius rate format:

$$k=10^A T^{-b} \exp(-E/RT). \quad [A5-2]$$

The rate of char oxidation can be limited by diffusion rate or chemical kinetic rate. The main limiting criterion is the size of the char particle. Malte et al. (1996) proposed sorting the particles according to their size and assigning different kinetic rates to each size class. The rates of char particle oxidation are shown in Table A5-10.

**Table A5-10. Char Particle oxidation rate used in the UW chemical kinetic code for reaction  $\text{Char} + 0.5O_2 \rightarrow \text{CO}$ , temperature range is 1200-2000K; the units are**

$k(\text{cm}^3/\text{gmol-s})=10^A T^{-b} \exp(E/RT)$ , from Malte et al., 1996.

Particle diameter, micron	A	b	$E/R$ (K)
65	28.967	5	19280
150	27.734	5	16900
190	27.384	5	16247
225	27.134	5	15793
270	26.868	5	15318
340	26.535	5	14744
490	26.023	5	13903

A parametric analysis is performed using the CRN. The flow inputs into the network are varied according to the experimental data of Scharfe (1998). The CRN NO predictions are compared with the experimental data. The results of analysis are plotted in Figure A5-35 as a percent of fuel nitrogen converted to NO as a function of overall fuel-air equivalence ratio. In these experiments, secondary air was not added, so the  $\phi$  stays constant throughout the combustor. Note that the highest conversion of the fuel nitrogen to nitrogen oxides occurs at the leanest conditions.

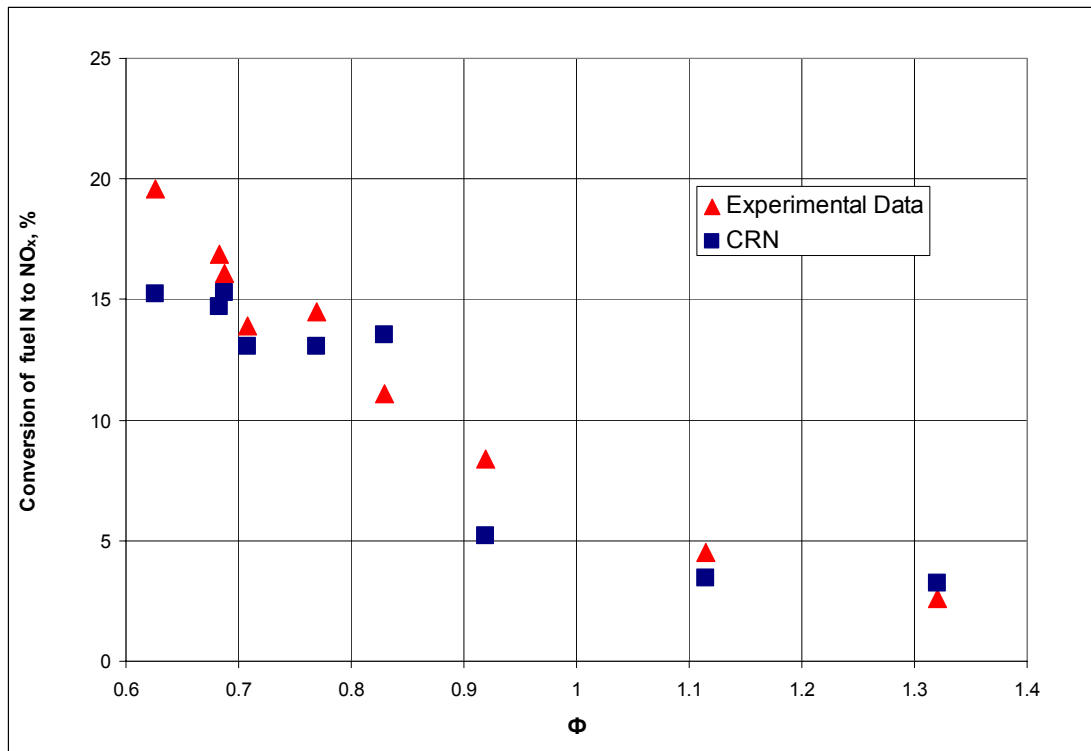


**Figure A5-35. Percentage conversion of fuel nitrogen to NO<sub>x</sub> emission at the exit of CRN as a function of fuel-air equivalence ratio.**



### ***Industrial Wood Dust Burner***

Modeling of the industrial cyclonic wood dust burner is discussed in this section. This type of burner is used in the wood products industry in a number of applications. The design of cyclonic wood dust burner goes back to the 1920s. Some minor modifications have been made since then but the conceptual design has not changed. Figure A5-37 shows the system. The recent jump in natural gas prices (to the \$12-\$15 per million BTU range) has made the wood dust burner very attractive from the economic view point. The cost of fuel for the dust burner is much less expensive. However the combustion process in this type of burner is not well understood in detail. Some of the points for concern are: high NO<sub>x</sub> and particulate emissions – the particulate emission may include unburned char, soot, and mineral matter. An effort to model the industrial burner (of Figure A5-37) is undertaken to gain insight for eventually exploring ways to reduce emissions.

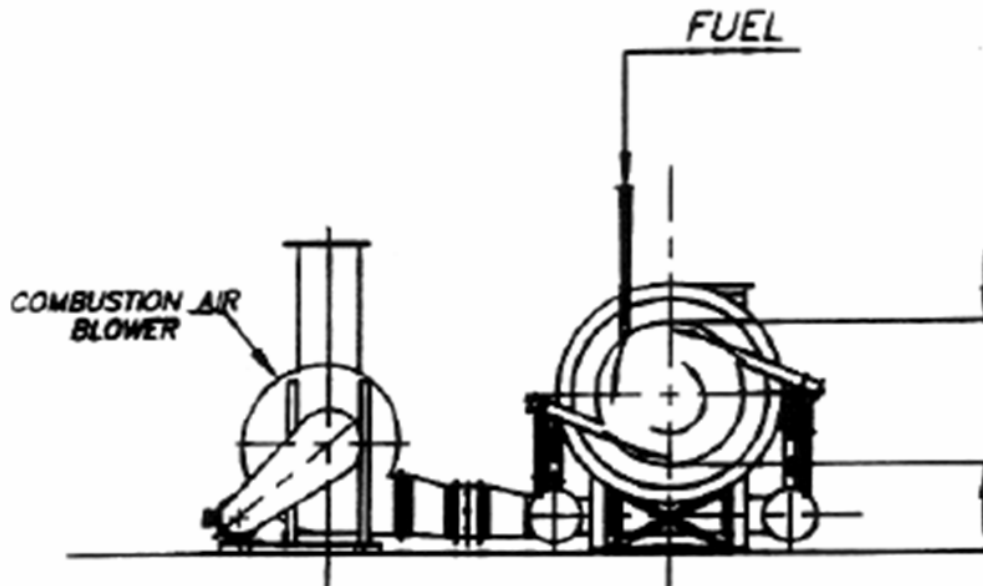


Figure A5-37. Combustion system using the industrial wood dust burner.

The CFD for the burner is performed using Fluent 6.1. The grid used in this simulation is about 800,000 cells. Figure A5-38 shows the computational domain including the main combustion chamber and the downstream burnout chamber. A flow coke separates the two chambers. Flow, turbulence, energy, and species transport equations are solved using the finite volume scheme. The Reynolds stress model is used for turbulence closure. The limiting rate approach is used for modeling the chemical terms.

The main issue in the CFD modeling is the convergence of the flow field in the downstream burnout chamber. The grid is constructed based on the design drawings of the burner manufacturer. The burnout zone modeled facilitates a strong recirculation region behind the choke between the primary and burnout chambers. This recirculation zone extends to the outlet where it creates divergence in the turbulent parameters. A number of exit plane boundary conditions have been examined in order to handle the flow field in the burnout chamber, but none of the schemes has led to a converged solution. To tackle this problem a new grid with longer burnout section should be constructed. However, the flow field in the primary chamber appears to be reasonable, and is similar to earlier CFD results obtained for the primary chamber alone (de Bruyn Kops and Malte, 2003).

Figures A5-39 through A5-47 show the contour plots of the velocity, temperature, and species fields. Figures A5-48 through A5-51 show the particle tracks colored by their properties. Although the results are initial, some useful information is gained. The simulation shows that oxygen does not mix into the central combustion zone. This creates the fuel rich region in the middle of the burner. The implication of the fuel rich zone is two fold.

On one hand, the absence of oxygen facilitates the reduction of fuel NO<sub>x</sub> in the burner. On the other hand, the lack of oxygen creates the difficulty for char and soot oxidation, thereby increasing the particulate emissions from the burner. Further analysis is needed for determining the optimal air distribution and possible burner geometry improvements.

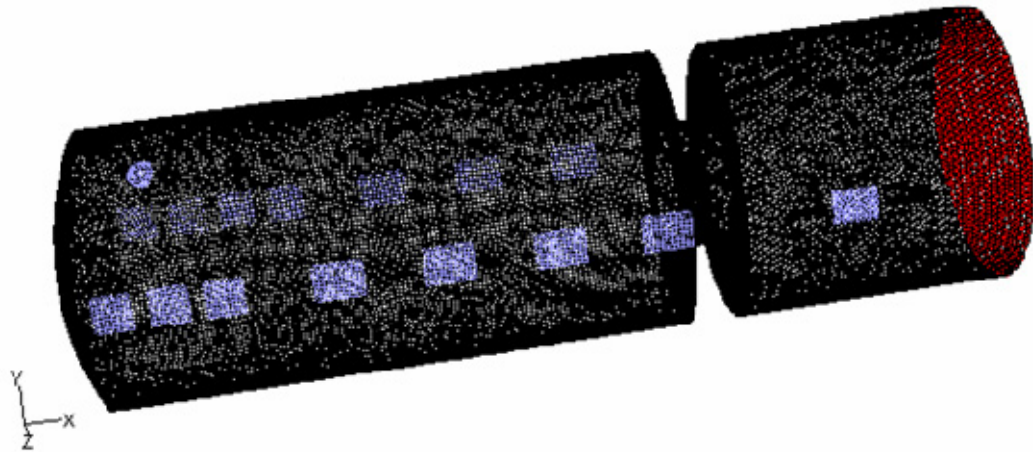


Figure A5-38. Grid for McConnell 48 wood dust burner.

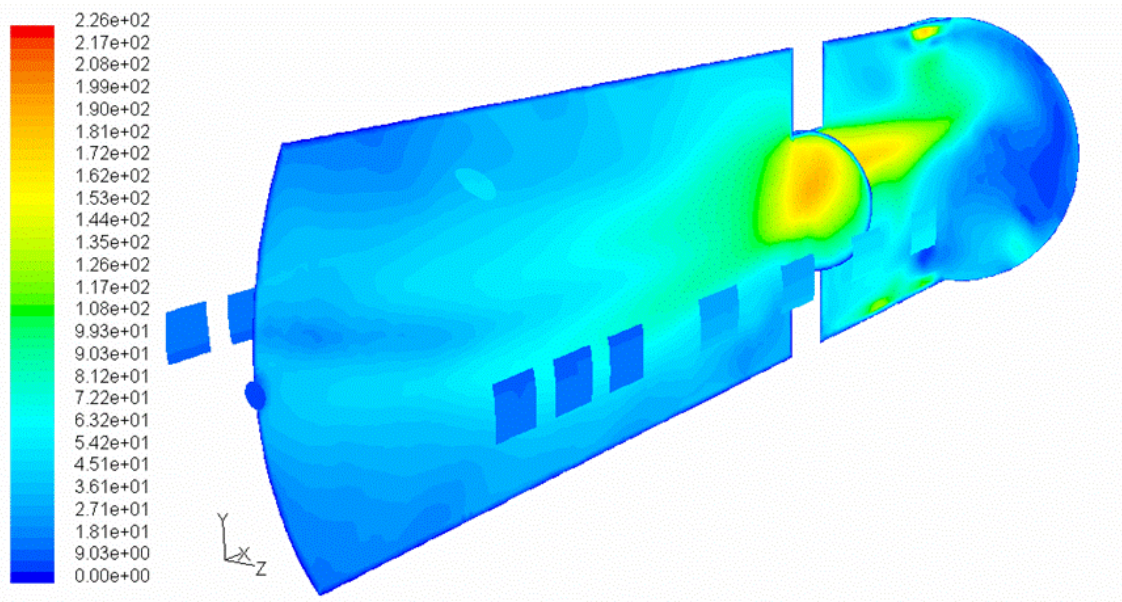
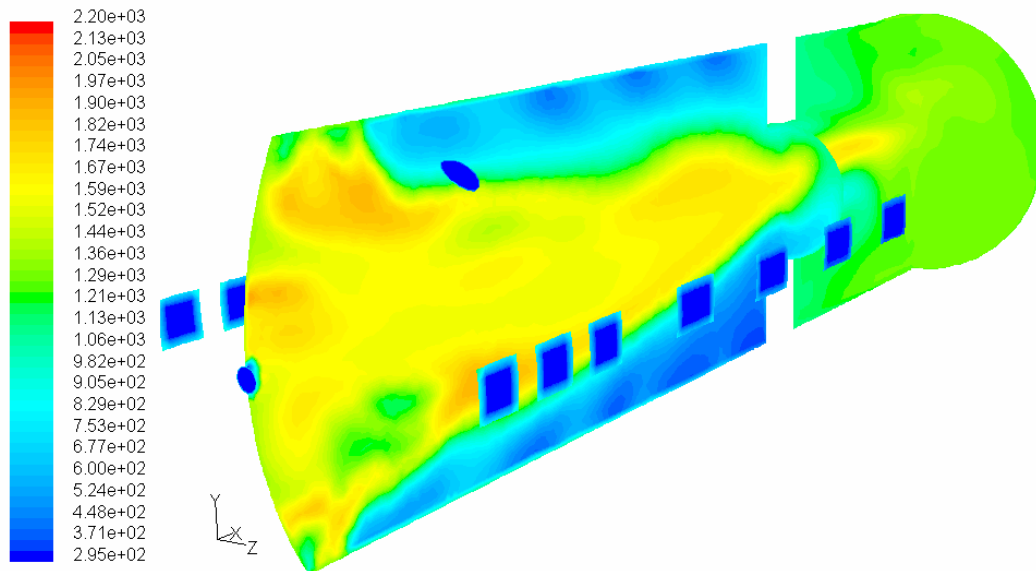
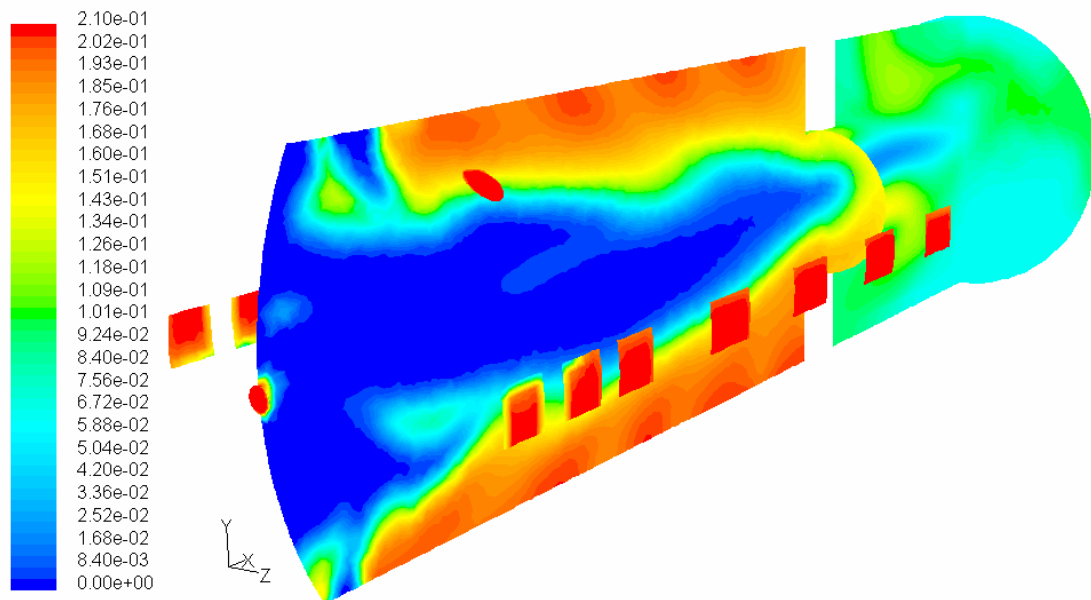


Figure A5-39. Contour plot of velocity magnitude in xy-plane, choke cross-section and exit plane.



**Figure A5-40.** Contour plot of temperature in xy-plane, choke cross-section and exit plane, Maximum value is 2200K, average flame temperature is 1800 K, choke exit temperature is 1130K.



**Figure A5-41.** Contour plot of oxygen mole fraction in xy-plane, choke cross-section and exit plane, the plot shows characteristics of diffusion flame: fuel rich and oxygen rich regions are depicted.

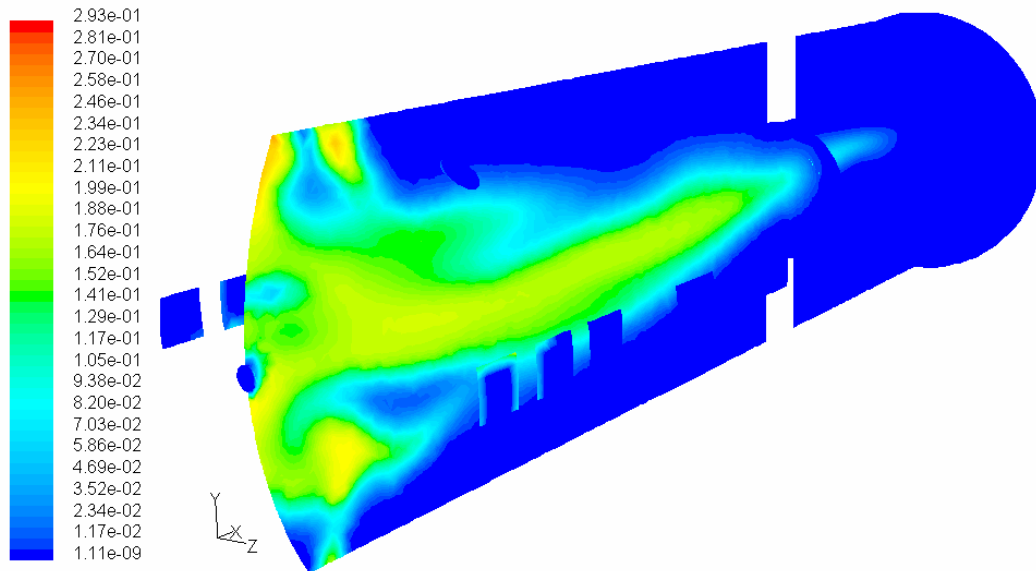


**Figure A5-42.** Contour plot of carbon monoxide mole fraction in xy-plane, choke cross-section and exit plane, the plot shows high concentration (15%) of carbon monoxide in the fuel rich region, CO concentration at the choke plane is 1.9%.

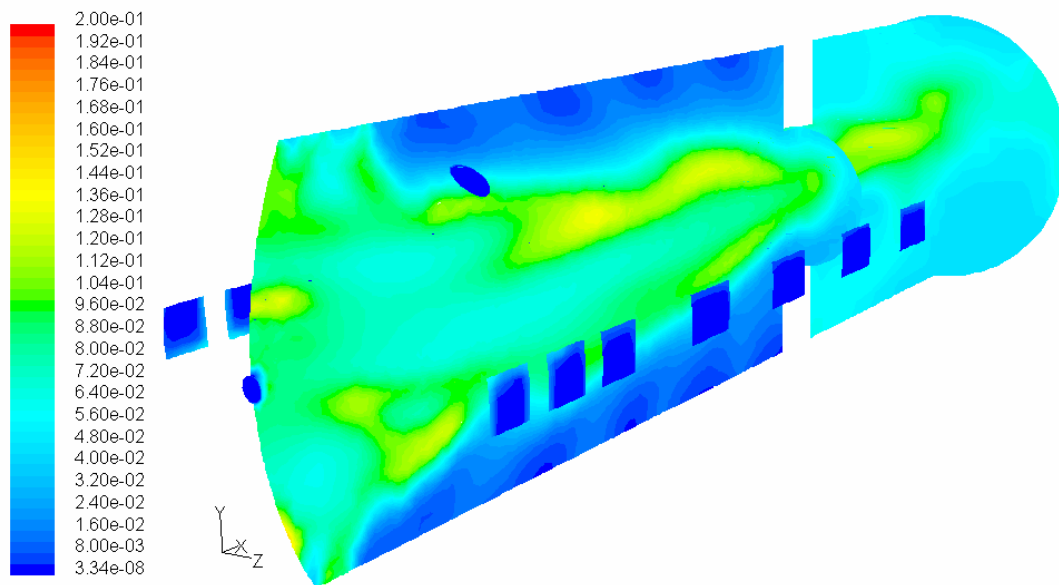


**Figure A5-43.** Contour plot of carbon dioxide mole fraction in xy-plane, choke cross-section and exit plane. CO<sub>2</sub> concentrations in the rich core flame varies between 6-10%, the concentration in the flame is about 13%.

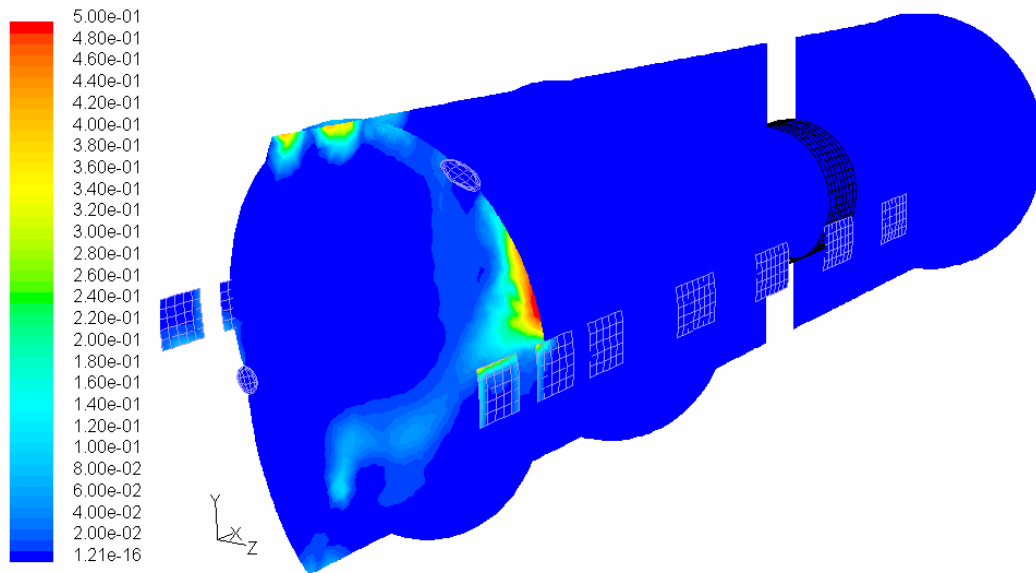


**Figure A5-44.** Contour plot of tar mole fraction in xy-plane, choke cross-section, fuel injection plane and exit plane, figure shows high concentration of tar near the fuel inlet. The maximum tar concentration reaches 50% by volume.

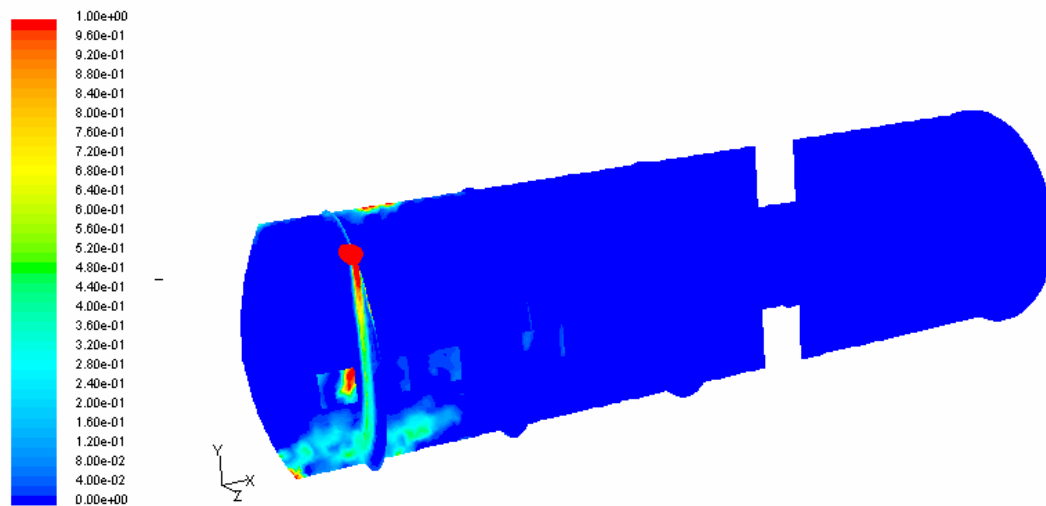


**Figure A5-45.** Contour plot of particle concentration ( $\text{kg/m}^3$ ), figure shows high concentration of particles near the fuel inlet. Maximum value is  $12 \text{ kg/m}^3$  at the inlet. The values on the plot are clipped to  $1 \text{ kg/m}^3$  for better resolution, all concentrations above this value are in red.

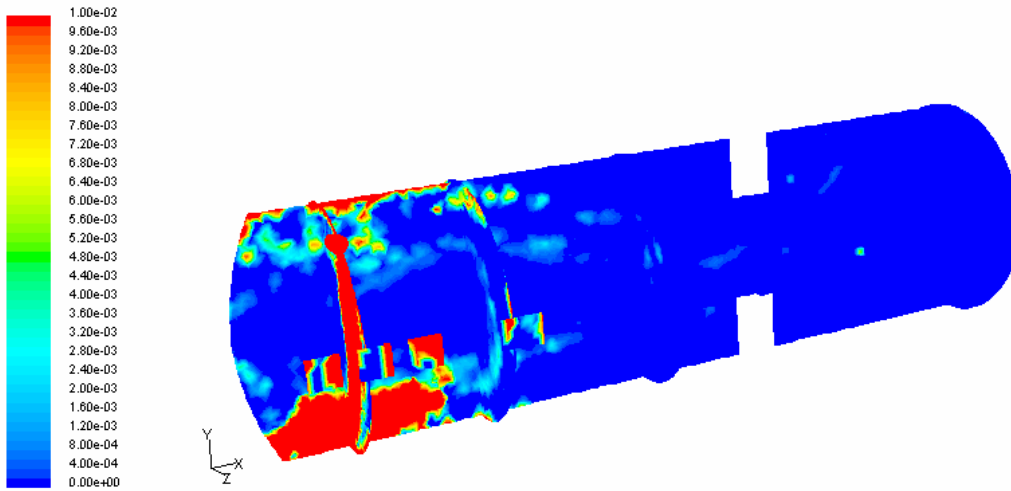


**Figure A5-46. Contour plot of particle concentration ( $\text{kg/m}^3$ ), the values on the plot are clipped to  $0.01\text{kg/m}^3$ , all concentrations above this value are in red.**

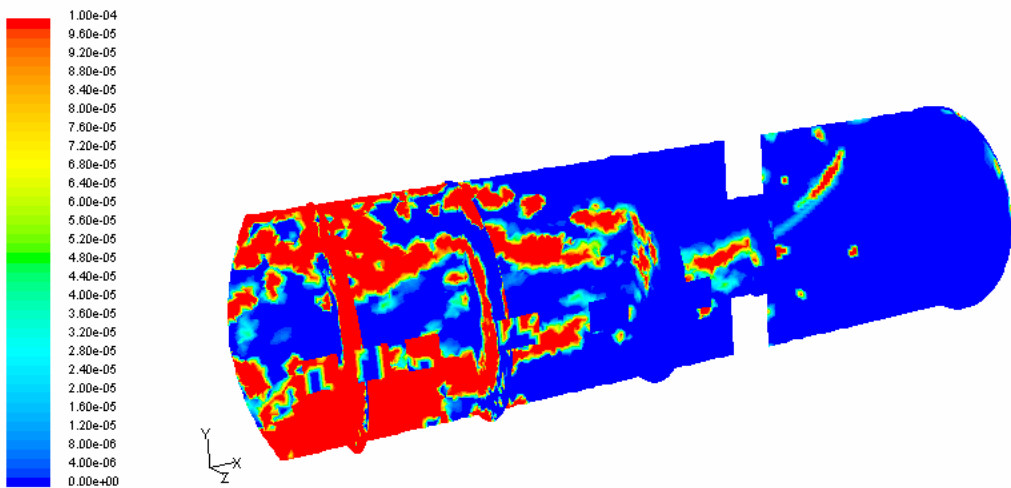


**Figure A5-47. Contour plot of particle concentration ( $\text{kg/m}^3$ ), the values on the plot are clipped to  $0.0001\text{kg/m}^3$ , all concentrations above this value are in red.**

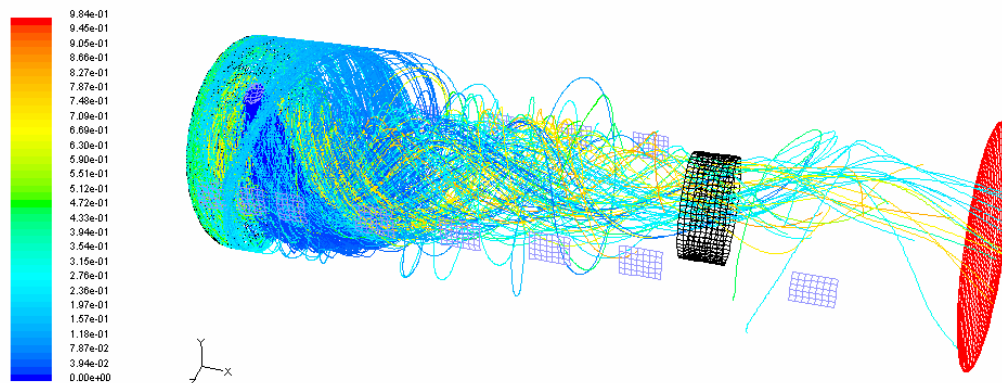


**Figure A5-48. Particle tracks colored by their residence time. Maximum residence time is about 1 second, 400 particles tracked -- 12 of them do not burn out completely**

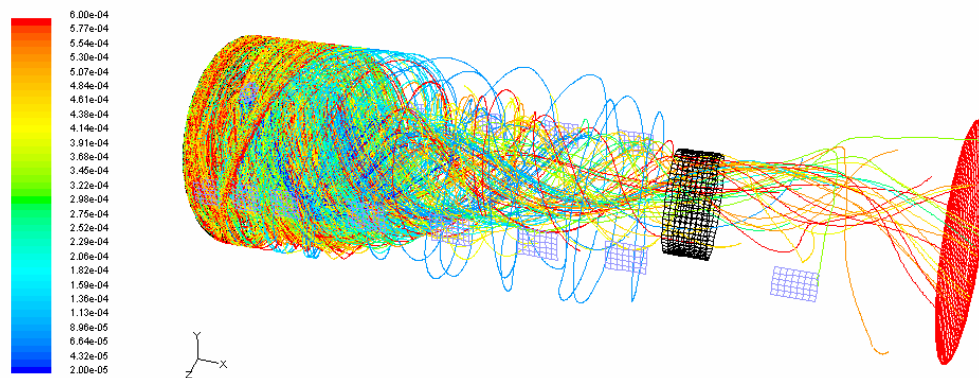


**Figure A5-49. Particle tracks colored by their diameter. Diameter range is 25 -600 microns (mean 250). Swelling coefficient is assigned as unity, so the particle diameter does not change throughout. The minimum diameter of escaped particle is 350 micron, all of the small particles burned out completely.**

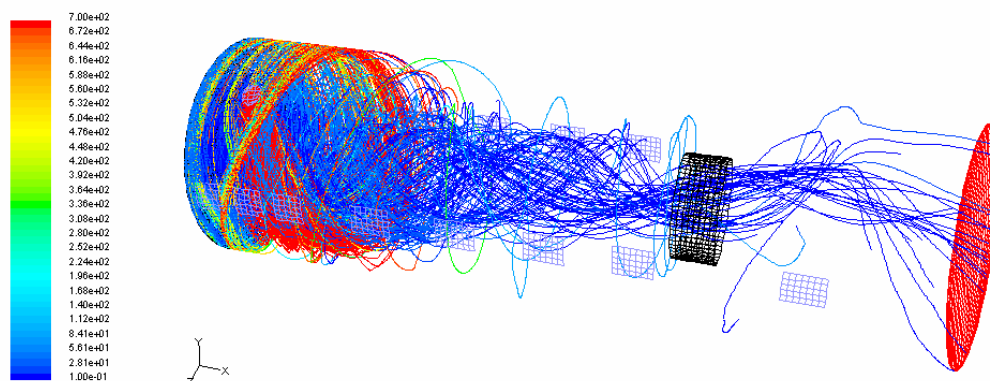


**Figure A5-50. Particle tracks colored by their density. The original density of the particle is 700 kg/m<sup>3</sup> (red). As the volatiles escape from the particle the density drops. The density of char is 49 kg/m<sup>3</sup> (dark blue).**

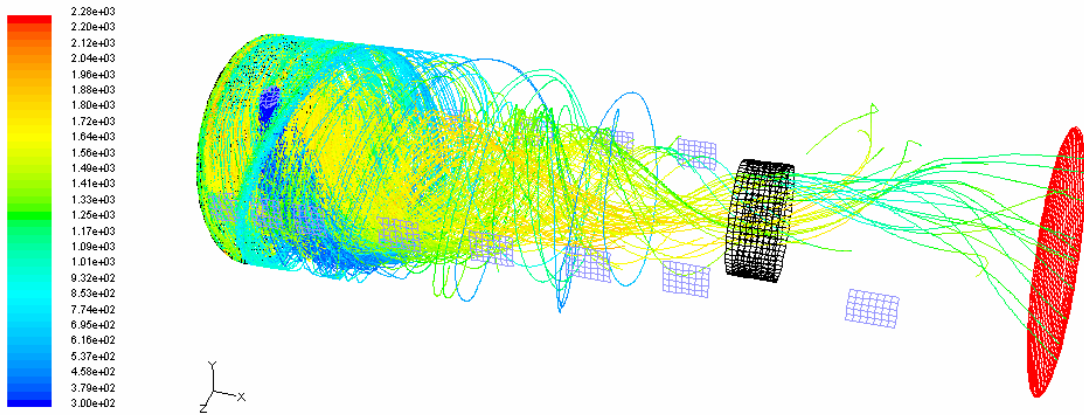


**Figure A5-51. Particle tracks colored by their temperature. Particles trapped near the wall have enough oxygen, but do not have sufficient temperature to burn, these particles have the longest residence time.**

### ***CRN Modeling of the Industrial Cyclone Burner***

The results of the chemical reactor network for the industrial wood dust burner are presented in this section. The modeling is based on the CFD results for the industrial cyclone burner described in the previous section. The CRN can be useful in analyzing the formation and reduction of nitrogen oxides emissions, particulate emission including unburned char, soot, and mineral matter. The University of Washington chemical reactor code is used for CRN development. As mentioned earlier, the application of wood dust combustion in the chemical kinetic code is developed in Malte et al. (1996) and Malte and Nicol (1997).

The CFD simulation shows that even for overall lean fuel-air equivalence ratio locally rich conditions exit in the core of the flame. Figure A5-41 shows oxygen concentration in the burner. Note a typical diffusion flame characteristic: the fuel rich flame core in the center surrounded by combustion air on the outside. The flame front is located at the interface between the locally rich and lean mixtures. This situation is a reverse of the laboratory wood dust burner described in the earlier section, where the rich mixture is located near the combustor walls.

Similar to the CRN for the UW laboratory wood dust burner, the CRN for the industrial cyclone combustor consists of two parallel streams. The inner stream represents the rich combustor core and the outer stream represents the combustion air near the walls of the burner. Figure A5-52 shows the CRN diagram of the industrial wood burner. Combustion air enters the burner through 14 air ports, which are categorized into three combustion air zones by the burner manufacture. Zone 1 brings in 20% of combustion air, zone 2 –

30% and zone 3 – 50%. The chemical mechanism is described in the laboratory burner modeling section.

The fuel (wood and resin) and transport air enter the CRN in PSR2. Figure A5-44 shows high tar concentration close to the wood entrance suggesting that the wood particles devolatilize to tar and light gases ( $\text{CO}$ ,  $\text{CH}_4$ ,  $\text{C}_2\text{H}_4$ , etc.) rather quickly. The tar and light gases enter the combustor fuel rich core represented by PFR 4. Since the flame anchors downstream of the first two air inlets, most of the zone 1 air also penetrates into the rich flame core. The amount of zone 1 air in this zone is found based on the carbon monoxide concentration (about 15%, see Figure A5-42) and temperature in the rich flame core. In the absence of oxygen the tar formed in the primary pyrolysis of the wood particle undergoes secondary pyrolysis, this element produces large amounts of free radicals and carbon monoxide. The next element, PST 6 represents the fuel rich inner flame zone of the flame (with temperature assigned from the CFD). As the rich mixture moves toward the flame front, more oxygen becomes available for combustion due to the turbulent diffusion of zone 2 combustion air. The fuel-air equivalence ratio in PST 6 is about 1.3, this  $\Phi$  assignment is somewhat arbitrary but it is necessary to facilitate fuel nitrogen conversion to  $\text{N}_2$  rather than to  $\text{NO}$ . The element is modeled as a PSR at the assigned temperature (1800K); the temperature is obtained from the CFD solution (Figure A5-40). The flame front is modeled in PST 8 at assigned temperature of 1800 K. The fuel-air equivalence ratio in the element is unity; it is set by allowing more combustion air from near the wall region to mix with the gases from PST 6.

The region near the wall contains mostly combustion air and the chemical reactions in this region are quenched. In the CRN this region is represented by a series of the MIX elements. The two parallel streams are mixed in the

PFR 13 which represents the combustor choke. Though the CFD simulation shows that the combustion might not be completed at the choke plane, the burner extension and the addition of the secondary air are not modeled by the CRN. The region downstream from the choke is not very important for NO chemistry, and since the primary purpose of this CRN is NO formation, modeling the burner extension is not conducted with the CRN.

Using the full chemical mechanism, a parametric analysis is performed to find the NO formation dependency on the fuel nitrogen percentage. The fuel nitrogen is adjusted by introducing high nitrogen resin in the fuel stream. The wood fuel nitrogen is small (0.086%), however with the addition of the high nitrogen resin the total fuel nitrogen mass fraction is taken as high as 5.65%. In the literature search, very little NO<sub>x</sub> emission data is found for wood dust combustion. Fry, (1993) points out that virtually no documented emissions are found in the literature for wood dust combustion systems. The author mentions that for boiler applications the NO<sub>x</sub> emissions of the system fired on the clean wood is about 0.25 lb/MMBTU. However, these emissions would vary for different wood species as well as for wood waste fired systems. Nichols, 2004 suggests that NO<sub>x</sub> emissions of the typical suspension wood dust burner operated on resin containing fuel is in the range of 100-200 ppmvd, corrected to 18% O<sub>2</sub>.

The results of the CRN modeling are presented below. Figure A5-53 shows the fuel N to NO<sub>x</sub> conversion as a function of fuel nitrogen content. The conversion of fuel nitrogen to NO<sub>x</sub> is the smallest at the highest fuel N contents (5%). Figures A5-54 and A5-55 show the predicted NO<sub>x</sub> emissions as a function of the fuel nitrogen. The predicted emissions are close to the experimental levels reported by Fry (1993) and Nichols (2004). The NO emissions level off at the higher fuel nitrogen mass fraction due to the low fuel

N to NO<sub>x</sub> conversion. This conversion occurs in the rich inner flame zone (PSR 6) at fuel-air equivalence ratios of 1.1-1.4.

The CRN can be a valuable tool for predicting and analyzing the NO<sub>x</sub> formation in the wood dust combustion systems. It also can be used for optimizing the combustion condition in the burner to achieve the lowest fuel N to NO<sub>x</sub> conversion. However, the main difficulty in developing such a CRN is obtaining reliable CFD simulations for the combustor. The CRN developed herein could be used to explore the effects of core zone temperature and fuel-air ratio on NO<sub>x</sub> emission. Typically, the greatest conversion of fuel N to N<sub>2</sub> occurs when  $f$  is in the 1.3-1.5 range and the temperature is high.

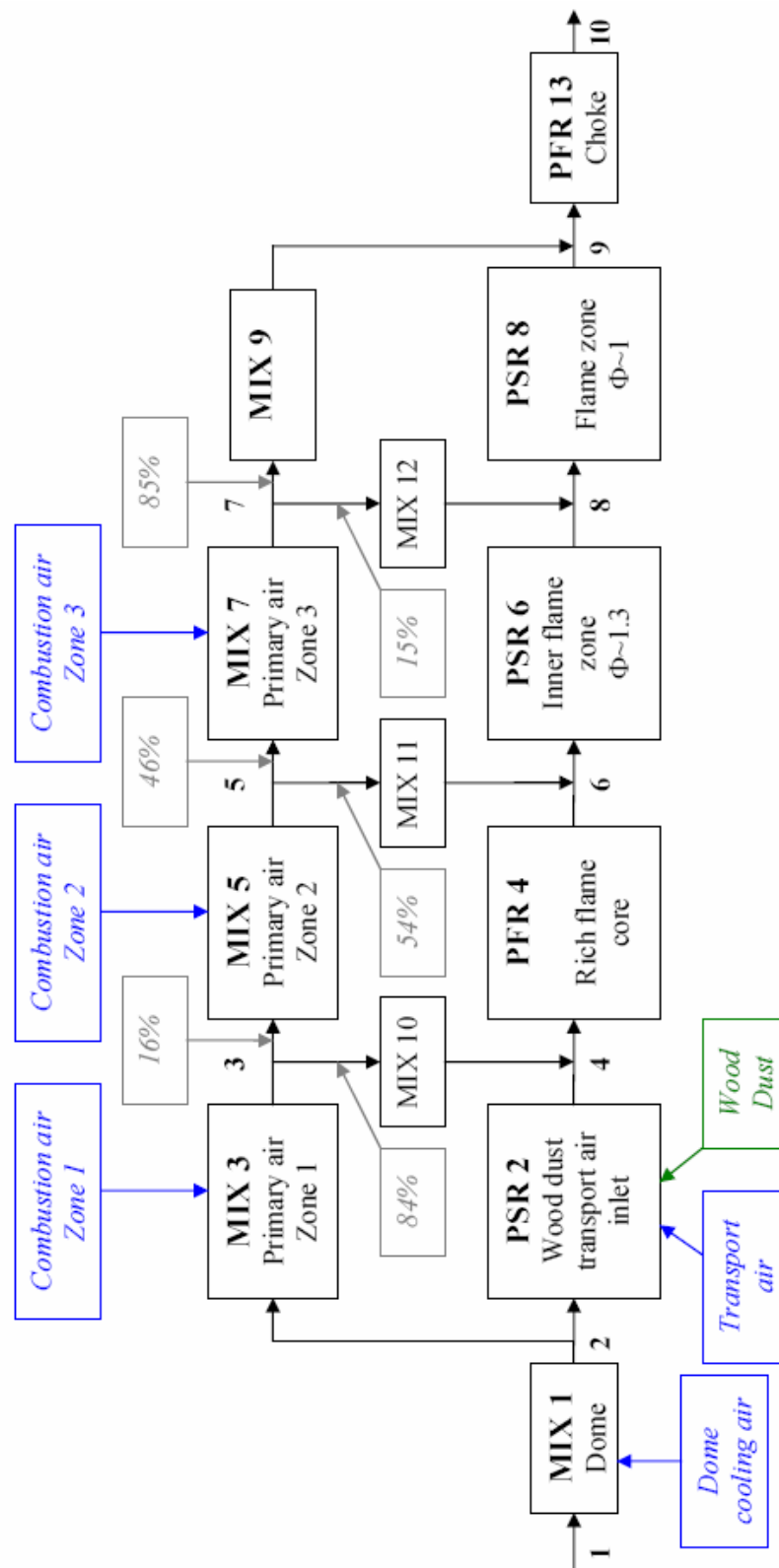


Figure A5-52. Chemical reactor network for industrial cyclone wood dust burner

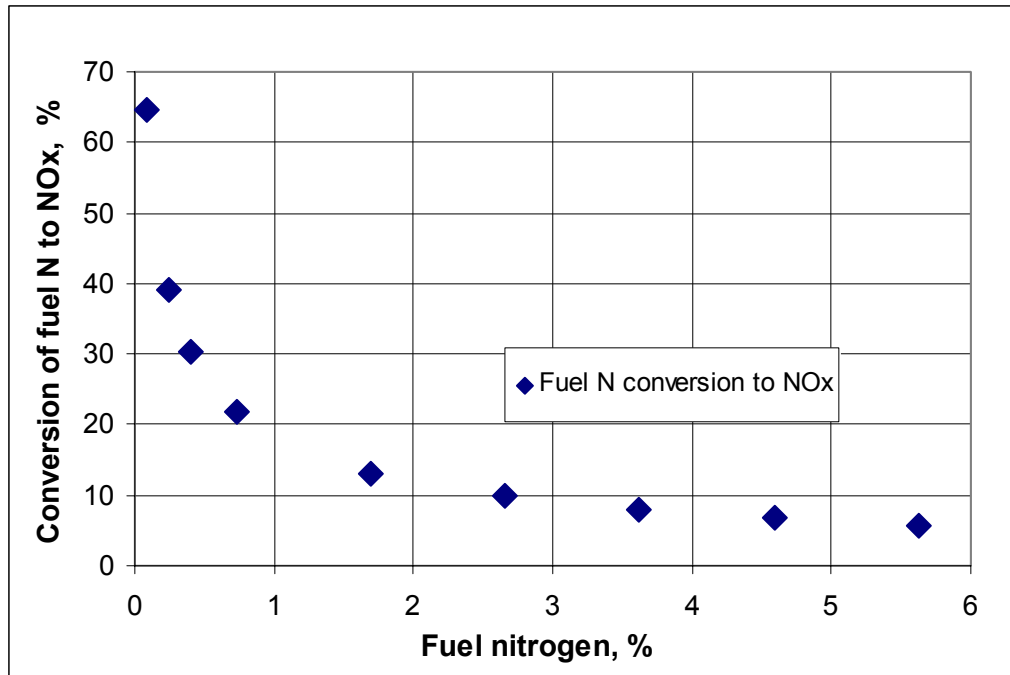


Figure A5-53. CRN fuel N to NO<sub>x</sub> conversion prediction for industrial cyclone wood dust burner.

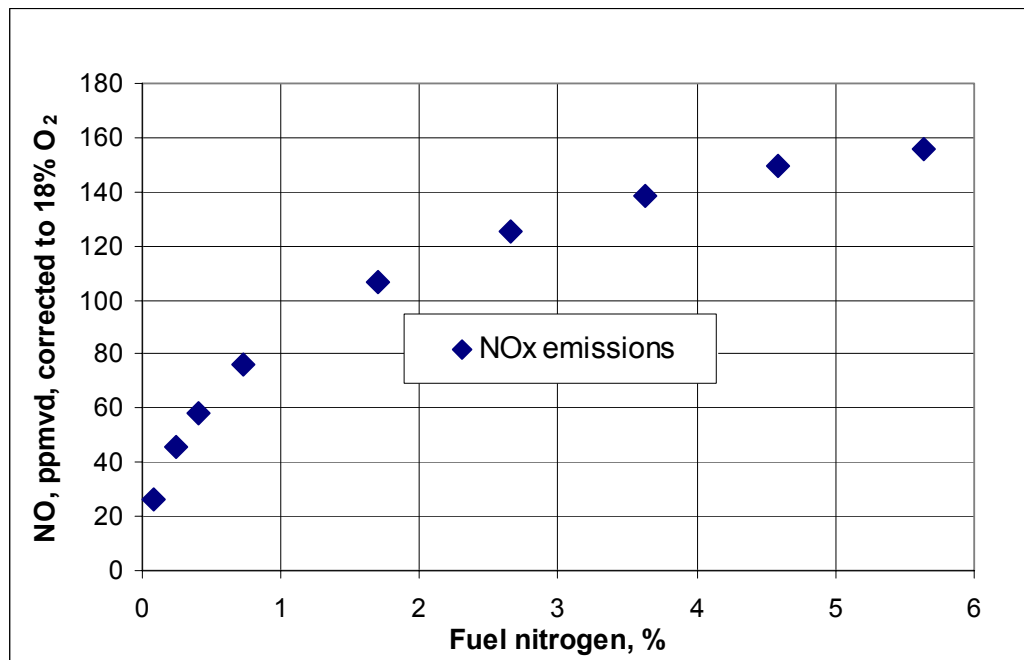
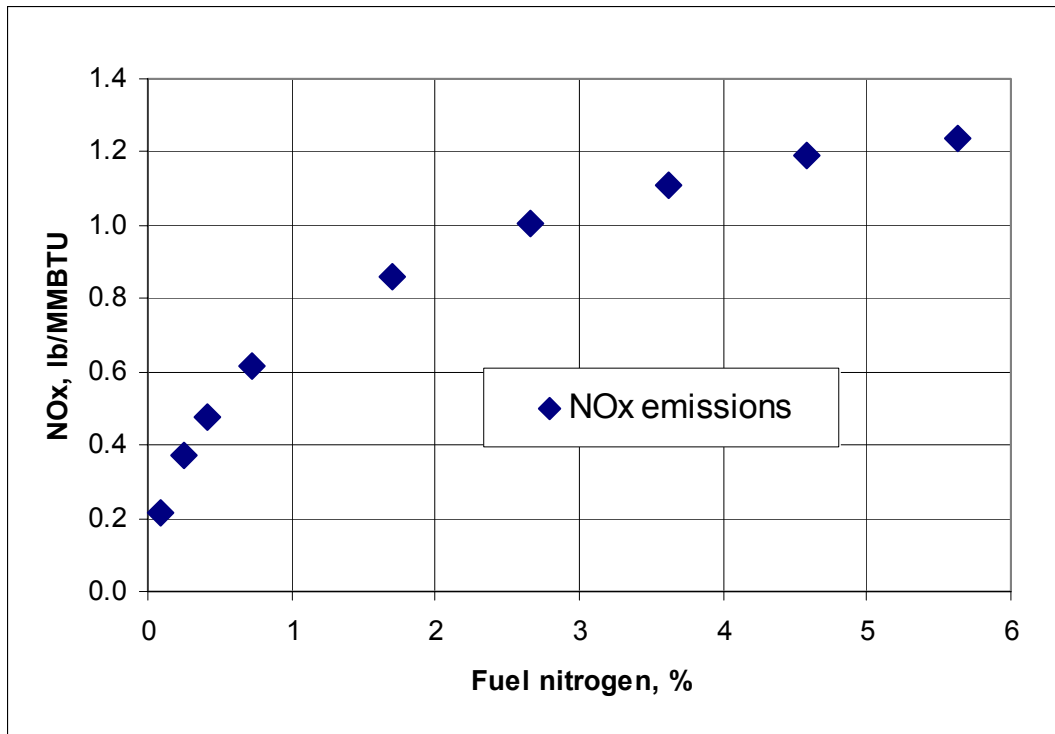


Figure A5-54. CRN NO emission prediction (ppmvd at 18%O<sub>2</sub>) for industrial cyclone wood dust burner.



**Figure A5-55. CRN NO<sub>x</sub> emission prediction (lb/MMBTU) for industrial cyclone wood dust burner.**

## Vita

I was born in a small town of Belovo, Russia. At age of four my family moved to Yaroslavl where I spent most of my young years. Growing up I was heavily involved in the sport of gymnastics. I graduated from high school in 1988 and started my studies at Yaroslavl Polytechnic University. After graduating in 1993, I started to work and did many different things: engineering, English-Russian translation, gymnastics instruction. In 1999, I entered the University of Washington, where I earned the MSME degree in 2002 and the PhD degree in 2006.

My areas of interest are computer modeling of flow systems including two-phase flow and combustion systems.

### Education:

Jan 2002 - Mar 2006      **University of Washington**, Seattle, WA  
 PhD 2006, Defended Dissertation: "Chemical Reactor Networks for Modeling Combustion Systems."  
 Sep 1999 – Jan 2002      **University of Washington**, Seattle, WA  
 MSME 2002, Defended thesis: "Eight-Step Global Kinetic Mechanism on Methane Oxidation with Nitric Oxide Formation for Lean-Premixed Combustion Turbines."  
 Sep 1997 - Aug 1998      **University of Idaho**, Idaho Falls, ID  
 Part time graduate study  
 Aug 1988 – July 1993      **Yaroslavl Polytechnic Institute**  
 Mechanical Engineer 1993, with high honors.  
 Defended Thesis: Modeling of Injector Pump Regulator

**Languages:**      Russian – fluent, English – fluent

**Computer skills:** CFD software (Fluent, Star CD, Gambit, ProAm), Chemical Reactor Modeling Software, Techplot, Matlab, Maple, experience with MAC OS, Unix OS, Windows, parallel computing

### Work Experience:

Feb 2006 – present      **Enertech Inc**, Maple Valley, WA  
 Senior Research Scientist: Modeling and validation of two-phase flows systems in bio-medical applications  
 Jan 2000 – Mar 2006      **University of Washington**, Seattle, WA  
 Research Assistant / Teaching Assistant: Fluid Dynamics and Chemical Kinetics Modeling of turbulent combustion systems, such as: lean-premixed gas turbine combustors, cyclone wood dust burners; modeling of liquid fuel injectors and atomizers

- Sep 1998 - present      **Seattle Gymnastics Academy**, Seattle, WA  
                                  Head Coach: training competitive gymnastics team, supervising other  
                                  instructors, developing curriculum
- July 1995 – Aug 1998      **Idaho Falls Gymnastics Training**, Idaho Falls, ID  
                                  Head Coach: training competitive gymnastics team, supervising other  
                                  instructors, developing curriculum
- Sep 1994 – June 1995      **GlavNeftMetal**, Moscow, Russia  
                                  Commercial Director: supervising commercial activity in a brokerage firm
- Aug 1993 – Sep 1994      **Yaroslavl Diesel Equipment Corp.**, Yaroslavl, Russia  
                                  Mechanical Engineer - Design and repair of injection pumps
- Aug 1988 – July 1993      **Yaroslavl Olympic School of Artistic Gymnastics**, Yaroslavl,  
                                  Russia  
                                  Gymnastics coach: training of competitive gymnastics team

**Contact information:**      Email: [ivn@u.washington.edu](mailto:ivn@u.washington.edu)